Mathematical modelling of flow and transport phenomena in tissue engineering

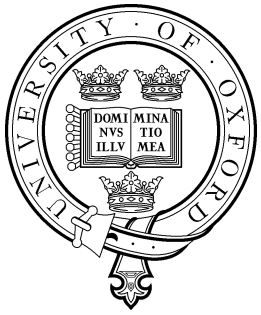

Natalie C. Pearson
Corpus Christi College
University of Oxford

A thesis submitted for the degree of
Doctor of Philosophy

Trinity Term 2014

Mathematical modelling of flow and transport phenomena in tissue engineering

Natalie C. Pearson
Corpus Christi College, University of Oxford
A thesis submitted for the degree of *Doctor of Philosophy*

Trinity Term 2014

Tissue engineering has great potential as a method for replacing or repairing lost or damaged tissue. However, progress in the field to date has been limited, with only a few clinical successes despite active research covering a wide range of cell types and experimental approaches. Mathematical modelling can complement experiments and help improve understanding of the inherently complex tissue engineering systems, providing an alternative perspective in a more cost- and time-efficient manner.

This thesis focusses on one particular experimental setup, a hollow fibre membrane bioreactor (HFMB). We develop a suite of mathematical models which consider the fluid flow, solute transport, and cell yield and distribution within a HFMB, each relevant to a different setup which could be implemented experimentally. In each case, the governing equations are obtained by taking the appropriate limit of a generalised multiphase model, based on porous flow mixture theory. These equations are then reduced as far as possible, through exploitation of the small aspect ratio of the bioreactor and by considering suitable parameter limits in the subsequent asymptotic analysis. The reduced systems are then either solved numerically or, if possible, analytically. In this way we not only aim to illustrate typical behaviours of each system in turn, but also highlight the dependence of results on key experimentally controllable parameter values in an analytically tractable and transparent manner. Due to the flexibility of the modelling approach, the models we present can readily be adapted to specific experimental conditions given appropriate data and, once validated, be used to inform and direct future experiments.

Acknowledgements

First and foremost I would like to thank my supervisors Becky, Jim, and Sarah. I have learnt an incredible amount from each of them and am extremely grateful for their time and patience, especially in the last few months of writing up. Most of all, their enthusiasm and sense of humour has made the last three years all the more enjoyable. On the experimental side, I would also like to thank Marianne and her group in Bath for many beneficial visits and helpful discussions.

I would like to acknowledge EPSRC for funding me through the Systems Biology DTC, and the Mathematical Institute for enabling me to go on several interesting conferences and study groups.

I have made many friends during the course of my DPhil: the DTC class of 2010 made the first year truly enjoyable, and I have valued their continued friendship as we went our separate ways for our research projects. I have also enjoyed being part of OCIAM and the wider Maths Institute and will miss the daily coffee and lunch time chats.

As a graduate student, I was fortunate to have the chance to teach at several colleges and am especially thankful for the opportunities given to me at Corpus as a lecturer. The alternative focus of undergraduate teaching was a rewarding experience which complemented my doctoral research and which I thoroughly enjoyed.

Further thanks are due to the fantastic teachers I had during my school years, in particular Mrs Bentley and Mrs Hardern for their help and encouragement during my application to Oxford. I am lucky to have always been surrounded by an incredibly loving and supportive family. I have fond memories of Gran teaching me times tables on family walks in Yorkshire, as a young child with a growing interest in maths. My parents, Jo and Mark, and brother James have always had confidence in me and have been a much appreciated source of support throughout my studies. Finally, I thank my husband Alex, for his continual love and friendship, and constant belief in me.

for my family, with love

Contents

List of Figures

List of Tables

Chapter 1

Introduction

The field of tissue engineering covers a wide spectrum of techniques, all with the central aim of developing biological replacements for damaged tissue or organs. When tissue function is impaired due to disease, trauma, or old age, current therapies generally rely upon donor transplants or artificial implants. However, there is a chronic shortage of donors: for example, there are approximately 27,000 deaths from liver disease annually in the United States, but less than 7,000 transplants take place. In addition, US waiting lists for all organ transplants are growing by around 5% each year [53]. Even when a suitable donor can be found, additional complications can arise due to infection or rejection of the new tissue. Issues can also arise from the artificial materials used, for example, in hip and knee replacements; these have a limited lifespan and may cause allergic reactions [137]. As a result of our ageing population and the limitations of existing approaches, there is an increasing clinical need for alternative procedures. The potential impact is great: a 2001 review by Lysaght and Reyes [97] reported that tissue replacement treatments account for around 8% of all medical expenditure worldwide, at an annual cost of $350 billion. Tissue engineering is a promising alternative providing it can be made affordable on a clinical scale. The implantable tissue can be grown using cells which are often much more readily available than donor organs, removing the problem of supply shortage and reducing waiting times. In addition, in the cases where the patient's own (autologous) cells are used, there is a significantly reduced risk of rejection and viral infection and hence an improved prognosis [158].

There are two main approaches to tissue engineering: *in vivo* and *in vitro*. Both can involve the expansion of a cell population which is then seeded onto a biocompatible scaffold, designed eventually to degrade and be fully replaced by extracellular matrix [100, 158]. The *in vivo* method transplants the cell-seeded scaffold (which we refer to as the cell-scaffold

construct) directly to the appropriate site in the body where it is left to develop and integrate into the surrounding tissue over time (see *e.g.* [55, 157]). For *in vitro* tissue engineering, which is the focus of this thesis, the construct is first cultured in a bioreactor. This closed, fluid-filled system allows extra control of the tissue's mechanical and chemical external environments as it grows. Only once the desired quantity and type of fully developed, functional tissue is produced is it then implanted into the body (see [34, 158]). Figure 1.1 gives a schematic overview of the *in vitro* process. Tissue constructs engineered in this way can also be used for toxicity testing in the development of drugs. This reduces the need for animal testing and, as human cells are used, is also more reliable in predicting adverse effects of drugs earlier on in the development process, minimising the occurrence of drug withdrawal at later stages and significantly reducing the associated costs [36, 102, 167, 179, 183].

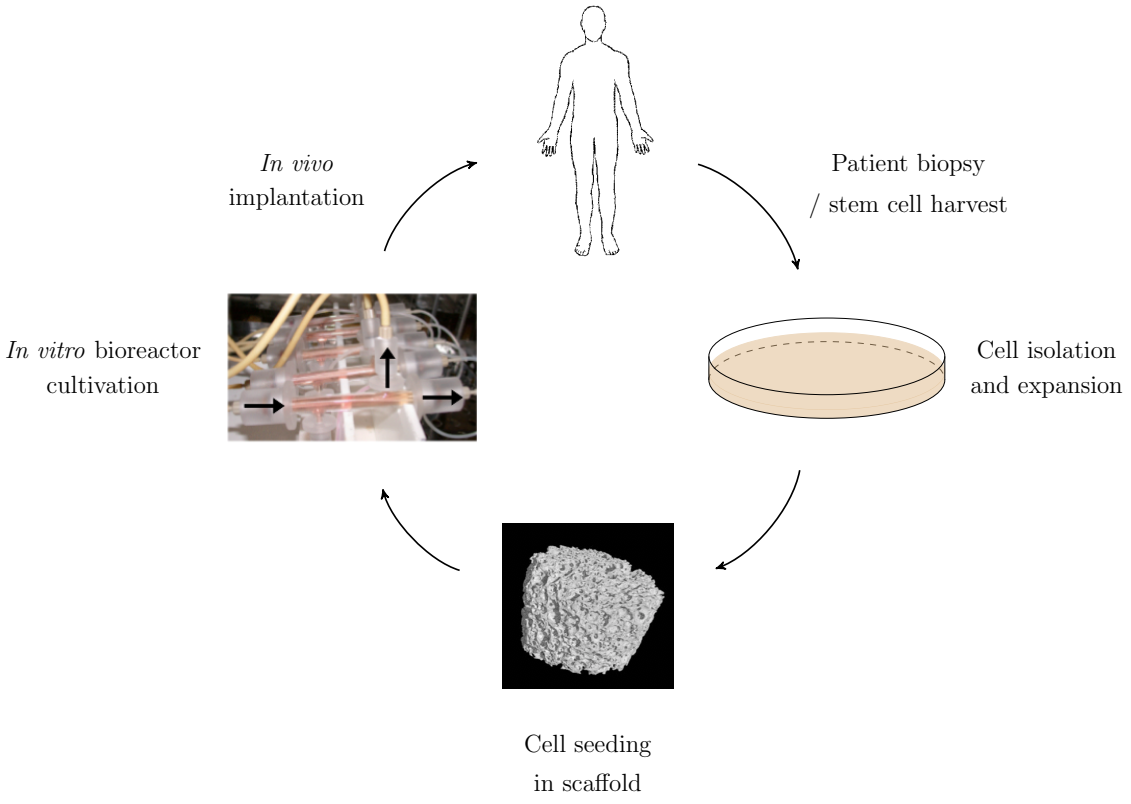

Figure 1.1: Overview of the *in vitro* tissue engineering process (based on figures from [30, 34, 103, 158]). Bioreactor photo courtesy of the Tissue Engineering Group, University of Bath.

This thesis focusses on one particular bioreactor, namely a single-module hollow fibre

membrane bioreactor (HFMB), which is currently under investigation for use in bone, cardiac, and liver tissue engineering by Dr Marianne Ellis' group in the Centre for Regenerative Medicine, University of Bath. This bioreactor can be used in numerous configurations for a variety of purposes, including cultivation of a tissue, and expansion and/or differentiation of a cell population. We have developed a number of mathematical models for the fluid flow, mass transport, and cell dynamics within these systems, investigating the possible cell yields and distributions which arise from different experimental regimes. In §1.1 of this chapter we discuss in more detail the biological background to tissue engineering, including a detailed description of the HFMB setup, why and when it is used in preference to alternative experimental approaches, and open questions which we aim to address through the modelling work in this thesis. We motivate these models in §1.2 by illustrating how mathematical models can aid experimental progress. We also review the relevant experimental and theoretical literature, including the different mathematical modelling approaches which are commonly employed. An outline of the thesis is given in §1.3, in which we summarise the aims and methods of each chapter in turn. In §1.4 we present the generalised mathematical model which forms the basis for the more specialised models in each chapter. Finally, in §1.5 we summarise the novel aspects of this work, including details of existing and submitted publications arising from this thesis.

1.1 Biological background

We begin this section by reviewing the existing successes and remaining challenges in tissue engineering, before discussing in more detail several important features which must be taken into consideration when pursuing research in this field: the cell types under investigation and their sources, the cell processes involved, and choices of scaffold materials and bioreactor designs. The section concludes with a description of the HFMB setup which is the focus of this thesis.

1.1.1 Successes and challenges in tissue engineering

There have been a number of notable achievements in tissue engineering to date. Many skin substitutes have been developed and implemented clinically [60], and cartilage defects have been repaired using *in vitro*-expanded chondrocytes [19]. More recently, Jungebluth *et al.* reported a successful tracheobronchial transplant using an engineered substitute [73].

These are just a few of the numerous success stories in the field; however, a number of challenges remain. Firstly, the vast range of cell types which are under investigation are extremely sensitive to their surrounding environment and so a specially tailored experimental setup is needed for each to enable them to grow [105]. Thus, progress for one particular cell or tissue does not necessarily inform research on another. Secondly, advances thus far have been limited to tissues which are relatively thin (effectively two-dimensional, such as skin) or avascular (such as cartilage) [103, 158]. The reason for this lies in nutrient supply constraints. Without a network of blood vessels to transport nutrients and waste products, the cells must rely on diffusion alone to receive the nutrients necessary for survival. For thin or avascular cell types as mentioned above this does not pose a problem, but once a tissue reaches a certain thickness (depending on the tissue type, this can be just a few hundred micrometres), the supply of nutrients via diffusion is no longer able to balance the metabolic requirements of the cells. As a consequence, cells start to become nutrient depleted and necrotic regions can form [61, 104]. This highlights the importance of being able to vascularise engineered tissue, which is a focus of ongoing research [30] and notably absent from clinical solutions to date. Finally, laboratory-scale experiments are extremely expensive, which has further limited scale-up to viable clinical procedures.

1.1.2 Cell types

As mentioned above, research into tissue engineering covers a wide variety of cell types, encompassing most tissues and organs present in the human body; see [158] and references therein for a summary of active research areas. Each therapy requires an initial cell population, and in deciding upon the most appropriate cell source there are a number of choices to be made. Firstly, the cells can be autologous (obtained from the patient via a biopsy), allogeneic (from *e.g.* a human donor or embryo), or even xenogeneic (from a different species). Autologous cells are desirable for reasons already stated, but a direct biopsy may not always be possible (for instance in the case of neural tissues [158]), or a sufficient quantity of healthy cells may not be available [38]. All other sources bring with them the risk of disease transmission and immunological rejection, and whilst embryonic and xenogeneic sources avoid the problem of low yields, they raise many complicated ethical issues [60, 146].

No matter what the primary source of cells, there is also the choice of nonspecific (stem) cells, tissue-specific cells, or a mixture of the two. Stem cells are difficult to isolate and identify, but in general have a high proliferative capacity and the potential to differentiate into

many different cell types [43,60,146]. However, once the population has been expanded various growth factors must be supplied in order for the cells to differentiate into the required type, and controlling this process is not necessarily straightforward [30,158,161]. Differentiated cells do not have this additional complication, yet also do not proliferate as readily. Therefore obtaining a sufficiently large population of such cells can be a challenge [38,144].

Given that there are significant drawbacks no matter which route is taken, there is a significant amount of ongoing research dedicated to overcoming these problems. Finding alternative sources of stem cells which avoid the ethical problems associated with the use of embryonic stem cells is a core focus. One example is mesenchymal stem cells (MSCs) which are found in various adult human tissues [139,168]. Perhaps more promising, as they avoid the need for invasive procedures, are stem cells obtained from the placenta [52], umbilical cord blood [90], umbilical cord tissue [96], or dental pulp [63,78]. Current work also includes improving cell isolation and identification protocols, and developing techniques to increase the proliferative capacity of cells in culture [27,34,139,168].

1.1.3 Cell processes

Cells are extremely sensitive to their surrounding environment, and processes such as cell migration, proliferation, and differentiation, to name but a few, can all be affected by cues in their external environment [22]. The models presented in this thesis will include the effects of both chemical and mechanical signals on cell dynamics, and in the following we discuss biological examples relevant to our modelling.

Chemical sensitivity

We will consider several forms of chemical sensitivity in our modelling. Firstly, nutrient concentration can affect rates of cell proliferation. One example of this behaviour is the regulation of fibroblast proliferation rate by oxygen concentrations [116]. Chemical signals will also be included in the form of chemotaxis, that is the directed movement of cells in response to a chemical concentration gradient. We consider chemicals, known as chemoattractants, which induce cellular movement up gradients in their concentration. Such behaviour has been documented experimentally for several cell types, including neutrophils in response to varying interleukin-8 concentrations [71], fibroblasts subject to gradients in transforming growth factor (TGF)-β concentration [138], and osteoblasts exposed to variations in vascular endothelial growth factor (VEGF) [107]. In addition, recent advances

include work on quantifying the speed of fibroblast migration through collagen constructs for given oxygen concentration gradients [10]. Finally, differentiation of one cell type into another can be stimulated by chemical cues in their environment, often by growth factors. Several examples of this type of stimulus exist in the literature, in particular relating to osteogenesis [106, 110] and endothelial differentiation [18, 106, 132].

Mechanical sensitivity

Mechanotransduction is the name given to the mechanism by which physical forces are converted into biochemical signals and integrated into a cellular response [69]. Specifically, the mechanical effect that we will consider is that of fluid shear stress on both cell proliferation and differentiation. Firstly, cell proliferation can either be enhanced or inhibited by increased levels of fluid shear stress. Cells whose proliferation is enhanced include osteoblasts [74], chondrocytes [101], and (more controversially) endothelial progenitor cells [185], whilst inhibited proliferation has been observed in smooth muscle cells [127] and certain types of endothelial cells (*e.g.* human aortic endothelial cells [70] and human umbilical vein endothelial cells [4]). Secondly, cell differentiation can be induced mechanically as well as chemically. Examples of cell types whose differentiation rates are enhanced as a result of applied fluid shear stress include osteoblasts [13, 74] and endothelial cells [118, 184].

Finally, as well as having potentially important effects on proliferation and differentiation rates, fluid shear stress is thought to be an important factor in ensuring the mechanical integrity of tissue such as bone and cartilage, stimulating higher rates of matrix deposition and cartilage formation, respectively [15, 54]. Thus levels of shear stress experienced by cultured cell populations are an important consideration for tissue engineering research.

1.1.4 Scaffolds

Irrespective of the particular tissue engineering application, there are a number of essential criteria which a scaffold must meet. Most importantly, the material needs to be biocompatible in order for it to safely and successfully integrate with the host tissue upon implantation. For this reason, natural materials such as decellularised allogeneic or xenogeneic matrices are a promising option for scaffolds, although artificial polymers such as polyglycolide (PGA) can also be used. Synthetic substances offer additional advantages: for example, properties such as surface hydrophobicity/hydrophilicity or degradation rate can be carefully controlled [43, 158]. Growth factors or other signalling molecules can also be incorporated

into a scaffold during the manufacturing process, and their subsequent release over time as the polymer degrades offers an alternative and predictable way of delivering these chemicals to the growing tissue [38, 43]. For more examples of scaffold materials, see [38, 43, 158, 161].

A vital role of a scaffold is to provide structure to the seeded cell population given the initial lack of extracellular matrix (ECM). Hence the material chosen for the scaffold must be able to withstand any mechanical loading (*in* and/or *ex vivo*) and retain the desired shape of the construct. This is particularly crucial, for instance, in bone regeneration, where the engineered tissue will be under a significant amount of stress/strain in the body [43, 146]. However, over time the cells will produce ECM until eventually the scaffold is no longer needed. Therefore the material must also be biodegradable: ideally, the degradation should be controlled to complement ECM deposition and ensure a smooth transition from cell-scaffold composite to functional tissue [79, 146, 161].

Additional desired features of a scaffold are related to its internal architecture. Firstly, the porosity and pore size must be such that cells can be seeded at a high enough density throughout the construct. Secondly, the permeability must also allow sufficient nutrient/growth factor delivery to, and waste removal from, the cell population. Both of these need to be achieved without compromising the mechanical integrity of the scaffold. The surface properties can also greatly affect tissue development. Cells must be able to adhere to and interact with the scaffold to a certain extent, but should also be free to migrate where necessary [146]. Finally, as mentioned above, scaffolds can aid in the delivery of chemicals which need to be supplied to the cells over a long period of time, once the construct has been transplanted into the patient, or to specific regions of the tissue. For example, this may be the case with certain growth factors if the rate and extent of cell differentiation needs to be carefully controlled, or to encourage the onset of angiogenesis. In such a situation the scaffold can be impregnated with the necessary chemicals and designed to release them at the required rate and time [43, 79, 115].

Clearly, affordably manufacturing a scaffold to meet the above requirements is a complex process, and the result can have a huge impact upon the success or failure of a procedure. The challenge is not only to find an appropriate material and design for a given tissue type, but also a successful fabrication procedure, which can greatly affect the end result [79]. As such a great deal of ongoing research concerns the development of methods and materials which can reliably generate a scaffold with the desired characteristics [115, 144, 158].

1.1.5 Bioreactors

As a further consequence of the sensitivity of cells to their surroundings, bioreactors must mimic the *in vivo* environment as closely as possible in order to successfully grow functional tissue. Experimental requirements may also differ for separate stages of the culture process, for example cell population expansion compared to differentiation [83]. As a result of this, a vast array of bioreactor designs exist, and within each of these optimal operating conditions need to be found for each cell and/or tissue type. The simplest bioreactors involve static culture, in which cells are bathed in culture medium containing the necessary nutrients and growth factors. Here, there is no flow of fluid through the bioreactor; instead the culture medium is replenished when needed to remove potentially toxic waste products. Such systems are primarily used for monolayer cell cultures, and examples include a Petri dish or T-flask. Although appealing in their ease of use, there is a limit to the number of cells which can be grown in such setups due to the physical size of the vessel and the fact that mass transport is dependent solely on diffusion. Furthermore, there is relatively little control over the extracellular environment [95, 105, 137].

To improve nutrient delivery and waste removal and thus grow larger, three-dimensional tissues with properties matching those *in vivo*, various 'dynamic' bioreactors have been developed which incorporate fluid flow. For some tissues such as cartilage and blood vessels, this has the added benefit of exposing the cells to a certain amount of shear stress which has been shown to improve tissue quality [158]. However, care must be taken to ensure stress levels do not result in damage to more sensitive cell types (*e.g.* hematopoietic stem cells) [95, 105]. Stirred or shake flasks are the simplest extension to static culture and significant increases in tissue thickness have been reported using these systems. However, tissue damage due to turbulent eddies in the flow (impeller Reynolds numbers of $O(10^4)$) has also been found and there is little scope for growing tissues on a clinical scale [104, 105, 158]. Another design is the rotating-wall bioreactor, in which the cell-scaffold constructs are placed in a fluid-filled vessel and the whole system rotated at a rate which ensures the construct is maintained in a state of free fall. This increases mass transport in a low shear stress environment, but the rotation rate must be continuously adjusted to allow for the size of the growing tissue [104, 105, 137]. A third option is the perfusion bioreactor, where fluid is pumped directly through the scaffold pores. As well as greatly improving mass transport, this setup allows constant replenishment of the culture medium and has also been shown to

result in a more uniform distribution of cells throughout the scaffold. A potential limitation of this approach is the close proximity of the cells to the imposed flow and resulting exposure to shear stresses [104]. Finally, dynamic compression bioreactors apply mechanical load to tissue during cultivation with the aim of replicating the forces experienced by cells *in vivo*; this is of importance, for instance, in bone and cartilage tissue culture and can be used in combination with perfusion or rotation of the construct [46, 47, 104].

The bioreactor upon which this thesis focusses has many features in common with the systems described above, but also a few notable differences. In the following section we describe this HFMB in detail, and explain its great potential for use in tissue engineering.

Hollow fibre membrane bioreactors

There are a variety of applications for HFMBs, including filtration in wastewater treatment [172, 180], production of biopharmaceuticals [137, 173], enzymatic reactions [75, 145], and bioartificial livers (BALs) [5,117,128,182]. For tissue engineering purposes, the main method involves using a single porous hollow fibre, or bundle of several aligned fibres, inside a bioreactor (see Figures 1.2(a) and (b)). As well as ensuring mass transport throughout the system, these fibres mimic a capillary *in vivo* [187] and could provide an initial template for vascularisation as required [48]. Cells are seeded either in the lumen of the hollow fibre(s), or in the space exterior to the fibre(s) [57, 135, 143]. Culture medium can then be perfused over the outside fibre surface(s), or through the fibre centre(s), or both. In this way, if necessary, the cells can be protected from the main fluid flow so that relatively large flow rates can be used without exposing the cells to the resulting high fluid shear stresses. In this case, the permeability of the fibre wall(s) means that the cells can still receive sufficient nutrients and growth factors. Alternatively, it is also possible to expose the cells directly to the fluid flow if desired. Thus the HFMB is ideal for both shear-sensitive cells that have high nutrient demands, such as hepatocytes [104, 135], and also cells which require a certain level of shear stress exposure (*e.g.* osteoblasts and chondrocytes, as discussed above). Furthermore, HFMBs have great potential for generating replacement tissues on a clinical scale. A key advantage of the design when used for monolayer culture is that the surface area available for seeding cells is large compared to the bioreactor volume, providing efficient mass transfer conditions and minimising the use of expensive growth factors [57]. As a specific comparison to standard flask culture, a 1000 l flask would be required in order to grow the same number of cells as in a 0.5 l HFMB, assuming a monolayer seeded on

the fibre surface [156]. In addition, HFMBs are capable of growing cells at high densities, even comparable to those of tissue *in vivo* [85,86,165]. Finally, using bioreactors containing multiple parallel fibres opens up the possibility of generating tissues or quantities of cells on a larger (and eventually clinical) scale.

In spite of the above, using HFMBs for tissue engineering is still very much an open research area, and outstanding questions include how best to tune the operating conditions to obtain the desired final cell yield or distribution (*e.g.* uniform or non-uniform), and how to ensure sufficient delivery of nutrients to, and removal of waste products from, the cells. Only when these issues have been resolved will such procedures present feasible and affordable future alternatives to current tissue replacement strategies. Experimental parameters which can be varied include bioreactor geometry, fibre porosity and permeability, seeding regime, inlet fluid flux values, flow regimes, and concentrations of culture medium components. Hence in order to determine these optimal operating conditions, a significant amount of research must first be carried out at the laboratory scale.

Answering such questions is the aim of work being carried out by Dr Marianne Ellis' group in the Centre for Regenerative Medicine, University of Bath. Their system consists of a cylindrical, hollow glass module with a port at each of the up- and downstream ends (see Figure 1.2(a)). A single synthetic, porous hollow fibre (which is impermeable to cells) is inserted through the centre and fixed to the module at the ends. The choice of fibre materials can vary, but recent research has focussed on using poly(vinyl alcohol)-poly(lactide-co-glycolide acid) (PVA-PLGA), which results in fibres which are more hydrophilic than those made using PVA alone, removing the need for wetting agents [109, 156]. Here, cells are seeded in the ECS; there are two main methods to achieve this. The first involves suspending the cells in a collagen gel solution which is then injected through the ports, and the gel left to set (see [187] for more details). This results in a cell-seeded natural scaffold occupying all, or part of, the extracapillary space (ECS), and is applicable when growing a three-dimensional tissue; the models developed in this thesis are based upon such a setup. In the second method, which is an appropriate choice when expanding a cell population, cells are suspended in culture media and the mixture is again injected through the ports. The bioreactor is then rotated for a period of time to allow the cells to settle on the outer surface of the fibre, forming a layer of attached cells [48]. Culture medium is then driven through the fibre lumen and/or the ECS ports by a pump at a prescribed flux. In the case of lumen-

(a)

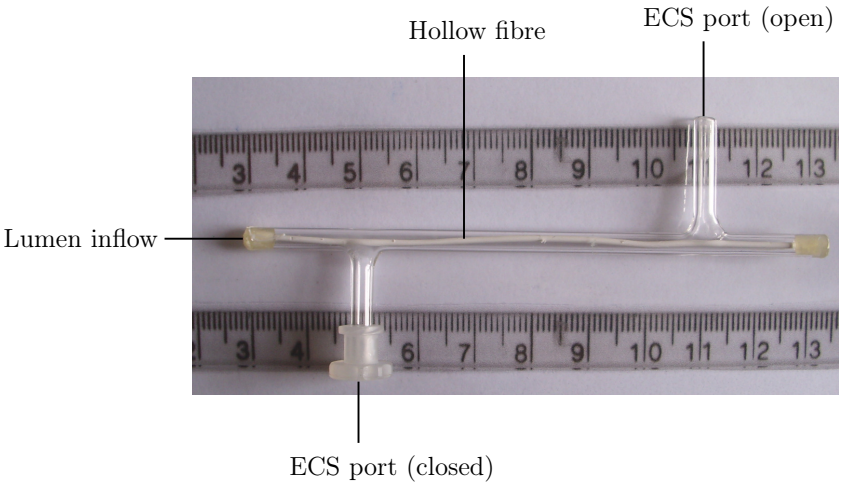

(b)

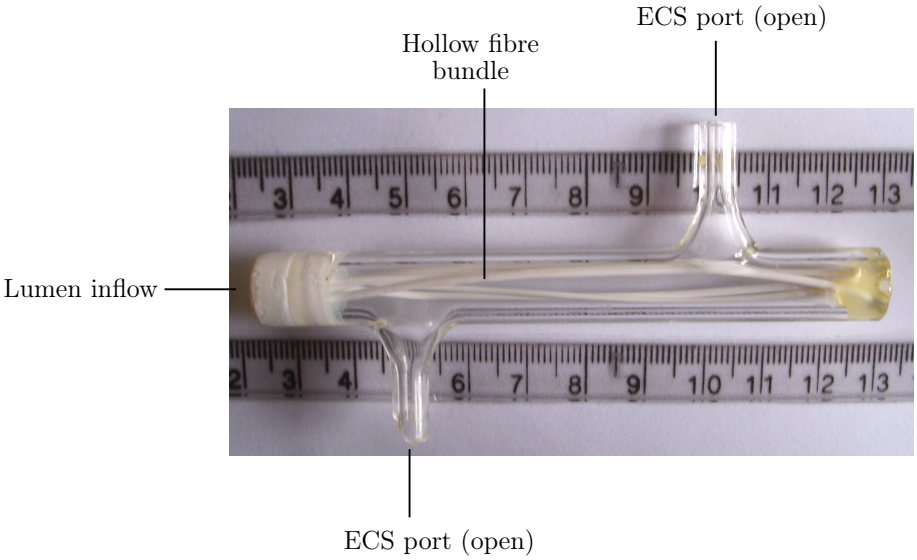

Figure 1.2: Photographs of representative hollow fibre membrane bioreactor modules (ruler scales in cm) with (a) a single hollow fibre, and (b) a bundle of hollow fibres running through the centre of the module. The ports (one of which is closed off in (a)) can be seen at either end.

driven flow, the medium reaches the cells via the porous fibre walls, and flows out through the end of the fibre lumen (the retentate) or either of the ECS ports (the permeate). The ratio of retentate to permeate is controlled by imposing a downstream pressure via a clamp at the lumen exit, the outlet ECS port being left open to the atmosphere.

1.2 Mathematical modelling

Given the considerable cost and complexity of tissue engineering experiments, it is clear that mathematical modelling of the systems could be of great benefit. Modelling has the advantage of having the flexibility to allow parameters and geometries to be changed more quickly and easily than in an experimental setup, as well as being much cheaper than experiments. Furthermore, once validated, mathematical models are able to provide spatial and temporal information that is hard or impossible to obtain experimentally. Online monitoring of experiments can be carried out using biosensors, either invasively or non-invasively. Invasive monitoring allows increased accuracy of measurements, but problems can arise with sterilisation and re-calibration of the devices [46]. In addition, the small sizes of certain bioreactors (for instance, some HFMBs) mean that invasive techniques are not always practical [186]. Non-invasive methods avoid these complications, but are only feasible for certain variables [31, 46, 111, 186]. As an example, it is possible to monitor the change in spatial composition of an engineered tissue over time, as long as highly sophisticated imaging techniques are used [31]. On the other hand, detailed information about the nutrient concentration within a bioreactor is much harder to obtain: only inlet and outlet concentrations can be measured, but not local variations within the bioreactor, which could be determined using a validated mathematical model [186]. In this section we give a broad overview of the existing literature on mathematical models of tissue engineering, highlighting the different techniques and approaches which are typically employed and the insights which they can provide. More detail can be found in the comprehensive reviews [20] and [150].

Since many bioreactor experiments are still at a relatively early stage of development, a rare opportunity exists to use mathematical modelling to inform and direct experimental work. For example, determining optimal operating conditions experimentally must be done using trial and error, but this can be avoided if a theoretical approach is included alongside experiments [104]. This was demonstrated by Shipley *et al.* [156], who derived a model for

the retentate and permeate flow rates in a HFMB using lubrication theory, by exploiting the small aspect ratio of the bioreactor. Theoretical values for the membrane permeability were determined and validated against experimental data. This led to the identification of equations which could be used by a tissue engineer to determine bioreactor operating conditions (*e.g.* flow rates, pressures, and bioreactor geometries) correlated to a specific cell culture environment. A HFMB was also modelled in [155], where the ECS was assumed to be seeded with cells, and fluid flow through both the porous membrane and cell-packed ECS was modelled using Darcy's law. Concentrations of both oxygen and lactate were tracked, with, respectively, a constant rate of uptake and production by the cells. Two experimental configurations were considered, with the ECS ports (modelled as a single distributed port) either open or closed, and operating conditions were found in each case to satisfy required bounds on the solute concentrations.

Another example of mathematical modelling being used to suggest suitable experimental setups is the paper by Davidson *et al.* [41]. Here, a two-dimensional, axisymmetric model of oxygen transport in a single hollow fibre of a bioartificial liver (BAL) device was developed. The governing equations were solved numerically and the results were used to find and plot 'operating regions' within which two operating constraints were satisfied. The first of these was the maximum number of fibres that the device can support without any of the cells being exposed to hypoxic conditions. The second was the minimum number of fibres possible such that a given number of cells, at a given density, could be seeded onto their outer surfaces. The authors investigated the dependence of these regions on variations in key operating parameters, namely the lumen radius, fibre length, total flow rate through the device, cell number, and membrane thickness. Subsequent application of the model to a specific BAL device could in theory allow its design to be optimised to avoid hypoxia. In addition, more qualitative results could be taken from this work, as the graphical depiction of the operating regions indicated 'safer' modes of operation in which there is more room for experimental error before hypoxic conditions are encountered.

Cummings and Waters [37] developed a model for tissue growth in a rotating high-aspect ratio vessel bioreactor, again with the aim of informing bioreactor design and operating conditions. By rotating the bioreactor about its cylindrical axis at an appropriate rate, it is possible to keep the tissue construct suspended in the nutrient-rich culture medium. An asymptotic approach was taken, exploiting the high aspect ratio of the bioreactor (its

depth being small relative to its radius) in order to simplify the governing equations. The different timescales inherent in the setup allowed the authors to solve for the fluid flow, construct position, nutrient concentration, and construct growth rate in distinct stages. The possible trajectories of the tissue construct within the bioreactor were determined in two distinguished parameter limits, corresponding to flow regimes which are near to, or far from, rigid body rotation. The first regime was shown to result in orbits in which the construct drifts towards the centre or edge of the bioreactor, whilst the second always led to a periodic construct orbit. The subsequent dependence of the nutrient distribution and construct growth rate on the supplied nutrient concentration and uptake rate was then determined.

Mathematical models can also help identify the roles of the most important regulatory stimuli in tissue growth (for example, an appropriate fluid shear stress distribution), as different aspects of the model can be adjusted independently of each other. This separation is often not possible in experiments, and the results of such theoretical studies can help interpret experimental results as well as suggesting the focus for future experimental work [150,186]. In [149], Sanz-Herrera *et al.* investigated the effect of different scaffold properties on bone regeneration using a multiscale approach and a combination of asymptotics and finite element methods. By varying the parameter under investigation whilst keeping the others constant, they were able to determine the effect of scaffold porosity, pore size, stiffness, degradation rate, and cell pre-seeding on the quality of the regenerated tissue. Trends in the results were supported by experimental data.

In another study by Ye *et al.* [186], a theoretical framework was developed for modelling nutrient distribution within a HFMB used for engineering three-dimensional bone tissue. The Krogh cylinder assumption was made, which is commonly used when modelling HFMBs containing several fibres. This states that the behaviour of the system can be represented by modelling a single fibre surrounded by an annular ECS, thus ignoring the remaining interstitial space between the fibres. In the setup considered by the authors, the ECS consisted entirely of a cellular matrix. Both oxygen and glucose concentrations were modelled, and solutions determined using the finite element method. The results demonstrated that at sufficiently high cell densities glucose was significantly more depleted than oxygen within the device. This suggested that for the existing operating conditions (specifically, the device length) glucose was the limiting nutrient for tissue growth. However, if longer fibres were

considered, this dependence switched and oxygen concentration became the limiting factor. In addition, the sensitivity of the results to variations in key parameters, such as lumen flow rate and cellular matrix thickness, was investigated. The work aimed to support and inform ongoing experimental studies by the authors.

Once the effect of different mechanisms has been determined, mathematical models can be developed and simplified in order to focus on one or two specific aspects of interest. This was demonstrated in Shipley *et al.* [153], where the problem of oxygen delivery was addressed. It is known that oxygen is often the limiting nutrient in tissue growth *in vitro* [104, 105]. By developing operating equations that linked flow rates and bioreactor geometry to critical oxygen levels in HFMBs for a variety of cell types, Shipley *et al.* [153] provided tissue engineers with a way of optimizing bioreactor design to ensure sufficient oxygen delivery to cells throughout the bioreactor. Michaelis-Menten kinetics described the nonlinear dependence of oxygen uptake on the underlying concentration, and a combination of analytical and numerical techniques were used to simplify and solve the model's governing equations. Model reduction as demonstrated in [153] can have many benefits. As well as reducing computation time compared to solving the full system numerically, it can give insight into the relative balance of the physical and biological processes present in a model.

Hay *et al.* also focussed on oxygen delivery, this time in a hollow fibre BAL, with hepatocytes attached to microcarriers seeded in the ECS [64]. Concentrating solely on transport and uptake of oxygen reduced the complexity of the system and allowed the authors to focus on the effect of key parameters governing these dynamics. These included the maximal oxygen consumption constant used in Michaelis-Menten kinetics, the ECS permeability (which was taken to be constant), and the inlet flow rate and partial oxygen pressure. Flow in the fibre membrane and ECS was modelled using Darcy's law. Model solutions were obtained numerically, and suggested that there were significant regions of hypoxia within the device. These results were compared to experimental data where possible, with some success. Those cases in which theoretical and experimental findings did not match well were attributed to a lack of consistent experimental data, and the modelling assumption of a constant ECS permeability.

A further use of mathematical models can be to compare and contrast different experimental approaches, which again would not be straightforward to set up in practice. An example of such work can be found in the paper by Abdullah *et al.* [3]. Here, the suit-

ability of three bioreactors for growing bone tissue was investigated: a HFMB, suspended tube bioreactor, and confined perfusion bioreactor. Glucose was assumed to be the main limiting nutrient in this study, and concentration profiles within the bioreactors were taken to be indicative of cell viability. Results were obtained using a finite element approach, and operating conditions such as inlet velocity, cell density, and scaffold hindrance factor were varied in order to determine their effect on the nutrient distribution. The HFMB was found to provide improved mass transfer compared to the other bioreactors, and therefore was the most appropriate design for growing cells in the high densities required for generating bone tissue.

Similarly, Whittaker *et al.* [178] developed a mathematical model for the flow field and nutrient transport within a perfusion bioreactor. Three different setups were considered. In each, a porous hollow fibre was inserted into the bioreactor scaffold, serving as an extra source of fluid and transport route for nutrients. The various configurations involved different numbers and orientations of fibres, with the exterior scaffold surface either acting as a distributed outlet for flow, or having specific inlet and outlet pipes. Through analytical simplification and numerical solution of the governing equations for each setup, the authors were able to determine and compare the corresponding distributions of fluid shear stress and nutrient and waste product concentrations throughout the bioreactor. The results indicated that the setup in which the exterior scaffold surface was a distributed outlet led to fewer regions of stagnant flow than if specific inlet and outlet pipes were inserted, but also resulted in higher rates of shear overall. The framework developed could thus be used to provide insight into which choice of setup is most appropriate for a particular experiment.

Given the complexity of the physical systems being modelled in tissue engineering, a variety of mathematical techniques and approaches exist in the literature and each method can be extremely powerful if applied to the right problem. The most appropriate choice will depend on the focus and scope of the model in question. Inherent in any biological problem is the vast range of spatial scales, and models can capture behaviour on single or multiple levels. At the microscale are the dynamics of individual cells and their interactions with each other and the surrounding environment, as well as the finer detail of scaffold geometries. A discrete modelling approach, such as that taken in [23], is useful for accurately capturing all of this information. However, a downside of this approach is that it is computationally expensive and not particularly flexible to, for instance, changes in key parameter values. On

the other hand, continuum models such as those discussed above capture the macroscale tissue dynamics and can easily and quickly be adjusted for different setups or operating conditions. The disadvantage here is the loss of more detailed microscale information.

A number of models have employed techniques to combine these length scales (for examples, see [40,148,154]). In [154], the authors employed asymptotic homogenisation techniques to determine fluid flow and nutrient/waste transport within a tissue engineering construct. The construct consisted of a printed hydrogel scaffold in which the cells were seeded, and through which culture medium flowed. The printed scaffold was built from several cylindrical strands of gel, and could thus be assembled in various configurations. Through the homogenisation procedure, the effect of the microscale scaffold structure on the solid fraction and permeability of the entire construct could be found. Results were used to determine optimal configurations and bounds on parameters (such as the strand diameter and separation) which satisfied mass transfer requirements throughout the construct and were therefore more favourable for tissue growth.

Another common way of incorporating information from both the micro- and macroscales when modelling cell populations is to use porous flow mixture theory, which involves taking volume averages across an intermediate spatial scale. This method is comparable to a homogenisation approach: for a thorough comparison of the two techniques, see the review by Davit *et al.* [42]. The majority of the work in this thesis is based upon models which have been developed using mixture theory, which we extend and apply to HFMB tissue engineering scenarios. In §1.4 we present the generalised multiphase framework from which the models in this thesis are derived. In the next section we focus on reviewing existing multiphase models of tissue engineering; we refer the reader to [119,150] for a more in-depth discussion of the merits of different types of models.

1.2.1 Multiphase models

Porous flow mixture theory can be applied to a system of two or more interacting and interpenetrating phases (which can either be solid, liquid, or gas); see [44,58,142,176,177] for more detail. In brief, the dynamics of each phase are tracked via an assigned volume fraction, a continuous quantity which can vary both spatially and temporally. Microscale governing equations for the conservation of mass and momentum of each phase are then averaged over a suitable representative volume, resulting in a system of equations which describe the macroscale dynamics of each phase. Microscale properties such as interactions between

phases (both active and passive) and intraphase pressures are incorporated via constitutive laws. As a result, each phase can be tracked independently on the macroscale without needing to resolve microscale dynamics, but still allowing for the incorporation of important microscale effects. This allows the behaviour of inherently complex systems to be modelled relatively simply, with the possibility of solution by analytical and/or numerical methods. In the present context of tissue engineering, an entire cell population in a bioreactor can be treated as one continuous phase through which the macroscale behaviour of the cells can be modelled. This averaging approach enables inclusion of microscale interactions such as those between cells, but without needing to track each individual cell. As well as tissue engineering, porous flow mixture theory has been used to model tumour growth [24, 50], biofilms [32, 33], cell motility [8, 25, 80–82, 84, 124], and even soil dynamics [166].

One such model was developed by Lemon *et al.* [92] and applied to *in vitro* tissue growth. The scaffold, cells, and culture medium (modelled as water) were all treated as separate phases. Constitutive equations were chosen to describe the interactions between, the rate of production of, and the stress terms in each phase, and the linear stability of the system to perturbations about its equilibrium state was analysed. This analytical approach was used to show that cells seeded into a scaffold in a static setup can either disperse or aggregate depending on the relative strengths of cell-cell interactions and cell-scaffold tractions, a behaviour also observed experimentally. This model was extended in [91] to include cell proliferation and death, and a spatially varying scaffold volume fraction in a one-dimensional geometry. Initial conditions were chosen to represent either a static or a dynamic seeding regime, and the edges of the seeded cell population were treated as free boundaries. Solutions for the cell population distribution and nutrient concentration were obtained in different limits of the cell-scaffold drag: zero (highly motile cells), infinite (immobile cells), and intermediate values. Parameter values for nutrient uptake, mitosis, and apoptosis were obtained by fitting solutions to experimental data for chondrocytes, enabling the model setup to be applied to tissue engineering of cartilage. Results indicated that in the absence of cell migration, a necrotic region developed in the centre of the scaffold due to insufficient supply of nutrient. At the other extreme, however, the case of highly motile cells led to either uniform distribution of cells throughout the scaffold, or a single cell aggregate in a similar manner to Lemon *et al.* [92]. In regard to tissue engineering of cartilage, it was thus suggested that it may be preferable to initially seed a scaffold with

mesenchymal stem cells, which have the ability to differentiate into chondrocytes at a later point in time, instead of starting with a population of the differentiated cells which are less motile.

In vitro culture of hepatocytes was the focus of the paper by Green *et al.* [59]. Here, the aim was to determine favourable conditions for the formation of cell aggregates. Experiments have found that culturing hepatocytes in clusters is more likely to be successful than culturing them in monolayers, as they more closely replicate the three-dimensional structure of liver tissue *in vivo*. The model in [59] described a one-dimensional culture well containing a deformable, viscoelastic layer of extracellular matrix (ECM), on top of which lay a two-phase mixture of cells and culture medium. Constitutive laws described the mechanical properties of each phase, and the nature of the interactions between phases. Results from numerical simulations and a linear stability analysis predicted that large-scale aggregates were most likely to form with a relatively high initial cell density, low cell-ECM and low cell-culture medium drag, whilst the effects of viscosity and elastic modulus of the ECM were fairly negligible.

Finally, Mohebbi-Kalhori and co-authors took a computational approach in [111]. Using a computational fluid dynamics (CFD) code to solve their model permitted a more complicated geometrical setup: a HFMB containing a hexagonal array of hollow fibres, and cells seeded in a gel matrix in the ECS. Cell proliferation was assumed to be nutrient-dependent, and the effect of several key parameters on cell volume fraction and oxygen and glucose concentration was determined. These parameters included the interfibre spacing, which is ignored in the typical Krogh cylinder assumption when modelling HFMBs (see, for example, [153, 156, 186]), and was found to have a significant effect on cell growth in the long, but not the short, term.

In this thesis we develop a number of multiphase models of HFMBs which include cell kinetics. As discussed in §1.1.3, there are various stimuli which can affect the behaviour of a cell population. In addition to nutrient concentration (models of which have already been discussed in detail above), we will investigate the respective roles of chemotaxis and mechanotransduction (via fluid shear stress) on cell motility and cell proliferation/differentiation. In the following sections we review relevant models which also incorporate these effects.

1.2.2 Chemotaxis

There have been many different attempts to model chemotaxis, spanning stochastic [159], discrete [39], and continuum [77] descriptions of cellular motion, and connections between the various approaches [7, 9, 14]. The existing literature is extensive and common applications include cell migration in angiogenesis (for instance in wound healing [133] or tumour growth [9, 28]) and morphogenesis [14, 94], to name but a few.

Incorporation of chemotactic effects in multiphase models is relatively rare, however. Cristini *et al.* [35] considered the role of chemotaxis in tumour invasion, through a multiphase model in which the nutrient acted as a chemoattractant for the cell population. Their results suggested that this chemotaxis may lead to fingering instabilities in the tumour growth dynamics, which are augmented by the presence of nutrient gradients or under conditions of reduced cell proliferation. Findings were reminiscent of experimental observations of invasive tumour morphology. Improving drug delivery to hypoxic tumours was the focus of the multiphase model by Webb *et al.* [175]. An avascular tumour spheroid was modelled, in which hypoxic cells produced macrophage chemoattractants. This setup was used to investigate the potential efficacy of two cancer treatments involving engineered macrophages. In the first, hypoxia induced the production of an enzyme by the macrophages which then activated a therapeutic drug, whilst in the second the macrophages released a cytotoxic factor directly. These two modes of operation were compared to a model for standard chemotherapy, with the second method showing improved results as it acted more locally and was thus more successful in targeting hypoxic regions.

The approach which we follow in Chapter 2 of this thesis is that taken by Byrne and Owen [25]. The model in [25] was motivated by an earlier paper by Keller and Segel [76]. This was one of the first to propose a mathematical description of chemotaxis and has influenced much of the subsequent work in the field; for a thorough review of models influenced by [76], see the review by Hillen and Painter [66]. In [76], movement in response to gradients in chemical concentration was assumed to occur in a similar manner to Brownian motion. The hypothesis was that individual cells detect and respond to changes in their local chemical environment, resulting in stochastic behaviour on the microscale, but that the average behaviour on the macroscale is directed movement up chemical concentration gradients. The presentation of the model was phenomenological; however, Byrne and Owen demonstrated that the relevant equations could be derived more formally if a multiphase

approach was taken [25]. Here, a one-dimensional Cartesian geometry was assumed for the two-phase model, and equations were obtained via conservation of mass and momentum in the usual way. The effect of chemotaxis was introduced through the addition of a potential function to the constitutive law for the cell stress, the idea being that movement up a chemical gradient relieves the pressure in the cell phase. Further analysis demonstrated that this description resulted in the concentration affecting not only movement up chemical gradients (*i.e.* chemotaxis), but also the random motion of the cells (chemokinesis), an observation that has also been made experimentally. In the remainder of [25], the stability of the system was analysed in the context of pattern formation in slime mold.

1.2.3 Mechanotransduction

Previous work on multiphase modelling of mechanotransduction in tissue engineering includes a series of papers by O'Dea and co-workers [120, 122, 123]. These build upon the model developed by Lemon *et al.* [92] by applying it to a perfusion bioreactor setup. In [122], the authors considered a two-dimensional, two-phase model of tissue growth in a perfusion bioreactor. This consisted of a cell-scaffold construct placed in a cylindrical chamber through which culture medium was driven using a pump. They included dependence of cell proliferation, ECM deposition, and cell death on the local cell density and fluid pressure. Modelling predictions indicated that these effects could dramatically alter the composition of the resulting tissue construct. This model was extended to include an extra porous scaffold phase in [123], in which the system was simplified analytically by taking the long-wavelength limit appropriate for a small channel aspect ratio. The effect of fluid shear stress, as well as cell density and fluid pressure, on the construct composition was considered. Findings supported the earlier conclusion that mechanotransduction can significantly affect cell distribution. The same setup was modelled by Osborne *et al.* [125], who solved the full system from [123] numerically using the finite element method. They found that the long-wavelength approach used in [123] was good at predicting average behaviour; however to determine the detailed spatial distribution of cells it was necessary to consider solutions of the full system. A further extension of this work is given in [120] in which degradation of the scaffold was included, and whose spatially non-constant porosity was informed by experimental data. Each of these studies provides a qualitative description of the dynamic processes at work in a perfusion bioreactor, and has the potential to be

used to optimise operating conditions and identify dominant regulatory stimuli given data relevant to a specific setup.

As well as cell proliferation and death, mechanotransduction can affect cell differentiation. This is the focus of a paper by Byrne *et al.* [23], in which finite element analysis was used to model a poroelastic cell-scaffold construct for bone regeneration with the objective of determining optimal scaffold porosity, stiffness, and degradation rate under different mechanical loading conditions. The dependence of stem cell differentiation on fluid velocity and shear strain was considered by employing the mechanoregulation framework developed by Prendergast *et al.* [141]. Depending on the stimulus level, differentiation into fibroblasts, chondrocytes, or osteoblasts could occur. Aiming to identify possible treatment options in fracture healing, Lacroix and Prendergast [88] developed a three-dimensional model of a human tibia fracture, again using the mechanoregulation framework proposed in [141]. Two different compressive loading magnitudes were simulated, and it was shown that only the lower load led to successful healing.

Driessen *et al.* [45] also used the finite element method to model the effect of the different mechanical loading regimes resulting from closed and open configurations on collagen fibre content and orientation in an aortic valve. The mechanical properties of the tissue construct were shown to depend on the type of configuration, as the fibres aligned with the principal strain directions, and results were validated against experimental data where possible. Cardiac tissue was also the focus of the work by Latimer *et al.* [89], who determined the stress and strain distribution in two- and three-dimensional tissues. Analytical solutions were found and exploited to predict mechanotransduction effects on the tissue following ischemia, and could be combined with models of the heart's electrical activity to determine mechanisms leading to stretch-induced arrhythmias. Finally, the importance of scaffold design in bone tissue engineering motivated the theoretical study by Sanz-Herrera *et al.* [148]. The need for an implantable construct that has the required macroscale properties, but which is affected by biophysical phenomena on the microscale, led to the development of a multiscale model which incorporated a realistic scaffold microstructure. Bone regeneration on the microscale was assumed to be dependent on mechanical stimuli, and properties of the macroscale model such as the scaffold stress and strain, and cell migration, were obtained through analysis of the underlying microstructure using a homogenisation process. This microstructure then in turn evolved as a result of macroscale cell migration. The resulting

governing equations were solved using the finite element method.

In this section we have reviewed a number of mathematical models pertinent to the work in this thesis, and shown how such studies can help inform and direct experiments. However, it should be noted that there are also significant limitations associated with mathematical modelling of such complex biological systems. Firstly, all mathematical models are necessarily only approximations of the physical system they aim to describe. Thus, although modelling can be invaluable in gaining insight into a particular aspect of a system, any model runs the risk of excluding potentially crucial components. For this reason, close interaction with experimentalists is vital to ensure theoretical models are biologically well grounded and retain key features. Secondly, for a mathematical model to provide any quantitative predictions it must first be validated against experimental results. This is often not straightforward, for instance if the theoretical model predicts information which cannot be obtained experimentally [3, 186], or if the theoretical and experimental work progress at different rates. To overcome this, models can be partly verified against existing (analytical or numerical) theoretical results if possible, or developed in a generalised, flexible framework which easily permits adaptation once data are available. Furthermore, it may be possible to validate global quantities (*e.g.* predicted bioreactor inlet and outlet nutrient concentrations) against experimental data even if this cannot be done for local information (such as the spatial concentration field within the bioreactor).

1.3 Thesis aims and outline

In this thesis we develop a number of different models of fluid flow, cell dynamics, and solute transport within the HFMB setup depicted in Figure 1.2(a), each exploring a different experimental scenario. We work in two-dimensional, Cartesian coordinates throughout. Common to each model is the assumption that the cells are seeded in a natural scaffold (formed from a solidified collagen gel, as described in §1.1.5), instead of in a monolayer on the outer surface of the hollow fibre, so that we model the dynamics of a bioactive cell-scaffold construct. Due to the current early stage of experimental work, direct comparison of the results of our theoretical models with experimental data has not been possible. We instead explore a number of the possible bioreactor configurations and operating regimes which could be employed experimentally, and for each setup provide a modelling framework which demonstrates the range of behaviours to be expected. In each case the modelling

approach taken is flexible and could be readily adapted to specific experimental conditions given appropriate data; in Chapter 6 we discuss potential experiments which would be useful in this regard.

In each chapter, the model governing equations are obtained by taking a different limit of a generalised multiphase model, which is based on porous flow mixture theory and presented in §1.4. To the best of our knowledge, the application of porous flow mixture theory to a single-fibre HFMB setup has not been carried out before. We then reduce the relevant governing equations as far as possible by employing asymptotic analysis, through exploitation of the small aspect ratio of HFMBs and consideration of a physically relevant distinguished limit. The reduced system is either solved numerically or, if possible, analytically. By considering different experimentally motivated setups we not only aim to illustrate typical behaviours of each system in turn, but also highlight the dependence of results on key experimentally controllable parameter values (such as inlet fluid fluxes and solute concentration) in an analytically tractable and transparent manner.

In Chapter 2, we consider a 3-layer modelling domain consisting of the lumen, porous membrane, and ECS. The cell-scaffold construct occupies the entire ECS, in which we employ a multiphase modelling approach to track the dynamics of each phase, as well as the concentration of a dissolved solute (either a nutrient or chemoattractant). A number of experimentally motivated case studies are presented, considering either different flow regimes or different interactions between the solute and cell population. These interactions take the form of nutrient-limited cell proliferation, or chemotaxis in response to a supplied or produced chemoattractant. In each case, the effect of inlet fluid flux on cell distribution and yield is investigated, and 'optimal' fluxes determined for the candidate case in which a spatially uniform cell population is desired. In addition, when the solute of interest is a nutrient, we also analyse the concentration throughout the bioreactor for different operating conditions to ensure that it is sufficient for cell survival. This model is adapted to include four layers in Chapter 3, so that the ECS is split into a multiphase cell layer surrounding the hollow fibre and an exterior layer of free-flowing fluid. We still assume that cell proliferation is limited by nutrient concentration, however we now focus on the effects of mechanotransduction, instead of chemotaxis, on the cell population. Through consideration of cell types whose proliferation rates are affected (adversely or favourably) by fluid shear stress, we investigate the effect of the cell layer thickness and exterior fluid layer inlet fluid

flux on cell distribution and yield.

Chapter 4 incorporates both the 3- and 4-layer models discussed above, but is extended to include two cell populations (one undifferentiated and one differentiated). Cell differentiation is assumed to depend on either the concentration of a growth factor, or both growth factor concentration and the fluid shear stress experienced by the cells. The effect of inlet growth factor concentration and fluid fluxes on the percentage and yield of differentiated cells is investigated.

In Chapter 5 we derive a 4-layer model in which we neglect cell kinetics, so that the cell-scaffold construct is modelled as a rigid porous medium. The focus is instead on the distribution of a solute throughout the system and its dependence on key parameters (which would be either measurable or controllable experimentally). The model permits analysis analogous to classical Taylor dispersion.

Finally, in Chapter 6 we conclude by summarising the main results from each model, and indicate possible future extensions to the work in this thesis.

1.4 Generalised multiphase model

In this section we outline a generalised model for a multiphase flow, following closely the work of Lemon *et al.* [92] and O'Dea *et al.* [123]. As mentioned in §1.2.1, similar approaches have been used to model a wide variety of processes, including tumour growth [24, 50], biofilms [32,33], cell motility [8,25,80–82,84,124], and soil dynamics [166]. The multiphase region we consider consists of one culture medium phase (modelled as water), k other active (cell) phases, and one scaffold phase. For simplicity, throughout this thesis we neglect degradation of the scaffold and deposition of ECM by the cells, so that the scaffold is inert. In addition, we assume a rigid scaffold. Although some deformation of the solidified collagen gel would be expected physically, this is a reasonable first approximation given that the behaviour of such scaffolds under experimental operating conditions is unknown [1]. We also include the equation for the mass transport of m dissolved solutes in the water phase. This model will be given in a general coordinate system, with t denoting time; the specific spatial coordinates used for each of our models will be stated at the beginning of the relevant chapter.

The volume fraction of the ith cell phase is denoted by θ_i $(i = 1, \ldots, k)$, that of the water phase by θ_{w}, and that of the scaffold phase by θ_{s}. Given our assumption of a rigid,

inert scaffold, θ_{s} is constant. We assume that there are no voids in the mixture, so that

$$\theta_{\mathrm{w}} + \theta_{\mathrm{s}} + \sum_{i=1}^{k} \theta_i = 1. \tag{1.1}$$

The remaining governing equations are in the form of conservation of mass and of momentum for each active phase. We begin with conservation of mass, given by

$$\frac{\partial \theta_i}{\partial t} + \nabla \cdot (\theta_i \mathbf{u}_i) = J_i \quad (i = \mathrm{w}, 1, \ldots, k), \tag{1.2}$$

where $\mathbf{u}_i$ is the velocity of the ith phase, $\nabla\cdot$ is the usual divergence operator, and J_i represents the net rate of production of phase i. Here we have assumed that the density ρ_i of the ith (cell) phase is constant, and we have made the assumption that the cells and water are of equal and constant density, *i.e.* that $\rho_i = \rho_{\mathrm{w}}$ $(i = 1, \ldots, k)$. This is a good approximation since cells are mainly comprised of water, and this assumption is consistent with that taken in many other multiphase models, for example, [24, 59, 91, 92]. Note that for the work in this thesis we will always take

$$J_{\mathrm{w}} + \sum_{i=1}^{k} J_i = 0 \tag{1.3}$$

so that mass is conserved. Each of these mass transfer functions J_{w}, J_i $(i = 1, \ldots k)$ may depend on any of the volume fractions θ_j $(j = \mathrm{s}, \mathrm{w}, 1, \ldots, k)$, the fluid shear stress, and also the concentration of any dissolved solutes in the mixture, and are prescribed constitutively in each chapter.

Conservation of momentum for the ith phase (neglecting inertial effects) is given by

$$\nabla \cdot (\theta_i \boldsymbol{\sigma}_i) + \sum_{j \neq i} \mathbf{f}_{ij} - \theta_i \rho_i \mathbf{g} = \mathbf{0} \quad (i = \mathrm{w}, 1, \ldots, k), \tag{1.4}$$

where $\boldsymbol{\sigma}_i$ is the macroscale stress tensor for the ith phase, $\mathbf{f}_{ij}$ represents the interphase force exerted on the ith phase by the jth phase, and $\mathbf{g}$ is the acceleration due to gravity. By Newton's third law we have $\mathbf{f}_{ij} = -\mathbf{f}_{ji}$, $\forall i, j,\ i \neq j$.

We pose constitutive forms for $\boldsymbol{\sigma}_i$ and $\mathbf{f}_{ij}$, following the approach in [92]. Beginning with the water phase, we assume the stress tensor is given by

$$\boldsymbol{\sigma}_{\mathrm{w}} = -\bar{p}_{\mathrm{w}} \mathbf{I}, \tag{1.5}$$

where $\bar{p}_{\mathrm{w}}$ is the water pressure and $\mathbf{I}$ is the identity tensor. The form (1.5) is chosen so that the relevant force balance from (1.4) and the constitutive laws prescribed below for the

interphase forces (see (1.9)) lead to the transport of water being governed by Darcy's law, and thus the microscale effects of the water viscosity are included in the macroscale model through this formulation.

We model the remaining active (cell) phases as viscous liquids, setting

$$\boldsymbol{\sigma}_i = -\bar{p}_i \mathbf{I} + \boldsymbol{\tau}_i \quad (i = 1, \ldots, k), \tag{1.6}$$

where $\bar{p}_i$ is the ith intraphase pressure and $\boldsymbol{\tau}_i$ is the deviatoric stress tensor for the ith phase, given by

$$\boldsymbol{\tau}_i = \mu_i \left(\nabla \mathbf{u}_i + (\nabla \mathbf{u}_i)^{\mathrm{T}} - \frac{2}{3} (\nabla \cdot \mathbf{u}_i) \mathbf{I} \right) \quad (i = 1, \ldots, k), \tag{1.7}$$

where superscript T denotes transpose and μ_i is the (effective) viscosity of the ith cell phase. We decompose the intraphase pressure $\bar{p}_i$ into the water pressure $\bar{p}_{\mathrm{w}}$ plus an extra component Π_i,

$$\bar{p}_i = \bar{p}_{\mathrm{w}} + \Pi_i \quad (i = 1, \ldots, k), \tag{1.8}$$

where Π_i may depend on any of the θ_j and any solute concentrations. This extra pressure Π_i accounts for cell-cell interactions and, if applicable, chemotaxis, and will be specified as necessary in each chapter.

Next we impose constitutive laws for the interphase forces $\mathbf{f}_{ij}$ in equation (1.4) of the form

$$\mathbf{f}_{ij} = p_{ij}\theta_j \nabla \theta_i - p_{ji}\theta_i \nabla \theta_j + \gamma_{ij}\theta_i \theta_j (\mathbf{u}_j - \mathbf{u}_i) = -\mathbf{f}_{ji} \\ (i, j = \mathrm{s}, \mathrm{w}, 1, \ldots, k,\ i \neq j), \tag{1.9}$$

where p_{ij} represents the interphase pressure exerted on the ith phase by the jth phase, with $p_{ij} = p_{ji}$. Each interphase force $\mathbf{f}_{ij}$ is decomposed into three components; see [92] for details. The first represents the interfacial force exerted on the ith phase by the jth phase. The second term represents the reaction to the corresponding interfacial force exerted on the jth phase by the ith phase. Finally, the third term represents drag between the phases, where γ_{ij} is the drag coefficient (assumed constant). We note that, for i or $j = \mathrm{s}$ the above forms will be simplified somewhat given our assumption of a constant scaffold volume fraction.

The interphase pressure $p_{ij} = p_{ji}$ is assumed to consist of the water pressure $\bar{p}_{\mathrm{w}}$, which is 'contact independent', and an extra pressure ψ_{ij} due to the tractions between the ith and jth phases:

$$p_{ij} = \bar{p}_{\mathrm{w}} + \psi_{ij}. \tag{1.10}$$

In this thesis we include tractions between the cells and the scaffold only, assuming that those between the cells and fluid, between the fluid and scaffold, and between different cell phases, are negligible by comparison. This simplifying assumption is motivated by the fact that we would expect the cells to strongly adhere to the scaffold. We therefore take $\psi_{ij} = \psi_{ji} = 0$ $(i, j = \mathrm{w}, 1, \ldots, k,\ i \neq j)$ and $\psi_{\mathrm{ws}} = \psi_{\mathrm{sw}} = 0$. In order to keep the derivations in each chapter as general as possible, for now we assume only that $\psi_{i\mathrm{s}} = \psi_{i\mathrm{s}}(\theta_i)$ $(i = 1, \ldots, k)$, motivated by the form used in [123]. When a specific form is required, we take a simplified version of that used in [123], setting $\psi_{i\mathrm{s}}$ to be a constant function:

$$\psi_{i\mathrm{s}} = -\eta \quad (i = 1, \ldots, k), \tag{1.11}$$

where η is a positive constant representing the cells' affinity for the scaffold.

Finally, the concentrations of any dissolved solutes in the multiphase mixture are tracked in the water phase only, where their transport is governed by

$$\frac{\partial(\theta_{\mathrm{w}} c_i)}{\partial t} + \nabla \cdot (\theta_{\mathrm{w}} c_i \mathbf{u}_{\mathrm{w}}) = D_i \nabla \cdot (\theta_{\mathrm{w}} \nabla c_i) + \mathcal{R}_i \quad (i = 1, \ldots, m), \tag{1.12}$$

where c_i is the concentration of the ith solute per unit volume of water, D_i is the diffusion coefficient for the ith solute in water (assumed constant), and $\mathcal{R}_i$ is a reaction term which accounts for the production or uptake of solute i per unit volume of mixture by any of the active phases. This reaction term may depend on any of the θ_j and c_i and is given a constitutive form as necessary in each chapter.

It remains to prescribe constitutive forms for the functions J_i, Π_i (with or without chemotaxis), and $\mathcal{R}_i$; these will be specified in each chapter as required, along with the exact phases included in each model.

1.5 Novel contributions

To the best of our knowledge, the application of multiphase modelling to the different HFMB setups considered in this thesis has not yet been reported. Further novel aspects are the solution of the models by asymptotic reduction and numerical methods and, in Chapter 5, the formulation and numerical solution of the unsteady problem in a manner analogous to that of classical Taylor dispersion. The majority of Chapter 2 has been published in Mathematical Medicine and Biology: A Journal of the IMA [129]. The work comprising Chapter 3 has been published in Biomechanics and Modeling in Mechanobiology [131]. Most

of the work in Chapter 5 has been submitted for publication in the Journal of Engineering Mathematics [130].

Chapter 2

Three-layer multiphase model

2.1 Introduction

This chapter closely follows Pearson *et al.* [129]. A multiphase model is developed for fluid flow, solute transport, and the evolution of a single cell population in a HFMB. Motivated by a candidate experimental setup for culture of a tissue construct, we consider the scenario in which the cells are seeded in a scaffold throughout the ECS, so that there are three distinct layers (the lumen, porous membrane, and ECS). The model presented is two-dimensional for simplicity, to enable analytical progress. It is expected, however, that results from a three-dimensional setup would be qualitatively similar; this could be a focus of future work (see Chapter 6). The flow in the lumen is modelled by the incompressible Stokes equations and the flow in the membrane is governed by Darcy's law. In the ECS the governing equations are derived from the generalised mixture theory model introduced in §1.4, and we model the scaffold, culture medium (modelled as water), and cells as three distinct phases. Interactions between these phases are incorporated via extra pressure, force, and drag terms in the governing equations, as shown in §1.4. The water contains a solute of interest, which is either a nutrient (*e.g.* oxygen) or chemoattractant (for examples see [30, 56, 138]). In particular, we are concerned with the yield and distribution of the cell population, and how these depend on experimentally controllable aspects of the bioreactor environment such as inlet fluid flux and inlet solute concentration. We focus on obtaining 'optimal' inlet fluid fluxes in the situation where a spatially uniform distribution of cells is desired.

2.1.1 Chapter outline

In §2.2 we describe the model setup, outlining the governing equations and boundary conditions in each layer in §§2.3.1-2.3.4. In §2.4 we argue that a simplified geometry may be considered, which permits analytical progress whilst still incorporating the key features of the system. This simplified system is summarised in §2.4.1. The resulting system is non-dimensionalised in §2.5.1, exploiting the small aspect ratio of the bioreactor and considering the transport regime in which axial advection and diffusion of solute are in balance in the lumen. In §§2.5.2-2.5.4 we use systematic asymptotic methods to reduce the system from sixteen to three unknowns. This results in a coupled system of partial differential equations (PDEs) at leading order in the lumen aspect ratio for the cell volume fraction, solute concentration, and reduced water pressure, along with analytical expressions for the remaining variables. Typical dimensional and dimensionless parameter values for this model are given in §2.5.5. In §2.5.6 we perform a linear stability analysis of the system on an unbounded domain. We describe the numerical scheme used to solve the reduced coupled system in §2.6, along with convergence checks and comparisons to analytical results. In §2.7 we present and compare results from a number of different case studies relating to possible experimental setups, including nutrient-limited cell growth, response to a delivered or produced chemoattractant, and backflow through the ECS. We consider the effect of inlet fluid flux on cell yield and distribution, and determine optimal fluxes for each case study in order to achieve a spatially uniform cell distribution. We conclude by discussing our findings in §2.8.

2.2 Model description

We consider an idealised two-dimensional problem in Cartesian coordinates (x, y), motivated by taking a cross section of the HFMB module in Figure 1.2, and shown schematically in Figure 2.1. In the geometry of the cross section, we have included two up- and two downstream ECS ports to mimic the fact that, in the full three-dimensional setup, the ECS ports are connected to the entire ECS due to its annular geometry. Firstly, we consider the setup in which only the downstream ECS ports are open. The water is pumped into the lumen and, due to an imposed pressure downstream, flows out either through the lumen outlet or the downstream ECS ports. In §2.7.6 we briefly look at the case where all of the ECS ports are open and there is an additional flow driven through the downstream ECS ports in the opposing direction to the flow in the lumen. In both setups the up- and

downstream ends of the porous membrane are sealed so that no fluid or cells can leave the system there. The ECS is comprised of the cells (one cell type only), water, and a (rigid, inert) natural scaffold. The porous membrane is impermeable to the cells so that they cannot leave the ECS. In addition to the assumptions made about interphase tractions in §1.4, here we also assume that the drag between the water and cells is much smaller than that between the scaffold and water or between the scaffold and cells. These simplifying assumptions are again motivated by the fact that we expect the cells to strongly adhere to the scaffold.

In Figure 2.1, the layers Ω_i $(i = 1, 2, 3)$ respectively denote the lumen, porous membrane, and ECS. The (permeable) interfaces between the lumen and porous membrane, and between the porous membrane and ECS, are respectively given by $\partial\Omega_{12}$ and $\partial\Omega_{23}$, and the remaining (impermeable) boundaries of each layer are denoted by $\partial\Omega_i$ $(i = 2, 3)$. Finally, $\mathcal{A}$, $\mathcal{B}$, $\mathcal{C}$, and $\mathcal{D}$ represent line segments across the pipes a finite distance away from the lumen inlet, upstream ECS ports, lumen outlet, and downstream ECS ports, respectively. The up- and downstream regions containing these ports (within the dashed boxes in Figure 2.1) will subsequently be neglected in the simplified modelling domain introduced in §2.4; in this first presentation of the model we include them for completeness.

2.3 Governing equations

Now we outline the governing equations for each of the three layers in the bioreactor: the lumen, the porous membrane, and the ECS. We state relevant boundary conditions in §2.3.4 to couple the layers and close the system. Parameter values are determined later in §2.5.5.

2.3.1 Lumen

In the lumen (Ω_1) there are no cells, and so we consider the flow of water and transport of solute only. The former is modelled using the incompressible Stokes equations. Conservation of mass gives

$$\nabla \cdot \mathbf{u}_\mathrm{l} = 0, \tag{2.1}$$

where $\mathbf{u}_\mathrm{l} = (u_\mathrm{l}, v_\mathrm{l})$ is the water velocity in the lumen, and the density of water, ρ_w, is assumed constant. We exploit the fact that inertial effects in the lumen are negligible (this is confirmed *a posteriori* in §2.5.5), so that conservation of momentum yields

$$\nabla \cdot \boldsymbol{\sigma}_\mathrm{l} - \rho_\mathrm{w}\mathbf{g} = \mathbf{0}, \tag{2.2}$$

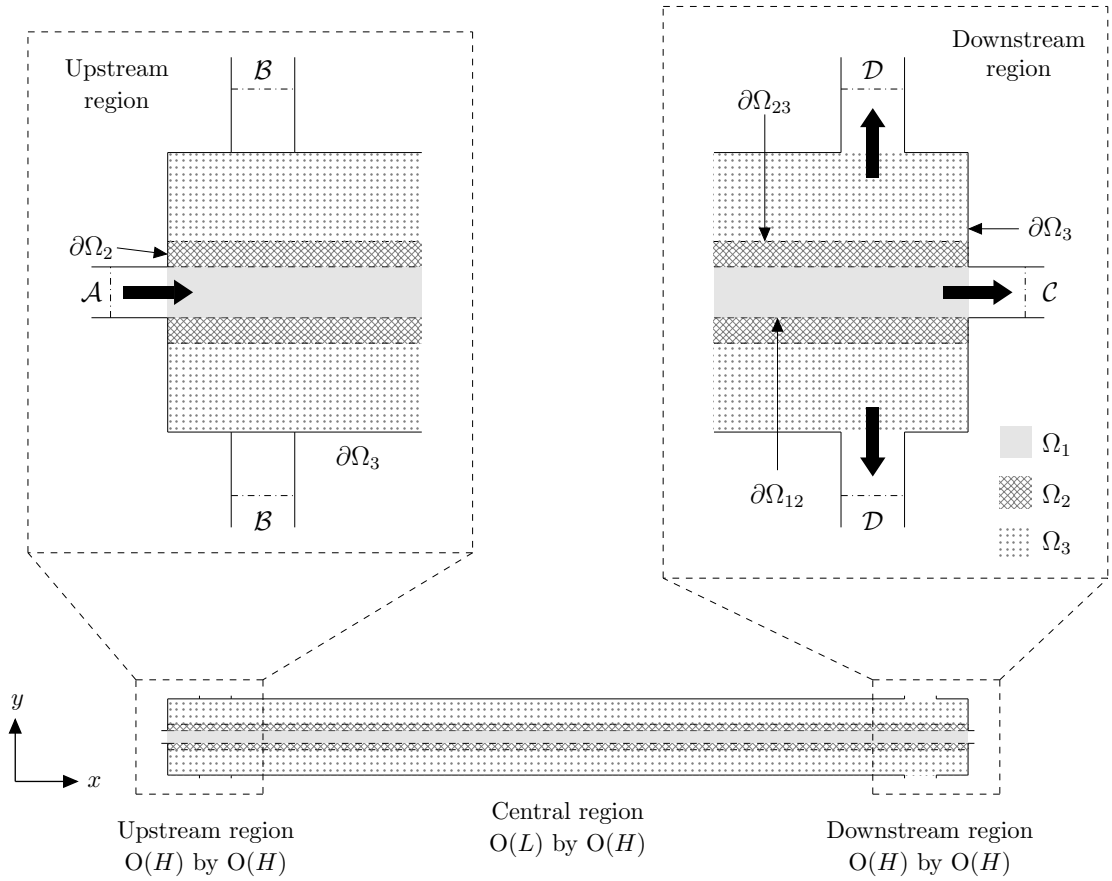

Figure 2.1: 3-layer modelling domain in a two-dimensional Cartesian geometry, with the up- and downstream regions near the ECS ports enlarged (not to scale). The solid black arrows denote the direction of fluid flow in the first setup considered, where only the downstream ECS ports are open. The lumen, porous membrane, and ECS respectively occupy Ω_i $(i = 1, 2, 3)$. Dashed lines represent the permeable boundaries $\partial\Omega_{12}$ and $\partial\Omega_{23}$ between the lumen and membrane, and membrane and ECS, and solid lines denote the impermeable boundaries $\partial\Omega_2$ and $\partial\Omega_3$. The dash-dotted lines $\mathcal{A}$, $\mathcal{B}$, $\mathcal{C}$, and $\mathcal{D}$ respectively denote line segments across the width of the pipes a finite distance away from the lumen inlet, upstream ECS ports (which are closed in this diagram), lumen outlet, and downstream ECS ports. Here H and L, $H \ll L$, are typical vertical and horizontal length scales, respectively, and will be specified during the asymptotic analysis in §2.5.

where $\boldsymbol{\sigma}_\mathrm{l}$ is the stress tensor for the water in the lumen, given by

$$\boldsymbol{\sigma}_\mathrm{l} = -\bar{p}_\mathrm{l}\mathbf{I} + \mu_\mathrm{w}\left(\nabla\mathbf{u}_\mathrm{l} + (\nabla\mathbf{u}_\mathrm{l})^\mathrm{T}\right), \tag{2.3}$$

and where $\bar{p}_\mathrm{l}$ is the water pressure in the lumen, μ_w is the water viscosity (assumed constant), and $\mathbf{g} = (0, g)$ is the acceleration due to gravity. In this work we shall consider flow rates which are towards the lower end of those employed experimentally (see discussion in §2.5.5),

and we must account for the effects of gravity in this instance. We introduce the reduced water pressure p_l, given by $p_\mathrm{l} = \bar{p}_\mathrm{l} + \rho_\mathrm{w} g y$, and subsequently similarly define reduced pressures in the porous membrane and ECS.

Conservation of mass for the solute concentration is given by the advection-diffusion equation

$$\frac{\partial c_\mathrm{l}}{\partial t} + \nabla \cdot (c_\mathrm{l} \mathbf{u}_\mathrm{l}) = D \nabla^2 c_\mathrm{l}, \tag{2.4}$$

where c_l is the solute concentration per unit volume in the lumen and D is the diffusion coefficient for the solute in water (assumed constant).

2.3.2 Porous membrane

In the porous membrane (Ω_2) we model the flow using Darcy's law for flow in porous media, which takes into account the microscale effects of viscosity on the macroscale:

$$\mathbf{u}_\mathrm{m} = -\frac{k_\mathrm{m}}{\mu_\mathrm{w}} \nabla p_\mathrm{m}, \tag{2.5}$$

where $\mathbf{u}_\mathrm{m} = (u_\mathrm{m}, v_\mathrm{m})$ is the water velocity in the porous membrane, k_m is the porous membrane permeability (assumed constant), and $p_\mathrm{m} = \bar{p}_\mathrm{m} + \rho_\mathrm{w} g y$ is the reduced water pressure in the membrane. Furthermore, conservation of fluid mass yields

$$\nabla \cdot \mathbf{u}_\mathrm{m} = 0, \tag{2.6}$$

where we have assumed that the porous membrane pore fraction ϕ_m is constant. Similarly to above, and following our discussion in §1.4, conservation of mass for the solute concentration is given by the advection-diffusion equation

$$\frac{\partial c_\mathrm{m}}{\partial t} + \nabla \cdot (c_\mathrm{m} \mathbf{u}_\mathrm{m}) = D \nabla^2 c_\mathrm{m}, \tag{2.7}$$

where c_m is the solute concentration per unit volume of water in the membrane.

2.3.3 Extracapillary space

Finally we consider the ECS (Ω_3), comprised of cells, water, and scaffold. We derive the governing equations for the multiphase flow in the ECS from the generalised multiphase model presented in §1.4.

The three phases in this model are the cells, water, and scaffold, with volume fractions θ_n, θ_w, and θ_s, respectively. Therefore the no voids constraint (1.1) is now

$$\theta_\mathrm{n} + \theta_\mathrm{w} + \theta_\mathrm{s} = 1. \tag{2.8}$$

Conservation of mass for the cells and water is given by

$$\frac{\partial \theta_{\mathrm{n}}}{\partial t} + \nabla \cdot (\theta_{\mathrm{n}} \mathbf{u}_{\mathrm{n}}) = J_{\mathrm{n}}, \qquad \frac{\partial \theta_{\mathrm{w}}}{\partial t} + \nabla \cdot (\theta_{\mathrm{w}} \mathbf{u}_{\mathrm{w}}) = J_{\mathrm{w}}, \tag{2.9}$$

where $\mathbf{u}_{\mathrm{n}} = (u_{\mathrm{n}}, v_{\mathrm{n}})$ and $\mathbf{u}_{\mathrm{w}} = (u_{\mathrm{w}}, v_{\mathrm{w}})$ in our Cartesian coordinate system. We recall that $J_{\mathrm{w}} = -J_{\mathrm{n}}$ so that mass is conserved. In this chapter we assume that J_{n} is a function of θ_{n} and c_{w} (the solute concentration per unit volume of water in the ECS) to keep our model as general as possible. We prescribe a functional form in §2.7 for each experimentally motivated case study that is considered.

Conservation of momentum for the cell and water phases (neglecting inertia) is given by

$$\nabla \cdot (\theta_{\mathrm{n}} \boldsymbol{\sigma}_{\mathrm{n}}) + \sum_{j \neq \mathrm{n}} \mathbf{f}_{\mathrm{n}j} - \theta_{\mathrm{n}} \rho_{\mathrm{w}} \mathbf{g} = \mathbf{0}, \qquad \nabla \cdot (\theta_{\mathrm{w}} \boldsymbol{\sigma}_{\mathrm{w}}) + \sum_{j \neq \mathrm{w}} \mathbf{f}_{\mathrm{w}j} - \theta_{\mathrm{w}} \rho_{\mathrm{w}} \mathbf{g} = \mathbf{0}, \tag{2.10}$$

where $\boldsymbol{\sigma}_{\mathrm{n}}$ and $\boldsymbol{\sigma}_{\mathrm{w}}$ are the stress tensors for the cell and water phases, given by (1.5) and (1.6) respectively. We recall the form for the cell pressure $\bar{p}_{\mathrm{n}}$ introduced in §1.4:

$$\bar{p}_{\mathrm{n}} = \bar{p}_{\mathrm{w}} + \Pi. \tag{2.11}$$

For now we assume only that Π is a function of θ_{n} and c_{w}. In §2.7, motivated by [25] and [123], we split Π into two components Π_{n} and Π_{c} which, respectively, account for cell-cell interactions (such as osmotic stress and surface tension in the cell membranes) and chemotaxis, and take the following forms:

$$\Pi = \Pi_{\mathrm{n}} + \Pi_{\mathrm{c}}, \qquad \Pi_{\mathrm{n}} = \theta_{\mathrm{n}} \left(-\nu + \frac{\delta_{\mathrm{a}} \theta_{\mathrm{n}}}{1 - \theta_{\mathrm{s}} - \theta_{\mathrm{n}}} \right), \qquad \Pi_{\mathrm{c}} = \chi \exp\left(-\frac{c_{\mathrm{w}}}{\bar{c}} \right), \tag{2.12}$$

where ν, δ_{a}, χ, and $\bar{c}$ are positive constants. The first term in Π_{n} represents the fact that cells tend to aggregate at low densities, *i.e.* when θ_{n} is small, whilst the second models the repulsive forces which arise due to contact inhibition [123]. The function Π_{c} represents chemotactic movement up gradients in the solute, with a greater effect in areas of lower concentration, a behaviour which has been observed experimentally [71]. The effect of both Π_{n} and Π_{c} on the cell phase dynamics can be seen more clearly once we have derived the reduced equation for θ_{n} (see equation (2.59*a*)).

Recalling that the interphase forces $\mathbf{f}_{ij}$ as presented in equation (1.9) are simplified by our assumption of a constant scaffold volume fraction and the fact that $\psi_{ij} = \psi_{ji} = 0$ unless $i = \mathrm{n}$ and $j = \mathrm{s}$, we have

$$\mathbf{f}_{\mathrm{nw}} = p_{\mathrm{w}} \theta_{\mathrm{w}} \nabla \theta_{\mathrm{n}} - p_{\mathrm{w}} \theta_{\mathrm{n}} \nabla \theta_{\mathrm{w}} + \gamma_{\mathrm{nw}} \theta_{\mathrm{n}} \theta_{\mathrm{w}} (\mathbf{u}_{\mathrm{w}} - \mathbf{u}_{\mathrm{n}}) = -\mathbf{f}_{\mathrm{wn}}, \tag{2.13}$$

$$\mathbf{f}_{\mathrm{ns}} = (p_{\mathrm{w}} + \psi_{\mathrm{ns}})\, \theta_{\mathrm{s}} \nabla \theta_{\mathrm{n}} - \gamma_{\mathrm{ns}} \theta_{\mathrm{n}} \theta_{\mathrm{s}} \mathbf{u}_{\mathrm{n}} = -\mathbf{f}_{\mathrm{sn}}, \tag{2.14}$$

$$\mathbf{f}_{\mathrm{ws}} = p_{\mathrm{w}} \theta_{\mathrm{s}} \nabla \theta_{\mathrm{w}} - \gamma_{\mathrm{ws}} \theta_{\mathrm{w}} \theta_{\mathrm{s}} \mathbf{u}_{\mathrm{w}} = -\mathbf{f}_{\mathrm{sw}}, \tag{2.15}$$

where, as stated in §1.4, $\psi_{\rm ns}$ is a constant ($\psi_{\rm ns} = -\eta$); however for the sake of generality we delay inclusion of this form until obtaining our results in §2.7.

We define reduced pressures in the ECS as in the lumen and porous membrane by setting

$$p_{\rm w} = \bar{p}_{\rm w} + \rho_{\rm w} g y, \qquad p_{\rm n} = \bar{p}_{\rm n} + \rho_{\rm w} g y = p_{\rm w} + \Pi. \tag{2.16}$$

Making use of the constitutive relations (2.11) and (2.13)-(2.15), neglecting drag between the cells and water as stated in §2.2, and substituting in for $p_{\rm w}$ from (2.16), the resulting governing equations for the cell phase in the ECS are given by

$$\begin{aligned} \frac{\partial \theta_{\rm n}}{\partial t} + \nabla \cdot (\theta_{\rm n} \mathbf{u}_{\rm n}) &= J_{\rm n}, \\ -\theta_{\rm n} \nabla p_{\rm w} - \nabla(\theta_{\rm n} \Pi) + \nabla \cdot (\theta_{\rm n} \boldsymbol{\tau}_{\rm n}) + \psi_{\rm ns} \theta_{\rm s} \nabla \theta_{\rm n} - \gamma_{\rm ns} \theta_{\rm n} \theta_{\rm s} \mathbf{u}_{\rm n} &= \mathbf{0}, \end{aligned} \tag{2.17}$$

and for the water phase they are given by

$$\frac{\partial \theta_{\rm w}}{\partial t} + \nabla \cdot (\theta_{\rm w} \mathbf{u}_{\rm w}) = -J_{\rm n}, \qquad -\theta_{\rm w} \nabla p_{\rm w} - \gamma_{\rm ws} \theta_{\rm w} \theta_{\rm s} \mathbf{u}_{\rm w} = \mathbf{0}. \tag{2.18a,b}$$

We note that in (2.18b) we have indeed recovered Darcy's law, which models the microscale effects of the water viscosity on the macroscale. Now we return briefly to the membrane flow model to define the stress tensor in the context of the multiphase formulation. We note that within the multiphase framework Darcy's law (2.5) corresponds to the force balance

$$\nabla \cdot (\phi_{\rm m} \boldsymbol{\sigma}_{\rm m}) - \frac{\phi_{\rm m} \mu_{\rm w}}{k_{\rm m}} \mathbf{u}_{\rm m} - \phi_{\rm m} \rho_{\rm w} \mathbf{g} = \mathbf{0}, \tag{2.19}$$

with

$$\boldsymbol{\sigma}_{\rm m} = -\bar{p}_{\rm m} \mathbf{I}, \tag{2.20}$$

this being the only choice for $\boldsymbol{\sigma}_{\rm m}$ which is consistent with the choice for $\boldsymbol{\sigma}_{\rm w}$ above.

Finally, again following §1.4, conservation of mass for the (single) solute in the ECS is given by

$$\frac{\partial (\theta_{\rm w} c_{\rm w})}{\partial t} + \nabla \cdot (\theta_{\rm w} c_{\rm w} \mathbf{u}_{\rm w}) = D \nabla \cdot (\theta_{\rm w} \nabla c_{\rm w}) + \mathcal{R}, \tag{2.21}$$

assuming that mass transport only occurs in the water phase as stated in §1.4. Here, the reaction term $\mathcal{R}$ may depend on $\theta_{\rm n}$ and/or $c_{\rm w}$. Specific forms will be given in §2.7, to model either the uptake of nutrient, or the production or uptake of chemoattractant.

Across the three layers, we have a system of sixteen equations for the sixteen unknowns u_i, v_i ($i = {\rm l}, {\rm m}, {\rm n}, {\rm w}$), p_i, c_i ($i = {\rm l}, {\rm m}, {\rm w}$), $\theta_{\rm n}$, and $\theta_{\rm w}$. Next we impose boundary conditions to close the problem.

2.3.4 Boundary conditions

Boundary conditions for the fluid on each of the interfaces between the layers will take the form of continuity of fluid flux and of normal stress, and on the impermeable bioreactor boundaries we impose no flux and no slip of fluid. In addition, the lumen/membrane interface is a boundary between free-flowing fluid and flow through a porous medium and hence needs an extra condition; we shall impose no slip of fluid in the lumen on this interface for reasons discussed below. We impose continuity of solute concentration and of solute flux on the interfaces between layers, and no flux of solute out of the impermeable bioreactor boundaries. Boundary conditions are also needed for the cell phase on the membrane/ECS interface and bioreactor top; these are presented below. In the following, $\mathbf{t}_{ij}$ is the unit tangent to $\partial\Omega_{ij}$, $\mathbf{n}_i$ is the outward pointing unit normal to $\partial\Omega_i$ and $\mathbf{n}_{ij}$ is the unit normal to $\partial\Omega_{ij}$ pointing into Ω_j.

Therefore, as discussed, on the lumen/membrane interface we impose no slip, as well as continuity of water flux, of normal stress, of concentration, and of solute flux, so that

$$\begin{gathered}\mathbf{u}_\mathrm{l}\cdot\mathbf{t}_{12}=0, \qquad \mathbf{u}_\mathrm{l}\cdot\mathbf{n}_{12}=\phi_\mathrm{m}\mathbf{u}_\mathrm{m}\cdot\mathbf{n}_{12}, \qquad \mathbf{n}_{12}\cdot\boldsymbol{\sigma}_\mathrm{l}\cdot\mathbf{n}_{12}=\mathbf{n}_{12}\cdot\boldsymbol{\sigma}_\mathrm{m}\cdot\mathbf{n}_{12},\\ c_\mathrm{l}=c_\mathrm{m}, \qquad \nabla c_\mathrm{l}\cdot\mathbf{n}_{12}=\phi_\mathrm{m}\nabla c_\mathrm{m}\cdot\mathbf{n}_{12} \qquad \text{on} \quad \partial\Omega_{12},\end{gathered} \tag{2.22a-e}$$

where we have assumed that all of the fluid stress from the lumen is taken up by the fluid in the membrane. This results in condition (2.22c) reducing to continuity of (reduced) pressure in the leading-order model as the gravitational contributions cancel (see §2.5.1). The assumption of continuity of pressure at the boundary between flow through materials of different permeabilities is also taken in [16,72]. The no slip condition (2.22a) is motivated by the work of Shipley *et al.* [156] who found that slip is insignificant for the membranes used by our experimental collaborators in Bath.

The membrane/ECS interface is impermeable to cells as the mean pore radius (≈ 1 μm) is much smaller than that of a cell (≈ 5 μm) [155], and hence we impose no flux of cells here. In addition we impose no slip of cells, along with continuity of flux of water, of normal stress, of solute concentration, and of flux of solute. We make the constitutive assumption that all the stress is taken up by the water in the ECS, not the cells, which again leads to continuity of (reduced) water pressure across the membrane/ECS interface at leading order in §2.5.1. These give

$$\begin{gathered}\mathbf{u}_\mathrm{n}=\mathbf{0}, \qquad \theta_\mathrm{w}\mathbf{u}_\mathrm{w}\cdot\mathbf{n}_{23}=\phi_\mathrm{m}\mathbf{u}_\mathrm{m}\cdot\mathbf{n}_{23}, \qquad \mathbf{n}_{23}\cdot\boldsymbol{\sigma}_\mathrm{m}\cdot\mathbf{n}_{23}=\mathbf{n}_{23}\cdot\boldsymbol{\sigma}_\mathrm{w}\cdot\mathbf{n}_{23},\\ c_\mathrm{m}=c_\mathrm{w}, \qquad \phi_\mathrm{m}\nabla c_\mathrm{m}\cdot\mathbf{n}_{23}=\theta_\mathrm{w}\nabla c_\mathrm{w}\cdot\mathbf{n}_{23} \qquad \text{on} \quad \partial\Omega_{23}.\end{gathered} \tag{2.23a-e}$$

The outer boundary of the porous membrane is sealed, as mentioned above, and hence we impose no flux of water or of solute there:

$$\mathbf{u}_{\mathrm{m}} \cdot \mathbf{n}_2 = 0, \qquad \nabla c_{\mathrm{m}} \cdot \mathbf{n}_2 = 0 \qquad \text{on} \quad \partial\Omega_2. \tag{2.24}$$

The bioreactor boundary $\partial\Omega_3$ is a solid boundary on which we impose no flux and slip of cells, and no flux of water or solute, so that

$$\mathbf{u}_{\mathrm{n}} = \mathbf{0}, \qquad \mathbf{u}_{\mathrm{w}} \cdot \mathbf{n}_3 = 0, \qquad \theta_{\mathrm{w}} \nabla c_{\mathrm{w}} \cdot \mathbf{n}_3 = 0 \qquad \text{on} \quad \partial\Omega_3. \tag{2.25}$$

It now remains to prescribe boundary conditions at the lumen inlet $\mathcal{A}$, lumen outlet $\mathcal{C}$, and the ECS ports at $\mathcal{B}$ and $\mathcal{D}$. The exact conditions depend on the precise flow regime and setup under consideration, and so will change for each of the case studies presented in §2.7. For the sake of brevity, here we give only the physical description of the boundary conditions required, delaying their mathematical statement until analysis of the reduced model in §2.5.3.

In the pipe entering the lumen inlet, we assume that the flow is of Poiseuille form with prescribed inlet volume flux $Q_{\mathrm{l,in}}$ per unit length in the z-direction (here and henceforth taken to be perpendicular to both x and y). Depending on whether solute is being delivered into the bioreactor or not, we also prescribe either the solute concentration at $\mathcal{A}$, or no flux of solute in there. Downstream, the lumen outlet pressure is controlled experimentally by a clamp on the outlet pipe; this condition is set via continuity of normal stress at $\mathcal{C}$ and will be in terms of reduced pressures. We also assume no transverse flow in the lumen outlet pipe. The final condition required in the lumen is for the solute concentration at $\mathcal{C}$. There is no constraint here experimentally, and so we prescribe no diffusive flux of solute. This is the condition that will have the least effect on the theoretical results (prescribing a downstream concentration, for instance, would have a large effect on the concentration elsewhere in the bioreactor), and we note that this still allows an advective flux of solute out of the bioreactor. This choice is motivated by the expectation that the solute concentration is constant in space as it leaves the bioreactor due to the effect of diffusion, and is investigated in more detail in Chapter 5.

The up- and downstream conditions in the ECS will depend on the flow regime: in this chapter we consider two cases, as mentioned above. In the first setup, the upstream ports at $\mathcal{B}$ are closed and those at $\mathcal{D}$ are open (as is the case in Figure 2.1), whilst in the second (considered in §2.7.6 only) both sets of ports are open and there is an imposed flow

into the ECS at $\mathcal{D}$ in the opposing direction to that in the lumen. If the upstream ECS ports are closed, we remove the inlet pipes at $\mathcal{B}$ from the geometry of the modelling domain so that $\partial\Omega_3$ is just a continuous wall in the upstream region. When the ports at $\mathcal{D}$ are open and are therefore inlets to fluid flow, we assume Poiseuille flow entering the pipes and prescribe an inlet volume flux $Q_{\mathrm{e,in}}$ per unit length in the z-direction. Depending on the setup being considered, we also prescribe either the solute concentration or zero solute flux at $\mathcal{D}$. Whenever ports are outlets to fluid flow, we prescribe conditions analogous to those at the lumen outlet $\mathcal{C}$: no transverse flow, continuity of normal stress, and no diffusive flux of solute, for the same reasons discussed above. Additionally, we assume that the cells cannot leave the scaffold and so impose no flux of cells out of the bioreactor through any open ECS ports (at $\mathcal{D}$ and, if open, those at $\mathcal{B}$).

In §2.5.3 when we impose the up- and downstream conditions on the reduced model, we will see that not all of the boundary conditions described above are needed. The adjustment from the prescribed value in the full system to the value which is taken by our reduced model occurs in boundary layer regions at the up- and downstream ends near the ECS ports. We examine the boundary layer structure in detail for the regime considered in Chapter 5, in which cell kinetics are neglected and solute is supplied at the lumen inlet and upstream ECS ports.

2.4 Simplification of the modelling domain

The modelling domain illustrated in Figure 2.1 is complicated by the up- and downstream ECS ports. Numerical approaches would be needed to make any progress in solving this system, and this would be computationally expensive. We instead simplify the modelling domain to consider the central region, excluding the ECS ports. This makes the problem amenable to analytical techniques whilst still capturing key features of the bioreactor, and allows a rapid exploration of the subset of parameter space most relevant in practice. This assumption is similar to the Krogh cylinder assumption often taken when modelling HFMBs in an axisymmetric geometry (see [2, 20, 153, 186] for examples). The influence of the regions near the ports will be included through the up- and downstream boundary conditions imposed on our simplified domain. We note that in order to determine these conditions exactly, it would be necessary to match with the solutions obtained in the up- and downstream regions near the ports. This is not something we pursue here; we instead

refer ahead to Chapter 5, where we perform an analysis of these regions in a setup which neglects cell kinetics.

Even though we have included the effects of gravity in our model, the governing equations are symmetric about the lumen centreline (which is assumed straight) when expressed in terms of the reduced pressures. Therefore, for simplicity, we consider the upper half of the bioreactor only, so that the modelling region $0 < x < L$, $0 < y < H$ consists of three rectangular compartments: the lumen, porous membrane, and ECS (see Figure 2.2). We note that this requires additional boundary conditions on the line of symmetry $y = 0$. We take the origin of the Cartesian coordinate system, $(x, y) = (0, 0)$, to be at the bottom left of the domain, so that the x-axis lies along the lumen centreline. We denote by h_1, h_2, and h_3 the heights of the lumen, porous membrane, and ECS respectively, with the total height of the half-bioreactor given by $H := h_1 + h_2 + h_3$. The total domain length is denoted by L, and we note that h_1, h_2, and h_3 are comparable, with $h_1/L \ll 1$, so that the aspect ratio of each layer is small. The simpler geometry and small aspect ratio of the domain motivate the non-dimensionalisation in §2.5.1 and allow the system of governing equations in the lumen, porous membrane, and ECS to be studied analytically.

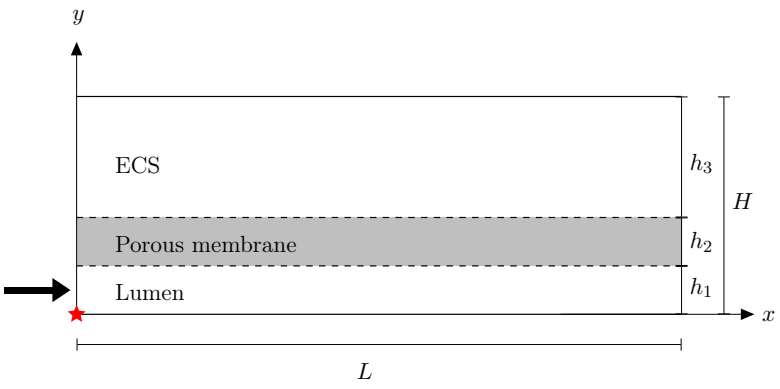

Figure 2.2: Simplified modelling domain with the x-axis running along the lumen centreline (not to scale). The red star denotes the origin $(x, y) = (0, 0)$, and the solid black arrow denotes the direction of the imposed fluid flux into the lumen.

2.4.1 Governing equations and boundary conditions for the simplified domain

The governing equations in each layer are unchanged from §2.3, as are the boundary conditions on the interfaces between the layers and on the bioreactor boundary $\partial\Omega_3$ (now $y = H$).

Only the boundary conditions at the up- and downstream ends of the bioreactor are altered. These are chosen to represent conditions in the excluded regions near the ECS ports and at the lumen inlet and outlet, and will be introduced as required in §2.5.3 after reduction of the dimensionless system in §2.5.2. In addition, as we now consider the upper half of the bioreactor only, we impose the following symmetry conditions on the lumen centreline:

$$\frac{\partial u_\mathrm{l}}{\partial y} = 0, \qquad v_\mathrm{l} = 0, \qquad \frac{\partial c_\mathrm{l}}{\partial y} = 0 \qquad \text{on} \quad y = 0. \tag{2.26}$$

Initial conditions are imposed as necessary in §2.7.

2.5 Model reduction

The choice of non-dimensionalisation in the lumen reflects its small aspect ratio ε, and leads to the equations for lubrication theory in this layer at leading order. This results in a reduced pressure in the lumen which is independent of y, allowing us to explicitly solve for the flow velocity there. Similar scalings are physically relevant in the remaining two layers as well, as they also have a small aspect ratio. In the ECS, this leads to the reduced water pressure gradient term dominating in the y-force balance in the water phase, and both the reduced water pressure and intra-/interphase pressure terms dominating in the y-force balance in the cell phase. As a result, both the reduced water pressure and cell volume fraction are independent of y at leading order in the ECS, as well as the leading-order solute concentration in each layer. This allows significant simplification of the governing equations, and results in a coupled system of three second-order nonlinear PDEs at leading order in the lumen aspect ratio to solve for the cell volume fraction, solute concentration, and reduced water pressure in the ECS, along with corresponding expressions for the remaining leading-order unknowns.

2.5.1 Non-dimensionalisation

We non-dimensionalise as follows, using hats to denote dimensionless variables:

$$\begin{gathered}
x = L\hat{x}, \qquad y = \varepsilon L\hat{y}, \qquad h_i = \varepsilon L\hat{h}_i \quad (i = 2, 3), \qquad H = \varepsilon L\hat{H}, \qquad t = \frac{L}{U^*}\hat{t}, \\
u_\mathrm{l} = \frac{\mu_\mathrm{n}}{\mu_\mathrm{w}}U^*\hat{u}_\mathrm{l}, \qquad v_\mathrm{l} = \frac{\varepsilon\mu_\mathrm{n}}{\mu_\mathrm{w}}U^*\hat{v}_\mathrm{l}, \qquad u_i = U^*\hat{u}_i, \qquad v_i = \varepsilon U^*\hat{v}_i \quad (i = \mathrm{m}, \mathrm{w}, \mathrm{n}), \\
p_i = p_\mathrm{atm} + \frac{\mu_\mathrm{n}U^*}{\varepsilon^2 L}\hat{p}_i \quad (i = \mathrm{l}, \mathrm{m}, \mathrm{w}), \qquad \Pi_i = \frac{\mu_\mathrm{n}U^*}{\varepsilon^2 L}\hat{\Pi}_i \quad (i = \mathrm{n}, \mathrm{c}), \\
\psi_\mathrm{ns} = \frac{\mu_\mathrm{n}U^*}{\varepsilon^2 L}\hat{\psi}_\mathrm{ns}, \qquad c_i = C^*\hat{c}_i \quad (i = \mathrm{l}, \mathrm{m}, \mathrm{w}), \qquad \mathcal{R} = R^*\hat{\mathcal{R}}, \qquad J_\mathrm{n} = \frac{U^*}{L}\hat{J}_\mathrm{n},
\end{gathered} \tag{2.27}$$

where $\varepsilon = h_1/L$ is the (small) aspect ratio of the lumen, C^*, R^*, and U^* are, respectively, typical concentration, reaction, and porous membrane/ECS velocity scales, and p_{atm} is (reduced) atmospheric pressure. We consider the biologically plausible regime where the viscosity of the cell phase (on the macroscale) is much greater than that of water due to the presence of the cytoskeletal network, the cells' adherence to the scaffold, and the effect of cell-cell interactions (on the microscale). In particular, we consider the limit in which $\mu_{\text{w}}/\mu_{\text{n}} = \lambda\varepsilon$ for some $\lambda = \text{O}(1)$ as $\varepsilon \to 0$ (see §2.5.5). We note that other limits could be considered, for instance taking the cell and water phases to be of comparable viscosity (as in [50, 122, 123], which here would involve solving a much more complex system) or taking the cell phase to be inviscid (as in [92]).

We have multiplied the velocity scales in the lumen by a factor of $\mu_{\text{n}}/\mu_{\text{w}}$ so that the same pressure scales can be applied throughout the system. This choice is also motivated by the fact that we would expect the porous structures to hinder the fluid flow in the membrane and ECS. In addition, this choice enables substantial analytical progress to be made in the mathematical reduction of §2.5. As previously stated, we expect inertial effects to be negligible compared to viscosity, and hence have employed a viscous pressure scaling throughout. The resulting horizontal velocity scale in the lumen, $\mu_{\text{n}}U^*/\mu_{\text{w}}$, represents the typical horizontal velocity of the fluid flowing through the lumen as determined by the imposed lumen inlet fluid flux. We choose the timescale L/U^* and take the inverse of this as the scale for J_{n} so that the timescales for advection in the ECS/porous membrane layers and proliferation are assumed comparable. This is appropriate given that we consider very slow flows (see discussion in §2.5.5). We also choose $R^* = DC^*/L^2$ so that uptake/production of solute occurs on the same timescale as axial diffusion. This is chosen for illustrative purposes, as it yields a non-trivial dominant balance in the solute governing equations, with the reaction term appearing in the reduced model at leading order (as will be shown in §2.5.2). Relevant dimensionless parameter values will be determined in §2.5.5.

In the following we move into component form, substituting for the reduced pressures throughout and eliminating v_{m} in favour of $\partial p_{\text{m}}/\partial y$ in the boundary conditions (2.22*b*) and (2.23*b*) using the y-component of equation (2.5). Dropping hats, the dimensionless system

of equations in the lumen ($0 < y < 1$) is therefore

$$\frac{\partial u_\mathrm{l}}{\partial x} + \frac{\partial v_\mathrm{l}}{\partial y} = 0, \qquad -\frac{\partial p_\mathrm{l}}{\partial x} + \varepsilon^2\frac{\partial^2 u_\mathrm{l}}{\partial x^2} + \frac{\partial^2 u_\mathrm{l}}{\partial y^2} = 0, \qquad -\frac{\partial p_\mathrm{l}}{\partial y} + \varepsilon^4\frac{\partial^2 v_\mathrm{l}}{\partial x^2} + \varepsilon^2\frac{\partial^2 v_\mathrm{l}}{\partial y^2} = 0, \quad (2.28)$$

$$\varepsilon^2\mathrm{Pe}\left(\lambda\varepsilon\frac{\partial c_\mathrm{l}}{\partial t} + \nabla\cdot(c_\mathrm{l}\mathbf{u}_\mathrm{l})\right) = \varepsilon^2\frac{\partial^2 c_\mathrm{l}}{\partial x^2} + \frac{\partial^2 c_\mathrm{l}}{\partial y^2}, \quad (2.29)$$

where $\mathrm{Pe} = LU^*/(\lambda\varepsilon D)$ is the Péclet number for axial flow in the lumen. Similarly, the porous membrane equations become (for $1 < y < 1 + h_2$)

$$u_\mathrm{m} = -\varepsilon^2\kappa_\mathrm{m}\frac{\partial p_\mathrm{m}}{\partial x}, \qquad v_\mathrm{m} = -\kappa_\mathrm{m}\frac{\partial p_\mathrm{m}}{\partial y}, \qquad \varepsilon^2\frac{\partial^2 p_\mathrm{m}}{\partial x^2} + \frac{\partial^2 p_\mathrm{m}}{\partial y^2} = 0, \quad (2.30a\text{-}c)$$

and

$$\lambda\varepsilon^3\mathrm{Pe}\left(\frac{\partial c_\mathrm{m}}{\partial t} + \nabla\cdot(c_\mathrm{m}\mathbf{u}_\mathrm{m})\right) = \varepsilon^2\frac{\partial^2 c_\mathrm{m}}{\partial x^2} + \frac{\partial^2 c_\mathrm{m}}{\partial y^2}, \quad (2.31)$$

where $\kappa_\mathrm{m} = k_\mathrm{m}/(\lambda\varepsilon^5 L^2)$ is the dimensionless permeability. We will assume a dominant balance between the radial terms in equation (2.30*b*), and so take $\kappa_\mathrm{m} = \mathrm{O}(1)$ (see §2.5.5).

In the ECS ($1 + h_2 < y < 1 + h_2 + h_3$), the no voids condition is unchanged:

$$\theta_\mathrm{n} + \theta_\mathrm{w} + \theta_\mathrm{s} = 1. \quad (2.32)$$

The dimensionless conservation of mass equations are

$$\frac{\partial\theta_\mathrm{n}}{\partial t} + \frac{\partial}{\partial x}(\theta_\mathrm{n}u_\mathrm{n}) + \frac{\partial}{\partial y}(\theta_\mathrm{n}v_\mathrm{n}) = J_\mathrm{n}, \qquad \frac{\partial\theta_\mathrm{w}}{\partial t} + \frac{\partial}{\partial x}(\theta_\mathrm{w}u_\mathrm{w}) + \frac{\partial}{\partial y}(\theta_\mathrm{w}v_\mathrm{w}) = -J_\mathrm{n}, \quad (2.33)$$

conservation of momentum for the cell phase is given by

$$-\theta_\mathrm{n}\frac{\partial p_\mathrm{w}}{\partial x} - \frac{\partial}{\partial x}(\theta_\mathrm{n}\Pi) + \psi_\mathrm{ns}\theta_\mathrm{s}\frac{\partial\theta_\mathrm{n}}{\partial x} + \frac{2\varepsilon^2}{3}\frac{\partial}{\partial x}\left[\theta_\mathrm{n}\left(2\frac{\partial u_\mathrm{n}}{\partial x} - \frac{\partial v_\mathrm{n}}{\partial y}\right)\right] + \frac{\partial}{\partial y}\left[\theta_\mathrm{n}\left(\frac{\partial u_\mathrm{n}}{\partial y} + \varepsilon^2\frac{\partial v_\mathrm{n}}{\partial x}\right)\right] - \zeta_\mathrm{ns}\theta_\mathrm{n}\theta_\mathrm{s}u_\mathrm{n} = 0, \quad (2.34)$$

$$-\theta_\mathrm{n}\frac{\partial p_\mathrm{w}}{\partial y} - \frac{\partial}{\partial y}(\theta_\mathrm{n}\Pi) + \psi_\mathrm{ns}\theta_\mathrm{s}\frac{\partial\theta_\mathrm{n}}{\partial y} + \varepsilon^2\frac{\partial}{\partial x}\left[\theta_\mathrm{n}\left(\frac{\partial u_\mathrm{n}}{\partial y} + \varepsilon^2\frac{\partial v_\mathrm{n}}{\partial x}\right)\right] + \frac{2\varepsilon^2}{3}\frac{\partial}{\partial y}\left[\theta_\mathrm{n}\left(2\frac{\partial v_\mathrm{n}}{\partial y} - \frac{\partial u_\mathrm{n}}{\partial x}\right)\right] - \varepsilon^2\zeta_\mathrm{ns}\theta_\mathrm{n}\theta_\mathrm{s}v_\mathrm{n} = 0, \quad (2.35)$$

and for the water phase is given by

$$-\theta_\mathrm{w}\frac{\partial p_\mathrm{w}}{\partial x} - \zeta_\mathrm{ws}\theta_\mathrm{w}\theta_\mathrm{s}u_\mathrm{w} = 0, \qquad -\theta_\mathrm{w}\frac{\partial p_\mathrm{w}}{\partial y} - \varepsilon^2\zeta_\mathrm{ws}\theta_\mathrm{w}\theta_\mathrm{s}v_\mathrm{w} = 0, \quad (2.36)$$

where $\zeta_{i\mathrm{s}} = \gamma_{i\mathrm{s}}L^2\lambda\varepsilon^3/\mu_\mathrm{w}$ ($i = \mathrm{n}, \mathrm{w}$) are dimensionless. The dimensionless solute transport equation is

$$\lambda\varepsilon^3\mathrm{Pe}\left(\frac{\partial}{\partial t}(\theta_\mathrm{w}c_\mathrm{w}) + \nabla\cdot(\theta_\mathrm{w}c_\mathrm{w}\mathbf{u}_\mathrm{w})\right) = \varepsilon^2\frac{\partial}{\partial x}\left(\theta_\mathrm{w}\frac{\partial c_\mathrm{w}}{\partial x}\right) + \frac{\partial}{\partial y}\left(\theta_\mathrm{w}\frac{\partial c_\mathrm{w}}{\partial y}\right) + \varepsilon^2\mathcal{R}. \quad (2.37)$$

Finally, the boundary conditions on the lumen centreline become

$$\frac{\partial u_\mathrm{l}}{\partial y} = 0, \qquad v_\mathrm{l} = 0, \qquad \frac{\partial c_\mathrm{l}}{\partial y} = 0 \qquad \text{on} \quad y = 0, \tag{2.38}$$

on the lumen/membrane interface

$$\begin{gathered} u_\mathrm{l} = 0, \qquad \varepsilon \frac{\partial p_\mathrm{m}}{\partial y} = -\frac{1}{\lambda \kappa_\mathrm{m} \phi_\mathrm{m}} v_\mathrm{l}, \qquad p_\mathrm{l} + \frac{2\varepsilon^2}{3}\left(\frac{\partial u_\mathrm{l}}{\partial x} - 2\frac{\partial v_\mathrm{l}}{\partial y}\right) = p_\mathrm{m}, \\ c_\mathrm{l} = c_\mathrm{m}, \qquad \frac{\partial c_\mathrm{l}}{\partial y} = \phi_\mathrm{m} \frac{\partial c_\mathrm{m}}{\partial y} \qquad \text{on} \quad y = 1, \end{gathered} \tag{2.39a-e}$$

on the membrane/ECS interface

$$\begin{gathered} u_\mathrm{n} = v_\mathrm{n} = 0, \qquad v_\mathrm{w} = -\frac{\kappa_\mathrm{m} \phi_\mathrm{m}}{\theta_\mathrm{w}} \frac{\partial p_\mathrm{m}}{\partial y}, \qquad p_\mathrm{w} = p_\mathrm{m}, \\ c_\mathrm{m} = c_\mathrm{w}, \qquad \phi_\mathrm{m} \frac{\partial c_\mathrm{m}}{\partial y} = \theta_\mathrm{w} \frac{\partial c_\mathrm{w}}{\partial y} \qquad \text{on} \quad y = 1 + h_2, \end{gathered} \tag{2.40}$$

and on the bioreactor boundary

$$u_\mathrm{n} = v_\mathrm{n} = v_\mathrm{w} = 0, \qquad \theta_\mathrm{w} \frac{\partial c_\mathrm{w}}{\partial y} = 0 \qquad \text{on} \quad y = H. \tag{2.41}$$

2.5.2 Derivation of the reduced model

Next we use asymptotic analysis to derive a reduced system of governing equations at leading order in ε, before introducing up- and downstream boundary conditions to close the problem. We begin by expanding each dependent variable as an asymptotic series in powers of ε. For example, we let $u_\mathrm{l} \sim u_{\mathrm{l}_0} + \varepsilon u_{\mathrm{l}_1} + \varepsilon^2 u_{\mathrm{l}_2} + \ldots$ and similarly expand the remaining velocities v_l, u_i, v_i $(i = \mathrm{m}, \mathrm{w}, \mathrm{n})$, the reduced pressures p_i $(i = \mathrm{l}, \mathrm{m}, \mathrm{w})$, the concentrations c_i $(i = \mathrm{l}, \mathrm{m}, \mathrm{w})$, and the volume fractions θ_n and θ_w. We will consider the transport regime where $\mathrm{Pe} = \mathrm{O}(1)$ (see §2.5.5), corresponding to a dominant balance between axial diffusion and advection in the lumen. In the following we consider the leading-order system in each layer in turn, omitting the subscript 0 from the leading-order variables except where needed for clarity.

Substituting the expansions into the lumen equations (2.28) and (2.29), and boundary conditions (2.38) and (2.39*a*,*b*), and equating coefficients of ε^0 gives

$$\frac{\partial u_\mathrm{l}}{\partial x} + \frac{\partial v_\mathrm{l}}{\partial y} = 0, \qquad \frac{\partial^2 u_\mathrm{l}}{\partial y^2} = \frac{\partial p_\mathrm{l}}{\partial x}, \qquad \frac{\partial p_\mathrm{l}}{\partial y} = 0, \qquad \frac{\partial^2 c_\mathrm{l}}{\partial y^2} = 0, \tag{2.42}$$

with

$$\frac{\partial u_\mathrm{l}}{\partial y} = 0, \qquad v_\mathrm{l} = 0, \qquad \frac{\partial c_\mathrm{l}}{\partial y} = 0 \qquad \text{on} \quad y = 0, \tag{2.43}$$

and

$$u_{\rm l} = v_{\rm l} = 0 \qquad \text{on} \quad y = 1, \tag{2.44}$$

which yields

$$p_{\rm l} = p_{\rm l}(x,t), \qquad \frac{\partial^2 p_{\rm l}}{\partial x^2} = 0, \qquad u_{\rm l} = \frac{1}{2}\frac{\partial p_{\rm l}}{\partial x}(y^2-1), \qquad v_{\rm l} \equiv 0, \qquad c_{\rm l} = c_{\rm l}(x,t). \tag{2.45}$$

In the porous membrane, the governing equations (2.30) and (2.31) become

$$u_{\rm m} \equiv 0, \qquad v_{\rm m} = -\kappa_{\rm m}\frac{\partial p_{\rm m}}{\partial y}, \qquad \frac{\partial^2 p_{\rm m}}{\partial y^2} = 0, \qquad \frac{\partial^2 c_{\rm m}}{\partial y^2} = 0, \tag{2.46a-d}$$

and so our assumption on the size of $\kappa_{\rm m}$ leads to a reduced pressure gradient at leading order across the porous membrane. Boundary conditions (2.39c-e) yield

$$p_{\rm l} = p_{\rm m}, \qquad c_{\rm l} = c_{\rm m}, \qquad \phi_{\rm m}\frac{\partial c_{\rm m}}{\partial y} = \frac{\partial c_{\rm l}}{\partial y} = 0 \qquad \text{on} \quad y = 1. \tag{2.47}$$

Equations (2.46c,d) thus integrate to give

$$p_{\rm m} = P(x,t)(y-1) + p_{\rm l}(x,t), \qquad c_{\rm m}(x,t) \equiv c_{\rm l}(x,t), \tag{2.48}$$

for some function $P(x,t)$ which remains to be determined as part of the solution to the reduced model.

In the ECS, equating coefficients of ε^0 in equation (2.32) yields

$$\theta_{\rm n} + \theta_{\rm w} + \theta_{\rm s} = 1, \tag{2.49}$$

equation (2.33) becomes

$$\frac{\partial \theta_{\rm n}}{\partial t} + \frac{\partial}{\partial x}(\theta_{\rm n} u_{\rm n}) + \frac{\partial}{\partial y}(\theta_{\rm n} v_{\rm n}) = J_{\rm n}, \qquad \frac{\partial \theta_{\rm w}}{\partial t} + \frac{\partial}{\partial x}(\theta_{\rm w} u_{\rm w}) + \frac{\partial}{\partial y}(\theta_{\rm w} v_{\rm w}) = -J_{\rm n}, \tag{2.50a,b}$$

equations (2.34) and (2.35) give

$$-\theta_{\rm n}\frac{\partial p_{\rm w}}{\partial x} - \frac{\partial}{\partial x}(\theta_{\rm n}\Pi) + \psi_{\rm ns}\theta_{\rm s}\frac{\partial \theta_{\rm n}}{\partial x} - \zeta_{\rm ns}\theta_{\rm n}\theta_{\rm s}u_{\rm n} + \frac{\partial}{\partial y}\left(\theta_{\rm n}\frac{\partial u_{\rm n}}{\partial y}\right) = 0, \tag{2.51}$$

$$-\theta_{\rm n}\frac{\partial p_{\rm w}}{\partial y} - \frac{\partial}{\partial y}(\theta_{\rm n}\Pi) + \psi_{\rm ns}\theta_{\rm s}\frac{\partial \theta_{\rm n}}{\partial y} = 0, \tag{2.52}$$

and equations (2.36) and (2.37) are now

$$-\theta_{\rm w}\frac{\partial p_{\rm w}}{\partial x} - \zeta_{\rm ws}\theta_{\rm w}\theta_{\rm s}u_{\rm w} = 0, \qquad -\theta_{\rm w}\frac{\partial p_{\rm w}}{\partial y} = 0, \qquad \frac{\partial}{\partial y}\left(\theta_{\rm w}\frac{\partial c_{\rm w}}{\partial y}\right) = 0. \tag{2.53a-c}$$

Boundary conditions (2.40) and (2.41) yield

$$\begin{aligned} &u_\mathrm{n} = v_\mathrm{n} = 0, \qquad v_\mathrm{w} = -\frac{\kappa_\mathrm{m}\phi_\mathrm{m}}{\theta_\mathrm{w}}\frac{\partial p_\mathrm{m}}{\partial y}, \qquad p_\mathrm{w} = p_\mathrm{m}, \\ &c_\mathrm{m} = c_\mathrm{w}, \qquad \phi_\mathrm{m}\frac{\partial c_\mathrm{m}}{\partial y} = \theta_\mathrm{w}\frac{\partial c_\mathrm{w}}{\partial y} \qquad \text{on} \quad y = 1 + h_2, \end{aligned} \tag{2.54a-f}$$

and

$$u_\mathrm{n} = v_\mathrm{n} = v_\mathrm{w} = 0, \qquad \theta_\mathrm{w}\frac{\partial c_\mathrm{w}}{\partial y} = 0 \qquad \text{on} \quad y = H. \tag{2.55a-d}$$

From equation (2.53c) and boundary conditions (2.54e,f) and (2.55d), we find that the solute concentration is independent of y at leading order, and set $c_i := c(x,t)$ $(i = \mathrm{l}, \mathrm{m}, \mathrm{w})$ for some global concentration $c(x,t)$ which will also be determined as part of the solution to the reduced model.

Equation (2.53b) tells us that the reduced water pressure p_w is independent of y, and thus it follows from (2.52) and (2.49), respectively, that the leading-order cell and water volume fractions θ_n and θ_w are also independent of y. In addition, from (2.51) and boundary conditions (2.54a) and (2.55a) we can deduce that

$$u_\mathrm{n}(x,y,t) = \frac{M(x,t)}{\theta_\mathrm{s}\zeta_\mathrm{ns}}\left\{\frac{\sinh\left[\sqrt{\theta_\mathrm{s}\zeta_\mathrm{ns}}(y - H + h_3)\right] + \sinh\left[\sqrt{\theta_\mathrm{s}\zeta_\mathrm{ns}}(H - y)\right]}{\sinh\left(\sqrt{\theta_\mathrm{s}\zeta_\mathrm{ns}}h_3\right)} - 1\right\}, \tag{2.56}$$

where here

$$\begin{aligned} M(x,t) &:= \frac{\partial p_\mathrm{w}}{\partial x} + \frac{\Phi(\theta_\mathrm{n},c)}{\theta_\mathrm{n}}\frac{\partial \theta_\mathrm{n}}{\partial x} + \Pi_\mathrm{c}'\frac{\partial c}{\partial x}, \\ \Phi(\theta_\mathrm{n},c) &:= \Pi_\mathrm{n} + \Pi_\mathrm{c} + \theta_\mathrm{n}\Pi_\mathrm{n}' - \psi_\mathrm{ns}\theta_\mathrm{s}, \qquad \Pi_\mathrm{c}' = -\frac{\chi}{\bar{c}}\exp\left(-\frac{c}{\bar{c}}\right), \end{aligned} \tag{2.57a-c}$$

whilst (2.53a) and (2.54d) respectively give

$$u_\mathrm{w}(x,t) = -\frac{1}{\theta_\mathrm{s}\zeta_\mathrm{ws}}\frac{\partial p_\mathrm{w}}{\partial x}, \qquad p_\mathrm{w}(x,t) = h_2 P(x,t) + p_\mathrm{l}(x,t), \tag{2.58}$$

where $P(x,t)$ was introduced in (2.48). In equation (2.57), primes denote differentiation with respect to the argument of a function. Furthermore, by integrating (2.50) over the ECS and applying boundary conditions (2.54b,c) and (2.55b,c) we obtain the following equations for θ_n and p_w (via $P(x,t)$):

$$\frac{\partial \theta_\mathrm{n}}{\partial t} + \frac{\partial Q_\mathrm{n}}{\partial x} = J_\mathrm{n}, \qquad \frac{\partial}{\partial x}\left(Q_\mathrm{n} + Q_\mathrm{w}\right) = -\frac{\kappa_\mathrm{m}\phi_\mathrm{m}}{h_3}P(x,t), \tag{2.59a,b}$$

where the cell flux Q_n and water flux Q_w are given by

$$Q_\mathrm{n} = F\left(\frac{\partial p_\mathrm{w}}{\partial x}\theta_\mathrm{n} + \Phi(\theta_\mathrm{n},c)\frac{\partial \theta_\mathrm{n}}{\partial x} + \theta_\mathrm{n}\Pi_\mathrm{c}'\frac{\partial c}{\partial x}\right), \qquad Q_\mathrm{w} = -\frac{\theta_\mathrm{w}}{\theta_\mathrm{s}\zeta_\mathrm{ws}}\frac{\partial p_\mathrm{w}}{\partial x}, \tag{2.60a,b}$$

with

$$F := \frac{2\cosh(\alpha) - \alpha\sinh(\alpha) - 2}{\theta_{\mathrm{s}}\zeta_{\mathrm{ns}}\alpha\sinh(\alpha)}, \qquad \alpha := h_3\sqrt{\theta_{\mathrm{s}}\zeta_{\mathrm{ns}}}. \tag{2.61}$$

From (2.59a) and (2.60a) we can see more clearly the effect of the cell aggregation/repulsion term Π_{n} and chemotaxis term Π_{c} on the evolution of θ_{n}, through the contributions to the nonlinear advection (involving Π_{c}' only) and diffusion (involving Φ and therefore, from (2.57b), Π_{n}, Π_{n}', and Π_{c}) terms in Q_{n}.

Now we determine an equation for c before introducing up- and downstream boundary conditions to close the resulting coupled system. The solute equations (2.29), (2.31), and (2.37) at $\mathrm{O}(\varepsilon)$ are in terms of c_{i_1} $(i = \mathrm{l}, \mathrm{m}, \mathrm{w})$ and independent of $c(x,t)$, and hence we must go to $\mathrm{O}(\varepsilon^2)$ to find an equation for $c(x,t)$. Equating coefficients of ε^2 in the solute equations in each layer (briefly returning to subscript 0 notation for leading-order variables for clarity), we obtain

$$\mathrm{Pe}\left(\frac{\partial}{\partial x}(c_{\mathrm{l}_0}u_{\mathrm{l}_0}) + \frac{\partial}{\partial y}(c_{\mathrm{l}_0}v_{\mathrm{l}_0})\right) = \frac{\partial^2 c_{\mathrm{l}_0}}{\partial x^2} + \frac{\partial^2 c_{\mathrm{l}_2}}{\partial y^2}, \tag{2.62}$$

$$\frac{\partial^2 c_{\mathrm{m}_0}}{\partial x^2} + \frac{\partial^2 c_{\mathrm{m}_2}}{\partial y^2} = 0, \tag{2.63}$$

$$\frac{\partial}{\partial x}\left(\theta_{\mathrm{w}_0}\frac{\partial c_{\mathrm{w}_0}}{\partial x}\right) + \frac{\partial}{\partial y}\left(\theta_{\mathrm{w}_0}\frac{\partial c_{\mathrm{w}_2}}{\partial y} + \theta_{\mathrm{w}_2}\frac{\partial c_{\mathrm{w}_0}}{\partial y}\right) = -\mathcal{R}_0. \tag{2.64}$$

The corresponding boundary conditions are given by

$$\frac{\partial c_{\mathrm{l}_2}}{\partial y} = 0 \quad \text{on} \quad y = 0, \tag{2.65}$$

$$\frac{\partial c_{\mathrm{l}_2}}{\partial y} = \phi_{\mathrm{m}}\frac{\partial c_{\mathrm{m}_2}}{\partial y}, \qquad c_{\mathrm{l}_2} = c_{\mathrm{m}_2} \qquad \text{on} \quad y = 1, \tag{2.66a,b}$$

$$\phi_{\mathrm{m}}\frac{\partial c_{\mathrm{m}_2}}{\partial y} = \theta_{\mathrm{w}_0}\frac{\partial c_{\mathrm{w}_2}}{\partial y}, \qquad c_{\mathrm{m}_2} = c_{\mathrm{w}_2} \qquad \text{on} \quad y = 1 + h_2, \tag{2.67a,b}$$

and

$$\frac{\partial c_{\mathrm{w}_2}}{\partial y} = 0 \qquad \text{on} \quad y = H. \tag{2.68}$$

We integrate equations (2.62), (2.63), and (2.64) with respect to y across the lumen, porous membrane, and ECS respectively, and add them together (multiplying the integrated form of equation (2.63) by the pore fraction ϕ_{m} first). Applying boundary conditions (2.65), (2.66a), (2.67a), and (2.68) then yields

$$\frac{\partial Q_{\mathrm{c}}}{\partial x} = -h_3\mathcal{R}(\theta_{\mathrm{n}}, c), \tag{2.69}$$

where the solute flux Q_c is given by

$$Q_\mathrm{c} = \frac{1}{3}\mathrm{Pe}\frac{\partial p_\mathrm{l}}{\partial x}c + b(\theta_\mathrm{n})\frac{\partial c}{\partial x}, \qquad b(\theta_\mathrm{n}) := 1 + h_2\phi_\mathrm{m} + h_3(1-\theta_\mathrm{s}-\theta_\mathrm{n}). \tag{2.70}$$

2.5.3 Boundary conditions for the reduced model

To close the coupled system given by equations (2.59*a*,*b*) and (2.69), we prescribe up- and downstream boundary conditions appropriate to this flow regime. These are motivated by the boundary conditions for the full two-dimensional domain (including the ECS ports) discussed in §2.3.4. Firstly, we prescribe a volume flux of fluid per unit length in the z-direction (perpendicular to x and y) into the lumen, setting

$$\int_0^1 u_\mathrm{l}\,\mathrm{d}y = Q_\mathrm{l,in} \qquad \text{at} \quad x = 0, \tag{2.71}$$

where $Q_\mathrm{l,in}$ is dimensionless and assumed constant. Additionally, we anticipate a small flux of fluid into the ECS (due to fluid which has already permeated through the fibre from the lumen), and set

$$\int_{1+h_2}^{H} \theta_\mathrm{w}u_\mathrm{w}\,\mathrm{d}y = Q_\mathrm{e,in} \qquad \text{at} \quad x = 0, \tag{2.72}$$

where $Q_\mathrm{e,in}$ is also constant and dimensionless. Here, we fix a dimensional value for the ECS inlet fluid flux which is much less than that into the lumen, and leads to the dimensionless relationship $Q_\mathrm{e,in} = 2.5Q_\mathrm{l,in}$ (see §2.5.5). This is motivated by the expectation that the permeate flow rate in the ECS will be of $\mathrm{O}(\varepsilon)$ lower than that in the lumen due to the choice of velocity scales in §2.5.1. We also carry out a sensitivity analysis of this and other key parameters in §2.7.5.

Next, we prescribe a (reduced) downstream lumen pressure (to mimic the clamp present experimentally as discussed in §2.3.4), setting

$$p_\mathrm{l} = P_\mathrm{dwn} \qquad \text{at} \quad x = 1, \tag{2.73}$$

where P_dwn is dimensionless, fixed, and constant. At the downstream ECS end in an experiment, the bioreactor ECS port is left open to the atmosphere, and so to mimic this condition we take (given the choice of non-dimensionalisation in (2.27))

$$p_\mathrm{w} = 0 \qquad \text{at} \quad x = 1. \tag{2.74}$$

As discussed in §2.3.4, we impose no flux of cells out of the reduced region by setting

$$Q_\mathrm{n} = 0 \qquad \text{at} \quad x = 0, 1. \tag{2.75}$$

Depending on whether the solute is being delivered at the lumen inlet or not, we impose either a fixed concentration c_{in} upstream (in which case $C^* = c_{\mathrm{in}}$) or no total flux of solute into the lumen. These give, respectively,

$$c = 1 \qquad \text{or} \qquad Q_{\mathrm{c}} = 0 \qquad \text{at} \quad x = 0. \tag{2.76}$$

At the lumen outlet we impose no diffusive flux of solute, as discussed in §2.3.4:

$$\frac{\partial c}{\partial x} = 0 \qquad \text{at} \quad x = 1. \tag{2.77}$$

These boundary conditions allow us to solve explicitly for more of the leading-order unknowns in terms of θ_{n}, c, and p_{w}, so that, in the lumen,

$$u_{\mathrm{l}}(y) = -\frac{3}{2}Q_{\mathrm{l,in}}(y^2 - 1), \qquad v_{\mathrm{l}} \equiv 0, \qquad p_{\mathrm{l}}(x) = 3Q_{\mathrm{l,in}}(1 - x) + P_{\mathrm{dwn}}, \tag{2.78}$$

in the membrane,

$$\begin{gathered} u_{\mathrm{m}} \equiv 0, \qquad v_{\mathrm{m}}(x,t) = -\kappa_{\mathrm{m}} P(x,t), \\ p_{\mathrm{m}}(x,y,t) = 3Q_{\mathrm{l,in}}(1 - x) + P(x,t)(y - 1) + P_{\mathrm{dwn}}, \end{gathered} \tag{2.79}$$

and in the ECS,

$$\begin{gathered} u_{\mathrm{w}}(x,t) = -\frac{1}{\theta_{\mathrm{s}}\zeta_{\mathrm{ws}}}\frac{\partial p_{\mathrm{w}}}{\partial x}, \\ u_{\mathrm{n}}(x,y,t) = \frac{M(x,t)}{\theta_{\mathrm{s}}\zeta_{\mathrm{ns}}}\left\{\frac{\sinh\left[\sqrt{\theta_{\mathrm{s}}\zeta_{\mathrm{ns}}}(y - H + h_3)\right] + \sinh\left[\sqrt{\theta_{\mathrm{s}}\zeta_{\mathrm{ns}}}(H - y)\right]}{\sinh\left(\sqrt{\theta_{\mathrm{s}}\zeta_{\mathrm{ns}}}h_3\right)} - 1\right\}, \end{gathered} \tag{2.80}$$

where P is given in terms of p_{w} by

$$P(x,t) = \frac{1}{h_2}\left[p_{\mathrm{w}}(x,t) - 3Q_{\mathrm{l,in}}(1 - x) - P_{\mathrm{dwn}}\right], \tag{2.81}$$

and $M(x,t)$ is as defined in equation (2.57). We note that equations (2.50*a*,*b*) still hold for v_{n} and v_{w}, respectively.

2.5.4 Summary of the reduced model

To summarise, the reduced model for $\theta_{\mathrm{n}}(x,t)$, $c(x,t)$, and $p_{\mathrm{w}}(x,t)$ is given by

$$\begin{gathered} \frac{\partial \theta_{\mathrm{n}}}{\partial t} + \frac{\partial Q_{\mathrm{n}}}{\partial x} = J_{\mathrm{n}}, \qquad \frac{\partial Q_{\mathrm{c}}}{\partial x} = -h_3\mathcal{R}(\theta_{\mathrm{n}}, c), \\ \frac{\partial}{\partial x}\left(Q_{\mathrm{n}} + Q_{\mathrm{w}}\right) = -\frac{\kappa_{\mathrm{m}}\phi_{\mathrm{m}}}{h_2 h_3}\left[p_{\mathrm{w}} - 3Q_{\mathrm{l,in}}(1 - x) - P_{\mathrm{dwn}}\right], \end{gathered} \tag{2.82}$$

where the fluxes are given by

$$\begin{aligned} Q_{\mathrm{n}} &= F\left(\frac{\partial p_{\mathrm{w}}}{\partial x}\theta_{\mathrm{n}} + \Phi(\theta_{\mathrm{n}}, c)\frac{\partial \theta_{\mathrm{n}}}{\partial x} + \theta_{\mathrm{n}}\Pi_{\mathrm{c}}'\frac{\partial c}{\partial x}\right), \\ Q_{\mathrm{c}} &= -\mathrm{Pe}Q_{\mathrm{l,in}}c + b(\theta_{\mathrm{n}})\frac{\partial c}{\partial x}, \qquad Q_{\mathrm{w}} = -\frac{\theta_{\mathrm{w}}}{\theta_{\mathrm{s}}\zeta_{\mathrm{ws}}}\frac{\partial p_{\mathrm{w}}}{\partial x}, \end{aligned} \tag{2.83}$$

and we recall that

$$\begin{aligned} F &:= \frac{2\cosh(\alpha) - \alpha\sinh(\alpha) - 2}{\theta_{\mathrm{s}}\zeta_{\mathrm{ns}}\alpha\sinh(\alpha)}, \qquad \alpha := h_3\sqrt{\theta_{\mathrm{s}}\zeta_{\mathrm{ns}}}, \\ \Phi(\theta_{\mathrm{n}}, c) &= \Pi_{\mathrm{n}} + \Pi_{\mathrm{c}} + \theta_{\mathrm{n}}\Pi_{\mathrm{n}}' - \psi_{\mathrm{ns}}\theta_{\mathrm{s}}, \\ \Pi_{\mathrm{c}}' &= -\frac{\chi}{\bar{c}}\exp\left(-\frac{c}{\bar{c}}\right), \qquad b(\theta_{\mathrm{n}}) := 1 + h_2\phi_{\mathrm{m}} + h_3(1 - \theta_{\mathrm{s}} - \theta_{\mathrm{n}}). \end{aligned} \tag{2.84}$$

The boundary conditions are

$$Q_{\mathrm{n}} = 0, \qquad c = 1 \quad \text{or} \quad Q_{\mathrm{c}} = 0, \qquad Q_{\mathrm{w}} = \frac{Q_{\mathrm{e,in}}}{h_3} \qquad \text{at} \quad x = 0, \tag{2.85}$$

$$Q_{\mathrm{n}} = 0, \qquad \frac{\partial c}{\partial x} = 0, \qquad p_{\mathrm{w}} = 0 \qquad \text{at} \quad x = 1, \tag{2.86}$$

and the initial condition on θ_{n} is taken to be

$$\theta_{\mathrm{n}}(x, 0) = \theta_{\mathrm{n}}^*(x) \qquad \text{for } 0 < x < 1, \tag{2.87}$$

for some initial profile $\theta_{\mathrm{n}}^*(x)$. Thus, the original system (equations (2.1)-(2.6), (2.7), (2.8), and (2.17)-(2.21)) has been reduced from sixteen to three unknowns, and from two dimensions to one dimension, having eliminated the dependence on y. We now have a coupled system comprising an advection-reaction-diffusion PDE for θ_{n}, and quasi-steady second-order nonlinear ordinary differential equations (ODEs) for c and p_{w}. The main effects contributing to the cell flux Q_{n} are cell advection (dependent on the reduced water pressure gradient and chemotaxis), cell diffusion (dependent on the cell intraphase pressure and cell-scaffold interphase pressure), and the cell-scaffold drag (through F). The water flux Q_{w} contains an advection term which also depends on the reduced water pressure gradient and water-scaffold drag. Finally, the solute flux Q_{c} has an advective term dependent on the lumen inlet fluid flux, and a diffusive term which is affected by the widths and (effective) porosities of the membrane and ECS. This coupled system can now be solved numerically, given appropriate constitutive forms for J_{n} and $\mathcal{R}$.

2.5.5 Parameter values

Before solving the system from §2.5.4 we determine the sizes of the dimensionless parameters, guided by our experimental collaborators and dimensional values obtained from the

Table 2.1: Dimensional parameters.

Parameter	Dimensional value and units	Ref.
h_1	200 μm	[156]
h_2	200 μm	[156]
h_3	600 μm	[156]
L	0.1 m	[156]
ρ_{w}	1 g cm^{-3}	[155]
μ_{w}	10^{-3} Pa s	[155]
k_{m}	6.73×10^{-16} m^2	*
p_{atm}	14.69 psia	[156]
$Q_{\mathrm{l,in}}$	1.02×10^{-11} - 1.02×10^{-8} m^2 s^{-1}	†
Γ_{nw}	5.79×10^{-6} s^{-1}	†
Γ_{wn}	4.13×10^{-7} s^{-1}	†
c_{in}	0.22 mol m^{-3}	[155]
D	3×10^{-9} m^2 s^{-1}	[155]
U^*	1.02×10^{-8} m s^{-1}	†
C^*	0.22 mol m^{-3}	[155]

* Value obtained experimentally (unpublished data).

† Values based on estimations by our experimental collaborators.

literature where possible. This justifies the distinguished limit taken to obtain our leading-order system in §2.5.4. Typical dimensional parameter values are given in Table 2.1, with dimensionless parameters summarised in Table 2.2. Dimensional parameter values for which data could not be found are omitted from Table 2.1; instead, their dimensionless equivalents are defined in Table 2.2 and values chosen so that our asymptotic analysis retains as many features as possible at leading order. Once data for these parameter values are available, we could verify whether the distinguished limit taken here is relevant or not, and perform further reductions of the system if required. The column entitled 'Restriction' in Table 2.2 states any physical or asymptotic bounds on the parameter in question required for the validity of the analysis (compared to our small parameter $\varepsilon = 2 \times 10^{-3}$). We also discuss parameter choices for which either no data are available in the literature and therefore assumptions must be made, or there exist a variety of possible values. Throughout this section, we reintroduce hats denoting dimensionless parameters for clarity.

Firstly, we set the membrane/ECS velocity scaling U^* by using an experimental lumen inlet fluid flux of 3.86×10^{-5} ml min^{-1}. This has been chosen so that the maximum inlet flux considered (corresponding to a dimensionless flux of 10) is equivalent in volume to that used in flask culture (in which 50 ml of culture medium is supplied ev-

Table 2.2: Dimensionless parameters, along with any bounds imposed either physically or by the asymptotic analysis.

Parameter	Definition	Value	Restriction	Ref.
$\hat{h}_2$	$h_2/(\varepsilon L)$	1	$\hat{h}_2 > 0$	-
$\hat{h}_3$	$h_3/(\varepsilon L)$	3	$\hat{h}_3 > 0$	-
θ_s	-	0.4	$0 < \theta_\mathrm{s} < 1$	[92]
ε	h_1/L	2×10^{-3}	$0 < \varepsilon \ll 1$	-
λ	$\mu_\mathrm{w}/(\varepsilon\mu_\mathrm{n})$	1	$\varepsilon \ll \lambda \ll 1/\varepsilon$	-
$\varepsilon^2\mathrm{Pe}$	$\varepsilon L U^*/(\lambda D)$	6.83×10^{-4}	$\varepsilon^3 \ll \varepsilon^2\mathrm{Pe} \ll \varepsilon$	-
$\varepsilon^2\mathrm{Re}$	$\varepsilon\rho_\mathrm{w} L U^*/(\lambda\mu_\mathrm{w})$	2.05×10^{-6}	$\varepsilon^2\mathrm{Re} \ll 1$	-
ϕ_m	-	0.77	$0 < \phi_\mathrm{m} < 1$	[109]
κ_m	$k_\mathrm{m}/(\lambda\varepsilon^5 L^2)$	2.1	$\varepsilon \ll \kappa_\mathrm{m} \ll 1/\varepsilon$	-
$\hat{Q}_\mathrm{l,in}$	$\lambda Q_\mathrm{l,in}/(LU^*)$	0.01 - 10	$\varepsilon \ll \hat{Q}_\mathrm{l,in} \ll 1/\varepsilon$	-
$\hat{Q}_\mathrm{e,in}$	$Q_\mathrm{e,in}/(\varepsilon LU^*)$ $= 2.5Q_\mathrm{l,in}/(LU^*)$	0.025 - 25	$\varepsilon \ll \hat{Q}_\mathrm{e,in} \ll 1/\varepsilon$	-
$\hat{\nu}$	$\lambda\varepsilon^3 L\nu/(\mu_w U^*)$	0.3	$\varepsilon \ll \hat{\nu} \ll 1/\varepsilon$	[123]
$\hat{\delta}_\mathrm{a}$	$\lambda\varepsilon^3 L\delta_\mathrm{a}/(\mu_w U^*)$	0.1	$\varepsilon \ll \hat{\delta}_\mathrm{a} \ll 1/\varepsilon$	[123]
$\hat{\eta}$	$\lambda\varepsilon^3 L\eta/(\mu_w U^*)$	0.3	$\varepsilon \ll \hat{\eta} \ll 1/\varepsilon$	[123]
$\hat{\chi}$	$\lambda\varepsilon^3 L\chi/(\mu_w U^*)$	9.06	$\varepsilon \ll \hat{\chi} \ll 1/\varepsilon$	-
$\hat{\bar{c}}$	$\bar{c}/C^*$	5	$\varepsilon \ll \hat{\bar{c}} \ll 1/\varepsilon$	-
ζ_ns	$\gamma_\mathrm{ns} L^2\lambda\varepsilon^3/\mu_\mathrm{w}$	1	$\varepsilon \ll \zeta_\mathrm{ns} \ll 1/\varepsilon$	-
ζ_ws	$\gamma_\mathrm{ws} L^2\lambda\varepsilon^3/\mu_\mathrm{w}$	0.1	$\varepsilon \ll \zeta_\mathrm{ws} \ll 1/\varepsilon$	-
$\hat{\Gamma}_\mathrm{nw}$	$L\Gamma_\mathrm{nw}/U^*$	56.52	$\varepsilon \ll \hat{\Gamma}_\mathrm{nw} \ll 1/\varepsilon$	-
$\hat{\Gamma}_\mathrm{wn}$	$L\Gamma_\mathrm{wn}/U^*$	4.04	$\varepsilon \ll \hat{\Gamma}_\mathrm{wn} \ll 1/\varepsilon$	-
$\hat{\Gamma}_\mathrm{R1}$	$L^2\Gamma_\mathrm{R1}/(C^*D)$ or $L^2\Gamma_\mathrm{R1}/D$	50	$\varepsilon \ll \hat{\Gamma}_\mathrm{R1} \ll 1/\varepsilon$	-
$\hat{\Gamma}_\mathrm{R2}$	$L^2\Gamma_\mathrm{R2}/(C^*D)$	50	$\varepsilon \ll \hat{\Gamma}_\mathrm{R2} \ll 1/\varepsilon$	-
$\hat{K}$, $\hat{K}_1$	K/C^*, K_1/C^*	1	$\varepsilon \ll \hat{K},\ \hat{K}_1 \ll 1/\varepsilon$	-
$\hat{c}_\mathrm{in}$	c_in/C^*	1	$\varepsilon \ll \hat{c}_\mathrm{in} \ll 1/\varepsilon$	-
$\hat{P}_\mathrm{dwn}$	$\varepsilon^2 L(P_\mathrm{dwn} - p_\mathrm{atm})/(\mu_\mathrm{n} U^*)$	2.5	$\varepsilon \ll \hat{P}_\mathrm{d} \ll 1/\varepsilon$	-
$\hat{P}_\mathrm{up}$	$\varepsilon^2 L(P_\mathrm{up} - p_\mathrm{atm})/(\mu_\mathrm{n} U^*)$	6, 15	$\varepsilon \ll \hat{P}_\mathrm{u} \ll 1/\varepsilon$	-

ery 3 days to cells covering a 75 cm^2 cross section). The corresponding axial lumen velocity is $U^*/(\lambda\varepsilon) = 5.12 \times 10^{-6}$ m s^{-1} and hence our membrane/ECS velocity scaling $U^* = 1.02 \times 10^{-8}$ m s^{-1}. Achieving such a small flow rate in a HFMB setup is one of the aims of experiments being undertaken by our collaborators in Dr Marianne Ellis' group in the Centre for Regenerative Medicine, University of Bath. It is not known whether such a low flow rate will guarantee sufficient supply of nutrient to the cell population, and this is something that we will verify as part of our results in §2.7.

Using the parameter values in Table 2.1, we note that the reduced Reynolds number in

the lumen $\varepsilon^2\mathrm{Re} = \varepsilon\rho_{\mathrm{w}}LU^*/(\lambda\mu_{\mathrm{w}}) = 2.05\times10^{-6}$, which justifies the lubrication approximation taken in equation (2.2). The corresponding reduced Reynolds number in the ECS is equal to $\lambda\varepsilon^3\mathrm{Re} = 4.1\times10^{-9}$ and hence it was also appropriate to neglect inertial terms in this layer in (2.10). In fact, inertia is negligible in all limits considered in the remainder of this thesis. As mentioned in §2.5.2, we consider the regime in which $\mathrm{Pe} = \mathrm{O}(1)$. This is the appropriate distinguished limit given the choice of flow velocity U^*, and taking the solute diffusion coefficient D to be that for oxygen in water (see Table 2.1). We assume in this chapter that D is the same whether the solute under consideration is a nutrient or a chemoattractant. Whilst this assumption is valid (as oxygen itself, for instance, is a chemoattractant for *e.g.* fibroblasts [10]), much larger molecules can also be chemoattractants (such as the protein vascular endothelial growth factor (VEGF) [107]). In such cases D would be smaller in value, and thus it would yield a larger value for Pe. We do not consider this case here, as the alternative distinguished limit $\mathrm{Pe} = \mathrm{O}(1/\varepsilon)$ is considered in Chapter 4, but we note that the corresponding analysis for the model here would follow through in a similar way to that of Chapter 4. We set C^* to be 0.22 mol m^{-3}, a typical inlet concentration for oxygen when culturing a variety of cell types [155]. This choice of nutrient is motivated by the fact that the main cause of limited cell growth in *in vitro* tissue engineering (and, more specifically, HFMBs) is a deficiency in the delivery of oxygen [104, 105]. As for D, when chemoattractants are considered in §2.7 it is assumed that the typical concentration scalings for chemoattractants are similar to those for oxygen and so the same value for C^* is used throughout.

In the membrane, we set $\kappa_{\mathrm{m}} = \mathrm{O}(1)$ as discussed previously: in fact, $\kappa_{\mathrm{m}} \approx 2.1$ using the parameter values in Table 2.1.

In the ECS, although we do not have data indicating typical sizes of the drag terms, we take both ζ_{ns} and ζ_{ws} to be of $\mathrm{O}(1)$ so that their effects are retained at leading order in ε, but set $\zeta_{\mathrm{ws}} < \zeta_{\mathrm{ns}}$ (as we might expect physically). In Π_{n} and ψ_{ns}, the (dimensionless) constants $\hat{\nu}$, $\hat{\delta}_{\mathrm{a}}$, and $\hat{\eta}$ are taken to have the same values as their counterparts in [123]. In Π_{c}, the coefficient $\hat{\chi}$ is chosen so that the effects of chemotaxis appear at leading order, whilst the parameter $\hat{\bar{c}}$ is taken to have a value comparable to a typical concentration.

A number of dimensionless parameters appear in the constitutive forms of J_{n} and $\mathcal{R}$ in §2.7. In J_{n}, the (dimensional) cell proliferation rate coefficient Γ_{nw} is chosen to correspond to one cell division every 48 hours, and we assume that cells live, on average, 28 days when

fixing the (dimensional) cell death rate coefficient Γ_{wn} (these values are based on estimations by our experimental collaborators [1]). In $\mathcal{R}$, the dimensionless uptake coefficient $\hat{\Gamma}_{\mathrm{R1}}$ (taken to be the same for nutrient and chemoattractant) is taken to be O(1), as is the dimensionless chemoattractant production rate coefficient $\hat{\Gamma}_{\mathrm{R2}}$, so that we obtain a balance between uptake and production. The (dimensionless) uptake constants $\hat{K}$ and $\hat{K}_1$ which appear in J_{n} and $\mathcal{R}$, respectively, are taken to be comparable to a typical dimensionless concentration value.

Finally, we determine values for $Q_{\mathrm{l,in}}$. The velocity scale U^* was calculated based on a three-dimensional fluid flux of $Q_{\mathrm{l,in\,3D}} = 3.86 \times 10^{-5}$ ml min^{-1}, and we therefore choose a range of fluxes about this value, that is, $3.86{\times}10^{-7}$ - $3.86{\times}10^{-4}$ ml min^{-1}. These values have been converted into two-dimensional fluxes (which we state in m^2 s^{-1}) by first calculating the corresponding fluid velocity and then multiplying by the length scale in the y-direction, εL, so that $Q_{\mathrm{l,in}} = \varepsilon L Q_{\mathrm{l,in\,3D}}/A$ where A is the cross-sectional area of the three-dimensional lumen. The (reduced) dimensionless downstream pressure $\hat{P}_{\mathrm{dwn}}$ can take a range of values in an experimental setup and is set to be of order unity in our model, again so that we retain as many physical effects as possible at leading order. The (reduced) dimensionless upstream pressure $\hat{P}_{\mathrm{up}}$ appears in §2.7.6 when the backflow regime is considered, and is also taken to be of order unity.

2.5.6 Linear stability analysis (unbounded domain)

We wish to gain insight into the mechanisms governing the stability of the leading-order system to perturbations about an equilibrium state. However, the coupled system summarised in §2.5.4 does not have a spatially homogeneous steady state. Instead, we consider the simplified system which results from taking the limit where $1/\zeta_{\mathrm{ws}}$ (in Q_{w}) is large compared to $1/\zeta_{\mathrm{ns}}$ (which appears in Q_{n} through F) and $\kappa_{\mathrm{m}}\phi_{\mathrm{m}}$, but the product $\zeta_{\mathrm{ws}}Q_{\mathrm{e,in}} = \mathrm{O}(1)$ (see Table 2.2). This corresponds to the limit in which the water-scaffold drag is very small compared to the cell-scaffold drag, and the fluid flux into the ECS is large. In this case, we find that equation (2.82c) reduces to

$$\frac{\partial Q_{\mathrm{w}}}{\partial x} = 0, \tag{2.88}$$

and using boundary condition (2.85c) we find that the reduced water pressure gradient in the ECS

$$\frac{\partial p_{\mathrm{w}}}{\partial x} = -\frac{\theta_{\mathrm{s}}\zeta_{\mathrm{ws}}Q_{\mathrm{e,in}}}{h_3\theta_{\mathrm{w}}}. \tag{2.89}$$

This decouples equation (2.82c) from (2.82a,b), leaving us with two equations to solve for θ_n and c:

$$\frac{\partial \theta_\mathrm{n}}{\partial t} + \frac{\partial Q_\mathrm{n}}{\partial x} = J_\mathrm{n}(\theta_\mathrm{n}, c), \qquad \frac{\partial Q_\mathrm{c}}{\partial x} = -h_3 \mathcal{R}(\theta_\mathrm{n}, c), \tag{2.90a,b}$$

where

$$Q_\mathrm{n} = F\left(-\frac{\theta_\mathrm{s}\zeta_\mathrm{ws} Q_\mathrm{e,in}\theta_\mathrm{n}}{h_3(1-\theta_\mathrm{s}-\theta_\mathrm{n})} + \Phi(\theta_\mathrm{n}, c)\frac{\partial \theta_\mathrm{n}}{\partial x} + \theta_\mathrm{n}\Pi_\mathrm{c}'\frac{\partial c}{\partial x}\right), \tag{2.91}$$

and Q_c and F are unchanged from (2.70) and (2.61), respectively. We recall that F is given by (2.61), that is

$$F := \frac{2\cosh(\alpha) - \alpha\sinh(\alpha) - 2}{\theta_\mathrm{s}\zeta_\mathrm{ns}\alpha\sinh(\alpha)}, \qquad \alpha := h_3\sqrt{\theta_\mathrm{s}\zeta_\mathrm{ns}}. \tag{2.92}$$

We can now perform a linear stability analysis about a spatially homogeneous steady state $(\theta_\mathrm{n}, c) = (\theta_\mathrm{n,eq}, c_\mathrm{eq})$ on an unbounded domain. For the purposes of this analysis we leave J_n and $\mathcal{R}$ as unspecified functions of θ_n and c, and use subscript eq to denote a function evaluated at $(\theta_\mathrm{n,eq}, c_\mathrm{eq})$.

We begin by perturbing the system via

$$\theta_\mathrm{n}(x,t) = \theta_\mathrm{n,eq} + \delta\Re\left[\hat{\theta}_\mathrm{n} e^{ikx+\sigma t}\right], \qquad c(x,t) = c_\mathrm{eq} + \delta\Re\left[\hat{c} e^{ikx+\sigma t}\right], \tag{2.93}$$

for some constants $\hat{\theta}_\mathrm{n}$ and $\hat{c}$, wave number k, $0 < \delta \ll 1$, and where $\Re$ denotes the real part. Here, σ is the perturbation growth rate, so that $\Re[\sigma] > 0$ indicates exponential growth in time and hence instability, whilst $\Re[\sigma] < 0$ gives exponential decay in time and a stable solution.

Substituting these forms into (2.90) and equating coefficients at leading order in δ yields

$$J_\mathrm{n,eq} = 0, \quad \mathcal{R}_\mathrm{eq} = 0, \tag{2.94}$$

which gives two equations to solve for $\theta_\mathrm{n,eq}$ and c_eq. Assuming such a solution exists, the $\mathrm{O}(\delta)$ system gives

$$\begin{aligned}\sigma\hat{\theta}_\mathrm{n} - \frac{ik\theta_\mathrm{s}F\zeta_\mathrm{ws}Q_\mathrm{e,in}}{h_3(1-\theta_\mathrm{s}-\theta_\mathrm{n,eq})}\left(1 + \frac{\theta_\mathrm{n,eq}}{1-\theta_\mathrm{s}-\theta_\mathrm{n,eq}}\right)\hat{\theta}_\mathrm{n} \\ - k^2 F\Phi_\mathrm{eq}\hat{\theta}_\mathrm{n} - k^2 F\theta_\mathrm{n,eq}\Pi_\mathrm{c,eq}'\hat{c} = \left.\frac{\partial J_\mathrm{n}}{\partial\theta_\mathrm{n}}\right|_\mathrm{eq}\hat{\theta}_\mathrm{n} + \left.\frac{\partial J_\mathrm{n}}{\partial c}\right|_\mathrm{eq}\hat{c},\end{aligned} \tag{2.95}$$

and

$$ik\mathrm{Pe}Q_\mathrm{l,in}\hat{c} + k^2 b_\mathrm{eq}\hat{c} = h_3\left(\left.\frac{\partial\mathcal{R}}{\partial\theta_\mathrm{n}}\right|_\mathrm{eq}\hat{\theta}_\mathrm{n} + \left.\frac{\partial\mathcal{R}}{\partial c}\right|_\mathrm{eq}\hat{c}\right), \tag{2.96}$$

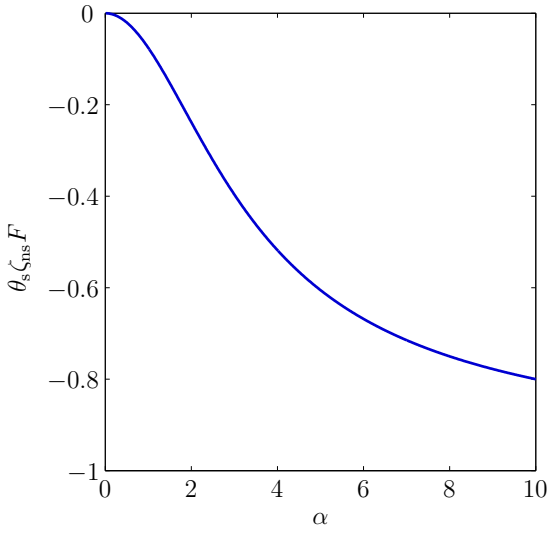

Figure 2.3: Plot of $\theta_s\zeta_{ns}F$ versus α (defined in (2.61)). Other parameter values are as in Table 2.2.

leading to the expression

$$\Re[\sigma(k)] = F\Phi_{eq}k^2 + \left.\frac{\partial J_n}{\partial\theta_n}\right|_{eq} + \frac{h_3\left.\frac{\partial\mathcal{R}}{\partial\theta_n}\right|_{eq}\left(-h_3\left.\frac{\partial\mathcal{R}}{\partial c}\right|_{eq} + b_{eq}k^2\right)\left(\left.\frac{\partial J_n}{\partial c}\right|_{eq} + F\theta_{n,eq}\Pi'_{c,eq}k^2\right)}{\mathrm{Pe}^2Q_{l,in}^2k^2 + \left(-h_3\left.\frac{\partial\mathcal{R}}{\partial c}\right|_{eq} + b_{eq}k^2\right)^2}. \tag{2.97}$$

We are now interested in specific parameter values which give positive $\Re[\sigma]$, and hence instability, for some value of k. A plot of $\theta_s\zeta_{ns}F$ versus α can be seen in Figure 2.3, which shows that $\theta_s\zeta_{ns}F < 0$, and therefore $F < 0$, for $0 < \alpha < 10$ (in fact this can be shown analytically to be true for all α). For the problem to remain well-posed we therefore require $\Phi > 0$ (and therefore also $\Phi_{eq} > 0$, which indeed it is given the chosen parameter values in Table 2.2). Negative Φ means that the coefficient of $\partial\theta_n/\partial x$ is positive in equation (2.91), so we have backwards diffusion in (2.90a) and the problem is ill-posed (see Byrne and Owen [25] for discussion of a similar system). Therefore, for a well-posed problem, the first term in (2.97) is negative. As $|k|$ becomes sufficiently large, this term dominates and hence we have stability regardless of our choices for J_n, $\mathcal{R}$, and specific parameter values.

To determine the signs of the remaining terms, we consider the following typical forms of J_n and $\mathcal{R}$ (see §2.7.3 for details):

$$J_n = \Gamma_{nw}\theta_n\theta_w - \Gamma_{wn}\theta_n, \qquad \mathcal{R} = \Gamma_{R2}\theta_n - \Gamma_{R1}\theta_n\theta_w c. \tag{2.98}$$

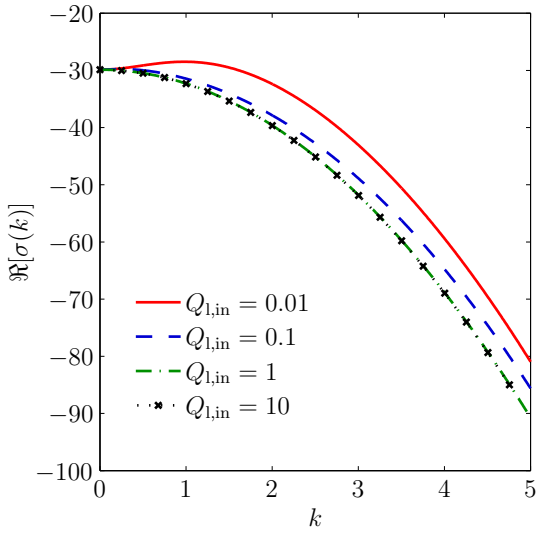

Figure 2.4: Graph of $\Re[\sigma(k)]$ for parameter values as in Table 2.2, for a range of lumen inlet fluxes $Q_{\mathrm{l,in}}$. For these chosen parameter values, $\Re[\sigma(k)] < 0$ for all k and hence the equilibrium state is stable.

The equilibrium state is therefore given by

$$\theta_{\mathrm{n,eq}} = 1 - \theta_{\mathrm{s}} - \frac{\Gamma_{\mathrm{wn}}}{\Gamma_{\mathrm{nw}}}, \qquad c_{\mathrm{eq}} = \frac{\Gamma_{\mathrm{R2}}\Gamma_{\mathrm{nw}}}{\Gamma_{\mathrm{R1}}\Gamma_{\mathrm{wn}}}. \tag{2.99}$$

Furthermore, the derivatives of J_{n} and $\mathcal{R}$ with respect to θ_{n} and c at equilibrium are

$$\begin{aligned} \left.\frac{\partial J_{\mathrm{n}}}{\partial \theta_{\mathrm{n}}}\right|_{\mathrm{eq}} &= \Gamma_{\mathrm{wn}} - (1-\theta_{\mathrm{s}})\Gamma_{\mathrm{nw}}, \qquad \left.\frac{\partial J_{\mathrm{n}}}{\partial c}\right|_{\mathrm{eq}} = 0, \\ \left.\frac{\partial \mathcal{R}}{\partial \theta_{\mathrm{n}}}\right|_{\mathrm{eq}} &= \Gamma_{\mathrm{R2}}\left(\frac{(1-\theta_{\mathrm{s}})\Gamma_{\mathrm{nw}}}{\Gamma_{\mathrm{wn}}} - 1\right) = -\frac{\Gamma_{\mathrm{R2}}}{\Gamma_{\mathrm{wn}}}\left.\frac{\partial J_{\mathrm{n}}}{\partial \theta_{\mathrm{n}}}\right|_{\mathrm{eq}}, \\ \left.\frac{\partial \mathcal{R}}{\partial c}\right|_{\mathrm{eq}} &= -\Gamma_{\mathrm{R1}}\theta_{\mathrm{n,eq}}(1-\theta_{\mathrm{s}}-\theta_{\mathrm{n,eq}}) < 0. \end{aligned} \tag{2.100}$$

We also know from equation (2.84*d*,*e*) that the leading-order chemotaxis term Π_{c}' is negative and b_{eq} is positive. Hence the second and third terms in equation (2.97) are of opposite signs. Given that there is then always one positive term in (2.97), for the choices of J_{n} and $\mathcal{R}$ from (2.98), instability is possible for suitable parameter values. However, we see that for the choice of parameter values in Table 2.2 this is not the case, and this equilibrium state is always linearly stable as illustrated in Figure 2.4. We also find that $\partial J_{\mathrm{n}}/\partial\theta_{\mathrm{n}} < 0$ at equilibrium, and so it is the (negative) first two terms in (2.97) which dominate the third (positive) term in this case.

For a more general characterisation of the stability of this equilibrium state for different parameter regimes, we would need to consider the values of k at which a maximum value of

$\Re[\sigma]$ is attained. This would involve solving a quartic in k^2, which we do not pursue here.

2.6 Numerical solutions

Now we present the method used to solve numerically the system of equations (2.82)-(2.87) for the leading-order cell volume fraction $\theta_{\rm n}$, solute concentration c, and reduced water pressure $p_{\rm w}$. We then summarise the checks which were performed on this scheme before using it to obtain the results in §2.7.

2.6.1 Method of lines

We use the method of lines to solve the system (2.82)-(2.87), which involves first discretising the system in x and then seeking approximate solutions to the resulting system of ODEs in time. We divide the region $0 < x < 1$ into N intervals of length $\Delta x = 1/N$, and denote the centres of these intervals by x_i, so that $x_i = (i - 0.5)\Delta x$ $(i = 1, \ldots, N)$. The half-grid points are denoted by $x_{i-1/2} = (i-1)\Delta x$ $(i = 1, \ldots, N+1)$ (see Figure 2.5(a)). Our choice of discretisation approximates each of $\theta_{\rm n}$, c, and $p_{\rm w}$ at the grid points x_i $(i = 1, \ldots, N)$ and enables a straightforward application of the boundary conditions at $x = 0, 1$. We first find approximate values for the fluxes $Q_{\rm n}$, $Q_{\rm w}$, and $Q_{\rm c}$ at the half-grid points $x_{i-1/2}$ $(i = 1, \ldots, N+1)$, using the grid points either side to approximate derivatives of $\theta_{\rm n}$, c, and $p_{\rm w}$. We can then use these expressions to approximate the x-derivatives of $Q_{\rm n}$, $Q_{\rm w}$, and $Q_{\rm c}$ at the grid points x_i $(i = 1, \ldots, N)$. Figure 2.5(b) illustrates this process, showing the resulting 5-point stencil required to approximate the solution at a general point x_i (away from $x = 0, 1$).

We denote the approximate solutions for $\theta_{\rm n}$, c, $p_{\rm w}$, $Q_{\rm n}$, $Q_{\rm c}$, $Q_{\rm w}$, $J_{\rm n}$, and $\mathcal{R}$ at each of the points by

$$\begin{gathered}
\theta_{{\rm n}_j} \approx \theta_{\rm n}|_{x=x_j}\,, \qquad c_j \approx c|_{x=x_j}\,, \qquad p_j \approx p_{\rm w}|_{x=x_j}\,, \\
Q_{{\rm n},j\pm1/2} \approx Q_{\rm n}|_{x=x_{j\pm1/2}}\,, \qquad Q_{{\rm c},j\pm1/2} \approx Q_{\rm c}|_{x=x_{j\pm1/2}}\,, \qquad Q_{{\rm w},j\pm1/2} \approx Q_{\rm w}|_{x=x_{j\pm1/2}}\,, \\
J_j \approx J_{\rm n}|_{x=x_j}\,, \qquad \mathcal{R}_j \approx \mathcal{R}|_{x=x_j} \quad (j = 1, \ldots, N).
\end{gathered} \tag{2.101}$$

Next we approximate $\partial\theta_{\rm n}/\partial x$, $\partial c/\partial x$, and $\partial p_{\rm w}/\partial x$ at $x_{i-1/2}$ using a central difference scheme

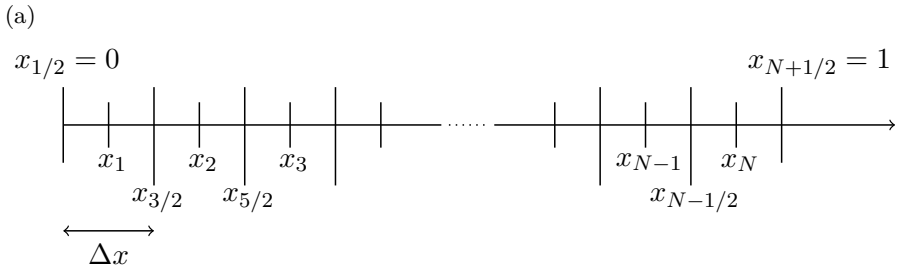

(b)

First discretisation, using values of variables at x_{i-1}, x_i, and x_{i+1} to approximate fluxes at $x_{i-1/2}$ and $x_{i+1/2}$.

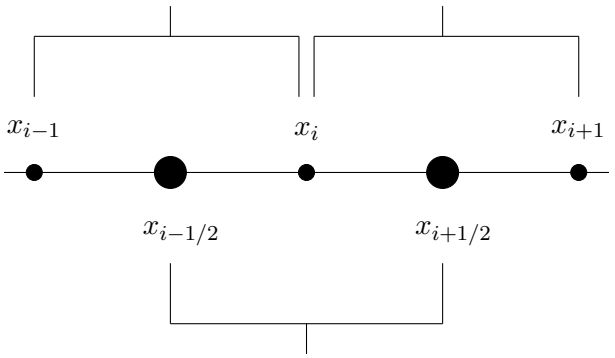

Second discretisation, using values of fluxes at $x_{i-1/2}$ and $x_{i+1/2}$ to enable solution to be approximated at x_i.

Figure 2.5: Diagram of (a) the x-discretisation used in the method of lines, showing the grid points x_i $(i = 1, \ldots N)$, and half-grid points $x_{i-1/2}$ $(i = 1, \ldots, N + 1)$; and (b) a representative stencil used to approximate the solution at general point x_i.

(see [114] for details):

$$\left.\frac{\partial \theta_{\mathrm{n}}}{\partial x}\right|_{x=x_{i-1/2}} \approx \frac{1}{\Delta x}\left(\theta_{\mathrm{n}}|_{x=x_i} - \theta_{\mathrm{n}}|_{x=x_{i-1}}\right) \quad (i = 2, \ldots, N), \tag{2.102}$$

$$\left.\frac{\partial c}{\partial x}\right|_{x=x_{i-1/2}} \approx \frac{1}{\Delta x}\left(c|_{x=x_i} - c|_{x=x_{i-1}}\right) \quad (i = 2, \ldots, N), \tag{2.103}$$

$$\left.\frac{\partial p_{\mathrm{w}}}{\partial x}\right|_{x=x_{i-1/2}} \approx \frac{1}{\Delta x}\left(p|_{x=x_i} - p|_{x=x_{i-1}}\right) \quad (i = 2, \ldots, N), \tag{2.104}$$

and for the fluxes employ the discretisation

$$Q_{\mathrm{n},i-1/2} = F\left(\frac{\theta_{\mathrm{n}_{\mathrm{av},i}}(p_i - p_{i-1})}{\Delta x} + \frac{\Phi(\theta_{\mathrm{n}_{\mathrm{av},i}}, c_{\mathrm{av},i})(\theta_{\mathrm{n}_i} - \theta_{\mathrm{n}_{i-1}})}{\Delta x} + \frac{\theta_{\mathrm{n}_{\mathrm{av},i}}\Pi_{\mathrm{c}}'(c_{\mathrm{av},i})\,(c_i - c_{i-1})}{\Delta x}\right) \qquad (i = 2,\ldots,N), \tag{2.105}$$

$$Q_{\mathrm{w},i-1/2} = -\frac{(1-\theta_{\mathrm{s}} - \theta_{\mathrm{n}_{\mathrm{av},i}})(p_i - p_{i-1})}{\theta_{\mathrm{s}}\zeta_{\mathrm{ws}}\Delta x} \qquad (i = 2,\ldots,N), \tag{2.106}$$

$$Q_{\mathrm{c},i-1/2} = -\mathrm{Pe}Q_{\mathrm{l,in}}c_{\mathrm{av},i} + \frac{b(\theta_{\mathrm{n}_{\mathrm{av},i}})\,(c_i - c_{i-1})}{\Delta x} \qquad (i = 2,\ldots,N), \tag{2.107}$$

$$Q_{\mathrm{n},1/2} = Q_{\mathrm{n},N+1/2} = 0, \tag{2.108}$$

$$Q_{\mathrm{w},1/2} = \frac{Q_{\mathrm{e,in}}}{h_3}, \tag{2.109}$$

$$Q_{\mathrm{w},N+1/2} = -\frac{(1-\theta_{\mathrm{s}} - \theta_{\mathrm{n}_{N+1/2}})\left(-6p_N + 3p_{av,N-1} - \frac{2}{3}p_{N-1}\right)}{\theta_{\mathrm{s}}\zeta_{\mathrm{ws}}\Delta x}, \tag{2.110}$$

$$Q_{\mathrm{c},1/2} = -\mathrm{Pe}Q_{\mathrm{l,in}} + \frac{b(\theta_{\mathrm{n}_{1/2}})}{\Delta x}\left(-\frac{11}{3} + 6c_1 - 3c_{\mathrm{av},1} + \frac{2}{3}c_2\right) \quad \text{or} \quad 0, \tag{2.111}$$

$$Q_{\mathrm{c},N+1/2} = -\frac{6\mathrm{Pe}Q_{\mathrm{l,in}}}{11}\left(\frac{1}{3}c_{N-1} - \frac{3}{2}c_{\mathrm{av},N} + 3c_N\right), \tag{2.112}$$

where

$$\theta_{\mathrm{n}_{\mathrm{av},i}} = \frac{\theta_{\mathrm{n}_i} + \theta_{\mathrm{n}_{i-1}}}{2}, \qquad c_{\mathrm{av},i} = \frac{c_i + c_{i-1}}{2}, \qquad p_{\mathrm{av},i} = \frac{p_i + p_{i-1}}{2} \quad (i = 2,\ldots,N),$$
$$\theta_{\mathrm{n}_{1/2}} \approx \theta_{\mathrm{n}}|_{x=0}\,, \qquad \theta_{\mathrm{n}_{N+1/2}} \approx \theta_{\mathrm{n}}|_{x=1}\,, \qquad c_{N+1/2} \approx c|_{x=1}\,. \tag{2.113}$$

The Fornberg formula [49] with $\mathrm{O}\left((\Delta x)^3\right)$ error (to ensure our scheme remains accurate to $\mathrm{O}\left((\Delta x)^2\right)$) has been used to find an approximation for $\partial c/\partial x|_{x=x_{1/2}}$ in (2.111), for $\partial p_{\mathrm{w}}/\partial x|_{x=x_{N+1/2}}$ in (2.110), and also for $c_{N+1/2}$ in (2.112) by setting $\partial c/\partial x|_{x=x_{N+1/2}}$ to zero. We also use this method to approximate $\theta_{\mathrm{n}_{1/2}}$ in (2.111) and $\theta_{\mathrm{n}_{N+1/2}}$ in (2.110), again with an $\mathrm{O}\left((\Delta x)^3\right)$ error:

$$\theta_{\mathrm{n}_{1/2}} = 3\theta_{\mathrm{n}_1} - 3\theta_{\mathrm{n}_{\mathrm{av},2}} + \theta_{\mathrm{n}_2}, \qquad \theta_{\mathrm{n}_{N+1/2}} = 3\theta_{\mathrm{n}_N} - 3\theta_{\mathrm{n}_{\mathrm{av},N-1}} + \theta_{\mathrm{n}_{N-1}}. \tag{2.114}$$

Finally, we approximate the x-derivatives of Q_{n}, Q_{w}, and Q_{c} at x_i, again using central differences:

$$\left.\frac{\partial Q_{\mathrm{n}}}{\partial x}\right|_{x=x_i} \approx \frac{1}{\Delta x}\left(Q_{\mathrm{n}}|_{x=x_{i+1/2}} - Q_{\mathrm{n}}|_{x=x_{i-1/2}}\right) \quad (i = 1,\ldots,N), \tag{2.115}$$

$$\left.\frac{\partial Q_{\mathrm{w}}}{\partial x}\right|_{x=x_i} \approx \frac{1}{\Delta x}\left(Q_{\mathrm{w}}|_{x=x_{i+1/2}} - Q_{\mathrm{w}}|_{x=x_{i-1/2}}\right) \quad (i = 1,\ldots,N), \tag{2.116}$$

$$\left.\frac{\partial Q_{\mathrm{c}}}{\partial x}\right|_{x=x_i} \approx \frac{1}{\Delta x}\left(Q_{\mathrm{c}}|_{x=x_{i+1/2}} - Q_{\mathrm{c}}|_{x=x_{i-1/2}}\right) \quad (i = 1,\ldots,N), \tag{2.117}$$

so that the system discretised in space is

$$\frac{\mathrm{d}\theta_{\mathrm{n}_i}}{\mathrm{d}t} = -\frac{1}{\Delta x}\left(Q_{\mathrm{n},i+1/2} - Q_{\mathrm{n},i-1/2}\right) + J_i \qquad (i = 1, \ldots, N), \tag{2.118}$$

$$0 = -\frac{1}{\Delta x}\left(Q_{\mathrm{c},i+1/2} - Q_{\mathrm{c},i-1/2}\right) + \mathcal{R}_i \qquad (i = 1, \ldots, N), \tag{2.119}$$

$$0 = -\frac{1}{\Delta x}\left(Q_{\mathrm{n},i+1/2} - Q_{\mathrm{n},i-1/2} + Q_{\mathrm{w},i+1/2} - Q_{\mathrm{w},i-1/2}\right) - \frac{\kappa_{\mathrm{m}}\phi_{\mathrm{m}}}{h_3}\left(\frac{p_i}{h_2} - 3Q_{\mathrm{l,in}}(1 - x_i) - P_{\mathrm{dwn}}\right) \qquad (i = 1, \ldots, N). \tag{2.120}$$

This is a coupled system comprising an ODE in time for θ_{n_i}, and algebraic equations for c_i and p_i, and can be solved in MATLAB using an inbuilt ODE solver given an initial profile for θ_{n}. For this work, we used `ode15s`, a solver for stiff ODEs based on numerical differentiation formulas which has a variable step size and uses backward difference schemes [151, 152].

2.6.2 Verification of the numerical scheme

Before using the scheme described in §2.6.1 to obtain results for a number of experimentally motivated case studies, several checks were performed, details of which are given in Appendix A.1. We began by ensuring that the scheme converges as expected for candidate constitutive laws. By further simplifying the system (2.90) and (2.91) from §2.5.6 to include no solute (taking $c = 0$ and the chemotaxis coefficient $\chi = 0$), we verified the numerical solution against the results of a linear stability analysis on a bounded domain, by setting the initial conditions on θ_{n} to be a small perturbation away from the steady state $\theta_{\mathrm{n,eq}}$ and comparing the growth rates of the two systems. Finally, we returned to the simplified system (2.90) and (2.91) and solved it analytically subject to a new inlet concentration boundary condition, perturbed slightly above the equilibrium concentration value. This yields a new analytical steady state (close to the original equilibrium state) for θ_{n} and c which we compared to numerical results with excellent agreement (maximum absolute errors of $\mathrm{O}\left(10^{-7}\right)$).

2.7 Experimental case studies

Having developed a model for the leading-order cell volume fraction θ_{n}, solute concentration c, and reduced water pressure p_{w}, we consider a number of case studies which correspond to typical experimental nutrient and chemoattractant scenarios. In §2.7.1 we neglect the effect of chemotaxis and consider the effect of nutrient limitation of the cell proliferation rate on the resulting cell distribution. As discussed in §2.5.5, the nutrient is taken to be that

most likely to limit cell growth, oxygen [104, 105]. In §2.7.2 we consider a chemoattractant delivered at the lumen inlet to mimic endocrine cell signalling (cells responding to an externally supplied stimulus) and in §2.7.3 we investigate a chemoattractant produced by the cells to model paracrine signalling (cells responding to a chemical secreted by nearby cells). In §2.7.4 we combine the case studies from §2.7.1 and §2.7.3 by modelling both delivered oxygen and a produced chemoattractant. For each experimental case study, we specify appropriate forms for the cell mass transfer term J_{n}, reaction term $\mathcal{R}$, and inlet concentration boundary condition. The forms for these terms are chosen based on discussions with our experimental collaborators, and results indicate the typical behaviour to be expected from the system in question, with the aim of informing bioreactor operating conditions (specifically, lumen inlet fluid fluxes). We investigate the sensitivity of these results to various parameter values of interest in §2.7.5. Finally, with the aim of counteracting downstream cell bunching effects without using a chemoattractant, in §2.7.6 we consider the alternative flow regime where we specify a downstream fluid flux into the lumen and a backflow in the ECS, instead of a downstream flux into both.

In each experimentally motivated case study in §§2.7.1-2.7.4, we first investigate the steady-state distributions of the cells, the relevant solute(s), and the reduced water pressure for a number of different inlet fluid fluxes in a representative range of $Q_{\mathrm{l,in}}$ for which our asymptotic solution is valid (see Table 2.2). We found that for arbitrary, smooth initial conditions, the steady state obtained is independent of the choice of θ_{n}^* in (2.87). Hence for the results presented here, we take θ_{n}^* to be the constant value 0.3 without loss of generality and, as pseudo-initial conditions for the numerics, set $c(x,0) = p_{\mathrm{w}}(x,0) = 1$. The system is deemed to have reached a steady state at time T if the maximum change in θ_{n}, c, and p_{w} between time $T - 0.062$ and T (corresponding to a dimensional time of around one week) is less than 10^{-4}, and hence the end times are different for each case study. We note that the maximum change in the solutions for each of θ_{n}, c, and p_{w} between these steady-state end times and an experimentally relevant end time is less than 10% for each case study. Hence results obtained within the time frame of an experiment would be very similar to those presented here. Specifically, the results from §2.7.6 are within 10% of the steady state after a dimensional time of around 2 weeks, those from §2.7.2 and §2.7.3 after 3 weeks, those from §2.7.5 after 4 weeks, and results from §2.7.1 and §2.7.4 after 6 weeks.

Next, we consider the effect of the lumen inlet fluid flux on cell yield and cell distribution

in each case study by finding the mean and standard deviation of θ_{n} for a range of $Q_{\mathrm{l,in}}$ values. In this work the mean μ is given by

$$\mu := \int_0^1 \theta_{\mathrm{n}}(x,T)\,\mathrm{d}x, \tag{2.121}$$

and the standard deviation σ by

$$\sigma := \sqrt{\int_0^1 \left[\theta_{\mathrm{n}}(x,T)-\mu\right]^2\,\mathrm{d}x}, \tag{2.122}$$

where T is the relevant end time. The MATLAB function `trapz` is used to estimate μ and σ for a given θ_{n}. This analysis is motivated by typical aims of experiments: to maximise either the cell yield or spatial uniformity of the cell population in a particular scenario. We choose to focus on the latter, and for each case study we minimise σ with respect to $Q_{\mathrm{l,in}}$ to find the inlet flux $Q_{\mathrm{l,opt}}$ which results in the most uniformly distributed cell population. For this, as well as plotting $Q_{\mathrm{l,in}}$ versus σ as described above, we use the inbuilt MATLAB function `fminbnd` to find the minimum standard deviation of θ_{n} within the flux range considered, that is, $0.01 < Q_{\mathrm{l,in}} < 10$. By also considering the value of μ as the inlet fluid flux is adjusted, we are able to determine whether or not cell yield is being compromised by requiring a uniform cell distribution.

In §2.7.5, we vary a number of key parameters and investigate their effect on μ and σ. Finally, in §2.7.6 where there is a backflow in the ECS, we consider steady-state results for a range of $Q_{\mathrm{e,in}}$ values, including the optimal ECS flux $Q_{\mathrm{e,opt}}$ for which the standard deviation σ of θ_{n} is at a minimum.

In the case studies in §2.7.1 and §2.7.4 which explicitly include oxygen, we additionally check that the optimal inlet fluid fluxes result in an oxygen concentration which is above the minimum required for cell viability throughout the bioreactor. This minimum is taken to be a dimensional concentration of 0.08 mol m^{-3}, which is at the upper end of the range of minimum oxygen concentrations required for functional cells (see [153]) and here corresponds to a dimensionless concentration of 0.36. For the case studies in which oxygen concentration is not explicitly taken into account (§2.7.2 and §2.7.3), we assume firstly that the cells are supplied with sufficient oxygen to remain functional for all fluid fluxes in the relevant range, and secondly that there is enough oxygen to ensure that there is no limiting effect on cell proliferation rate. However, care needs to be taken with this first assumption. It is supported by the results from §2.7.4 (where both oxygen and chemoattractant are explicitly modelled), where the oxygen concentration is (just) above 0.36 for all fluid

fluxes considered. On the other hand, in §2.7.1 where only oxygen is considered, the oxygen concentration does fall below 0.36 at the downstream end of the bioreactor for the lowest inlet flux $Q_{\mathrm{l,in}} = 0.01$. This suggests that if fluid fluxes at the lower end of the range considered here are to be used, the cells may not have a sufficient supply of oxygen throughout the bioreactor. The second assumption is shown not to have a significant effect on trends in results. This is seen by comparing the cell distributions from §2.7.3 (where oxygen is not included and assumed to be in abundance) and §2.7.4 (where oxygen concentration is explicitly modelled and has a limiting effect on cell proliferation rate). Unless stated otherwise, all parameter values are taken from Table 2.2 and the (dimensionless) fluid flux ratio $Q_{\mathrm{e,in}}/Q_{\mathrm{l,in}}$ is kept constant and equal to 2.5. We note that although the kinetic parameter values used here are fairly generic, specific cell types could be explored as required given the necessary data.

2.7.1 Nutrient-driven proliferation

In the first case study, we consider a nutrient (taken to be oxygen) of concentration $c(x,t)$ which is supplied at the lumen inlet and does not induce a chemotactic response from the cells. This situation is relevant to, for instance, hepatocytes in a liver sinusoid which can be modelled using a HFMB for tissue engineering applications. Gradients in many chemical components, including oxygen, are set up along the length of a sinusoid. These gradients correlate with changes in metabolic cell function along the sinusoid, but do not induce cellular migration [179]. The corresponding inlet boundary condition is

$$c = 1 \qquad \text{at} \quad x = 0, \tag{2.123}$$

and $\chi = 0$ in Π_{c} in equation (2.12). The cell mass transfer term J_{n} takes the form

$$J_{\mathrm{n}} = \frac{\Gamma_{\mathrm{nw}}\theta_{\mathrm{n}}\theta_{\mathrm{w}}c}{K+c} - \Gamma_{\mathrm{wn}}\theta_{\mathrm{n}}, \tag{2.124}$$

where Γ_{nw}, Γ_{wn}, and K are all constants. The first term in J_{n} is motivated by the form of the corresponding mass transfer terms in [92] and [123] with an additional dependence on the cell volume fraction so that there is no proliferation in the absence of either water (and hence solute) or cells. We have also included a dependence on the oxygen concentration via Michaelis-Menten type kinetics. The second term represents the rate of cell death which is assumed proportional to the cell volume fraction. The reaction term $\mathcal{R}$ is taken to be

$$\mathcal{R} = -\frac{\Gamma_{\mathrm{R1}}\theta_{\mathrm{n}}\theta_{\mathrm{w}}c}{K_1+c}, \tag{2.125}$$

where Γ_{R1} and K_1 are constant. This represents the rate of oxygen uptake by the cells, which is assumed to be of Michaelis-Menten form and proportional to the volume fractions of cells and water (for the same reasons as discussed above).

The results for this case study can be seen in Figures 2.6(a) and 2.8(a). We see in the plot of θ_{n} that for the lowest inlet fluid flux $Q_{\mathrm{l,in}} = 0.01$ there is slight bunching upstream of the cell population due to the higher oxygen concentration (and hence cell proliferation rate) in that region. As the flux is increased the distribution of cells becomes relatively uniform along the bioreactor, due to the concentration, and therefore proliferation rate, becoming more uniform (see c plot, Figure 2.6(a)). For the highest inlet fluid flux of 1, there is significant downstream bunching of cells as they are advected along the bioreactor. We note also that c is above the required minimum of 0.36 for cell viability except for the lowest inlet flux $Q_{\mathrm{l,in}} = 0.01$, when the cells towards the downstream end of the bioreactor may not have a sufficient oxygen supply. We can see that the optimal inlet flux $Q_{\mathrm{l,opt}} = 0.0732$ results in a relatively uniform distribution of cells along the bioreactor, with σ taking a minimum value of 6.4×10^{-3}. The plot of p_{w} shows that the reduced water pressure is monotonically decreasing along the bioreactor for all inlet fluid flux values. Figure 2.8(a) shows that there is a slight trade-off between cell yield and distribution in this case: the mean μ is at a maximum around $Q_{\mathrm{l,in}} = 1$, which does not correspond to the minimum value of σ, although the variation in σ is small.

2.7.2 Chemoattractant: endocrine signalling

The second situation we consider is that of a delivered chemoattractant to which the cells respond. This is similar to endocrine signalling, where the stimulus is delivered via the bloodstream (represented by the lumen in a HFMB). This type of signalling is involved in, for example, regulating the metabolic activity of liver and muscle cells [17]. In this case, we impose an inlet concentration so that

$$c = 1 \qquad \text{at} \quad x = 0. \tag{2.126}$$

We assume that cell proliferation is not limited by the chemoattractant concentration and that there is also sufficient oxygen in the system (the concentration of which we do not track) so that its concentration does not affect the growth rate. Therefore, motivated by the large c limit of (2.124), we take

$$J_{\mathrm{n}} = \Gamma_{\mathrm{nw}}\theta_{\mathrm{n}}\theta_{\mathrm{w}} - \Gamma_{\mathrm{wn}}\theta_{\mathrm{n}}, \tag{2.127}$$

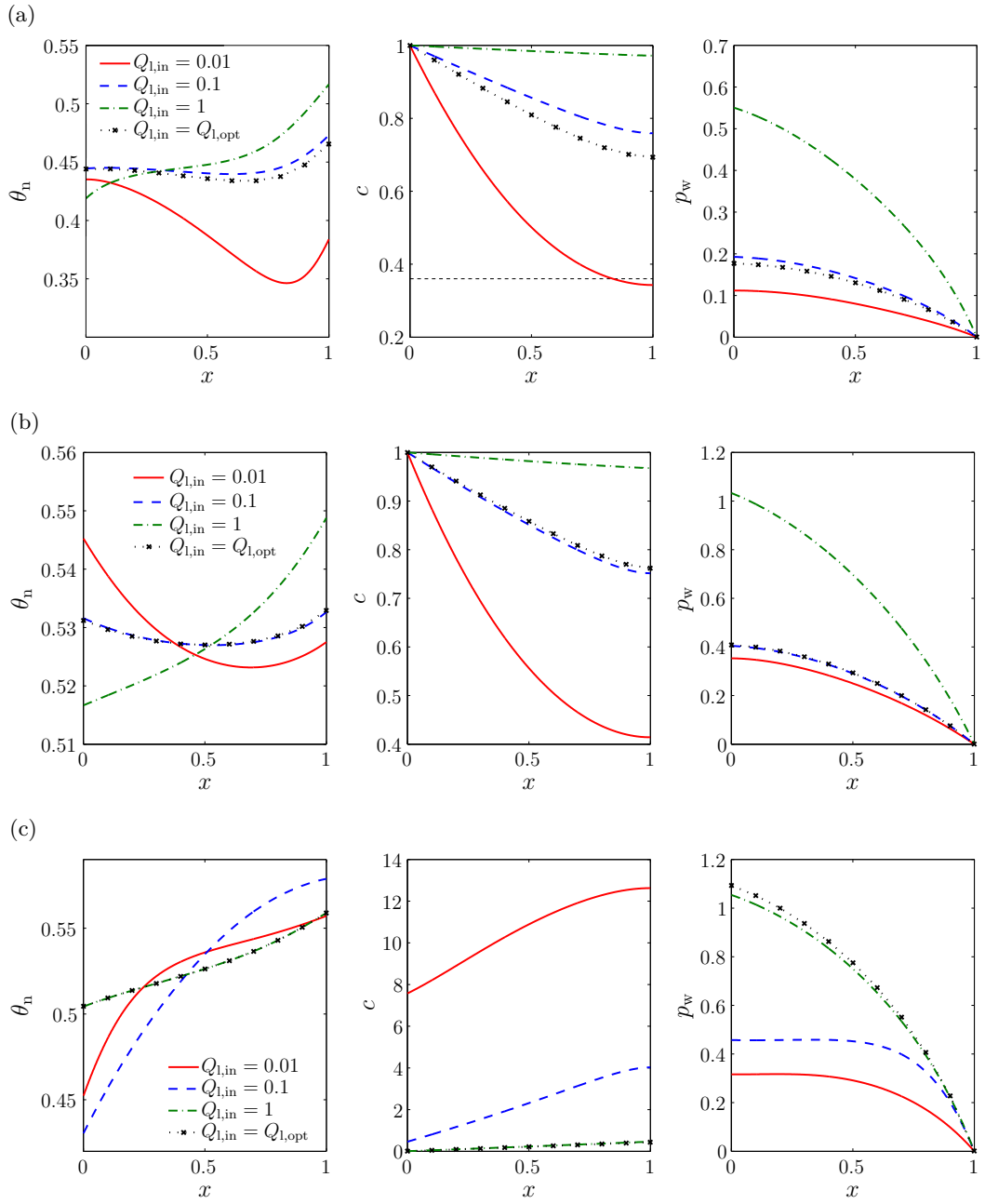

Figure 2.6: Steady-state distributions of the cell volume fraction θ_{n}, oxygen concentration c, and reduced ECS water pressure p_{w} versus x for a range of lumen inlet fluid fluxes $Q_{\mathrm{l,in}}$ including the optimal value $Q_{\mathrm{l,opt}}$. (a) Nutrient-driven proliferation case study results (from §2.7.1), end time $T = 1.3$, optimal inlet flux $Q_{\mathrm{l,opt}} = 0.0732$, and corresponding standard deviation $\sigma = 6.4 \times 10^{-3}$. The horizontal dashed black line in the graph of c denotes the minimum oxygen concentration 0.36 required for viable cells. (b) Endocrine signalling case study results (from §2.7.2), end time $T = 0.6$, optimal inlet flux $Q_{\mathrm{l,opt}} = 0.1061$, and corresponding standard deviation $\sigma = 1.6 \times 10^{-3}$. (c) Paracrine signalling case study results (from §2.7.3), end time $T = 0.6$, optimal inlet flux $Q_{\mathrm{l,opt}} = 1.053$, and corresponding standard deviation $\sigma = 0.0148$. Parameter values are as in Table 2.2.

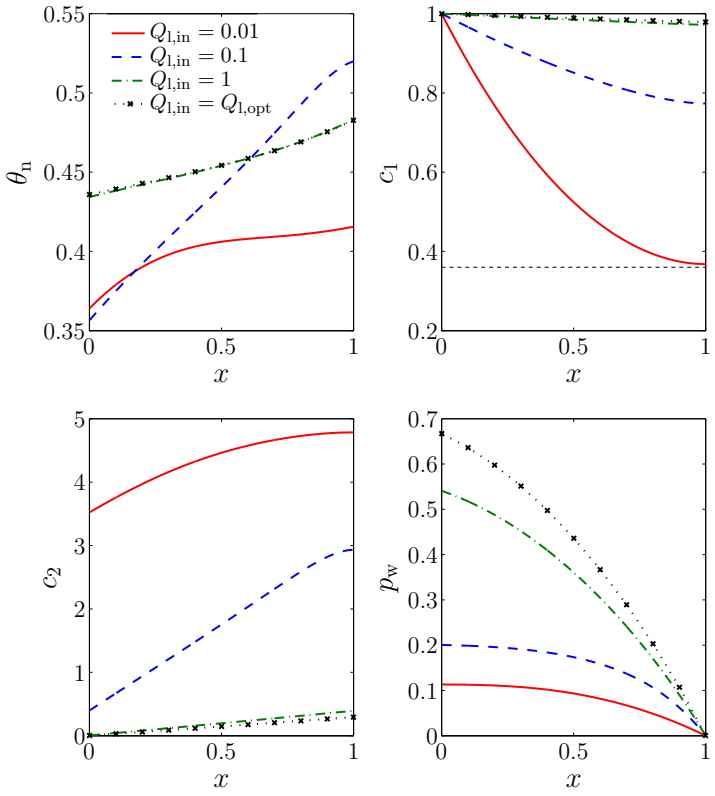

Figure 2.7: Steady-state distributions of the cell volume fraction θ_{n}, oxygen concentration c_1, chemoattractant concentration c_2, and reduced ECS water pressure p_{w} versus x for a range of lumen inlet fluxes $Q_{\mathrm{l,in}}$ including the optimal value $Q_{\mathrm{l,opt}}$. Results are from the nutrient and chemoattractant case study presented in §2.7.4, end time $T = 1.5$ and optimal inlet flux $Q_{\mathrm{l,opt}} = 1.341$ (corresponding standard deviation $\sigma = 0.013$). The horizontal dashed black line in the top-right plot denotes the minimum oxygen concentration $c_1 = 0.36$ required for viable cells. Parameter values are as in Table 2.2.

where Γ_{nw} and Γ_{wn} are constants. The reaction term takes the form

$$\mathcal{R} = -\Gamma_{\mathrm{R1}}\theta_{\mathrm{n}}\theta_{\mathrm{w}}c, \tag{2.128}$$

where Γ_{R1} is constant. This represents the rate of chemoattractant uptake by the cells, which is taken to be proportional to the concentration of chemoattractant and the volume fractions of cells and of water.

The results for this case study can be seen in Figures 2.6(b) and 2.8(b). Here, we see that for the lowest inlet fluid flux of 0.01 there is upstream bunching of the cells due to the negative gradient in c, which causes an increase in cells upstream due to chemotaxis. However, as the inlet flux increases further this gradient decreases, and the effect of chemotaxis is reduced so that θ_{n} is more uniform in x. Eventually, for $Q_{\mathrm{l,in}} = 1$, advection dominates and the cell volume fraction increases downstream. In this case study the most

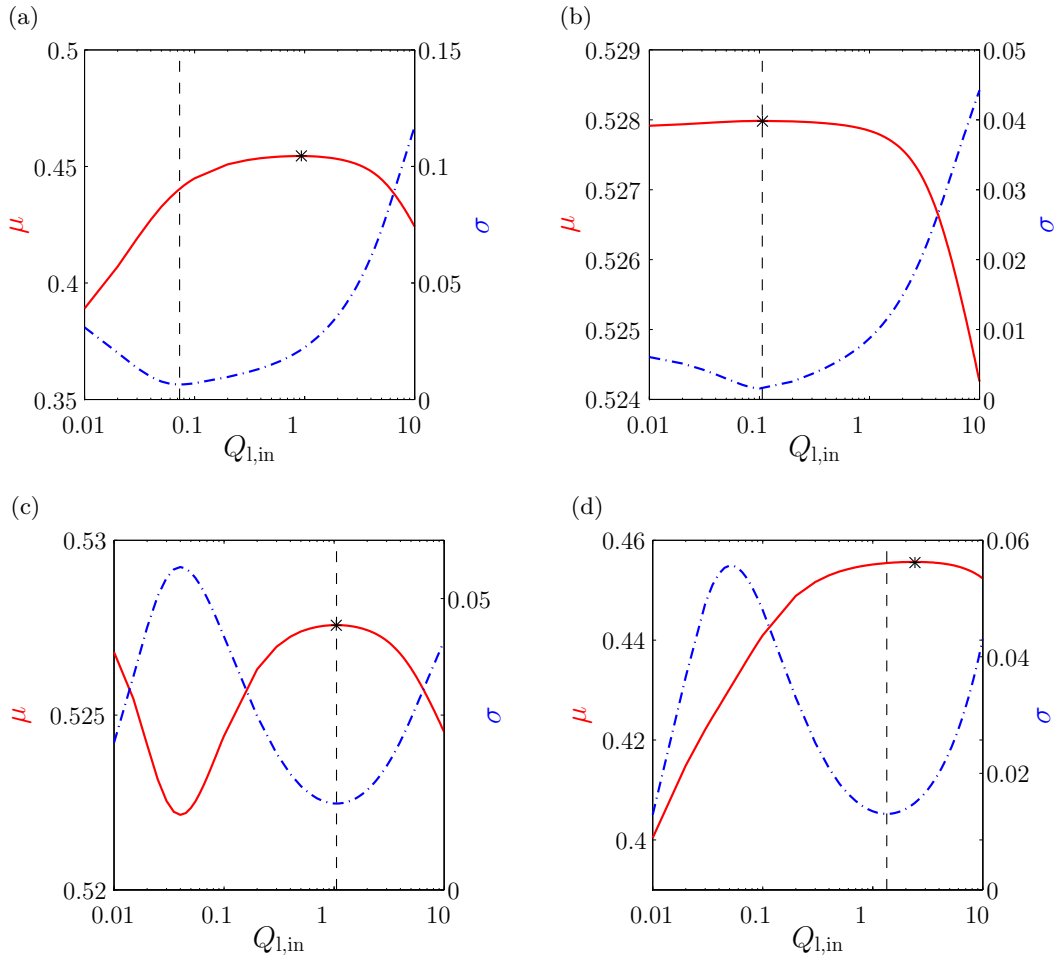

Figure 2.8: Plots of the mean μ of θ_{n} (solid red line) and the standard deviation σ of θ_{n} (dash-dotted blue line) versus $Q_{\mathrm{l,in}}$ for results from the (a) nutrient-driven proliferation (§2.7.1), (b) endocrine signalling (§2.7.2), (c) paracrine signalling (§2.7.3), and (d) nutrient and chemoattractant concentrations (§2.7.4) case studies. The dashed vertical line in each plot corresponds to the optimal inlet flux $Q_{\mathrm{l,opt}}$ for which σ is at its minimum value, and the black asterisk corresponds to the maximum value of μ. Parameter values are as in Table 2.2.

uniform distribution of cells occurs when these effects are in balance, for $Q_{\mathrm{l,opt}} = 0.1061$ with $\sigma = 1.6 \times 10^{-3}$. Once again, the reduced water pressure is monotonically decreasing in x for all fluid flux values. In Figure 2.8(b), we see that this time the value of μ is fairly constant across the range of inlet fluxes $0.01 < Q_{\mathrm{l,in}} < 10$, but drops off slightly as the flux value increases past 1. Furthermore, the maximum cell yield in this case is achieved at the same fluid flux as the minimum standard deviation.

2.7.3 Chemoattractant: paracrine signalling

The third case study models the concentration $c(x,t)$ of a chemoattractant which is produced by the cells and also induces a chemotactic response. This local signalling between cells is known as paracrine signalling, and controls processes such as neutrophil chemotaxis during inflammatory responses, and the migration of haematopoietic stem cells in bone marrow [17]. Bioreactor expansion of haematopoietic stem cells in particular is needed for many therapeutic applications (see [95]). In this situation, we assume that no chemoattractant is supplied at the inlet and hence impose the boundary condition

$$Q_{\mathrm{c}} = 0 \qquad \text{at} \quad x = 0. \tag{2.129}$$

We take the same mass transfer term as in §2.7.2:

$$J_{\mathrm{n}} = \Gamma_{\mathrm{nw}}\theta_{\mathrm{n}}\theta_{\mathrm{w}} - \Gamma_{\mathrm{wn}}\theta_{\mathrm{n}}. \tag{2.130}$$

Since we must also consider production of the chemoattractant here, $\mathcal{R}$ takes the form

$$\mathcal{R} = \Gamma_{\mathrm{R2}}\theta_{\mathrm{n}} - \Gamma_{\mathrm{R1}}\theta_{\mathrm{n}}\theta_{\mathrm{w}}c, \tag{2.131}$$

where Γ_{R2} is constant. The additional first term in (2.131) signifies production of chemoattractant by the cells at a rate proportional to the cell volume fraction and represents situations where the chemoattractant is always produced by the cells (and hence appears at higher concentrations where there are more cells, a situation which could arise, for instance, with stem cells [1]).

Results for this case are shown in Figures 2.6(c) and 2.8(c). As $Q_{\mathrm{l,in}}$ is increased from 0.01 to 0.1 we can see that the extent of the downstream bunching of cells increases. However, between $Q_{\mathrm{l,in}} = 0.1$ and $Q_{\mathrm{l,in}} = 1$, the opposite trend is seen. The explanation for this behaviour lies in the interplay between advection and chemotaxis. For the inlet flux $Q_{\mathrm{l,in}}$ between 0.01 and 0.1, there is a positive feedback between the distributions of c and θ_{n}: slight downstream bunching of cells due to advection results in more chemoattractant being produced towards $x = 1$, which increases the (positive) gradient in c and promotes further downstream bunching of cells due to chemotaxis. However, as $Q_{\mathrm{l,in}}$ is increased to 1, the chemoattractant concentration becomes much more uniform as a result of increased advection, and so too does the distribution of cells as chemotaxis has a lesser effect. When the

inlet fluid flux is further increased to 10, advection dominates and the cells are swept downstream (results not shown). As in §2.7.1, the reduced water pressure is again monotonically decreasing in x for all inlet fluid flux values.

Here, the optimal inlet fluid flux within the range considered is $Q_{\mathrm{l,opt}} = 1.053$, where the standard deviation of θ_{n} is at a minimum value of 0.0148. We also see in Figure 2.8(c) that the mean μ does not vary much with $Q_{\mathrm{l,in}}$ in this case, and hence we would expect a similar yield of cells no matter which fluid flux value was chosen. However, the optimal inlet flux $Q_{\mathrm{l,opt}}$ does correspond to a maximum cell yield, as well as a minimum in σ.

2.7.4 Nutrient and chemoattractant concentrations

We now consider two solutes: a nutrient (again, oxygen) which is supplied at the lumen inlet, and a chemoattractant which is produced by the cells and induces a chemotactic response. The governing equations can be derived as before but with two solutes, and a similar model reduction performed to yield (where subscript 1 refers to oxygen and subscript 2 to chemoattractant concentration)

$$c_{i,j} := c_j(x,t) \quad (i = \mathrm{l},\mathrm{m},\mathrm{w},\ j = 1,2), \tag{2.132}$$

where θ_{n}, c_1, c_2, and p_{w} satisfy

$$\begin{aligned} &\frac{\partial \theta_{\mathrm{n}}}{\partial t} + \frac{\partial Q_{\mathrm{n}}}{\partial x} = J_{\mathrm{n}}, \qquad \frac{\partial Q_{\mathrm{c}_i}}{\partial x} = -h_3 \mathcal{R}_i(\theta_{\mathrm{n}}, c_i) \quad (i = 1,2), \\ &\frac{\partial}{\partial x}\left(Q_{\mathrm{n}} + Q_{\mathrm{w}}\right) = -\frac{\kappa_{\mathrm{m}}\phi_{\mathrm{m}}}{h_2 h_3}\left[p_{\mathrm{w}} - 3Q_{\mathrm{l,in}}(1-x) - P_{\mathrm{dwn}}\right], \end{aligned} \tag{2.133}$$

and the fluxes are given by

$$\begin{aligned} Q_{\mathrm{n}} &= F\left(\frac{\partial p_{\mathrm{w}}}{\partial x}\theta_{\mathrm{n}} + \Phi(\theta_{\mathrm{n}}, c_2)\frac{\partial \theta_{\mathrm{n}}}{\partial x} + \theta_{\mathrm{n}}\Pi_{\mathrm{c}}'\frac{\partial c_2}{\partial x}\right), \\ Q_{\mathrm{c}_i} &= -\mathrm{Pe} Q_{\mathrm{l,in}} c_i + b(\theta_{\mathrm{n}})\frac{\partial c_i}{\partial x} \quad (i = 1,2), \qquad Q_{\mathrm{w}} = -\frac{\theta_{\mathrm{w}}}{\theta_{\mathrm{s}}\zeta_{\mathrm{ws}}}\frac{\partial p_{\mathrm{w}}}{\partial x}, \end{aligned} \tag{2.134}$$

again with

$$\begin{aligned} F &:= \frac{2\cosh(\alpha) - \alpha\sinh(\alpha) - 2}{\theta_{\mathrm{s}}\zeta_{\mathrm{ns}}\alpha\sinh(\alpha)}, \qquad \alpha := h_3\sqrt{\theta_{\mathrm{s}}\zeta_{\mathrm{ns}}}, \\ \Phi(\theta_{\mathrm{n}}, c_2) &= \Pi_{\mathrm{n}} + \Pi_{\mathrm{c}} + \theta_{\mathrm{n}}\Pi_{\mathrm{n}}' - \psi_{\mathrm{ns}}\theta_{\mathrm{s}}, \\ \Pi_{\mathrm{c}}' &= -\frac{\chi}{\bar{c}}\exp\left(-\frac{c_2}{\bar{c}}\right), \qquad b(\theta_{\mathrm{n}}) := 1 + h_2\phi_{\mathrm{m}} + h_3(1 - \theta_{\mathrm{s}} - \theta_{\mathrm{n}}). \end{aligned} \tag{2.135}$$

The corresponding boundary conditions are

$$Q_{\mathrm{n}} = 0, \qquad c_1 = 1, \qquad Q_{\mathrm{c}_2} = 0, \qquad Q_{\mathrm{w}} = \frac{Q_{\mathrm{e,in}}}{h_3} \qquad \text{at} \quad x = 0, \tag{2.136}$$

$$Q_{\mathrm{n}} = 0, \qquad \frac{\partial c_i}{\partial x} = 0 \quad (i = 1,2), \qquad p_{\mathrm{w}} = 0 \qquad \text{at} \quad x = 1. \tag{2.137}$$

The mass transfer term is taken to be that from §2.7.1, while the reaction terms take the appropriate forms from §2.7.1 and §2.7.3:

$$J_{\mathrm{n}} = \frac{\Gamma_{\mathrm{nw}}\theta_{\mathrm{n}}\theta_{\mathrm{w}}c_1}{K + c_1} - \Gamma_{\mathrm{wn}}\theta_{\mathrm{n}}, \qquad \mathcal{R}_1 = -\frac{\Gamma_{\mathrm{R1},1}\theta_{\mathrm{n}}\theta_{\mathrm{w}}c_1}{K_1 + c_1}, \qquad \mathcal{R}_2 = \Gamma_{\mathrm{R2},2}\theta_{\mathrm{n}} - \Gamma_{\mathrm{R1},2}\theta_{\mathrm{n}}\theta_{\mathrm{w}}c_2, \tag{2.138a-c}$$

with the uptake constants $\Gamma_{\mathrm{R1},1}$ and $\Gamma_{\mathrm{R1},2}$ and production constant $\Gamma_{\mathrm{R2},2}$ set to the same values as the corresponding parameters in the single-solute cases (where $\Gamma_{\mathrm{R1}} = \Gamma_{\mathrm{R2}} = 50$).

This case study corresponds to that from §2.7.3 with the addition of an explicitly modelled oxygen concentration, and therefore nutrient-limited proliferation. By comparing the two cases we can investigate the effect of explicitly including oxygen on cell distribution and yield, to see if the more complicated two-solute model is necessary, or if a single-solute model will suffice. Results for this two-solute system can be seen in Figures 2.7 and 2.8(d) and correspond to Figures 2.6(c) and 2.8(c), respectively, from the single-solute case. Figures 2.6(c) and 2.7 show the same overall trend in cell distribution as the inlet fluid flux increases, but from Figure 2.8(d) we can see that in the two-solute case there is an overall increase in cell yield as the inlet fluid flux increases. However, we also note from comparing Figures 2.8(c) and (d) that in the two-solute case the cell volume fraction is lower in general, due to the additional dependence of J_{n} on c_1 in equation (2.138a) compared to equation (2.130). We see similar trends in chemoattractant concentration and reduced water pressure between the two case studies, albeit with higher overall values when oxygen is not explicitly modelled. This is due to the higher cell volume fraction overall which results in more chemoattractant being produced. As a brief comparison to the nutrient-limited proliferation case from §2.7.1, we note that the distribution of oxygen in Figure 2.7 is similar to that seen in Figure 2.6(a) and that here the oxygen concentration is always above that required for cell viability. In this case, the optimal inlet flux is $Q_{\mathrm{l,opt}} = 1.341$, with a corresponding standard deviation of $\sigma = 0.013$. Figure 2.8(d) shows that this flux value produces a cell yield which is very close to the maximum value.

2.7.5 Parameter sensitivity

We now investigate how sensitive our model results are to the key dimensionless parameters $Q_{\mathrm{e,in}}$, η, ζ_{ns}, ζ_{ws}, κ_{m}, ϕ_{m}, and λ. In each case the parameter value in question is varied within a range which retains the validity of our asymptotic analysis. With the exception of the $Q_{\mathrm{e,in}}$ investigation, results throughout this section are from the nutrient-driven proliferation case study from §2.7.1, which we use as a simple candidate case since it neglects chemotaxis.

Effect of $Q_{\mathrm{e,in}}$

To examine how sensitive the results of our model are to the dimensionless ECS fluid flux, we calculate the mean and standard deviation of θ_{n} for a range of values of $Q_{\mathrm{e,in}}$. Results for all case studies are summarised in Table 2.3 and indicate that overall, increasing $Q_{\mathrm{e,in}}$ greatly increases the standard deviation σ of θ_{n} and also slightly reduces its mean μ (presumably through the contribution of numerous nonlinear effects in the model). Plots of the final cell, oxygen concentration, and pressure distributions for the case study from §2.7.1 can be seen in Figure 2.9 and show that increasing $Q_{\mathrm{e,in}}$ results in increased downstream bunching of cells as expected, due to a greater degree of advection.

Table 2.3: Values of the mean μ of θ_{n} and the standard deviation σ of θ_{n} for different values of the ECS flux $Q_{\mathrm{e,in}}$, and their percentage changes overall for each case study, which are defined by $100[(\text{value at } Q_{\mathrm{e,in}} = 10) - (\text{value at } Q_{\mathrm{e,in}} = 0.1)]/(\text{value at } Q_{\mathrm{e,in}} = 0.1)$. The lumen flux $Q_{\mathrm{l,in}}$ is fixed at 1 and all other parameter values are as in Table 2.2.

Case study	μ ($Q_{\mathrm{e,in}} = 0.1$)	μ ($Q_{\mathrm{e,in}} = 2.5$)	μ ($Q_{\mathrm{e,in}} = 10$)	Overall % change in μ
§2.7.1 Nutrient	0.4551	0.4544	0.4503	−1.05
§2.7.2 Endocrine	0.5279	0.5278	0.5273	−0.11
§2.7.3 Paracrine	0.5277	0.5276	0.5269	−0.15
§2.7.4 Nutrient and chemoattractant	0.4553	0.4551	0.4546	−0.15
	σ ($Q_{\mathrm{e,in}} = 0.1$)	σ ($Q_{\mathrm{e,in}} = 2.5$)	σ ($Q_{\mathrm{e,in}} = 10$)	Overall % change in σ
§2.7.1 Nutrient	0.0147	0.0223	0.0485	230
§2.7.2 Endocrine	5.4×10^{-3}	8.7×10^{-3}	0.0191	254
§2.7.3 Paracrine	0.0117	0.0148	0.0241	106
§2.7.4 Nutrient and chemoattractant	0.0112	0.0135	0.0207	84.8

Effect of η, ζ_{ns}, and ζ_{ws}

Now we compare steady-state cell distributions for varying values of the cell-scaffold affinity parameter η, and the dimensionless cell-scaffold drag ζ_{ns} and water-scaffold drag ζ_{ws} (see Figures 2.10(a)-(c)). As expected, increasing either η or ζ_{ns} results in less downstream cell bunching (and therefore a smaller standard deviation σ of θ_{n}) due to the increased cell-scaffold affinity and cell-scaffold drag, respectively. Increasing ζ_{ws} gives the opposite effect: this results in a higher drag between the water and scaffold, so that there is more

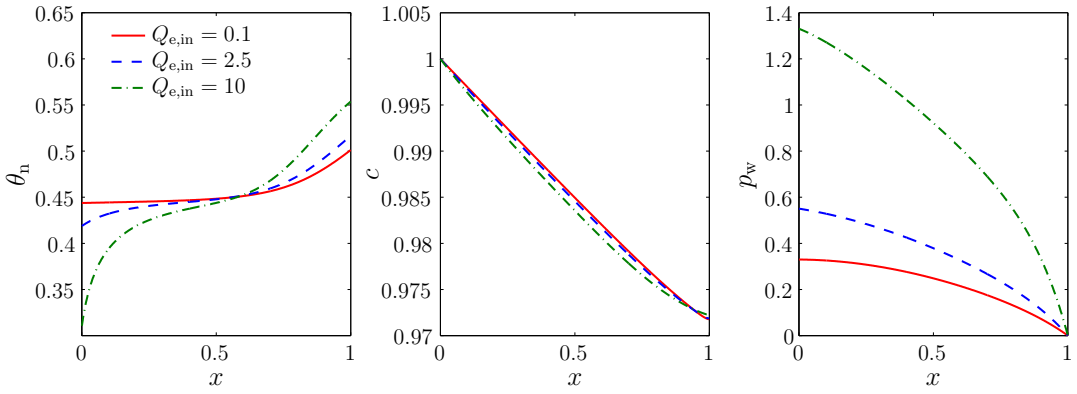

Figure 2.9: Steady-state distributions of the cell volume fraction θ_n, oxygen concentration c, and reduced ECS water pressure p_w versus x from the nutrient-driven proliferation case study (§2.7.1) for a range of values of the ECS flux $Q_{e,in}$ and fixed lumen flux $Q_{l,in} = 1$ (end time $T = 0.9$). All other parameter values are as in Table 2.2.

resistance to the fluid flowing downstream. This results in a comparatively higher water volume fraction upstream and therefore, by the no voids condition (2.49), an increase in θ_n downstream.

Effect of membrane properties κ_m and ϕ_m

Next we consider the effect of the membrane porosity ϕ_m and dimensionless permeability κ_m on the cell population distribution. Increasing both parameters results in more downstream bunching of cells and therefore a greater standard deviation σ of θ_n (see Figures 2.10(d) and (e)). This is due to the increased flow into the ECS from the membrane (from either a greater porosity or permeability) and therefore greater effect of advection on the cells.

Effect of viscosity parameter λ

Finally we look at the effect of λ, which enters the viscosity ratio through $\mu_w/\mu_n = \lambda\varepsilon$ so that decreasing λ increases the effective viscosity of the cells μ_n. Results show that when the cells are more viscous, the distribution is less uniform overall (*i.e.* the standard deviation σ of θ_n is greater) and the cells also have more of a tendency to bunch downstream (see Figure 2.10(f)). This downstream bunching is non-intuitive, but likely to be due to the interactions between many different parameters, as we note that λ appears in several dimensionless parameters (see definitions in Table 2.2).

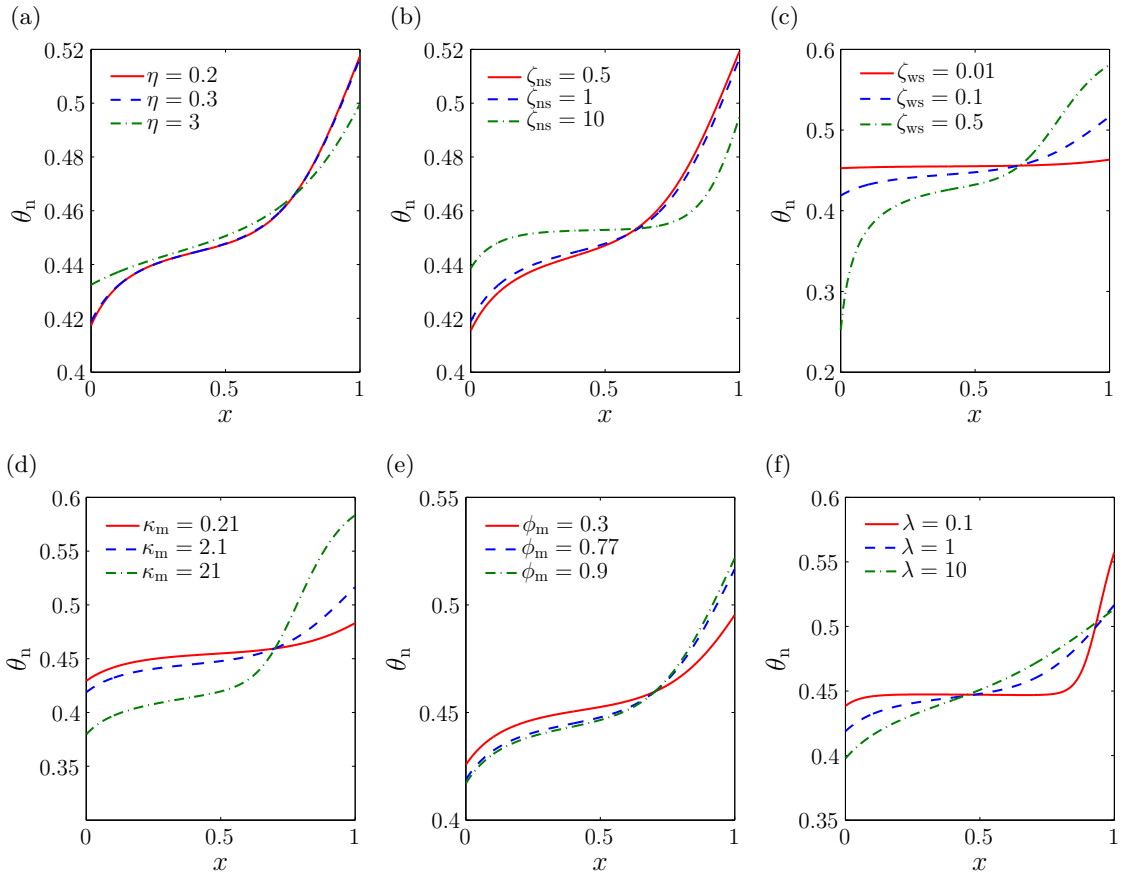

Figure 2.10: Steady-state distributions of the cell volume fraction θ_n versus x from the nutrient-driven proliferation case study in §2.7.1 (end time $T = 0.9$) for a range of values of (a) the cell-scaffold affinity parameter η, (b) the cell-scaffold drag ζ_{ns}, (c) the cell-water drag ζ_{ws}, (d) the dimensionless membrane permeability κ_m, (e) the membrane porosity ϕ_m, and (f) the viscosity parameter λ. The (dimensional) lumen flux $Q_{l,in}$ is fixed at 1.02×10^{-9} m^2 s^{-1}. All other parameter values are as in Table 2.2.

2.7.6 Backflow

We now consider the influence of an opposing flow in the ECS, which can be used experimentally for greater control of the cell environment (see Figure 2.11). Throughout this section, the 'upstream' and 'downstream' ends of the bioreactor should be interpreted as relative to the direction of flow in the lumen (*i.e.* at $x = 0$ and $x = 1$, respectively). We impose an inlet fluid flux at the downstream end of the ECS (mimicking a flow into the bioreactor through the open downstream ECS port):

$$\int_{1+h_2}^{H} \theta_w u_w \, dy = -Q_{e,in} \qquad \text{at} \quad x = 1, \tag{2.139}$$

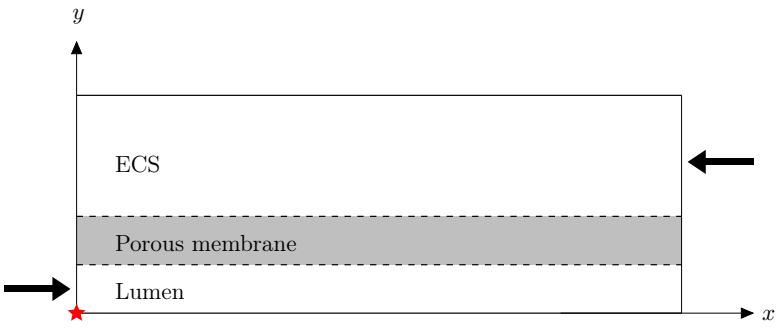

Figure 2.11: Simplified modelling domain in the backflow regime with the x-axis running along the lumen centreline (not to scale). The red star denotes the origin $(x, y) = (0, 0)$, and the solid black arrows denote the directions and locations of the imposed fluid fluxes into the lumen and ECS.

which corresponds to the following downstream boundary condition for the water flux

$$Q_{\mathrm{w}} = -\frac{Q_{\mathrm{e,in}}}{h_3} \qquad \text{at} \quad x = 1. \tag{2.140}$$

We also impose a prescribed (dimensionless, reduced) upstream pressure P_{up} so that

$$p_{\mathrm{w}} = P_{\mathrm{up}} \qquad \text{at} \quad x = 0. \tag{2.141}$$

Experimentally, this setup corresponds to an additional clamp controlling the pressure at the upstream ECS port. In our numerical simulations, we found that this was necessary to avoid a dominating upstream flow in this setup, and so to obtain a uniform cell population in the absence of chemotaxis. If a zero pressure was imposed upstream we would always have a positive water pressure gradient in the ECS and therefore net upstream advection of the cells. The value of P_{up} could be controlled experimentally, and here we choose illustrative values to demonstrate possible behaviours in this flow regime.

We now investigate the effect of this flow regime on the cell distribution, again using the nutrient-driven proliferation case study from §2.7.1 as a candidate example. Our aim is to see whether a uniform distribution of cells can be obtained without relying on the effect of chemotaxis, and for higher inlet fluid fluxes than those in §2.7.1 so that low oxygen concentrations are not a concern. Hence, once again we look for inlet fluid fluxes which minimise the standard deviation σ of θ_{n}. Given that the upstream lumen and downstream ECS inlet fluxes $Q_{\mathrm{l,in}}$ and $Q_{\mathrm{e,in}}$ are now independent of one another, we fix a value of $Q_{\mathrm{l,in}}$

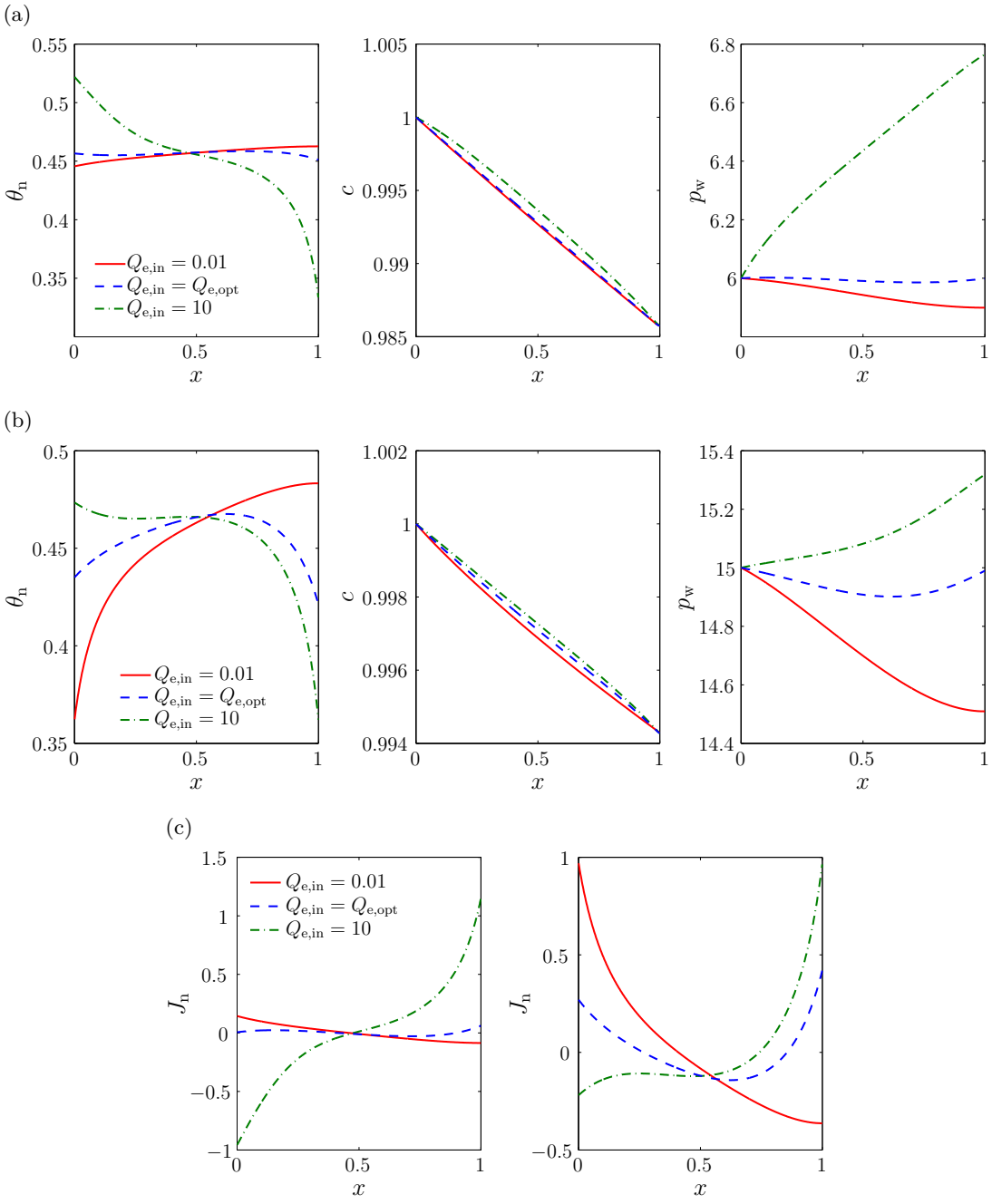

Figure 2.12: Steady-state distributions of the cell volume fraction θ_n, oxygen concentration c, reduced ECS water pressure p_w, and net cell proliferation function J_n versus x in the backflow regime of the nutrient-driven proliferation case study (§2.7.1) for a range of ECS inlet fluxes $Q_{e,in}$ including the optimal value $Q_{e,opt}$ (end time $T = 0.8$). Plots of (a) θ_n, c, and p_w for fixed $Q_{l,in} = 2$ and $P_{up} = 6$, optimal ECS flux $Q_{e,opt} = 1.1905$, with corresponding standard deviation $\sigma = 1.6 \times 10^{-3}$; (b) θ_n, c, and p_w for fixed $Q_{l,in} = 5$ and $P_{up} = 15$, optimal ECS flux $Q_{e,opt} = 5.9128$, with corresponding standard deviation $\sigma = 0.0105$; and (c) J_n for fixed $Q_{l,in} = 2$, $P_{up} = 6$ (left) and $Q_{l,in} = 5$, $P_{up} = 15$ (right). All other parameter values are as in Table 2.2.

and allow $Q_{\mathrm{e,in}}$ to vary. Plots of the cell, oxygen concentration, and reduced water pressure distributions, and the proliferation function J_{n} for a range of values of $Q_{\mathrm{e,in}}$, can be seen in Figure 2.12. These plots show that as $Q_{\mathrm{e,in}}$ is increased, the cell distribution switches from downstream to upstream bunching as expected, and we note that the pressure gradient changes from negative to positive. In addition, we can see that it is still possible to obtain a fairly uniform cell population in the case where $Q_{\mathrm{l,in}} = 2$ and $P_{\mathrm{up}} = 6$ (corresponding $\sigma = 1.6 \times 10^{-3}$, see Figure 2.12(a)), whereas for $Q_{\mathrm{l,in}} = 5$, $P_{\mathrm{up}} = 15$ the profile is peaked in shape ($\sigma = 0.0105$, Figure 2.12(b)). The plots of J_{n} show that regions of lower cell volume fraction correspond to a higher net proliferation rate.

To illustrate further the behaviour of the system in the case where $Q_{\mathrm{l,in}} = 5$ and $P_{\mathrm{up}} = 15$, Figure 2.13 shows plots of the cell and water streamlines, and the advective and diffusive cell flux contributions for each $Q_{\mathrm{e,in}}$ value. We only plot the water streamlines in the ECS and porous membrane, and not in the lumen, as those in the lumen are simply horizontal. In Figure 2.13(a), we observe a net flow of water downstream as the lumen flow is dominating, resulting in the downstream bunching of cells observed in Figure 2.12(b). In contrast, Figure 2.13(c) shows results for $Q_{\mathrm{e,in}} = 10$, when the ECS flow dominates and the net flow (and cell bunching) is upstream. In the flux figures, we note the switch in the respective directions of the advective and diffusive cell fluxes between Figures 2.13(a) and (c). Finally, in Figure 2.13(b), for the optimal value of $Q_{\mathrm{e,in}}$ we can see that there is a balance between forward and backward water flow in the ECS, with a stagnation point at around $x = 0.6$ which corresponds to the peak in θ_{n} observed in Figure 2.12(b). This stagnation point is also present in the cell velocity streamlines, which in general show a flow in the direction opposite to that of the water. Furthermore, we note that, apart from near $x = 0$, there is a flow of water into the membrane from the ECS for all values of $Q_{\mathrm{e,in}}$ considered.

2.8 Conclusions

We have developed a multiphase model of fluid flow, cell population evolution, and solute transport in a simplified HFMB setup. The governing equations have been reduced through careful asymptotic analysis to exploit the separation of length scales inherent in the experimental setup. The resulting leading-order system of equations has been solved numerically.

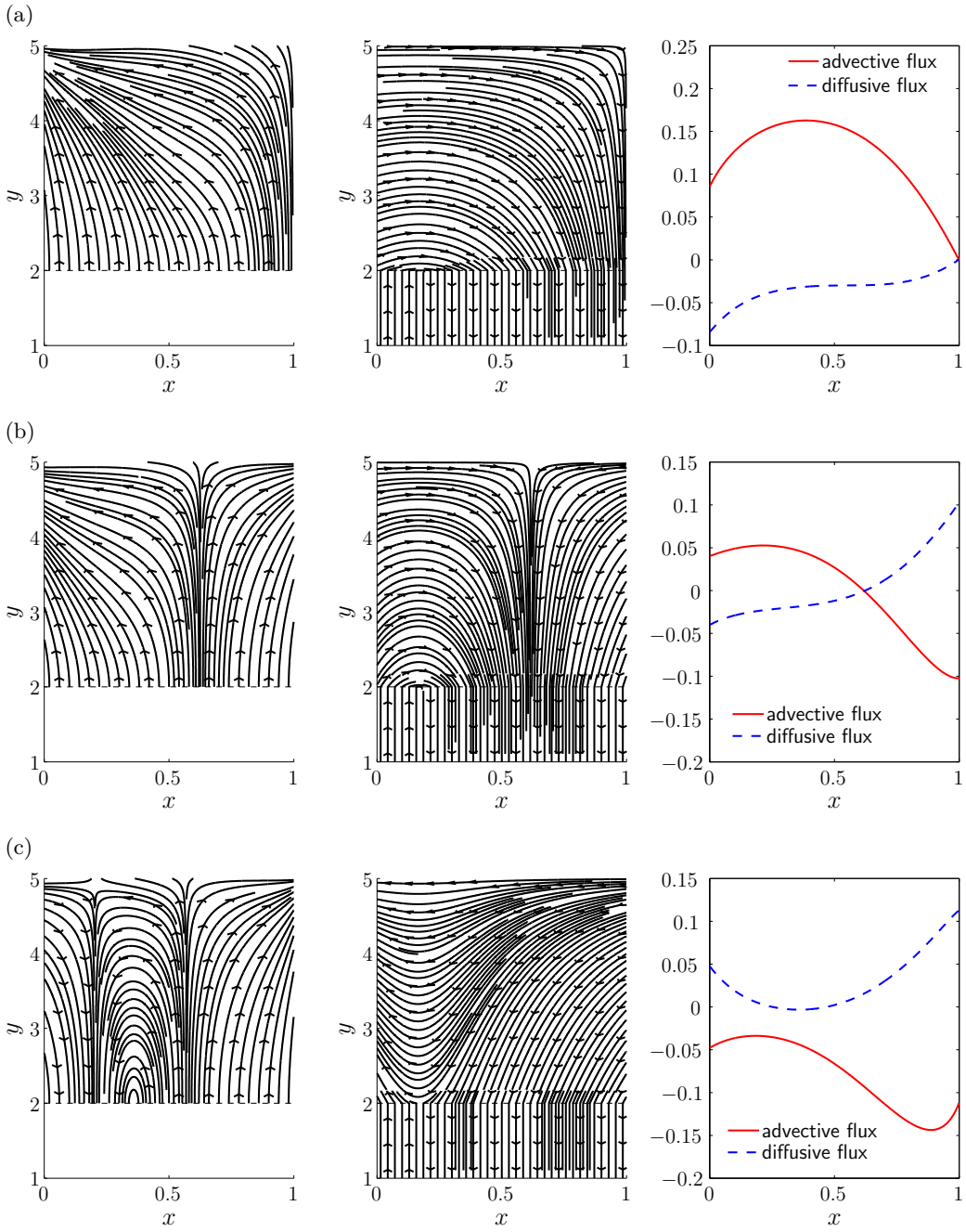

Figure 2.13: Plots of streamlines for the cell (left) and water (centre) velocities, and advective and diffusive cell fluxes (right), for the nutrient-driven proliferation case study (§2.7.1), with fixed $Q_{\mathrm{l,in}} = 5$ and $P_{\mathrm{up}} = 15$. In (a) $Q_{\mathrm{e,in}} = 0.01$, in (b) $Q_{\mathrm{e,in}} = Q_{\mathrm{e,opt}} = 5.9128$, and in (c) $Q_{\mathrm{e,in}} = 10$. All other parameter values are as in Table 2.2. Streamlines were calculated using the `streamslice` function in MATLAB.

To demonstrate the variety of possible steady-state cell distributions, we have investigated and compared a number of different case studies which represent different experimental setups. In each case there is a complex interaction between the effects of advection, diffusion, and chemotaxis on the cell population dynamics. This has been shown to result in a variety of steady states, with cells mainly aggregated up- or downstream, or being more uniformly distributed. We have shown that in almost all cases the requirement for a sufficient oxygen supply to maintain cell function is satisfied, but for the nutrient-only case study from §2.7.1 this may not be true throughout the bioreactor for the lowest fluid flux value considered. When chemoattractant is delivered into the system, we observe competition between advection and chemotaxis: initial upstream bunching of cells due to the chemoattractant concentration gradient is overcome by downstream advection of cells for large enough inlet fluid fluxes. This competition also results in the non-monotonic relationship between cell distribution and increasing inlet fluid flux which is observed in §2.7.3, where chemoattractant is produced by the cells. Downstream bunching of the cell population due to advection has also been observed experimentally [134]. By comparing the results from §2.7.3 to those in §2.7.4, we have shown that similar trends in cell distribution are observed as the lumen inlet fluid flux is increased, whether or not oxygen is explicitly included in the model. In the alternative flow regime where there is a backflow in the ECS, we have found that the competition between the up- and downstream fluid fluxes can result in bunching at either end of the bioreactor, or towards the centre. This central bunching of the cell population is reminiscent of cell distributions found experimentally when the direction of the imposed flow is periodically switched [134].

We have additionally found 'optimal' inlet fluid fluxes for each setup by minimising the standard deviation of the cell volume fraction and considering the corresponding cell yield. The extent to which a given setup is able to achieve a uniform cell population, and the shape of the resulting cell distribution, varies from case to case. For instance, when cells are undergoing paracrine signalling and/or nutrient-limited proliferation, the most uniform distribution possible has slight downstream bunching of the cell population. In contrast, in the case where endocrine signalling occurs, the most uniform distribution involves both up- and downstream cell aggregation, with a dip towards the middle of the modelling domain. However, our results all show that provided an appropriate inlet fluid flux value is chosen, each setup is capable of providing a cell population with relatively little spatial variation (the

largest standard deviation σ being 0.0148 in §2.7.3), and that despite the low experimental fluid fluxes considered here ($Q_{\mathrm{l,in}} = 0.01$ - 10 approximately corresponding to 3.86×10^{-7} - 3.86×10^{-4} ml min^{-1}), these fluxes ensure sufficient oxygen delivery to cells in all but one case. We also note that the minimum values of σ and optimal cell distributions found in the matching case studies with and without oxygen (from §2.7.3 and §2.7.4) are very similar, and hence we can conclude that the trends in cell population uniformity found here do not heavily depend upon the inclusion (or exclusion) of oxygen in the model.

Furthermore, in most cases we either see relatively little variation in the mean value μ of θ_{n}, or find that minimising the standard deviation σ of θ_{n} gives a value of μ that is very close to its maximum. Hence by choosing optimal inlet fluid fluxes based on cell distribution, we are not compromising on cell yield. In the nutrient-only case (§2.7.1), however, the optimal inlet fluid flux gives a lower cell yield than could be achieved with higher flux values, and hence in this situation a slight trade-off may have to be made between desired cell yield and distribution.

Finally, we have used the nutrient-limited growth case study from §2.7.1 to investigate the sensitivity of our results to a number of key dimensionless parameters, and the alternative flow regime where there is an upstream flux of fluid into the ECS. For instance, we have found that increasing the fluid flux into the ECS does not significantly affect cell yield, but does decrease the uniformity of the cell distribution by causing more downstream bunching. In the case of backflow, we have shown that by choosing an appropriate downstream lumen flux and upstream ECS flux, it is possible to generate a uniform distribution of cells in this alternative flow regime without the need for chemotaxis. This is more predictable as inlet fluid fluxes can be easily controlled in an experiment compared to chemotaxis effects and, in addition, the optimal flux values are higher than in the standard flow regime and thus oxygen limitations are less likely to affect cell viability.

We further note that the steady-state cell volume fractions (which were found to be independent of the choice of initial condition) were around 0.45 - 0.5 in each case study presented in this chapter. This is comparable to final densities obtained experimentally in HFMBs (around 10^8 cells ml^{-1}, see [86]), which are estimated to be equivalent to a volume fraction of 0.42 if we assume that cells are spherical, with a representative radius of 10 μm.

As mentioned previously, the constitutive forms of the kinetic functions J_{n} and $\mathcal{R}$ have been chosen to demonstrate the range of behaviour which could be expected from this

system, and would need validation in order for this model to be applied to a specific experimental setup. However, given that our analysis was carried out for general J_{n} and $\mathcal{R}$, it would be straightforward to obtain new results for different kinetic functions. In addition, the kinetic parameter values currently used are not specific to any one cell type and, again, the model could easily be altered for specific cell types given appropriate data. It is noted that these alterations could quantitatively alter our findings (for instance, proliferation could become the dominating effect over advection and therefore lead to more uniform cell distributions for higher fluid flux values than observed here), but we would expect results to correlate qualitatively to one of the case studies presented in §2.7. There are a number of other simplifications in our current model which could be explored further, and future work which would be necessary before it could be used to make any quantitative predictions. However, these are more generally applicable to the modelling approach taken throughout this thesis, and so we delay their discussion until Chapter 6.

Chapter 3

Four-layer multiphase model

3.1 Introduction

In this chapter we closely follow Pearson *et al.* [131], building on the model developed in Chapter 2 which described fluid flow, solute concentration, and cell distribution in a single HFMB module. In Chapter 2 the entire ECS was filled by the cell-scaffold construct, through which culture medium (modelled as water) could flow. Fluid velocities in the membrane and ECS were assumed to be an order of ε smaller than those in the lumen as a result of the resistance to flow through these porous layers, where $\varepsilon \ll 1$ is the lumen aspect ratio. As discussed in Chapter 1, a number of different cell seeding and flow regimes can be employed experimentally in HFMBs. In this chapter, we consider the alternative setup in which the cell-scaffold construct fills only part of the ECS (that directly above the porous membrane, which we define as the cell layer) and fluid can flow freely throughout the remainder. The depth of this cell layer can be controlled experimentally, and will be varied as part of our investigation. We also consider a different flow regime in which fluid is pumped into the system via both the lumen inlet and (now open) upstream ECS port (see Figure 3.1), such that the fluid velocity in this exterior fluid layer is of the same order of magnitude as in the lumen. As well as enabling the relevant solutes to be more quickly delivered to, or removed from, the cells, we expect the exterior fluid flow to enhance the flow through the cell layer so that the cells are exposed to a higher level of fluid shear stress. The impact of this setup remains an open question experimentally: as discussed in Chapter 1, depending on the cell type, fluid shear stress can be either beneficial or detrimental to cell growth and survival. In this chapter we consider the potential significance of mechanotransduction effects, which were not included in Chapter 2, by modelling cell populations whose proliferation rates are either enhanced or limited when they are exposed to certain levels of fluid shear stress. By

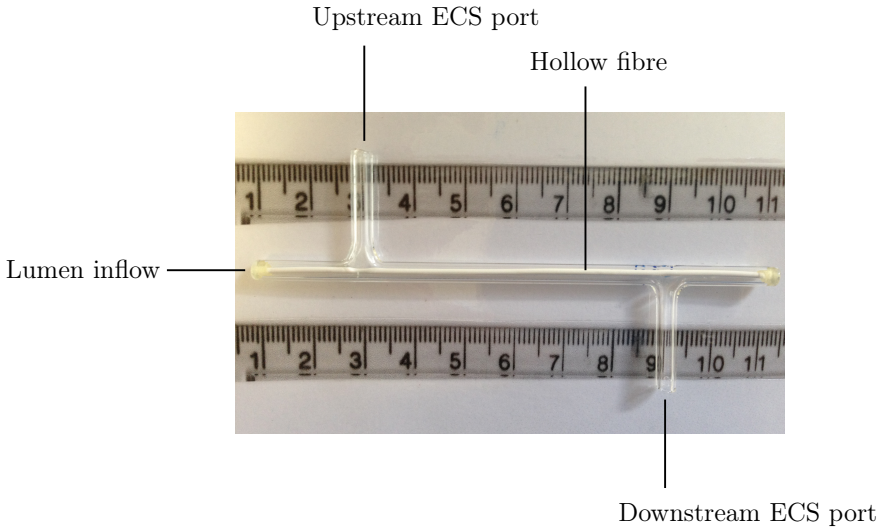

Figure 3.1: Photograph of a single HFMB module (ruler scale in cm) with both ECS ports open. The hollow fibre which runs through the centre of the module can again be seen. Cells are seeded in a natural scaffold on the outside of the fibre which partially fills the ECS.

varying the fluid flux into the exterior fluid layer, we can explore the effect of changes in this fluid shear stress on cell yield and distribution. We determine 'optimal' inlet fluid fluxes for which the fluid shear stress has an advantageous effect, *i.e.* enables a more spatially uniform cell population and/or a higher cell yield to be obtained. In addition, the fluid flux affects the concentration of a nutrient (taken to be oxygen), which can itself limit the cell proliferation rate. This effect is included in the cell proliferation rates in this chapter, however we do not explicitly analyse the variation in nutrient concentration that arises from different operating conditions, as results are very similar to those of §2.7.1. We instead simply verify that the nutrient concentration is above the threshold required for cell viability (as discussed in Chapter 2) for all operating conditions considered here.

3.1.1 Chapter outline

We begin in §3.2 by describing the full two-dimensional modelling domain, before making the same assumption in §3.2.1 as in Chapter 2 and considering the central region only, excluding the ECS ports. We then introduce the governing equations and boundary conditions for each layer in the simplified domain in §3.2.2 and §3.2.3. In §3.3.1 we introduce relevant parameter values. These motivate the non-dimensionalisation of the system, details of

which are given in §3.3.2. In §§3.3.3-3.3.5 we exploit the small aspect ratio of the lumen to reduce the system to two coupled PDEs for the leading-order cell volume fraction and solute concentration. Results for the cases in which cell proliferation is either enhanced or limited by fluid shear stress are presented in §3.4.1 and §3.4.2 respectively, and the sensitivity of our results to the cell layer height is investigated in §3.4.3. Finally, key findings and conclusions are discussed in §3.5.

3.2 Model description

As in Chapter 2, our modelling domain is motivated by taking a cross section of a single HFMB module and described using two-dimensional Cartesian coordinates (x, y). Two up- and two downstream ECS ports are included to mimic the connectivity, in three dimensions, of the ports to the entire ECS. A schematic of this setup can be seen in Figure 3.2, showing in red the new aspects of the model compared to Chapter 2: the cell layer occupying only part of the ECS with free-flowing fluid in the remainder, and the open upstream ECS ports through which an additional flux of fluid is driven. The remaining inlet/outlet conditions are unchanged: there is an imposed flux of fluid into the lumen at the upstream end and a prescribed pressure at the downstream end of the lumen, whilst the downstream ECS ports are at atmospheric pressure.

As in Chapter 2, we consider the cell layer to be a multiphase region consisting of the cells (one cell type only), water, and a rigid, inert scaffold, and thus it can be described using the same reduction of the generalised model presented in §1.4. Once again, the up- and downstream ends of the porous membrane are sealed so that no fluid or cells can leave the system there, and the porous membrane is impermeable to the cells so that they cannot leave the ECS. In addition, we assume that the cells remain within the scaffold so that they are confined to the cell layer only (and do not enter the exterior fluid layer). We again make the simplifying assumption that the drag between the water and cells is much smaller than that between the scaffold and water or between the scaffold and cells. The single solute of interest in the water in this chapter is a nutrient (*e.g.* oxygen).

In Figure 3.2, the layers Ω_i $(i = 1, 2, 3, 4)$ respectively denote the lumen, porous membrane, cell layer, and exterior fluid layer. The (permeable) interfaces between the lumen and porous membrane, between the porous membrane and cell layer, and between the cell

layer and exterior fluid layer are respectively given by $\partial\Omega_{12}$, $\partial\Omega_{23}$, and $\partial\Omega_{34}$ and the remaining (impermeable) boundaries of each layer are denoted by $\partial\Omega_i$ $(i = 2, 3, 4)$. Finally $\mathcal{A}$, $\mathcal{B}$, $\mathcal{C}$, and $\mathcal{D}$ represent line segments across the pipes a finite distance away from the lumen inlet, upstream ECS ports, lumen outlet, and downstream ECS ports respectively. The regions containing these ports (within the dashed boxes in Figure 3.2) will be neglected in the simplified modelling domain introduced in §3.2.1, as in Chapter 2.

To avoid unnecessary repetition of Chapter 2, we do not give explicit details of the governing equations and boundary conditions here, simply stating those that are new and delaying any mathematical presentation until §3.2.2 once the modelling domain has been simplified. However, it is worth mentioning that the governing equations in the lumen, porous membrane, and cell layer are unchanged from Chapter 2, as are the boundary conditions on the interfaces between them and on their (impermeable) boundaries.

The flow in the new exterior fluid layer Ω_4 is described by the incompressible Stokes equations as in the lumen. The boundary conditions on the cell layer/exterior fluid layer interface $\partial\Omega_{34}$ have much in common with the lumen/porous membrane interface $\partial\Omega_{12}$, as the cell layer/exterior fluid layer interface is also a boundary between a region of free-flowing fluid and porous media flow. We impose no slip of fluid in the exterior fluid layer, and continuity of fluid flux, of normal fluid stress (again assuming that all the stress is taken up by the water), of solute concentration, and of solute flux. The no slip condition is motivated by the assumption that the cell-scaffold construct can be treated similarly to the porous hollow fibre (on the surface of which a no slip condition is taken in the lumen). Alternatively, we could have imposed a non-zero slip length, which would require prescription of a slip function and thus the introduction of another constitutive law and more unknown parameters. However, this choice of boundary condition does not affect the analysis in this chapter, which could be followed through in exactly the same way if a finite slip condition were applied. We must also impose two boundary conditions on the cell phase at the cell layer/exterior fluid layer interface. We prescribe no flux of cells out of the cell layer due to our assumption that the cells remain within this layer. The second condition required is on the stress in the cell phase at this interface. The correct choice of condition is unclear as there is a lack of relevant data in the literature to inform our decision. For simplicity, we choose to impose no shear stress on the cell phase at this interface, assuming that the cells on the surface are to some degree 'protected' by the scaffold.

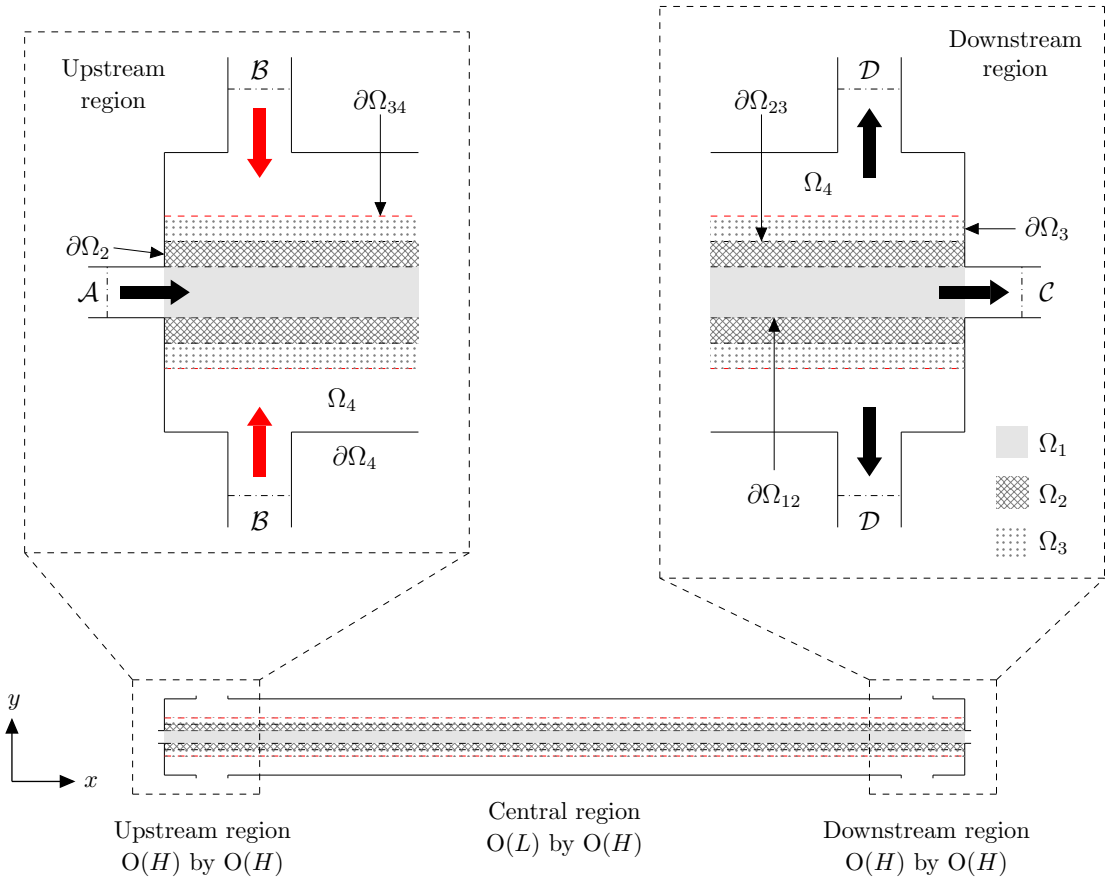

Figure 3.2: 4-layer modelling domain in a two-dimensional Cartesian geometry, with the up- and downstream inner regions near the ECS ports enlarged (not to scale). The differences between this modelling domain and that of Chapter 2 (depicted in Figure 2.1) are shown in red for ease of comparison: the imposed flow in through the open upstream ECS ports, and the edge of the cell layer in the ECS which results in a fourth layer of free-flowing fluid. The solid black/red arrows denote the direction of fluid flow. The lumen, porous membrane, cell layer, and upper fluid layer respectively occupy Ω_i $(i = 1, 2, 3, 4)$. Dashed lines represent permeable boundaries $\partial\Omega_{ij}$ between layers Ω_i and Ω_j, and solid lines denote impermeable boundaries $\partial\Omega_i$ where applicable. The dash-dotted lines $\mathcal{A}$, $\mathcal{B}$, $\mathcal{C}$, and $\mathcal{D}$ respectively denote line segments across the width of the pipes a finite distance away from the lumen inlet, upstream ECS ports, lumen outlet, and downstream ECS ports respectively. Again, H and L are typical vertical and horizontal length scales respectively, with $H \ll L$, and are specified in §3.3.

On the outer bioreactor boundary of the exterior fluid layer, $\partial\Omega_4$, we must now impose both no flux and no slip of fluid as it borders a region of free-flowing fluid. Finally, the upstream ECS ports are now open, and hence the appropriate boundary conditions to prescribe in the pipe entering the ECS at $\mathcal{B}$ are the same as at $\mathcal{A}$: we assume that the

flow is of Poiseuille form with a prescribed inlet volume flux $Q_{\mathrm{f,in}}$ per unit length in the z-direction, and impose an inlet concentration.

3.2.1 Simplified modelling domain

We simplify our modelling domain by excluding the up- and downstream regions near the ECS ports for the same reasons as in Chapter 2, namely to enable analytical progress and to avoid the need for extensive numerical computations, whilst still capturing key features of the system. As before, the influence of the regions near the ports will be captured through the up- and downstream boundary conditions imposed on our simplified domain. For simplicity, we again consider the upper half of the bioreactor only, with the modelling region thus consisting of four rectangular compartments (see Figure 3.3): the lumen, porous membrane, cell layer, and exterior fluid layer (which from now on we call the upper fluid layer). We again take the origin $(x, y) = (0, 0)$ to be at the bottom left of the domain, with the x-axis along the lumen centreline and the axial dimension of the modelling domain given by $0 < x < L$. The lumen and membrane are then respectively given by $0 < y < h_1$ and $h_1 < y < h_1 + h_2$ in the transverse direction. The cell layer is taken to be of comparable thickness to the membrane, occupying $h_1 + h_2 < y < h_1 + h_2 + h_3$, and the upper fluid layer occupies $H - h_4 < y < H$, where $H := h_1 + h_2 + h_3 + h_4$. Water variables in the lumen, membrane, cell layer, and upper fluid layer are denoted by subscripts l, m, w, and f respectively, with the velocities given by $\mathbf{u}_i = (u_i, v_i)$, the (reduced) water pressures by p_i, and the solute concentrations per unit volume of water by c_i $(i = \mathrm{l}, \mathrm{m}, \mathrm{w}, \mathrm{f})$. In the cell layer, we track the dynamics of the cell, water, and scaffold phases through their respective volume fractions θ_{n}, θ_{w}, and θ_{s}, where θ_{s} is again constant due to the assumption of a rigid, inert scaffold.

3.2.2 Governing equations

The dimensional governing equations in each layer take the form of conservation of mass and momentum for the water and (in the cell layer) the cell phase, and conservation of mass for the solute. As mentioned above, in the lumen, porous membrane, and cell layer these are the same as for the 3-layer system in Chapter 2, and the dynamics in the additional upper fluid layer are governed by the same equations as the lumen. We take the membrane porosity ϕ_{m} to be constant, and work with reduced pressures throughout since gravitational effects are not negligible at the flow rates considered, as discussed in Chapter 2. We also

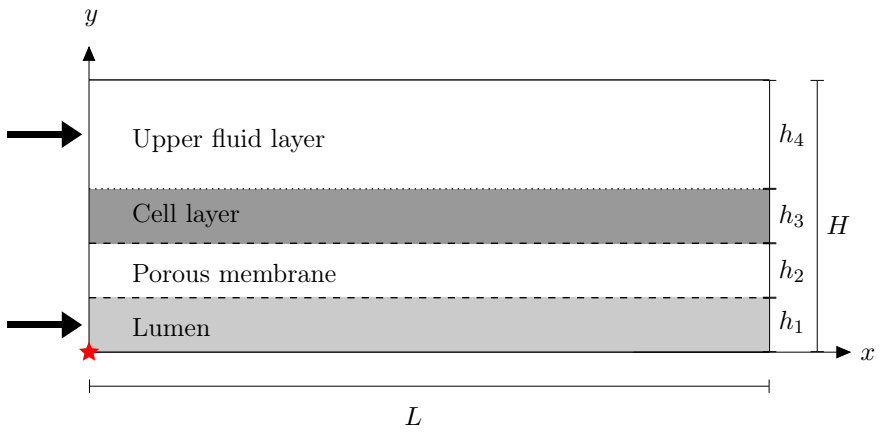

Figure 3.3: Simplified modelling domain with the x-axis running along the lumen centreline (not to scale). The red star denotes the origin $(x, y) = (0, 0)$, and the solid black arrows denote the directions of the imposed fluid fluxes into the lumen and upper fluid layer.

neglect inertial terms from the start as in Chapter 2. In the lumen the relevant water equations are those of Stokes flow, together with an advection-diffusion equation for the solute:

$$\nabla \cdot \mathbf{u}_\mathrm{l} = 0, \qquad -\nabla p_\mathrm{w} + \mu_\mathrm{w} \nabla^2 \mathbf{u}_\mathrm{l} = \mathbf{0}, \qquad \frac{\partial c_\mathrm{l}}{\partial t} + \nabla \cdot (c_\mathrm{l} \mathbf{u}_\mathrm{l}) = D \nabla^2 c_\mathrm{l}, \tag{3.1}$$

where μ_w is the water viscosity (assumed to be constant) and D is the diffusion coefficient for the solute in water (also assumed to be constant). In the porous membrane we use Darcy's law for flow in porous media, with

$$\begin{gathered} \mathbf{u}_\mathrm{m} = -\frac{k_\mathrm{m}}{\mu_\mathrm{w}} \nabla p_\mathrm{m}, \qquad \nabla \cdot \mathbf{u}_\mathrm{m} = 0, \\ \frac{\partial c_\mathrm{m}}{\partial t} + \nabla \cdot (c_\mathrm{m} \mathbf{u}_\mathrm{m}) = D \nabla^2 c_\mathrm{m}, \end{gathered} \tag{3.2}$$

where k_m is the (constant) membrane permeability. In the cell layer, the no voids condition is given by

$$\theta_\mathrm{n} + \theta_\mathrm{w} + \theta_\mathrm{s} = 1, \tag{3.3}$$

while conservation of mass and momentum for the cell phase are given by

$$\begin{gathered} \frac{\partial \theta_\mathrm{n}}{\partial t} + \nabla \cdot (\theta_\mathrm{n} \mathbf{u}_\mathrm{n}) = J_\mathrm{n}, \\ -\theta_\mathrm{n} \nabla p_\mathrm{w} - \nabla (\theta_\mathrm{n} \Pi) + \nabla \cdot (\theta_\mathrm{n} \boldsymbol{\tau}_\mathrm{n}) + \psi_\mathrm{ns} \theta_\mathrm{s} \nabla \theta_\mathrm{n} - \gamma_\mathrm{ns} \theta_\mathrm{n} \theta_\mathrm{s} \mathbf{u}_\mathrm{n} = \mathbf{0}, \end{gathered} \tag{3.4}$$

where we have already substituted in the forms for the stress tensor $\boldsymbol{\sigma}_\mathrm{n}$, (reduced) intraphase pressure p_n, and interphase forces $\mathbf{f}_{ij}$ $(i,j = \mathrm{n},\mathrm{w},\mathrm{s})$ given in §1.4 and §2.3.3. We recall that ψ_ns is assumed to be a negative constant representing the cells' affinity for the scaffold:

$$\psi_\mathrm{ns} = -\eta. \tag{3.5}$$

Here, we neglect the effect of chemotaxis and so take the extra pressure component Π to be a function of θ_n only. To obtain our results in §3.4 we will use the explicit form motivated by [123] and introduced in Chapter 2 which accounts for cell-cell interactions, namely

$$\Pi = \Pi_\mathrm{n} = \theta_\mathrm{n}\left(-\nu + \frac{\delta_\mathrm{a}\theta_\mathrm{n}}{1-\theta_\mathrm{s}-\theta_\mathrm{n}}\right), \tag{3.6}$$

where we recall that ν and δ_a are constants. The corresponding equations for the water phase are given by

$$\frac{\partial\theta_\mathrm{w}}{\partial t} + \nabla\cdot(\theta_\mathrm{w}\mathbf{u}_\mathrm{w}) = -J_\mathrm{n}, \qquad -\theta_\mathrm{w}\nabla p_\mathrm{w} - \gamma_\mathrm{ws}\theta_\mathrm{w}\theta_\mathrm{s}\mathbf{u}_\mathrm{w} = \mathbf{0}, \tag{3.7}$$

where we have used the fact that $J_\mathrm{w} = -J_\mathrm{n}$ so that mass is conserved. Conservation of solute mass in the cell layer yields:

$$\frac{\partial(\theta_\mathrm{w}c_\mathrm{w})}{\partial t} + \nabla\cdot(\theta_\mathrm{w}c_\mathrm{w}\mathbf{u}_\mathrm{w}) = D\nabla\cdot(\theta_\mathrm{w}\nabla c_\mathrm{w}) + \mathcal{R}, \tag{3.8}$$

where here the reaction term $\mathcal{R}$ accounts for nutrient uptake by the cells. Finally, in the upper fluid layer the governing equations are given by

$$\nabla\cdot\mathbf{u}_\mathrm{f} = 0, \qquad -\nabla p_\mathrm{f} + \mu_\mathrm{w}\nabla^2\mathbf{u}_\mathrm{f} = \mathbf{0}, \qquad \frac{\partial c_\mathrm{f}}{\partial t} + \nabla\cdot(c_\mathrm{f}\mathbf{u}_\mathrm{f}) = D\nabla^2 c_\mathrm{f}. \tag{3.9}$$

It remains to prescribe constitutive relationships for J_n and $\mathcal{R}$. Explicit forms will be given as needed in §3.4; for now we assume only that J_n and $\mathcal{R}$ are functions of the cell volume fraction θ_n, cell layer solute concentration c_w and, in the case of J_n, the fluid shear stress in the cell layer. As will be seen in §3.3.3, the fluid flow in the cell layer is independent of y, and thus we estimate the fluid shear stress by taking it to be proportional to the (reduced) water pressure gradient $\partial p_\mathrm{w}/\partial x$ (which is also independent of y).

3.2.3 Boundary conditions

The boundary conditions on the lumen centreline, the lumen/porous membrane interface, and the porous membrane/cell layer interface are as in Chapter 2. Those on the cell

layer/upper fluid layer interface and on the top of the bioreactor follow from our discussion in §3.2. In the following, $\mathbf{n}_i$ $(i = \mathrm{l}, \mathrm{m}, \mathrm{e})$ are, respectively, the unit normals to the lumen/membrane, membrane/cell layer, and cell layer/upper fluid layer interfaces pointing in the positive y-direction, and $\mathbf{t}_\mathrm{e}$ is the unit tangent to the cell layer/upper fluid layer interface.

On $y = 0$ symmetry requires that

$$\frac{\partial u_\mathrm{l}}{\partial y} = 0, \qquad v_\mathrm{l} = 0, \qquad \frac{\partial c_\mathrm{l}}{\partial y} = 0. \tag{3.10}$$

On the lumen/membrane interface $y = h_1$ we impose no slip of fluid, and continuity of fluid flux, of normal stress, of solute concentration, and of solute flux, *viz.*

$$\begin{aligned} u_\mathrm{l} = 0, \qquad v_\mathrm{l} = \phi_\mathrm{m} v_\mathrm{m}, \qquad \mathbf{n}_\mathrm{l} \cdot \boldsymbol{\sigma}_\mathrm{l} \cdot \mathbf{n}_\mathrm{l} = \mathbf{n}_\mathrm{l} \cdot \boldsymbol{\sigma}_\mathrm{m} \cdot \mathbf{n}_\mathrm{l}, \\ c_\mathrm{l} = c_\mathrm{m}, \qquad \frac{\partial c_\mathrm{l}}{\partial y} = \phi_\mathrm{m} \frac{\partial c_\mathrm{m}}{\partial y}. \end{aligned} \tag{3.11}$$

On the membrane/cell layer interface $y = h_1 + h_2$ we impose no flux and no slip of cells, and continuity of fluid flux, of normal stress, of solute concentration, and of solute flux,

$$\begin{aligned} \mathbf{u}_\mathrm{n} = \mathbf{0}, \qquad \phi_\mathrm{m} v_\mathrm{m} = \theta_\mathrm{w} v_\mathrm{w}, \qquad \mathbf{n}_\mathrm{m} \cdot \boldsymbol{\sigma}_\mathrm{m} \cdot \mathbf{n}_\mathrm{m} = \mathbf{n}_\mathrm{m} \cdot \boldsymbol{\sigma}_\mathrm{w} \cdot \mathbf{n}_\mathrm{m}, \\ c_\mathrm{m} = c_\mathrm{w}, \qquad \phi_\mathrm{m} \frac{\partial c_\mathrm{m}}{\partial y} = \theta_\mathrm{w} \frac{\partial c_\mathrm{w}}{\partial y}. \end{aligned} \tag{3.12}$$

On the cell layer/upper fluid layer interface $y = H - h_4$, we impose no flux and no shear stress on the cell phase, no slip of fluid, continuity of flux and of normal stress on the water phase, and continuity of concentration and of flux of solute:

$$\begin{aligned} v_\mathrm{n} = 0, \qquad \mathbf{n}_\mathrm{e} \cdot \boldsymbol{\sigma}_\mathrm{n} \cdot \mathbf{t}_\mathrm{e} = 0, \qquad u_\mathrm{f} = 0, \qquad \theta_\mathrm{w} v_\mathrm{w} = v_\mathrm{f}, \\ \mathbf{n}_\mathrm{e} \cdot \boldsymbol{\sigma}_\mathrm{w} \cdot \mathbf{n}_\mathrm{e} = \mathbf{n}_\mathrm{e} \cdot \boldsymbol{\sigma}_\mathrm{f} \cdot \mathbf{n}_\mathrm{e}, \qquad c_\mathrm{w} = c_\mathrm{f}, \qquad \theta_\mathrm{w} \frac{\partial c_\mathrm{w}}{\partial y} = \frac{\partial c_\mathrm{f}}{\partial y}. \end{aligned} \tag{3.13}$$

Finally, on the top of the bioreactor $y = H$ we impose no slip and no flux of fluid, and no flux of solute:

$$\mathbf{u}_\mathrm{f} = \mathbf{0}, \qquad \frac{\partial c_\mathrm{f}}{\partial y} = 0. \tag{3.14}$$

We impose boundary conditions at the up- and downstream ends of the bioreactor once the system has been reduced in dimension, as we shall now describe.

3.3 Model reduction

In this section we discuss relevant dimensional parameter values which motivate our choice of non-dimensionalisation in §3.3.2. The resulting dimensionless parameter values, and our asymptotic expansion of the system variables in powers of the lumen aspect ratio, allow the system of governing equations and boundary conditions to be reduced significantly to four coupled PDEs. Imposing up- and downstream boundary conditions closes the problem and eliminates two of these equations, leaving a system of two coupled PDEs for the cell volume fraction and solute concentration at leading order in the lumen aspect ratio. The remaining leading-order unknowns can be determined *a posteriori* via analytical expressions.

3.3.1 Parameter values

Typical dimensional parameter values are, where possible, taken from the literature or guided by our experimental collaborators. Those which are new to this chapter are presented in Table 3.1; for others see Table 2.1. All corresponding dimensionless parameters required in this chapter are given in Table 3.2 along with any physical or asymptotic (compared to our small parameter $\varepsilon = 2 \times 10^{-3}$) bounds on their size required for the validity of the subsequent analysis. A few choices are worth mentioning or reiterating here following our more in-depth discussion in Chapter 2. Firstly, we note that the aspect ratio of each layer is small; in particular, we define the lumen aspect ratio by $\varepsilon = h_1/L \ll 1$ and use this as the small parameter for our asymptotic analysis in §3.3.3. We again set the viscosity ratio $\mu_w/\mu_n = \lambda\varepsilon$ for some constant $\lambda = O(1)$, motivated by the fact that we would expect the (macroscale) viscosity of the cell phase to be much greater than that of water as a result of the cytoskeletal network, the cell-scaffold affinity, and microscale cell-cell interactions. We choose the dimensionless cell-scaffold and water-scaffold drag to be of O(1), so that their effects are retained in the leading-order model.

Table 3.1: Dimensional parameters new to this chapter.

Parameter	Dimensional value and units	Ref.
$h_3 + h_4$	600 μm	[156]
$Q_{l,in}$, $Q_{f,in}$	1.02×10^{-11} - 1.02×10^{-8} m^2 s^{-1}	†

† Values based on estimations by our experimental collaborators.

Table 3.2: Dimensionless parameters used in this chapter, along with any bounds imposed either physically or by the asymptotic analysis.

Parameter	Definition	Value	Restriction	Ref.
$\hat{h}_2$	$h_2/(\varepsilon L)$	1	$\hat{h}_2 > 0$	-
$\hat{h}_3 + \hat{h}_4$	$(h_3 + h_4)/(\varepsilon L)$	3	$\hat{h}_3,\ \hat{h}_4 > 0$	-
θ_s	-	0.4	$0 < s < 1$	[92]
ε	h_1/L	2×10^{-3}	$0 < \varepsilon \ll 1$	-
λ	$\mu_\mathrm{w}/(\varepsilon\mu_\mathrm{n})$	1	$\varepsilon \ll \lambda \ll 1/\varepsilon$	-
$\varepsilon^2\mathrm{Pe}$	$\varepsilon L U^*/(\lambda D)$	6.83×10^{-4}	$\varepsilon^3 \ll \varepsilon^2\mathrm{Pe} \ll \varepsilon$	-
$\varepsilon^2\mathrm{Re}$	$\varepsilon\rho_\mathrm{w} L U^*/(\lambda\mu_\mathrm{w})$	2.05×10^{-6}	$\varepsilon^2\mathrm{Re} \ll 1$	-
ϕ_m	-	0.77	$0 < \phi_\mathrm{m} < 1$	[109]
κ_m	$k_\mathrm{m}/(\lambda\varepsilon^5 L^2)$	2.1	$\varepsilon \ll \kappa_\mathrm{m} \ll 1/\varepsilon$	-
$\hat{Q}_{i,\mathrm{in}}\ (i = \mathrm{l}, \mathrm{f})$	$\lambda Q_{i,\mathrm{in}}/(LU^*)$	0.01 - 10	$\varepsilon \ll \hat{Q}_{i,\mathrm{in}} \ll 1/\varepsilon$	-
$\hat{\nu}$	$\lambda\varepsilon^3 L\nu/(\mu_w U^*)$	0.3	$\varepsilon \ll \hat{\nu} \ll 1/\varepsilon$	[123]
$\hat{\delta}_\mathrm{a}$	$\lambda\varepsilon^3 L\delta_\mathrm{a}/(\mu_w U^*)$	0.1	$\varepsilon \ll \hat{\delta}_\mathrm{a} \ll 1/\varepsilon$	[123]
$\hat{\eta}$	$\lambda\varepsilon^3 L\eta/(\mu_w U^*)$	0.3	$\varepsilon \ll \hat{\eta} \ll 1/\varepsilon$	[123]
ζ_ns	$\gamma_\mathrm{ns} L^2\lambda\varepsilon^3/\mu_\mathrm{w}$	1	$\varepsilon \ll \zeta_\mathrm{ns} \ll 1/\varepsilon$	-
ζ_ws	$\gamma_\mathrm{ws} L^2\lambda\varepsilon^3/\mu_\mathrm{w}$	0.1	$\varepsilon \ll \zeta_\mathrm{ws} \ll 1/\varepsilon$	-
$\hat{\Gamma}_\mathrm{nw}$	$L\Gamma_\mathrm{nw}/U^*$	56.52	$\varepsilon \ll \hat{\Gamma}_\mathrm{nw} \ll 1/\varepsilon$	-
$\hat{\Gamma}_\mathrm{wn}$	$L\Gamma_\mathrm{wn}/U^*$	4.04	$\varepsilon \ll \hat{\Gamma}_\mathrm{wn} \ll 1/\varepsilon$	-
$\hat{\Gamma}_\mathrm{R1}$	$L^2\Gamma_\mathrm{R1}/(C^*D)$	50	$\varepsilon \ll \hat{\Gamma}_\mathrm{R1} \ll 1/\varepsilon$	-
$\hat{K},\ \hat{K}_1$	$K/C^*,\ K_1/C^*$	1	$\varepsilon \ll \hat{K},\ \hat{K}_1 \ll 1/\varepsilon$	-
$\hat{c}_\mathrm{in}$	c_in/C^*	1	$\varepsilon \ll \hat{c}_\mathrm{in} \ll 1/\varepsilon$	-
$\hat{P}_\mathrm{dwn}$	$\varepsilon^2 L(P_\mathrm{dwn} - p_\mathrm{atm})/(\mu_\mathrm{n} U^*)$	2.5	$\varepsilon \ll \hat{P}_\mathrm{d} \ll 1/\varepsilon$	-

We define the velocity scale U^* to be a typical horizontal velocity of the water in the porous membrane. We then take the corresponding horizontal velocity scale in the cell layer to be U^*, and in both the lumen and upper fluid layer to be $\mu_\mathrm{n}U^*/\mu_\mathrm{w}$, as discussed in Chapter 2. The reduced Péclet number in the lumen and upper fluid layer, $\varepsilon^2\mathrm{Pe}$, is of order ε^2 which results in radial diffusion dominating advection throughout. The cell layer height could be varied in an experimental setup, and we investigate the effect of doing so in §3.4.3. Elsewhere, we set $h_3 = 1$ (and so $h_4 = 2$). The concentration scale C^* and inlet concentration c_in are both set to be a typical oxygen concentration used in cell culture [155], as oxygen is the solute of interest in §3.4. The two-dimensional lumen and upper fluid layer inlet fluxes $Q_\mathrm{l,in}$ and $Q_\mathrm{f,in}$ (which come into the upstream boundary conditions in §3.3.4) are assumed to be comparable in size and have been converted from three-dimensional experimental values by first calculating the corresponding fluid velocity and then multiplying by the length scale in the y-direction, εL. The (reduced) downstream

lumen outlet pressure P_{dwn} and atmospheric pressure p_{atm} are also introduced in §3.3.4, and the cell proliferation/death rates Γ_{nw} / Γ_{wn} and solute uptake rate $\Gamma_{\mathrm{R_1}}$ are parameters in the constitutive laws for J_{n} and $\mathcal{R}$, both of which we introduce in §3.4.

3.3.2 Non-dimensionalisation

Motivated by the discussion in §3.3.1, we non-dimensionalise as follows:

$$\begin{gathered} x = L\hat{x}, \qquad y = \varepsilon L\hat{y}, \qquad t = \frac{L}{U^*}\hat{t}, \qquad h_i = \varepsilon L\hat{h}_i \quad (i = 2,3,4), \qquad H = \varepsilon L\hat{H}, \\ u_i = \frac{\mu_{\mathrm{n}}}{\mu_{\mathrm{w}}}U^*\hat{u}_i, \qquad v_i = \frac{\varepsilon\mu_{\mathrm{n}}}{\mu_{\mathrm{w}}}U^*\hat{v}_i \quad (i = \mathrm{l},\mathrm{f}), \\ u_i = U^*\hat{u}_i, \qquad v_i = \varepsilon U^*\hat{v}_i \quad (i = \mathrm{m},\mathrm{w},\mathrm{n}), \\ p_i = p_{\mathrm{atm}} + \frac{\mu_{\mathrm{n}}U^*}{\varepsilon^2 L}\hat{p}_i \quad (i = \mathrm{l},\mathrm{m},\mathrm{w},\mathrm{f}), \qquad \Pi = \frac{\mu_{\mathrm{n}}U^*}{\varepsilon^2 L}\hat{\Pi}, \qquad \psi_{\mathrm{ns}} = \frac{\mu_{\mathrm{n}}U^*}{\varepsilon^2 L}\hat{\psi}_{\mathrm{ns}}, \\ c_i = C^*\hat{c}_i \quad (i = \mathrm{l},\mathrm{m},\mathrm{w},\mathrm{f}), \qquad \mathcal{R} = \frac{DC^*}{L^2}\hat{\mathcal{R}}, \qquad J_{\mathrm{n}} = \frac{U^*}{L}\hat{J}_{\mathrm{n}}, \end{gathered} \tag{3.15}$$

where we have employed a viscous pressure scaling throughout (motivated by lubrication theory as in Chapter 2). In choosing the timescale L/U^* and mass transfer scale U^*/L for J_{n} we have assumed that the timescales for advection in the porous membrane/cell layer and proliferation are comparable, an appropriate assumption given the very slow flow rates considered here (see Table 3.1).

Dropping hats on dimensionless variables, the dimensionless governing equations in the lumen ($0 < y < 1$) are therefore

$$\begin{gathered} \frac{\partial u_{\mathrm{l}}}{\partial x} + \frac{\partial v_{\mathrm{l}}}{\partial y} = 0, \qquad -\frac{\partial p_{\mathrm{l}}}{\partial x} + \varepsilon^2\frac{\partial^2 u_{\mathrm{l}}}{\partial x^2} + \frac{\partial^2 u_{\mathrm{l}}}{\partial y^2} = 0, \qquad -\frac{\partial p_{\mathrm{l}}}{\partial y} + \varepsilon^4\frac{\partial^2 v_{\mathrm{l}}}{\partial x^2} + \varepsilon^2\frac{\partial^2 v_{\mathrm{l}}}{\partial y^2} = 0, \\ \varepsilon^2\mathrm{Pe}\left(\lambda\varepsilon\frac{\partial c_{\mathrm{l}}}{\partial t} + \nabla\cdot(c_{\mathrm{l}}\mathbf{u}_{\mathrm{l}})\right) = \varepsilon^2\frac{\partial^2 c_{\mathrm{l}}}{\partial x^2} + \frac{\partial^2 c_{\mathrm{l}}}{\partial y^2}, \end{gathered} \tag{3.16}$$

and in the porous membrane ($1 < y < 1 + h_2$)

$$\begin{gathered} u_{\mathrm{m}} = -\varepsilon^2\kappa_{\mathrm{m}}\frac{\partial p_{\mathrm{m}}}{\partial x}, \qquad v_{\mathrm{m}} = -\kappa_{\mathrm{m}}\frac{\partial p_{\mathrm{m}}}{\partial y}, \qquad \varepsilon^2\frac{\partial^2 p_{\mathrm{m}}}{\partial x^2} + \frac{\partial^2 p_{\mathrm{m}}}{\partial y^2} = 0, \\ \lambda\varepsilon^3\mathrm{Pe}\left(\frac{\partial c_{\mathrm{m}}}{\partial t} + \nabla\cdot(c_{\mathrm{m}}\mathbf{u}_{\mathrm{m}})\right) = \varepsilon^2\frac{\partial^2 c_{\mathrm{m}}}{\partial x^2} + \frac{\partial^2 c_{\mathrm{m}}}{\partial y^2}, \end{gathered} \tag{3.17}$$

where $\kappa_{\mathrm{m}} = k_{\mathrm{m}}/(\lambda\varepsilon^5 L^2)$ is the O(1) dimensionless permeability (see Table 3.2). In the cell layer ($1 + h_2 < y < H - h_4$) the no voids condition is given by

$$\theta_{\mathrm{n}} + \theta_{\mathrm{w}} + \theta_{\mathrm{s}} = 1, \tag{3.18}$$

the cell equations are given by

$$\frac{\partial \theta_{\rm n}}{\partial t} + \frac{\partial}{\partial x}(\theta_{\rm n} u_{\rm n}) + \frac{\partial}{\partial y}(\theta_{\rm n} v_{\rm n}) = J_{\rm n}, \tag{3.19}$$

$$-\theta_{\rm n}\frac{\partial p_{\rm w}}{\partial x} - \frac{\partial}{\partial x}(\theta_{\rm n}\Pi) + \psi_{\rm ns}\theta_{\rm s}\frac{\partial \theta_{\rm n}}{\partial x} + \frac{2\varepsilon^2}{3}\frac{\partial}{\partial x}\left[\theta_{\rm n}\left(2\frac{\partial u_{\rm n}}{\partial x} - \frac{\partial v_{\rm n}}{\partial y}\right)\right] + \frac{\partial}{\partial y}\left[\theta_{\rm n}\left(\frac{\partial u_{\rm n}}{\partial y} + \varepsilon^2\frac{\partial v_{\rm n}}{\partial x}\right)\right] - \zeta_{\rm ns}\theta_{\rm n}\theta_{\rm s}u_{\rm n} = 0, \tag{3.20}$$

$$-\theta_{\rm n}\frac{\partial p_{\rm w}}{\partial y} - \frac{\partial}{\partial y}(\theta_{\rm n}\Pi) + \psi_{\rm ns}\theta_{\rm s}\frac{\partial \theta_{\rm n}}{\partial y} + \varepsilon^2\frac{\partial}{\partial x}\left[\theta_{\rm n}\left(\frac{\partial u_{\rm n}}{\partial y} + \varepsilon^2\frac{\partial v_{\rm n}}{\partial x}\right)\right] + \frac{2\varepsilon^2}{3}\frac{\partial}{\partial y}\left[\theta_{\rm n}\left(2\frac{\partial v_{\rm n}}{\partial y} - \frac{\partial u_{\rm n}}{\partial x}\right)\right] - \varepsilon^2\zeta_{\rm ns}\theta_{\rm n}\theta_{\rm s}v_{\rm n} = 0, \tag{3.21}$$

the water equations are given by

$$\begin{gathered}\frac{\partial \theta_{\rm w}}{\partial t} + \frac{\partial}{\partial x}(\theta_{\rm w}u_{\rm w}) + \frac{\partial}{\partial y}(\theta_{\rm w}v_{\rm w}) = -J_{\rm n},\\ -\theta_{\rm w}\frac{\partial p_{\rm w}}{\partial x} - \zeta_{\rm ws}\theta_{\rm w}\theta_{\rm s}u_{\rm w} = 0, \qquad -\theta_{\rm w}\frac{\partial p_{\rm w}}{\partial y} - \varepsilon^2\zeta_{\rm ws}\theta_{\rm w}\theta_{\rm s}v_{\rm w} = 0,\end{gathered} \tag{3.22}$$

and the solute equation is given by

$$\lambda\varepsilon^3{\rm Pe}\left(\frac{\partial}{\partial t}(\theta_{\rm w}c_{\rm w}) + \nabla\cdot(\theta_{\rm w}c_{\rm w}\mathbf{u}_{\rm w})\right) = \varepsilon^2\frac{\partial}{\partial x}\left(\theta_{\rm w}\frac{\partial c_{\rm w}}{\partial x}\right) + \frac{\partial}{\partial y}\left(\theta_{\rm w}\frac{\partial c_{\rm w}}{\partial y}\right) + \varepsilon^2\mathcal{R}, \tag{3.23}$$

where $\zeta_{ij} = \gamma_{ij}L^2\varepsilon^2/\mu_{\rm n}$ $(i = {\rm n}, {\rm w}, j = {\rm s})$ are dimensionless. In the upper fluid layer $(H - h_4 < y < H)$

$$\begin{gathered}\frac{\partial u_{\rm f}}{\partial x} + \frac{\partial v_{\rm f}}{\partial y} = 0, \qquad -\frac{\partial p_{\rm f}}{\partial x} + \varepsilon^2\frac{\partial^2 u_{\rm f}}{\partial x^2} + \frac{\partial^2 u_{\rm f}}{\partial y^2} = 0, \qquad -\frac{\partial p_{\rm f}}{\partial y} + \varepsilon^4\frac{\partial^2 v_{\rm f}}{\partial x^2} + \varepsilon^2\frac{\partial^2 v_{\rm f}}{\partial y^2} = 0,\\ \varepsilon^2{\rm Pe}\left(\lambda\varepsilon\frac{\partial c_{\rm f}}{\partial t} + \nabla\cdot(c_{\rm f}\mathbf{u}_{\rm f})\right) = \varepsilon^2\frac{\partial^2 c_{\rm f}}{\partial x^2} + \frac{\partial^2 c_{\rm f}}{\partial y^2}.\end{gathered} \tag{3.24}$$

The dimensionless boundary conditions on the lumen centreline are given by

$$\frac{\partial u_{\rm l}}{\partial y} = 0, \qquad v_{\rm l} = 0, \qquad \frac{\partial c_{\rm l}}{\partial y} = 0 \qquad \text{on} \quad y = 0, \tag{3.25}$$

on the lumen/membrane interface (substituting in for $p_{\rm m}$ in place of $v_{\rm m}$) by

$$\begin{gathered}u_{\rm l} = 0, \qquad \varepsilon\frac{\partial p_{\rm m}}{\partial y} = -\frac{1}{\lambda\kappa_{\rm m}\phi_{\rm m}}v_{\rm l}, \qquad p_{\rm l} + \frac{2\varepsilon^2}{3}\left(\frac{\partial u_{\rm l}}{\partial x} - 2\frac{\partial v_{\rm l}}{\partial y}\right) = p_{\rm m},\\ c_{\rm l} = c_{\rm m}, \qquad \frac{\partial c_{\rm l}}{\partial y} = \phi_{\rm m}\frac{\partial c_{\rm m}}{\partial y} \qquad \text{on} \quad y = 1,\end{gathered} \tag{3.26}$$

on the membrane/cell layer interface (again substituting in for p_m in place of v_m) by

$$\begin{gathered} u_\mathrm{n} = v_\mathrm{n} = 0, \qquad v_\mathrm{w} = -\frac{\kappa_\mathrm{m}\phi_\mathrm{m}}{\theta_\mathrm{w}}\frac{\partial p_\mathrm{m}}{\partial y}, \qquad p_\mathrm{w} = p_\mathrm{m}, \\ c_\mathrm{m} = c_\mathrm{w}, \qquad \phi_\mathrm{m}\frac{\partial c_\mathrm{m}}{\partial y} = \theta_\mathrm{w}\frac{\partial c_\mathrm{w}}{\partial y} \qquad \text{on} \quad y = 1 + h_2, \end{gathered} \tag{3.27}$$

on the cell/upper fluid layer interface by

$$\begin{gathered} v_\mathrm{n} = 0, \qquad \frac{\partial u_\mathrm{n}}{\partial y} + \varepsilon^2\frac{\partial v_\mathrm{n}}{\partial x} = 0, \qquad u_\mathrm{f} = 0, \qquad \lambda\varepsilon\theta_\mathrm{w}v_\mathrm{w} = v_\mathrm{f}, \\ -p_\mathrm{w} = -p_\mathrm{f} + \frac{2\varepsilon^2}{3}\left(2\frac{\partial v_\mathrm{f}}{\partial y} - \frac{\partial u_\mathrm{f}}{\partial x}\right), \qquad c_\mathrm{w} = c_\mathrm{f}, \qquad \theta_\mathrm{w}\frac{\partial c_\mathrm{w}}{\partial y} = \frac{\partial c_\mathrm{f}}{\partial y} \qquad \text{on} \quad y = 1 + h_2 + h_3, \end{gathered} \tag{3.28}$$

and finally on the bioreactor top by

$$u_\mathrm{f} = v_\mathrm{f} = 0, \qquad \frac{\partial c_\mathrm{f}}{\partial y} = 0 \qquad \text{on} \quad y = H. \tag{3.29}$$

3.3.3 Derivation of the reduced model

Having non-dimensionalised the governing equations and boundary conditions, we asymptotically expand each dependent variable in powers of ε, setting $u_\mathrm{l} \sim u_{\mathrm{l}_0} + \varepsilon u_{\mathrm{l}_1} + \varepsilon^2 u_{\mathrm{l}_2} + \ldots$ as $\varepsilon \to 0$, and similarly for the remaining velocities, reduced pressures, solute concentrations, and volume fractions. In the following we omit the subscript 0 from leading-order variables except where needed for clarity. Equating coefficients of ε^0 in the lumen then yields

$$\frac{\partial u_\mathrm{l}}{\partial x} + \frac{\partial v_\mathrm{l}}{\partial y} = 0, \qquad \frac{\partial^2 u_\mathrm{l}}{\partial y^2} = \frac{\partial p_\mathrm{l}}{\partial x}, \qquad \frac{\partial p_\mathrm{l}}{\partial y} = 0, \qquad \frac{\partial^2 c_\mathrm{l}}{\partial y^2} = 0, \tag{3.30a-d}$$

in the membrane,

$$u_\mathrm{m} \equiv 0, \qquad v_\mathrm{m} = -\kappa_\mathrm{m}\frac{\partial p_\mathrm{m}}{\partial y}, \qquad \frac{\partial^2 p_\mathrm{m}}{\partial y^2} = 0, \qquad \frac{\partial^2 c_\mathrm{m}}{\partial y^2} = 0, \tag{3.31a-d}$$

in the cell layer,

$$\begin{gathered} \theta_\mathrm{n} + \theta_\mathrm{w} + \theta_\mathrm{s} = 1, \qquad \frac{\partial \theta_\mathrm{n}}{\partial t} + \frac{\partial}{\partial x}(\theta_\mathrm{n}u_\mathrm{n}) + \frac{\partial}{\partial y}(\theta_\mathrm{n}v_\mathrm{n}) = J_\mathrm{n}, \\ \frac{\partial \theta_\mathrm{w}}{\partial t} + \frac{\partial}{\partial x}(\theta_\mathrm{w}u_\mathrm{w}) + \frac{\partial}{\partial y}(\theta_\mathrm{w}v_\mathrm{w}) = -J_\mathrm{n}, \\ -\theta_\mathrm{n}\frac{\partial p_\mathrm{w}}{\partial x} - \frac{\partial}{\partial x}(\theta_\mathrm{n}\Pi) + \theta_\mathrm{s}\psi_\mathrm{ns}\frac{\partial \theta_\mathrm{n}}{\partial x} - \zeta_\mathrm{ns}\theta_\mathrm{n}\theta_\mathrm{s}u_\mathrm{n} + \frac{\partial}{\partial y}\left(\theta_\mathrm{n}\frac{\partial u_\mathrm{n}}{\partial y}\right) = 0, \\ -\theta_\mathrm{n}\frac{\partial p_\mathrm{w}}{\partial y} - \frac{\partial}{\partial y}(\theta_\mathrm{n}\Pi) + \theta_\mathrm{s}\zeta_\mathrm{ns}\frac{\partial \theta_\mathrm{n}}{\partial y} = 0, \\ \theta_\mathrm{w}\frac{\partial p_\mathrm{w}}{\partial x} + \zeta_\mathrm{ws}\theta_\mathrm{w}\theta_\mathrm{s}u_\mathrm{w} = 0, \qquad \theta_\mathrm{w}\frac{\partial p_\mathrm{w}}{\partial y} = 0, \qquad \frac{\partial}{\partial y}\left(\theta_\mathrm{w}\frac{\partial c_\mathrm{w}}{\partial y}\right) = 0, \end{gathered} \tag{3.32a-h}$$

and in the upper fluid layer,

$$\frac{\partial u_\mathrm{f}}{\partial x}+\frac{\partial v_\mathrm{f}}{\partial y}=0, \qquad \frac{\partial^2 u_\mathrm{f}}{\partial y^2}=\frac{\partial p_\mathrm{f}}{\partial x}, \qquad \frac{\partial p_\mathrm{f}}{\partial y}=0, \qquad \frac{\partial^2 c_\mathrm{f}}{\partial y^2}=0. \tag{3.33a-d}$$

The leading-order boundary conditions on the lumen centreline are given by

$$\frac{\partial u_\mathrm{l}}{\partial y}=0, \qquad v_\mathrm{l}=0, \qquad \frac{\partial c_\mathrm{l}}{\partial y}=0 \qquad \text{on} \quad y=0, \tag{3.34a-c}$$

on the lumen/membrane interface by

$$u_\mathrm{l}=v_\mathrm{l}=0, \qquad p_\mathrm{l}=p_\mathrm{m}, \qquad c_\mathrm{l}=c_\mathrm{m}, \qquad \frac{\partial c_\mathrm{l}}{\partial y}=\phi_\mathrm{m}\frac{\partial c_\mathrm{m}}{\partial y} \qquad \text{on} \quad y=1, \tag{3.35a-e}$$

on the membrane/cell layer interface by

$$\begin{aligned} &u_\mathrm{n}=v_\mathrm{n}=0, \qquad v_\mathrm{w}=-\frac{\kappa_\mathrm{m}\phi_\mathrm{m}}{\theta_\mathrm{w}}\frac{\partial p_\mathrm{m}}{\partial y}, \qquad p_\mathrm{m}=p_\mathrm{w}, \\ &c_\mathrm{m}=c_\mathrm{w}, \qquad \phi_\mathrm{m}\frac{\partial c_\mathrm{m}}{\partial y}=\theta_\mathrm{w}\frac{\partial c_\mathrm{w}}{\partial y} \qquad \text{on} \quad y=1+h_2, \end{aligned} \tag{3.36a-f}$$

on the cell layer/upper fluid layer interface by

$$\begin{aligned} &v_\mathrm{n}=0, \qquad \frac{\partial u_\mathrm{n}}{\partial y}=0, \qquad u_\mathrm{f}=v_\mathrm{f}=0, \qquad p_\mathrm{w}=p_\mathrm{f}, \\ &c_\mathrm{w}=c_\mathrm{f}, \qquad \theta_\mathrm{w}\frac{\partial c_\mathrm{w}}{\partial y}=\frac{\partial c_\mathrm{f}}{\partial y} \qquad \text{on} \quad y=1+h_2+h_3, \end{aligned} \tag{3.37a-g}$$

and finally on the bioreactor top by

$$u_\mathrm{f}=0, \qquad v_\mathrm{f}=0, \qquad \frac{\partial c_\mathrm{f}}{\partial y}=0 \qquad \text{on} \quad y=H. \tag{3.38a-c}$$

Consideration of the above solute equations (3.30d), (3.31d), (3.32h), and (3.33d), and boundary conditions (3.34c), (3.35d,e), (3.36e,f), (3.37f,g), and (3.38c) shows that at leading order there is again a global concentration, independent of y: $c_i := c(x,t)$ $(i=\mathrm{l},\mathrm{m},\mathrm{w},\mathrm{f})$. To close the problem and find $c(x,t)$, we must also consider the solute equations at $\mathrm{O}(\varepsilon^2)$, as the $\mathrm{O}(\varepsilon)$ systems in each layer do not contain terms in $c(x,t)$. Therefore at $\mathrm{O}(\varepsilon^2)$ (in the lumen, membrane, cell layer, and upper fluid layer respectively, and reintroducing subscript 0 notation for clarity)

$$\begin{aligned} \mathrm{Pe}\left(\frac{\partial}{\partial x}(c_{\mathrm{l}_0}u_{\mathrm{l}_0})+\frac{\partial}{\partial y}(c_{\mathrm{l}_0}v_{\mathrm{l}_0})\right)&=\frac{\partial^2 c_{\mathrm{l}_0}}{\partial x^2}+\frac{\partial^2 c_{\mathrm{l}_2}}{\partial y^2}, \qquad \frac{\partial^2 c_{\mathrm{m}_0}}{\partial x^2}+\frac{\partial^2 c_{\mathrm{m}_2}}{\partial y^2}=0, \\ \frac{\partial}{\partial x}\left(\theta_{\mathrm{w}_0}\frac{\partial c_{\mathrm{w}_0}}{\partial x}\right)+\frac{\partial}{\partial y}\left(\theta_{\mathrm{w}_0}\frac{\partial c_{\mathrm{w}_2}}{\partial y}+\theta_{\mathrm{w}_2}\frac{\partial c_{\mathrm{w}_0}}{\partial y}\right)+\mathcal{R}&=0, \\ \mathrm{Pe}\left(\frac{\partial}{\partial x}(c_{\mathrm{f}_0}u_{\mathrm{f}_0})+\frac{\partial}{\partial y}(c_{\mathrm{f}_0}v_{\mathrm{f}_0})\right)&=\frac{\partial^2 c_{\mathrm{f}_0}}{\partial x^2}+\frac{\partial^2 c_{\mathrm{f}_2}}{\partial y^2}, \end{aligned} \tag{3.39}$$

together with boundary conditions

$$\frac{\partial c_{\mathrm{l}_2}}{\partial y} = 0 \qquad \text{on} \quad y = 0, \tag{3.40}$$

$$c_{\mathrm{l}_2} = c_{\mathrm{m}_2}, \qquad \frac{\partial c_{\mathrm{l}_2}}{\partial y} = \phi_{\mathrm{m}} \frac{\partial c_{\mathrm{m}_2}}{\partial y} \qquad \text{on} \quad y = 1, \tag{3.41}$$

$$c_{\mathrm{m}_2} = c_{\mathrm{w}_2}, \qquad \phi_{\mathrm{m}} \frac{\partial c_{\mathrm{m}_2}}{\partial y} = \theta_{\mathrm{w}} \frac{\partial c_{\mathrm{w}_2}}{\partial y} \qquad \text{on} \quad y = 1 + h_2, \tag{3.42}$$

$$c_{\mathrm{w}_2} = c_{\mathrm{f}_2}, \qquad \theta_{\mathrm{w}} \frac{\partial c_{\mathrm{w}_2}}{\partial y} = \frac{\partial c_{\mathrm{f}_2}}{\partial y} \qquad \text{on} \quad y = 1 + h_2 + h_3, \tag{3.43}$$

$$\frac{\partial c_{\mathrm{f}_2}}{\partial y} = 0 \qquad \text{on} \quad y = H. \tag{3.44}$$

A substantial amount of analytical progress can be made in the distinguished limit considered above, which closely follows the working for the 3-layer system in Chapter 2. Equations (3.30*c*), (3.32*g*), and (3.33*c*) respectively tell us that the leading-order reduced water pressures in the lumen, cell layer, and upper fluid layer are independent of y. From (3.32*e*), and given θ_{s} is constant, we can thus conclude that the cell volume fraction θ_{n} is also a function of x and t only, which again allows substantial simplifications to be made. We can obtain expressions for the leading-order variables in terms of the lumen reduced water pressure $p_{\mathrm{l}}(x,t)$, the upper fluid layer reduced pressure $p_{\mathrm{f}}(x,t)$, the cell volume fraction $\theta_{\mathrm{n}}(x,t)$, and the solute concentration $c(x,t)$. Thus the fluid velocities and solute concentration in the lumen are

$$u_{\mathrm{l}} = \frac{1}{2}\frac{\partial p_{\mathrm{l}}}{\partial x}(y^2 - 1), \qquad v_{\mathrm{l}} \equiv 0, \qquad c_{\mathrm{l}} = c(x,t), \tag{3.45}$$

the fluid velocities and reduced pressure, and solute concentration in the membrane are

$$u_{\mathrm{m}} \equiv 0, \qquad v_{\mathrm{m}} = -\frac{\kappa_{\mathrm{m}}}{h_2}(p_{\mathrm{w}} - p_{\mathrm{l}}), \qquad p_{\mathrm{m}} = \frac{1}{h_2}(p_{\mathrm{w}} - p_{\mathrm{l}})(y-1) + p_{\mathrm{l}}, \qquad c_{\mathrm{m}} = c(x,t), \tag{3.46}$$

the axial cell and water velocities, reduced water pressure, and solute concentration in the cell layer are

$$\begin{aligned} u_{\mathrm{w}} &= -\frac{1}{\theta_{\mathrm{s}}\zeta_{\mathrm{ws}}}\frac{\partial p_{\mathrm{w}}}{\partial x}, \qquad p_{\mathrm{w}} \equiv p_{\mathrm{f}}(x,t), \qquad c_{\mathrm{w}} = c(x,t), \\ u_{\mathrm{n}} &= \frac{M(x,t)}{\zeta_{\mathrm{ns}}\theta_{\mathrm{s}}}\left\{\frac{\cosh\left[\sqrt{\zeta_{\mathrm{ns}}\theta_{\mathrm{s}}}\,(1 + h_2 + h_3 - y)\right]}{\cosh\left(\sqrt{\zeta_{\mathrm{ns}}\theta_{\mathrm{s}}}h_3\right)} - 1\right\}, \end{aligned} \tag{3.47a-d}$$

and the fluid velocities and solute concentration in the upper fluid layer are

$$u_{\mathrm{f}} = \frac{1}{2}\frac{\partial p_{\mathrm{w}}}{\partial x}\left[y^2 + (h_4 - 2H)(y - H) - H^2\right], \qquad v_{\mathrm{f}} \equiv 0, \qquad c_{\mathrm{f}} = c(x,t), \tag{3.48}$$

where here $M(x,t)$ is defined by

$$M(x,t) := \frac{\partial p_\mathrm{w}}{\partial x} + \frac{1}{\theta_\mathrm{n}}\Phi(\theta_\mathrm{n})\frac{\partial \theta_\mathrm{n}}{\partial x}, \qquad \Phi(\theta_\mathrm{n}) := \Pi + \theta_\mathrm{n}\Pi_\mathrm{n}' - \psi_\mathrm{ns}\theta_\mathrm{s}. \tag{3.49a,b}$$

Hence, at leading order, we have Poiseuille flow in the lumen and upper fluid layer, and transverse flow only in the porous membrane. In the cell layer, the horizontal fluid flow is Darcy-like (*i.e.* u_w is proportional to the pressure gradient $\partial p_\mathrm{w}/\partial x$). The remaining variables v_n and v_w can be determined from the leading-order conservation of mass equations (3.32b,c), respectively.

In addition, we have the following equations for p_l, θ_n, the global leading-order concentration c, and p_f:

$$\frac{\partial^2 p_\mathrm{l}}{\partial x^2} = 0, \qquad \frac{\partial \theta_\mathrm{n}}{\partial t} + \frac{\partial Q_\mathrm{n}}{\partial x} = J_\mathrm{n}, \qquad \frac{\partial Q_\mathrm{c}}{\partial x} = -h_3\mathcal{R}, \qquad \frac{\partial^2 p_\mathrm{f}}{\partial x^2} = 0, \tag{3.50a-d}$$

where the cell flux Q_n is given by

$$Q_\mathrm{n} = \frac{M(x,t)}{\zeta_\mathrm{ns}\theta_\mathrm{s}}\left(\frac{\tanh(\alpha)}{\alpha} - 1\right)\theta_\mathrm{n}, \qquad \alpha := \sqrt{\zeta_\mathrm{ns}\theta_\mathrm{s}}h_3, \tag{3.51}$$

and the solute flux Q_c by

$$Q_\mathrm{c} = \left(\frac{1}{3}\mathrm{Pe}\frac{\partial p_\mathrm{l}}{\partial x} + \frac{h_4^3}{12}\mathrm{Pe}\frac{\partial p_\mathrm{f}}{\partial x}\right)c + b(\theta_\mathrm{n})\frac{\partial c}{\partial x}, \qquad b(\theta_\mathrm{n}) := 1 + h_2\phi_\mathrm{n} + h_3(1-\theta_\mathrm{s}-\theta_\mathrm{n}) + h_4. \tag{3.52}$$

Equations (3.50a,b,d) for p_l, θ_n, and p_f come from integrating the respective conservation of mass equations (3.30a), (3.32b), and (3.33a) across the lumen, cell layer, and upper fluid layer. The remaining equation (3.50c) has been obtained by summing the $\mathrm{O}(\varepsilon^2)$ solute equations in (3.39) after averaging each across the appropriate layer and (in the porous membrane) weighting by porosity. We now impose up- and downstream boundary conditions to close the problem.

3.3.4 Boundary conditions for the reduced model

As described above, we mimic the experimental setup where fluid is pumped into the bioreactor via both the lumen inlet and (upstream) ECS port, and so impose

$$Q_\mathrm{l,in} = \int_0^1 u_\mathrm{l}\,\mathrm{d}y, \qquad Q_\mathrm{f,in} = \int_{H-h_4}^{H} u_\mathrm{f}\,\mathrm{d}y \qquad \text{at} \quad x = 0, \tag{3.53}$$

where $Q_\mathrm{l,in}$ and $Q_\mathrm{f,in}$ are prescribed (dimensionless) volume fluxes per unit length in the z-direction into the lumen and upper fluid layer respectively, and are assumed constant.

We note that in this case, the dimensional version of $Q_{\mathrm{f,in}}$ is of the same order as the dimensional version of $Q_{\mathrm{l,in}}$ given that the velocity scales in the lumen and upper fluid layer are the same. We also prescribe a downstream lumen pressure and mimic the atmospheric pressure conditions at the downstream ECS port by setting

$$p_{\mathrm{l}} = P_{\mathrm{dwn}}, \qquad p_{\mathrm{f}} = 0 \qquad \text{at} \quad x = 1. \tag{3.54}$$

For the cells, we again impose no flux out of the modelling domain:

$$Q_{\mathrm{n}} = 0 \qquad \text{at} \quad x = 0, 1. \tag{3.55}$$

Finally, we prescribe an inlet solute concentration and assume no diffusive flux of solute at the downstream end of the bioreactor, as discussed in Chapter 2:

$$c = 1 \qquad \text{at} \quad x = 0, \tag{3.56}$$

$$\frac{\partial c}{\partial x} = 0 \qquad \text{at} \quad x = 1. \tag{3.57}$$

It is worth recalling here that in the experimental setup considered in this chapter, solute is supplied to the bioreactor at both the lumen inlet and upstream ECS port and these inlet concentrations could be set to be different. However, given our leading-order solute concentration is independent of y, we can only prescribe a single inlet concentration at $x = 0$ at leading order. We do not investigate this condition further here, but instead refer ahead to Chapter 5 where analysis of the neglected regions near the up- and downstream ECS ports is performed for the case of constant cell volume fraction (the analysis is also applicable to the multiphase case (results not shown)).

Applying boundary conditions (3.53) and (3.54) allows us to solve (3.50*a*,*d*) explicitly for p_{l} and p_{f}, giving

$$p_{\mathrm{l}} = 3Q_{\mathrm{l,in}}(1 - x) + P_{\mathrm{dwn}}, \qquad p_{\mathrm{f}} = \frac{12Q_{\mathrm{f,in}}}{h_4^3}(1 - x), \tag{3.58}$$

and thereby specific expressions for u_{l}, v_{m}, p_{m}, u_{w}, p_{w}, and u_{f} from (3.45)-(3.48). In particular, we note the form for the reduced water pressure in the cell layer, which is equivalent to p_{f} (see (3.47*b*)),

$$p_{\mathrm{w}} = \frac{12Q_{\mathrm{f,in}}}{h_4^3}(1 - x), \tag{3.59}$$

which will be required for the fluid shear stress approximation in §3.4.

3.3.5 Summary of the reduced model

To summarise, we have derived the following coupled system to solve for θ_{n} and c:

$$\frac{\partial \theta_{\mathrm{n}}}{\partial t} + \frac{\partial Q_{\mathrm{n}}}{\partial x} = J_{\mathrm{n}}, \qquad \frac{\partial Q_{\mathrm{c}}}{\partial x} = -h_3 \mathcal{R}, \tag{3.60}$$

where

$$Q_{\mathrm{n}} = \frac{M(x,t)}{\zeta_{\mathrm{ns}}\theta_{\mathrm{s}}} \left(\frac{\tanh(\alpha)}{\alpha} - 1 \right) \theta_{\mathrm{n}}, \qquad Q_{\mathrm{c}} = -\mathrm{Pe}\,(Q_{\mathrm{l,in}} + Q_{\mathrm{f,in}})\, c + b(\theta_{\mathrm{n}}) \frac{\partial c}{\partial x}, \tag{3.61}$$

with the boundary conditions

$$Q_{\mathrm{n}} = 0 \qquad \text{at} \quad x = 0, 1, \tag{3.62}$$

$$c = 1 \qquad \text{at} \quad x = 0, \tag{3.63}$$

$$\frac{\partial c}{\partial x} = 0 \qquad \text{at} \quad x = 1. \tag{3.64}$$

Here M, α, and b are as in (3.49a), (3.51), and (3.52) respectively, and the only initial condition required is the prescription of θ_{n} at $t = 0$ for $0 < x < 1$. We can compare this to the corresponding system (2.82)-(2.86) from Chapter 2: it is interesting to see that, despite the apparently more complex setup here (with four layers in the modelling domain instead of three), the governing equations can be reduced to a system of two, instead of three, coupled PDEs. The elimination of one of the PDEs is due to the fact that in the 4-layer setup we can explicitly solve for the reduced water pressure in the upper fluid layer, p_{f}. This yields an analytical expression for the reduced water pressure in the cell layer, since $p_{\mathrm{w}} \equiv p_{\mathrm{f}}$, and hence only two unknowns remain, θ_{n} and c.

3.4 Numerical results

The reduced system (3.60)-(3.64) was solved numerically using the method of lines as described in detail in §2.6.1, first discretising in x and then performing the time integration using the MATLAB function `ode15s`. A convergence check was carried out on the scheme before it was used to obtain our numerical results, a graph of which can be found in Appendix A.2. We are interested in steady states of the system, as these arise on timescales comparable to the long culture time of experiments (see §2.7 for a more thorough discussion). These states were found to be independent of the choice of initial condition in our simulations, but for completeness we note that in the simulations presented in this chapter we set $\theta_{\mathrm{n}}(x, 0) = 0.3$ and (as a pseudo-initial condition for the numerics) $c(x, 0) = 1$ for

$0 < x < 1$. We confirm that, as stated in §3.1, the nutrient concentration is above the threshold required for cell viability (as discussed in Chapter 2) for all operating conditions considered here (results not shown).

We consider the effect of the fluid shear stress on the cell distribution and yield in the case where the solute of interest is a nutrient (*e.g.* oxygen), and with the aim of determining optimal experimental conditions which result in both a spatially uniform cell population and high cell yield.

In each of the following sections, we consider the Michaelis-Menten type reaction term used for oxygen uptake in the nutrient-limited proliferation case study of Chapter 2:

$$\mathcal{R} = -\frac{\Gamma_{\mathrm{R1}}\theta_{\mathrm{n}}\theta_{\mathrm{w}}c}{K_1 + c}, \tag{3.65}$$

where we recall that Γ_{R1} and K_1 are constants. We take the cell mass transfer term J_{n} to have the form

$$J_{\mathrm{n}} = \frac{F(S)\Gamma_{\mathrm{nw}}\theta_{\mathrm{n}}\theta_{\mathrm{w}}c}{K + c} - \Gamma_{\mathrm{wn}}\theta_{\mathrm{n}}, \tag{3.66}$$

where Γ_{nw}, Γ_{wn}, and K are constants, and S is a variable capturing the (dimensionless) fluid shear stress in the cell layer which we define below (see equation (3.67)). If $F(S)$ were equal to unity, then we would recover the form used in the nutrient-driven proliferation case study in Chapter 2. In the following analysis we take $F(S)$ to have different forms depending on the cells' response to shear stress. As we effectively have Darcy flow of water through the cell layer, we find an estimate for S motivated by a similar expression in [178], which is based upon the assumption that there is Poiseuille flow through each of the 'pores' in the cell layer, with the pores approximated as circular ducts, and results in an expression for the shear stress which is proportional to the modulus of the pressure gradient (see [178] for details). Given that in our setup, $\partial p_{\mathrm{w}}/\partial x$ is (spatially and temporally) constant, we make the constitutive choice to additionally weight the shear stress by $1/\theta_{\mathrm{w}}$ so that we can investigate the effect of spatially varying shear stress on the cell population. This choice reflects the fact that we would expect the cells to experience higher levels of shear stress in smaller 'pores' (*i.e.* in regions where θ_{w} is lower), as they effectively occupy more of the pore space and hence are exposed to faster flow [65]. We thus take

$$S = \frac{\left|\frac{\partial p_{\mathrm{w}}}{\partial x}\right|}{\theta_{\mathrm{w}}}. \tag{3.67}$$

Given the assumed form (3.67) for S, and the expression for $\partial p_{\mathrm{w}}/\partial x$ in (3.59), we see that the fluid shear stress is dependent on both the upper fluid layer flux $Q_{\mathrm{f,in}}$ and cell layer height

h_3 (via $h_4 = H - (1 + h_2 + h_3)$), both of which can be controlled experimentally. In what follows we investigate the sensitivity of our results to variations in these two parameters. Moreover, for a given upper fluid layer inlet flux and cell layer height, we note that variations in S can also arise purely through variations in θ_{w}.

In each case study, we present results for the steady-state cell volume fraction, where the criteria for the solution having reached steady state are the same as in Chapter 2. That is, the solution is assumed to be at steady state if the maximum change in θ_{n} and c between the end time T and $T - 0.062$ (corresponding to a dimensional time of around one week) is less than 10^{-4}. For all simulations presented here this corresponds to setting $T = 1.5$. As in Chapter 2, we use the mean μ and standard deviation σ of $\theta_{\mathrm{n}}(x, T)$ to characterise the cell yield and distribution, where

$$\mu := \int_0^1 \theta_{\mathrm{n}}(x, T)\,\mathrm{d}x, \qquad \sigma := \sqrt{\int_0^1 \left[\theta_{\mathrm{n}}(x, T) - \mu\right]^2\,\mathrm{d}x}. \tag{3.68}$$

3.4.1 Shear stress-enhanced proliferation

Firstly, we consider the case when cell proliferation is enhanced by increased levels of fluid shear stress, which has been observed in cells such as osteoblasts [74], chondrocytes [101], and (more controversially) endothelial progenitor cells [185], and is thought to be an important factor in ensuring the mechanical integrity of tissue such as bone and cartilage [15,54]. The exact nature of the dependence is not known and will depend on the cell type in question. To capture the qualitative aspects of the dependence, and motivated by similar forms used in [123] we set

$$F(S) = 0.3 + 0.5\tanh(2S - 4) - 0.8\tanh(2S - 15), \tag{3.69}$$

so that the cell proliferation rate increases with shear stress up to a maximal level, but sufficiently high levels of shear stress result in a reduced proliferation rate (see Figure 3.4). The coefficients in (3.69) have been chosen to capture the possible qualitative behaviours of the cell population within the range of computed shear stresses in our model.

Results from this case study can be seen in Figure 3.5, where the steady-state cell population distribution obtained with $F(S)$ from equation (3.69) is compared to that when $F(S) \equiv 1$ (denoted the shear-insensitive population, *i.e.* when the fluid shear has no effect on the cells) for a range of upper fluid layer inlet fluxes $Q_{\mathrm{f,in}}$. From Figures 3.5(a) and (b) we see that for the lowest flux of $Q_{\mathrm{f,in}} = 0.1$, the cell volume fraction of the shear-sensitive (hereby

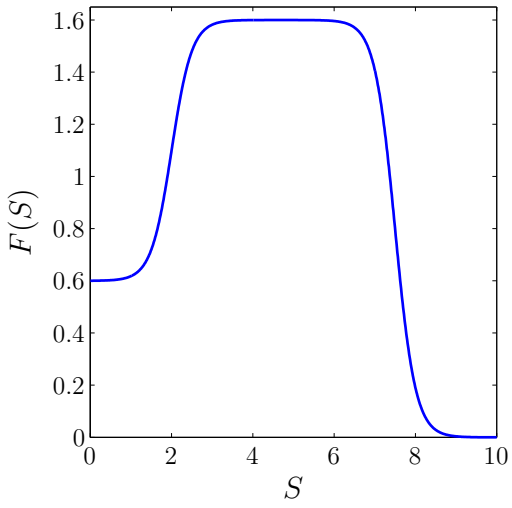

Figure 3.4: Plot of $F(S)$ in the case where increasing shear stress first enhances cell proliferation (equation (3.69)).

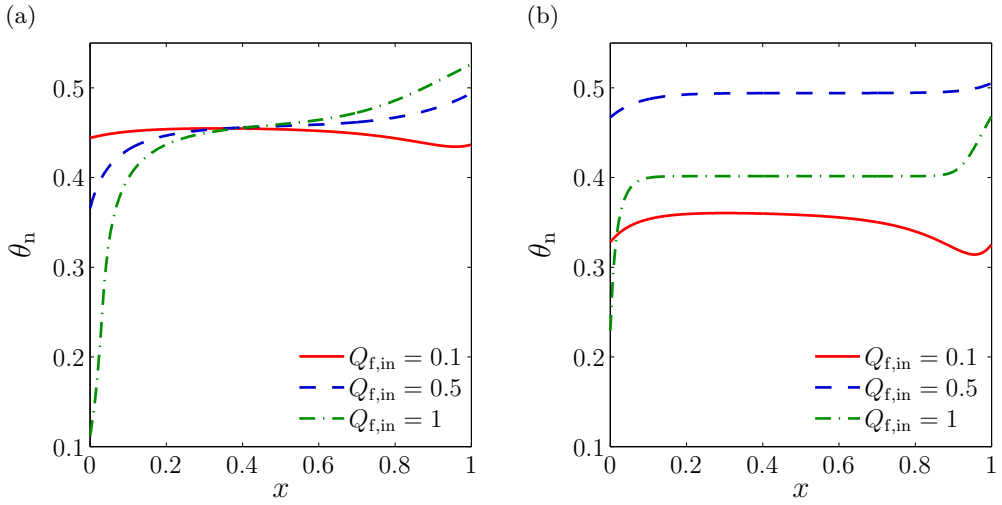

Figure 3.5: Plots of the steady-state cell volume fraction for a range of values of the upper fluid layer inlet flux $Q_{f,in}$, in the (a) shear-insensitive, and (b) shear-enhanced proliferation cases. The lumen inlet flux $Q_{l,in} = 0.1$, the cell layer height $h_3 = 1$, and other parameter values are as in Table 3.2.

called shear-enhanced) population is less than that of the shear-insensitive population for $0 < x < 1$, but then it increases above the shear-insensitive volume fraction once $Q_{f,in}$ is increased to 0.5. This corresponds to the shear stress exceeding the value (around 2.5) at which $F(S)$ is increased above 1 and is to be expected given our chosen form of $F(S)$. The increase in θ_n is observed across the whole bioreactor domain as a result of the relatively

small variation in θ_n (and hence θ_w) for $0 < x < 1$, which in turn means that there is little spatial variation in S. At the intermediate flux value ($Q_{f,in} = 0.5$) we also see that the shear-enhanced population becomes much more spatially uniform than the shear-insensitive cells. For the highest flux $Q_{f,in} = 1$, the shear-enhanced θ_n decreases at each point in x as the shear stress reaches levels which decrease the cell proliferation rate. In addition, greater up- and downstream variation is seen in θ_n for both populations due to advection, but the changes are less extreme for the shear-enhanced cells. Hence, overall, the effect of the shear stress is to 'smooth out' the cell population: an increase in θ_n corresponds to a decrease in θ_w, and thus a higher value of S. Thus regions where θ_n is relatively high experience a fluid shear stress sufficient to decrease $F(S)$ and hence the proliferation rate, whilst regions where θ_n is relatively low experience a lower shear stress and therefore increased proliferation rate.

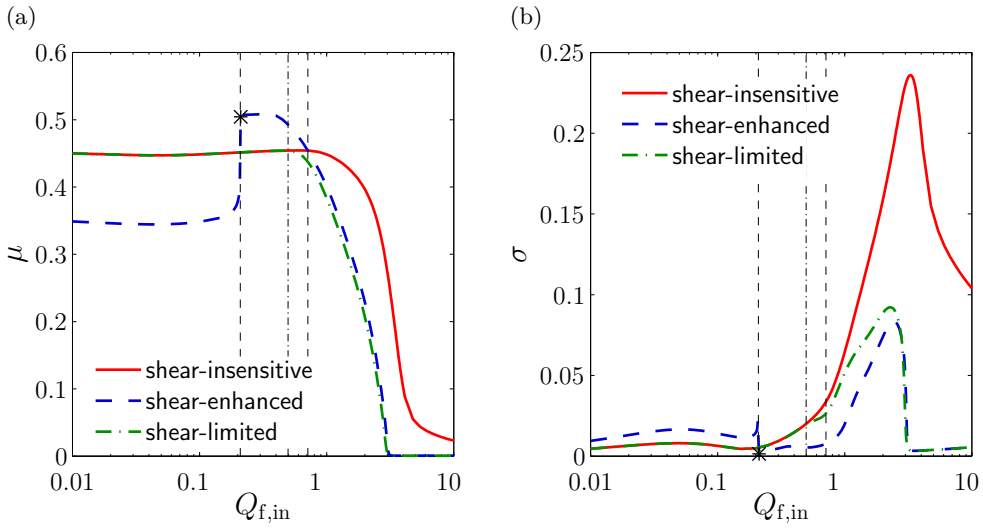

Figure 3.6: Plots of (a) the mean μ, and (b) the standard deviation σ of θ_n, for a range of $Q_{f,in}$ values in the shear-insensitive, shear-enhanced proliferation, and shear-limited proliferation cases. The vertical dashed lines indicate the optimal fluid flux range for the shear-enhanced case, within which the cell yield is higher than the shear-insensitive population, and the black asterisks denote the values of μ and σ at the optimal flux $Q_{f,opt}$. The vertical dash-dotted line indicates the critical fluid flux value for the shear-limited case, below which the shear-limited and shear-insensitive cases are indistinguishable (see text for details). The lumen inlet flux $Q_{l,in} = 0.1$, the cell layer height $h_3 = 1$, and other parameter values are as in Table 3.2.

The effect of shear on the cell yield and population uniformity can be seen more clearly in Figure 3.6, and the plots support the findings discussed above. The mean μ and standard deviation σ of θ_n are plotted for a range of values of $Q_{f,in}$, for the shear-enhanced and

shear-insensitive cases. Figure 3.6 shows that the shear-enhanced population has a lower yield and greater standard deviation than the shear-insensitive population for low $Q_{\mathrm{f,in}}$ values, but that this relationship is reversed when $Q_{\mathrm{f,in}}$ increases beyond a critical value just above 0.2. This switch corresponds to the critical value of S being reached, above which $F(S) > 1$ and the cell proliferation rate is enhanced. As can be seen in the graphs for both μ and σ, the change occurs relatively abruptly; this is due to the fact that (as mentioned above) there is relatively little variation in θ_{n} at this value of $Q_{\mathrm{f,in}}$ so the fluid shear stress (and therefore $F(S)$) is relatively constant along the domain. The standard deviation of the shear-enhanced population remains lower than the shear-insensitive population for all subsequent values of $Q_{\mathrm{f,in}}$, but the yield drops below that of the shear-insensitive population once another critical value of $Q_{\mathrm{f,in}}$ is reached, around 0.7, at which point the value of $F(S)$ falls below 1. Thus between these critical values (shown by vertical dashed lines in Figure 3.6), there is an optimum range of $Q_{\mathrm{f,in}}$ within which shear stress helps to promote both cell yield and population uniformity. Within this range, the most uniform population is obtained at the (optimal) inlet flux of $Q_{\mathrm{f,opt}} = 0.2137$. We also note that, for an inlet fluid flux above the first critical value, the shear-enhanced population is always more spatially uniform than the shear-insensitive population for a given yield.

3.4.2 Shear stress-limited proliferation

The second case study considers cells whose proliferation rate is inhibited by high levels of fluid shear stress (hereby denoted the shear-limited population). Cells which have been shown to be sensitive to shear stress in this way include smooth muscle cells [127] and certain types of endothelial cells (*e.g.* human aortic endothelial cells [70] and human umbilical vein endothelial cells [4]). As in the previous case, the exact form of the cells' shear stress dependence is unknown, and our choice of $F(S)$ and corresponding parameter values have been chosen so that our model captures the range of possible qualitative behaviours. We thus take $F(S)$ to be of the following form

$$F(S) = \frac{1}{2}\left[1 - \tanh(2S - 15)\right], \tag{3.70}$$

so that the cell proliferation rate decreases for sufficiently high fluid shear stress values (see Figure 3.7).

Figure 3.8 shows the steady-state results for θ_{n} obtained from this case study. For low values of $Q_{\mathrm{f,in}}$ (below 0.3), the shear stress has no effect on cell proliferation (as $F(S)$ is

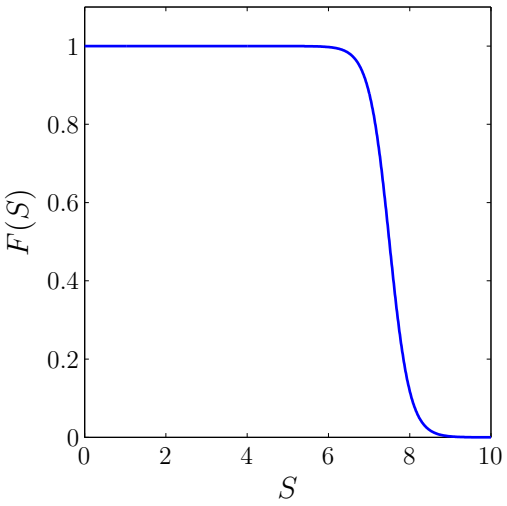

Figure 3.7: Plot of $F(S)$ in the case where increasing shear stress inhibits cell proliferation (equation (3.70)).

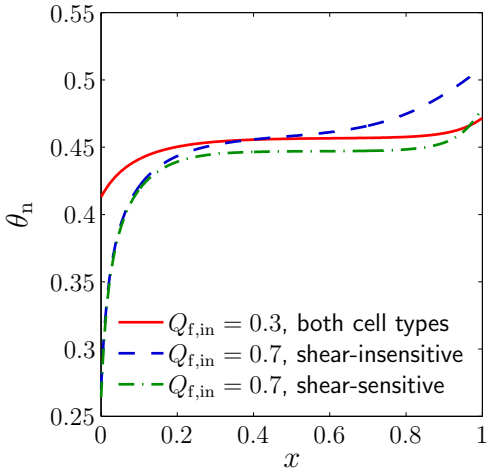

Figure 3.8: Plots of θ_n in the shear-limited proliferation and shear-insensitive cases, for a range of values of the upper fluid layer inlet flux $Q_{f,in}$. The lumen inlet flux $Q_{l,in} = 0.1$, the cell layer height $h_3 = 1$, and other parameter values are as in Table 3.2.

equal to 1) and thus the shear-limited and shear-insensitive population distributions are the same. As $Q_{f,in}$ is increased, however, there is increased bunching of cells downstream due to advection so that θ_w is lower in this region. This in turn increases S, and so the cells downstream experience a greater level of shear stress which is now high enough to decrease the proliferation rate of the shear-limited population. This results in the shear-limited population becoming more uniform than the shear-insensitive population. In contrast to the previous section, we note that regions of lower cell volume fraction are unchanged by

Table 3.3: Comparison of cell yield μ and standard deviation σ for the shear-limited and shear-insensitive populations, for a range of $Q_{\mathrm{f,in}}$ values.

	μ		
$Q_{\mathrm{f,in}}$	Stress-insensitive	Stress-limited	% change
0.4	0.4539	0.4539	-1.1×10^{-4}
0.6	0.4545	0.4501	-0.97
0.8	0.4531	0.4228	-6.7
1	0.4484	0.3837	-14.45
	σ		
$Q_{\mathrm{f,in}}$	Stress-insensitive	Stress-limited	% change
0.4	0.0147	0.0147	-0.002
0.6	0.0259	0.0226	-13.0
0.8	0.0415	0.0328	-20.92
1	0.0644	0.0515	-20.05

the shear sensitivity, as the fluid shear stress is lower there (due to the greater water volume fraction) and hence has no effect on proliferation rate. Thus the increased uniformity of the shear-limited population is at a cost of a lower overall volume fraction compared to the shear-insensitive cells. The plots of μ and σ in Figure 3.6 show that there is just one critical value of $Q_{\mathrm{f,in}}$ in this case (around 0.4, shown by the vertical dash-dotted line in Figure 3.6), below which the shear-limited and shear-insensitive cases are indistinguishable. Above this, the shear-limited population is more uniform than the shear-insensitive population, but also has a lower yield. In spite of this, Table 3.3 demonstrates that the percentage decrease in σ is (at least three times) larger than the percentage decrease in μ for $0.4 \lesssim Q_{\mathrm{f,in}} \lesssim 0.8$, and thus this provides a potentially optimal inlet fluid flux range if a uniform cell population is more important than a high cell yield.

3.4.3 Sensitivity to cell layer height

Finally, we investigate the sensitivity of our results to the cell layer height h_3, which may be prescribed experimentally. In each case we compare the steady-state cell volume fraction $\theta_{\mathrm{n}}(x,T)$, and note that, physically, larger values of h_3 correspond to greater overall cell numbers, and vice versa for smaller values of h_3. The cell layer height also affects the pressure gradient in the cell and upper fluid layers, since $\partial p_{\mathrm{w}}/\partial x$ depends linearly on $h_4^{-1} = [H - (1 + h_2 + h_3)]^{-1}$. Figures 3.9(a) and (b) show plots of the mean μ and stan-

dard deviation σ of θ_n for a range of values of $Q_{f,in}$ for a thinner cell layer than Figure 3.6, whilst Figures 3.9(c) and (d) show the corresponding plots for a thicker cell layer. In Figure 3.9(a), we see that the optimal ranges for $Q_{f,in}$ are now higher. The corresponding optimal inlet flux is also higher than before, with $Q_{f,opt} = 0.9955$. This results from the form of $|\partial p_w/\partial x|$, which decreases with h_3 as stated above. The shear stress therefore also decreases as h_3 decreases and so we need higher fluid fluxes in order to obtain the same behaviour from the cell populations as in §3.4.1 and §3.4.2. As expected, this trend is reversed in Figure 3.9(c) when h_3 takes the higher value of 1.5, with an optimal inlet flux in this case of $Q_{f,opt} = 0.0911$. In addition, for $h_3 = 1.5$ and $Q_{f,in}$ greater than around 1 we see that the cell population decreases significantly, no matter what the shear stress dependence. We therefore conclude that, for both shear-enhanced and shear-limited populations, a thinner cell layer makes the cell population less sensitive to the upper fluid layer inlet flux, as higher fluid fluxes can be used before compromising on cell yield, and vice versa for a thicker cell layer. In each case the maximum value of μ is very similar, and hence (as θ_n is independent of y) the higher the value of h_3, the higher the maximum achievable cell yield.

3.5 Conclusions

We have developed a multiphase model of fluid flow, solute transport, and cell distribution in a simplified HFMB. This extends the work presented in Chapter 2 by considering the alternative setup in which the cell-scaffold construct only partially occupies the ECS and there is an additional upper layer of free-flowing fluid. Fluid is pumped into the upper fluid layer via the upstream ECS port, and hence this region experiences higher flow rates compared to when fluid is only supplied at the lumen inlet. It is therefore hypothesised that this could result in a greater fluid shear stress in the cell layer which could have an important, and possibly beneficial, effect on the cell dynamics. This is confirmed from our model results which imply that the fluid shear stress in the cell layer is dependent on both the upper fluid layer inlet flux and cell layer height, both of which were varied as part of our investigation.

We have presented results from two different case studies. In the first (relevant to osteoblasts, chondrocytes, or endothelial progenitor cells), the cell proliferation rate was enhanced by fluid shear stress, but only up to a certain critical level. Results demonstrated that the shear-enhanced cell population required a certain minimum upper fluid layer inlet

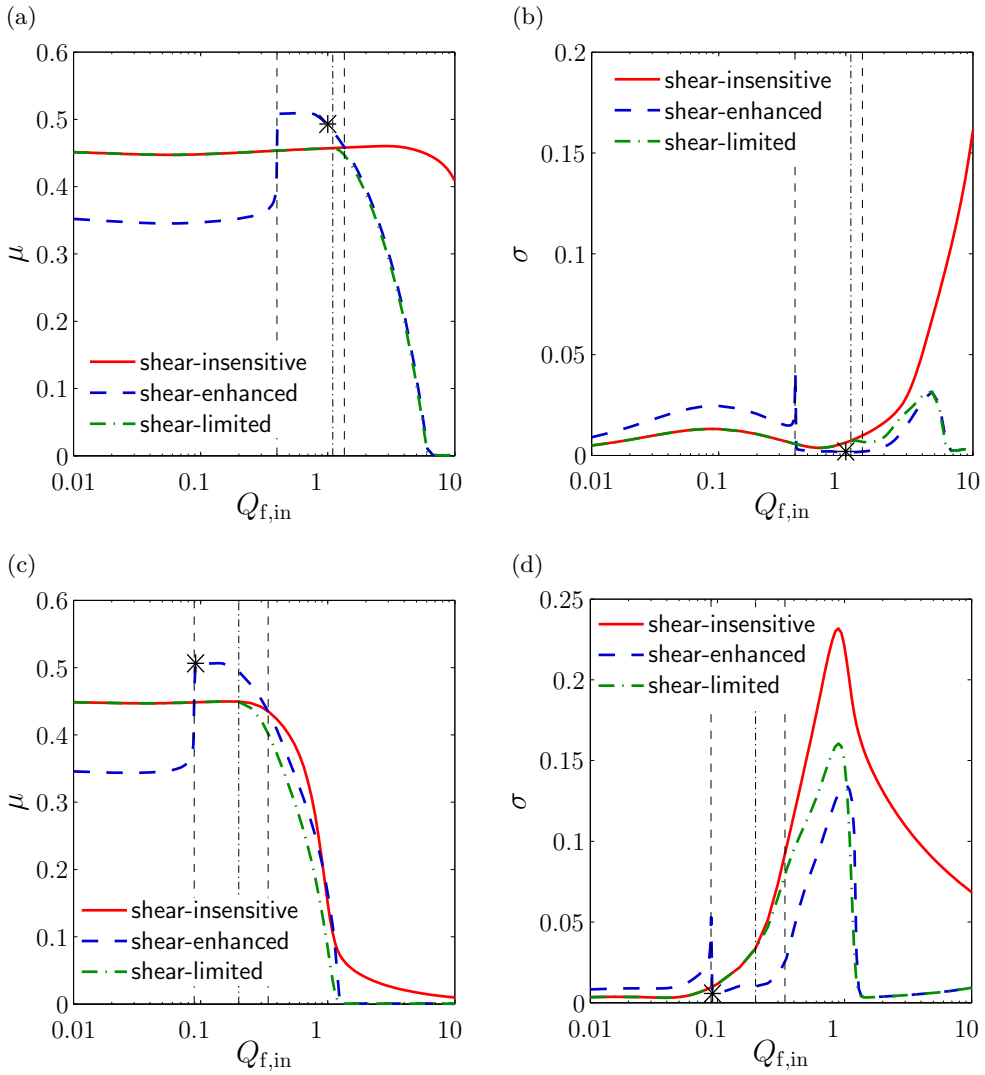

Figure 3.9: Plots of the mean μ and standard deviation σ of θ_{n}, for a range of $Q_{\mathrm{f,in}}$ values in the shear-insensitive, shear-enhanced proliferation, and shear-limited proliferation cases. For (a), (b) $h_3 = 0.5$; and for (c), (d) $h_3 = 1.5$. The vertical dashed lines indicate the optimal fluid flux range for the shear-enhanced case, and the black asterisks denote the values of μ and σ at the optimal flux $Q_{\mathrm{f,opt}}$. The vertical dash-dotted line indicates the critical fluid flux value for the shear-limited case (see text for details). The lumen inlet flux $Q_{\mathrm{l,in}} = 0.1$ and other parameter values are as in Table 3.2.

flux in order to reach yields comparable to the shear-insensitive population. Once inlet fluid fluxes were reached which resulted in fluid shear within the 'enhancing' range, however, the mechanosensitive population had a higher yield and was more uniform than the shear-insensitive cells. This uniformity persisted even once the shear levels became detrimental to the proliferation rate and the yield decreased.

In the second case study, fluid shear was assumed to have no effect on cell proliferation until a critical value was surpassed, after which it decreased the proliferation rate. This could be applicable to smooth muscle cells, or certain types of endothelial cells. Results again showed that the mechanosensitive cell population was more uniform than the shear-insensitive cells, but always had a lower cell yield. However, an ideal inlet fluid flux range could again be found, within which the mechanosensitive population was more uniform than the shear-insensitive population and the yield had not yet been significantly compromised.

Finally, we considered the effect of the cell layer height on these results, and found that a thinner cell layer experiences a lower level of shear stress than a thicker layer, and hence can withstand higher flow rates.

The results presented in this chapter are qualitative in nature, demonstrating the range of expected behaviours in each situation. In particular, the functional forms for $F(S)$ are constitutive and relatively simple, having been chosen to clearly demonstrate the possible effects of mechanotransduction on cell distribution in a HFMB. Any choice of $F(S)$ would need experimental validation to be applied to a specific experimental setup. However, the model framework developed here is extremely flexible and permits interrogation of different candidates for the constitutive laws, thus readily allowing its application to a particular cell population. We discuss in more detail the limitations of our modelling and relevant future work in Chapter 6.

Chapter 4

Three- and four-layer multiphase models: two cell populations

4.1 Introduction

In this thesis so far we have focussed on the yield and spatial distribution of a population of a single cell type in a HFMB, and how these measures are affected by various flow regimes and solute concentrations. This is relevant to, for instance, cell expansion experiments in which only one cell type is present. However, differentiation of one cell type into another is also required in tissue engineering setups (examples include differentiation of bone marrow mesenchymal stem cells into neuronal cells [140] and chondrocytes [93]). In this chapter we therefore extend the multiphase models considered thus far to include two cell populations, one undifferentiated and one differentiated. We also include the concentration of a single solute, which is taken to be a growth factor. This allows us to model cell differentiation induced both chemically (via a growth factor) and mechanically (via fluid shear stress), in the 3- and 4-layer HFMB setups of Chapters 2 and 3, respectively. By varying the inlet fluid fluxes and solute concentrations, we investigate their effect on the yield of differentiated cells, and the percentage of cells which are of the differentiated phenotype. This allows us to seek operating conditions which result in a high yield and percentage of differentiated cells, but also do not consume too much expensive growth factor. We show the potential of our model, once validated, to determine the experiment end time, inlet concentration, and inlet fluid fluxes which are 'optimal' given the relative importance of cell percentage, cell yield, and growth factor consumption. We note that differentiation of certain cell types has been found to be stimulated by fluid shear stress alone, without the need for growth factors (for instance, osteoblasts [13, 74] and endothelial cells [118, 184]). However, as we have chosen

to make growth factor consumption the focus of this chapter we do not consider this case here.

4.1.1 Chapter outline

We begin by describing the model setup in §4.2, again presenting the governing equations and boundary conditions in a simplified modelling domain. We discuss relevant dimensional and dimensionless parameter values in §4.3.1 and non-dimensionalise the governing equations and boundary conditions in §4.3.2, before considering a reduction of the 4-layer model in §4.3.3 and §4.3.4 that is appropriate when the aspect ratio of the modelling domain is small. In §4.3.5 we present the corresponding reduced 3-layer model. Numerical results for both the 3-layer and 4-layer models are presented in §4.4. In §4.4.1 we investigate the case where cell differentiation is dependent on growth factor concentration alone, whilst in §4.4.2 we consider differentiation dependent on both growth factor concentration and fluid shear stress. These dependences are incorporated via the constitutive laws for the cell mass transfer functions. Finally, we discuss our findings and conclude in §4.5.

4.2 Model description

As in Chapters 2 and 3 we model a HFMB in two-dimensional, Cartesian coordinates (x, y), motivated by taking a cross section of a single bioreactor module. In the 3-layer model, we consider the flow regime in which the upstream ECS ports are closed (as depicted in Figure 2.1) and fluid is pumped into the lumen inlet only. In the 4-layer model, we consider the regime shown in Figure 3.2, in which fluid is pumped in through both the lumen inlet and open upstream ECS ports.

In the multiphase layer (the ECS for the 3-layer setup or the cell layer for the 4-layer setup), we take the simplest mechanical model possible to gain insight into the effects caused by the differentiation stimuli. As in Chapters 2 and 3, we assume for both cell populations that the drag between the water and cells is much smaller than that between the cells and scaffold, or water and scaffold, and that the cells cannot leave the scaffold and so remain in the ECS (3-layer model) or cell layer (4-layer model). We additionally assume that there are no tractions or drag between the two cell phases. For simplicity and to focus on cell differentiation only, we neglect the effect of chemotaxis on both cell populations. We denote the volume fraction of the undifferentiated cell population by θ_{u}

and that of the differentiated cell population by θ_{d}. Corresponding parameters relating to the undifferentiated and differentiated populations are denoted with subscripts u and d respectively, and all other notation is unchanged from previous models. The scaffold is again assumed to be rigid and inert, with its volume fraction θ_{s} constant in space and time.

4.2.1 Simplified modelling domain

In this chapter we move straight to the simplified two-dimensional modelling domain, arguing as in Chapters 2 and 3 that by modelling the dynamics in the central region of the bioreactor only, excluding the ECS ports, we can make analytical progress whilst still capturing key features of the system. We also exploit the symmetry of this region and model the dynamics in the upper half of the domain only. The simplified domains for both the 3- and 4-layer models are depicted in Figure 4.1. Note that here H always denotes the height of the bioreactor, and so is given by $H = h_1 + h_2 + h_3$ in the 3-layer case, and by $H = h_1 + h_2 + h_3 + h_4$ in the 4-layer setup.

4.2.2 Governing equations

In the lumen, porous membrane, and (for the 4-layer system) upper fluid layer, the equations for fluid flow and mass transport are unchanged from the single cell population models in Chapters 2 and 3. We therefore do not present them here, but introduce them in dimensionless form in §4.3.3 once we have carried out our non-dimensionalisation. The governing equations in the multiphase region (either the whole ECS or the cell layer), however, are presented below. They are easily obtained from the generalised model in §1.4 in the case where there are two active cell phases.

In the ECS (3-layer system) or the cell layer (4-layer system) we begin with the no voids condition, that is, $\theta_{\mathrm{u}} + \theta_{\mathrm{d}} + \theta_{\mathrm{w}} + \theta_{\mathrm{s}} = 1$. Conservation of mass for each of the active phases is

$$\frac{\partial \theta_i}{\partial t} + \nabla \cdot (\theta_i \mathbf{u}_i) = J_i \quad (i = \mathrm{u}, \mathrm{d}), \qquad \frac{\partial \theta_{\mathrm{w}}}{\partial t} + \nabla \cdot (\theta_{\mathrm{w}} \mathbf{u}_{\mathrm{w}}) = J_{\mathrm{w}}, \tag{4.1}$$

where the mass transfer functions J_{u}, J_{d}, and J_{w} will be kept general for the time being, and only assumed to be functions of θ_{u}, θ_{d}, θ_{w}, the fluid shear stress (through $\partial p_{\mathrm{w}}/\partial x$ as in Chapter 3), and the growth factor concentration c_{w}. As before we assume conservation of mass so that $J_{\mathrm{u}} + J_{\mathrm{d}} + J_{\mathrm{w}} = 0$.

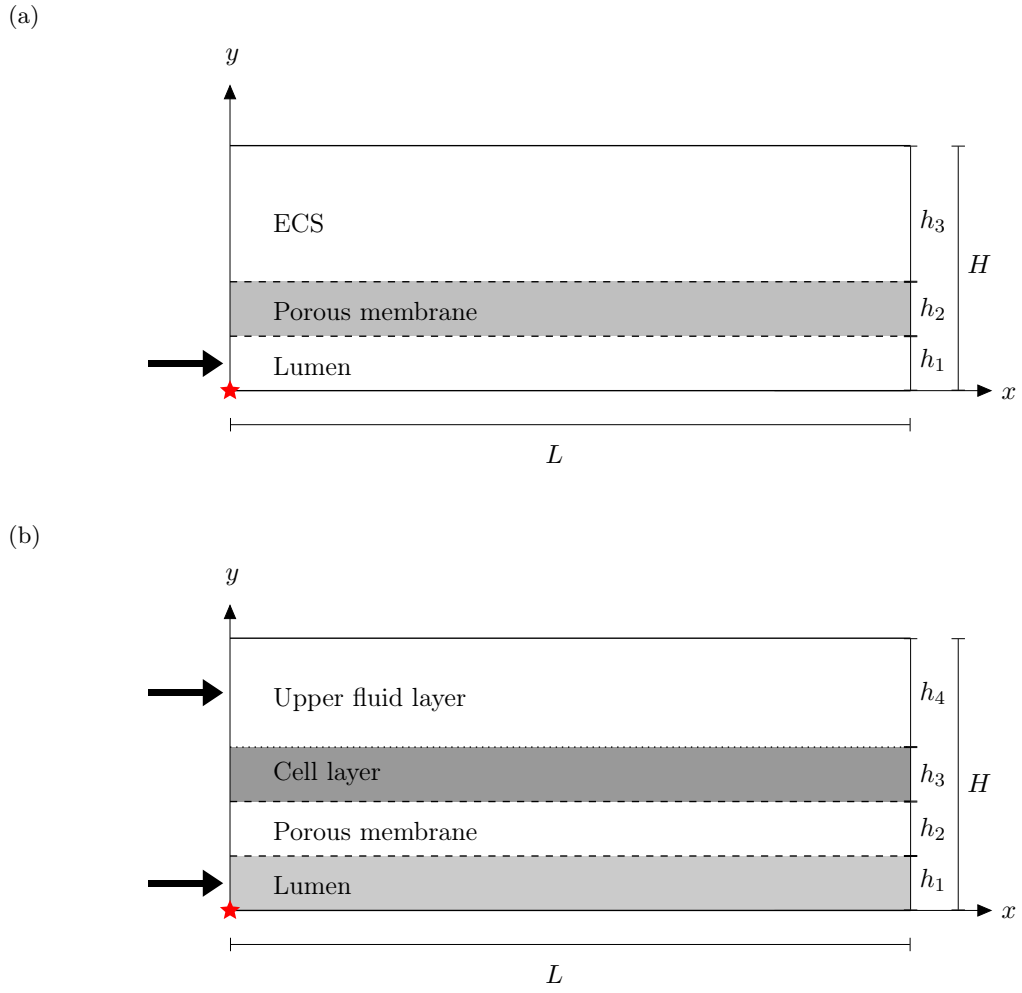

Figure 4.1: Simplified modelling domains for (a) the 3-layer model, and (b) the 4-layer model, with the x-axis running along the lumen centreline (not to scale). In each diagram the red star denotes the origin $(x, y) = (0, 0)$, and the solid black arrows denote the direction of the imposed fluid flux into the lumen and (in (b)) the upper fluid layer.

Conservation of momentum for each phase is of the form

$$-\theta_i \nabla p_\mathrm{w} - \nabla\left(\theta_i \Pi_i\right) + \nabla \cdot \left(\theta_i \boldsymbol{\tau}_i\right) + \psi_\mathrm{ns}\theta_\mathrm{s}\nabla\theta_i - \gamma_\mathrm{ns}\theta_i\theta_\mathrm{s}\mathbf{u}_i = \mathbf{0} \quad (i = \mathrm{u}, \mathrm{d}), \tag{4.2}$$

$$-\theta_\mathrm{w}\nabla p_\mathrm{w} - \gamma_\mathrm{ws}\theta_\mathrm{w}\theta_\mathrm{s}\mathbf{u}_\mathrm{w} = \mathbf{0}, \tag{4.3}$$

where we have substituted in for the cell stress tensors $\boldsymbol{\sigma}_\mathrm{u}$ and $\boldsymbol{\sigma}_\mathrm{d}$, the reduced intraphase pressures p_u and p_d, and the interphase forces $\mathbf{f}_{ij}$ $(i, j = \mathrm{u}, \mathrm{d}, \mathrm{w}, \mathrm{s},\ i \neq j)$ from §1.4. We note that they respectively take the same forms as $\boldsymbol{\sigma}_\mathrm{n}$, p_n, and $\mathbf{f}_{ij}$ $(i, j = \mathrm{n}, \mathrm{w}, \mathrm{s},\ i \neq j)$ as presented in Chapter 2. In the above we have also assumed that the two cell populations have the same effective viscosity μ_n. We note that this assumption could easily be relaxed,

and would just lead to the inclusion of an extra parameter representing the ratio of the two effective viscosities in the dimensionless system. We have further assumed that the extra pressure term ψ_{ns} and cell-scaffold drag coefficient γ_{ns} are the same for each cell population.

We recall from §1.4 that the extra pressure ψ_{ns} due to cell-scaffold tractions is assumed to be a negative constant, so that

$$\psi_{\mathrm{ns}} = -\eta. \tag{4.4}$$

As chemotaxis has been neglected in this model, the extra intraphase pressure term Π_i ($i = \mathrm{u}, \mathrm{d}$) for each cell population just consists of the term accounting for cell-cell interactions, first introduced in §2.3.3:

$$\Pi_i = \theta_i \left(-\nu + \frac{\delta_{\mathrm{a}} \theta_i}{1 - \theta_{\mathrm{s}} - \theta_i - \theta_j} \right) \quad (i, j = \mathrm{u}, \mathrm{d},\ i \neq j), \tag{4.5}$$

where ν and δ_{a} are constants and we have again assumed that they are the same for each cell population.

Finally, we model mass transport in the multiphase layer with the same equation employed previously, namely

$$\frac{\partial}{\partial t} (\theta_{\mathrm{w}} c_{\mathrm{w}}) + \nabla \cdot (\theta_{\mathrm{w}} c_{\mathrm{w}} \mathbf{u}_{\mathrm{w}}) = D \nabla \cdot (\theta_{\mathrm{w}} \nabla c_{\mathrm{w}}) + \mathcal{R}, \tag{4.6}$$

for some reaction term $\mathcal{R}$ which may depend on any of θ_{u}, θ_{d}, and c_{w}. We note here that growth factors are proteins, which are typically much larger than nutrient molecules such as oxygen which have featured in our models thus far. Hence it could be argued that a Fickian diffusion term is unsuitable, and an approach taking into account multi-component effects (*e.g.* interactions between solute molecules) would be more appropriate. Abdullah and Das included these effects via Maxwell-Stefan equations in their model of nutrient transport in a HFMB [2], and found that they could be of significance in reducing mass transfer in certain experimental configurations, namely sufficiently high inlet concentrations, solute molecular sizes, and ECS and fibre wall thicknesses. However, inclusion of such interactions necessitates a much more complicated modelling framework, involving additional parameter values which are currently unknown or difficult to interpret physically. We therefore neglect these effects in our first differentiation model and assume a Fickian diffusion term for the growth factor concentration, an approach also taken in, for example, [21, 26, 136].

It remains to prescribe constitutive forms for J_{u}, J_{d}, and $\mathcal{R}$; as in previous chapters we keep our analysis general and delay their specification until results are obtained in §4.4.

4.2.3 Boundary conditions

The boundary conditions for the water and solute concentration on the lumen centreline, interfaces between layers, and bioreactor top are unchanged from Chapters 2 and 3. We introduce these in §4.3.3 after we have non-dimensionalised, along with the up- and downstream conditions at the inlets and outlets.

Here we present only the boundary conditions applied to the cell phases, which are assumed to be the same as for the corresponding single cell population models. Thus on the membrane/ECS (3-layer model) or membrane/cell layer (4-layer model) interface we have no flux and no slip of cells,

$$\mathbf{u}_i = \mathbf{0} \quad (i = \mathrm{u}, \mathrm{d}) \qquad \text{on} \quad y = h_1 + h_2. \tag{4.7}$$

In addition, on the bioreactor top (3-layer model) we also have no flux and no slip of cells,

$$\mathbf{u}_i = \mathbf{0} \quad (i = \mathrm{u}, \mathrm{d}) \qquad \text{on} \quad y = H, \tag{4.8}$$

and on the cell layer/upper fluid layer interface (4-layer model) we impose no flux and no shear stress on the cell phase,

$$v_i = 0, \qquad \mathbf{n}_\mathrm{e} \cdot \boldsymbol{\sigma}_i \cdot \mathbf{t}_\mathrm{e} = 0 \quad (i = \mathrm{u}, \mathrm{d}) \qquad \text{on} \quad y = H - h_4, \tag{4.9}$$

where $\mathbf{n}_\mathrm{e}$ and $\mathbf{t}_\mathrm{e}$ are, respectively, the unit normal (positive y-direction) and unit tangent to the cell layer/upper fluid layer interface.

We also impose no flux of both cell populations out of the multiphase region at $x = 0, L$, and introduce this along with the other up- and downstream conditions as required in §4.3.3.

4.3 Model reduction

In this section, we begin by discussing dimensional and dimensionless parameter values before non-dimensionalising and reducing the 4-layer model to a coupled system of three PDEs. We then summarise the corresponding system of four coupled PDEs for the 3-layer model.

4.3.1 Parameter values

We take the majority of the dimensional parameter values to be the same as in our previous multiphase models, with a few exceptions. New dimensional parameter values can be found

in Table 4.1 (for others see Table 2.1) and all dimensionless parameters required in this chapter in Table 4.2. The key difference between this model and those of Chapters 2 and 3 is that the solute of interest in this model is a growth factor. These molecules are much larger than oxygen, and we take a representative value for D of 2×10^{-10} m^2 s^{-1}, an estimate for the diffusion coefficient for vascular endothelial growth factor (VEGF) in aqueous solution [99]. This results in a reduced Péclet number of 0.0102, so that $\varepsilon^2 \ll \varepsilon^2 \mathrm{Pe} \ll 1$, and hence we are in a different distinguished limit to Chapters 2 and 3 in the system of equations governing the solute concentration. The typical concentration used to set the scaling C^* is larger for growth factors than for oxygen; we choose $C^* = 7.69$ mol m^{-3}, an example inlet concentration of bone morphogenetic protein 2 human growth factor (BMP-2), following discussions with our experimental collaborators [1][1]. In §4.4 we then investigate the effect of varying the inlet growth factor concentration on the yield of the cell populations by considering a range of values of c_{in}. We correspondingly choose the reaction scale $R^* = C^* D/(\varepsilon L^2)$ so that $\mathcal{R}$ appears in the solute equations at $\mathrm{O}(\varepsilon)$, and as a result solute uptake appears in our leading-order model (see §4.3.3).

Table 4.1: Dimensional parameters.

Parameter	Dimensional value and units	Ref.
D	2×10^{-10} m^2 s^{-1}	[99]
C^*	7.69 mol m^{-3}	†
T	2.42×10^6 s	†

† Values based on estimations by our experimental collaborators.

Instead of considering steady-state results in this chapter, we fix a maximum end time T, and look at the percentage and yield of cells which are of the differentiated type within this time range. A typical length of the 'differentiation phase' of an experiment is 2-4 weeks [1], and so we set T to be the upper value of 4 weeks, corresponding to a dimensionless end time of 0.2477 (given the timescale L/U^* introduced in §4.3.2).

The dimensionless values of the constants appearing in the drag and pressure terms for the cell populations, ν, δ_{a}, and η, are set to be the same as the single cell population models in Chapters 2 and 3, as are the dimensionless cell-scaffold and water-scaffold drag

[1] We note that the values for D and C^* are for different growth factors; this is due to a scarcity of data as these parameters are rarely quantified experimentally.

Table 4.2: Dimensionless parameters used in this chapter, along with any bounds imposed either physically or by the asymptotic analysis.

Parameter	Definition	Value	Restriction	Ref.
$\hat{h}_2$	$h_2/(\varepsilon L)$	1	$\hat{h}_2 > 0$	-
$\hat{h}_3$	$h_3/(\varepsilon L)$	3[a]	$\hat{h}_3 > 0$	-
$\hat{h}_3 + \hat{h}_4$	$(h_3 + h_4)/(\varepsilon L)$	3[b]	$\hat{h}_3,\ \hat{h}_4 > 0$	-
θ_s	-	0.4	$0 < \theta_\mathrm{s} < 1$	[92]
ε	h_1/L	2×10^{-3}	$0 < \varepsilon \ll 1$	-
λ	$\mu_\mathrm{w}/(\varepsilon\mu_\mathrm{n})$	1	$\varepsilon \ll \lambda \ll 1/\varepsilon$	-
$\varepsilon^2\mathrm{Pe}$	$\varepsilon L U^*/(\lambda D)$	0.0102	$\varepsilon^2 \ll \varepsilon^2\mathrm{Pe} \ll 1$	-
$\varepsilon^2\mathrm{Re}$	$\varepsilon\rho_\mathrm{w} L U^*/(\lambda\mu_\mathrm{w})$	2.05×10^{-6}	$\varepsilon^2\mathrm{Re} \ll 1$	-
ϕ_m	-	0.77	$0 < \phi_\mathrm{m} < 1$	[109]
κ_m	$k_\mathrm{m}/(\lambda\varepsilon^5 L^2)$	2.1	$\varepsilon \ll \kappa_\mathrm{m} \ll 1/\varepsilon$	-
$\hat{Q}_{i,\mathrm{in}}\ (i = \mathrm{l}, \mathrm{f})$	$\lambda Q_{i,\mathrm{in}}/(LU^*)$	0.01 - 10	$\varepsilon \ll \hat{Q}_{i,\mathrm{in}} \ll 1/\varepsilon$	-
$\hat{\nu}$	$\lambda\varepsilon^3 L\nu/(\mu_w U^*)$	0.3	$\varepsilon \ll \hat{\nu} \ll 1/\varepsilon$	[123]
$\hat{\delta}_\mathrm{a}$	$\lambda\varepsilon^3 L\delta_\mathrm{a}/(\mu_w U^*)$	0.1	$\varepsilon \ll \hat{\delta}_\mathrm{a} \ll 1/\varepsilon$	[123]
$\hat{\eta}$	$\lambda\varepsilon^3 L\eta/(\mu_w U^*)$	0.3	$\varepsilon \ll \hat{\eta} \ll 1/\varepsilon$	[123]
ζ_ns	$\gamma_\mathrm{ns} L^2\lambda\varepsilon^3/\mu_\mathrm{w}$	1	$\varepsilon \ll \zeta_\mathrm{ns} \ll 1/\varepsilon$	-
ζ_ws	$\gamma_\mathrm{ws} L^2\lambda\varepsilon^3/\mu_\mathrm{w}$	0.1	$\varepsilon \ll \zeta_\mathrm{ws} \ll 1/\varepsilon$	-
$\hat{\Gamma}_\mathrm{nw}$	$L\Gamma_\mathrm{nw}/U^*$	6	$\varepsilon \ll \hat{\Gamma}_\mathrm{nw} \ll 1/\varepsilon$	-
$\hat{\Gamma}_\mathrm{wn}$	$L\Gamma_\mathrm{wn}/U^*$	4.04	$\varepsilon \ll \hat{\Gamma}_\mathrm{wn} \ll 1/\varepsilon$	-
$\hat{\Gamma}_\mathrm{ud}$	$L\Gamma_\mathrm{ud}/U^*$	70	$\varepsilon \ll \hat{\Gamma}_\mathrm{nw} \ll 1/\varepsilon$	-
$\hat{\Gamma}_\mathrm{R1}$	$\varepsilon L^2\Gamma_\mathrm{R1}/D$	1	$\varepsilon \ll \hat{\Gamma}_\mathrm{R1} \ll 1/\varepsilon$	-
$\hat{K}$	K/C^*	0.4	$\varepsilon \ll \hat{K} \ll 1/\varepsilon$	-
$\hat{c}_\mathrm{in}$	c_in/C^*	0.1 - 1	$\varepsilon \ll \hat{c}_\mathrm{in} \ll 1/\varepsilon$	-
$\hat{P}_\mathrm{dwn}$	$\varepsilon^2 L(P_\mathrm{dwn} - p_\mathrm{atm})/(\mu_\mathrm{n} U^*)$	2.5	$\varepsilon \ll \hat{P}_\mathrm{d} \ll 1/\varepsilon$	-
$\hat{T}$	$U^* T/L$	0.2477	-	-

[a] 3-layer model.

[b] 4-layer model.

parameters ζ_ns and ζ_ws. In the 4-layer model we once again take the cell layer height h_3 (and therefore also h_4) to be of O(1).

In the case studies that follow in §4.4, we also need to specify parameters within the constitutive forms for J_u, J_d, and $\mathcal{R}$. The cell death rate Γ_wn (assumed for simplicity to be the same for both populations) is taken to have the same dimensional value as before, corresponding to a dimensionless value of 4.04. The cell proliferation rate Γ_nw is also assumed to be the same for both populations and is taken to have a lower dimensional value than before (see below for the exact choice of value), as would be expected in the differentiation phase of an experiment [1].

The remaining parameters are the cell differentiation rate Γ_ud, the solute uptake rate

Γ_{R1}, and the Michaelis-Menten uptake constant K. Given that experimental data for these parameters are not available, their dimensionless equivalents (which are defined in Table 4.2) are chosen to be of O(1) for illustrative purposes, so that we retain as many effects as possible in our leading-order model. In addition, values are assigned according to two experimental observations [1]: (1) the cell differentiation rate is much faster than the cell proliferation rate (in the differentiation phase of experiments which we are modelling), and (2) at the end of an experiment almost all (98-99%) cells are of the differentiated type. To find values for Γ_{ud}, Γ_{R1}, Γ_{nw}, and K such that our model satisfies the second observation, we first set the other parameters whose values can vary to the following fixed values: $Q_{\mathrm{l,in}} = 1$, $Q_{\mathrm{f,in}} = 0.1$, $c_{\mathrm{in}} = 1$. The dimensionless values for Γ_{nw}, Γ_{ud}, Γ_{R1}, and K given in Table 4.2 were then chosen so that (to two significant figures) 99% of cells were of the differentiated type at the maximum end time T when solving the case study from §4.4.1.

4.3.2 Non-dimensionalisation

With the exception of the reaction scale R^* (as discussed in §4.3.1), we non-dimensionalise with the same scalings as in Chapters 2 and 3, assuming that the two cell populations have the same velocity scale:

$$\begin{gathered}
x = L\hat{x}, \qquad y = \varepsilon L\hat{y}, \qquad t = \frac{L}{U^*}\hat{t}, \qquad h_i = \varepsilon L\hat{h}_i \quad (i = 2,3,4), \qquad H = \varepsilon L\hat{H}, \\
u_i = \frac{\mu_{\mathrm{n}}}{\mu_{\mathrm{w}}}U^*\hat{u}_i, \quad v_i = \frac{\varepsilon\mu_{\mathrm{n}}}{\mu_{\mathrm{w}}}U^*\hat{v}_i \quad (i = \mathrm{l},\mathrm{f}), \qquad u_i = U^*\hat{u}_i, \quad v_i = \varepsilon U^*\hat{v}_i \quad (i = \mathrm{m},\mathrm{w},\mathrm{u},\mathrm{d}), \\
p_i = p_{\mathrm{atm}} + \frac{\mu_{\mathrm{n}}U^*}{\varepsilon^2 L}\hat{p}_i \quad (i = \mathrm{l},\mathrm{m},\mathrm{w},\mathrm{f}), \qquad \Pi_i = \frac{\mu_{\mathrm{n}}U^*}{\varepsilon^2 L}\hat{\Pi}_i \quad (i = \mathrm{u},\mathrm{d}), \qquad \psi_{\mathrm{ns}} = \frac{\mu_{\mathrm{n}}U^*}{\varepsilon^2 L}\hat{\psi}_{\mathrm{ns}}, \\
c_i = C^*\hat{c}_i \quad (i = \mathrm{l},\mathrm{m},\mathrm{w},\mathrm{f}), \qquad \mathcal{R} = \frac{DC^*}{\varepsilon L^2}\hat{\mathcal{R}}, \qquad J_i = \frac{U^*}{L}\hat{J}_i \quad (i = \mathrm{u},\mathrm{d}).
\end{gathered} \tag{4.10}$$

Substituting these scalings into just the multiphase equations for now (and dropping hats on dimensionless variables) yields for the cell phases

$$\frac{\partial\theta_i}{\partial t} + \frac{\partial}{\partial x}(\theta_i u_i) + \frac{\partial}{\partial y}(\theta_i v_i) = J_i \quad (i = \mathrm{u},\mathrm{d}), \tag{4.11}$$

and

$$-\theta_i\frac{\partial p_\mathrm{w}}{\partial x}-\frac{\partial}{\partial x}\left(\theta_i\Pi_i\right)+\frac{2\varepsilon^2}{3}\frac{\partial}{\partial x}\left[\theta_i\left(2\frac{\partial u_i}{\partial x}-\frac{\partial v_i}{\partial y}\right)\right]$$
$$+\frac{\partial}{\partial y}\left[\theta_i\left(\frac{\partial u_i}{\partial y}+\varepsilon^2\frac{\partial v_i}{\partial x}\right)\right]+\psi_\mathrm{ns}\theta_\mathrm{s}\frac{\partial\theta_i}{\partial x}-\zeta_\mathrm{ns}\theta_i\theta_\mathrm{s}u_i=0\quad(i=\mathrm{u},\mathrm{d}),\tag{4.12}$$

$$-\theta_i\frac{\partial p_\mathrm{w}}{\partial y}-\frac{\partial}{\partial y}\left(\theta_i\Pi_i\right)+\varepsilon^2\frac{\partial}{\partial x}\left[\theta_i\left(\frac{\partial u_i}{\partial y}+\varepsilon^2\frac{\partial v_i}{\partial x}\right)\right]$$
$$+\frac{2\varepsilon^2}{3}\frac{\partial}{\partial y}\left[\theta_i\left(2\frac{\partial v_i}{\partial y}-\frac{\partial u_i}{\partial x}\right)\right]+\psi_\mathrm{ns}\theta_\mathrm{s}\frac{\partial\theta_i}{\partial y}-\varepsilon^2\zeta_\mathrm{ns}\theta_i\theta_\mathrm{s}v_i=0\quad(i=\mathrm{u},\mathrm{d}),\tag{4.13}$$

and for the water phase

$$\begin{gathered}\frac{\partial\theta_\mathrm{w}}{\partial t}+\frac{\partial}{\partial x}\left(\theta_\mathrm{w}u_\mathrm{w}\right)+\frac{\partial}{\partial y}\left(\theta_\mathrm{w}v_\mathrm{w}\right)=J_\mathrm{w}=-(J_\mathrm{u}+J_\mathrm{d}),\\ -\theta_\mathrm{w}\frac{\partial p_\mathrm{w}}{\partial x}-\zeta_\mathrm{ws}\theta_\mathrm{w}\theta_\mathrm{s}u_\mathrm{w}=0,\qquad -\theta_\mathrm{w}\frac{\partial p_\mathrm{w}}{\partial y}-\varepsilon^2\zeta_\mathrm{ws}\theta_\mathrm{w}\theta_\mathrm{s}v_\mathrm{w}=0,\end{gathered}\tag{4.14}$$

where the dimensionless parameters have the same definitions as before, $\zeta_\mathrm{ns}=\gamma_\mathrm{ns}L^2\varepsilon^2/\mu_\mathrm{n}$ being the dimensionless cell-scaffold drag for each population. The dimensionless boundary conditions for the cell phases are

$$u_i=v_i=0\quad(i=\mathrm{u},\mathrm{d})\qquad\text{on } y=1+h_2,\tag{4.15}$$

$$u_i=v_i=0\quad(i=\mathrm{u},\mathrm{d})\qquad\text{on } y=H,\tag{4.16}$$

$$v_i=0,\qquad\frac{\partial u_i}{\partial y}+\varepsilon^2\frac{\partial v_i}{\partial x}=0\quad(i=\mathrm{u},\mathrm{d})\qquad\text{on } y=H-h_4,\tag{4.17}$$

where (4.16) applies to the 3-layer model and (4.17) to the 4-layer model.

4.3.3 Derivation of the reduced 4-layer model

We now present the asymptotic analysis for the 4-layer model, which is similar to that in Chapter 3 and reduces it to a coupled system of three PDEs which can be solved numerically. The 3-layer model can be reduced in an analogous way to the single cell population model from Chapter 2, and we therefore omit the detail but summarise the resulting system of four coupled PDEs in §4.3.5.

We expand all dependent variables in powers of the lumen aspect ratio ε, setting $u_\mathrm{l}\sim u_{\mathrm{l}_0}+\varepsilon u_{\mathrm{l}_1}+\varepsilon^2u_{\mathrm{l}_2}+\ldots$ and similarly for the remaining velocities v_l, u_i, v_i $(i=\mathrm{m},\mathrm{w},\mathrm{u},\mathrm{d},\mathrm{f})$, the reduced pressures p_i $(i=\mathrm{l},\mathrm{m},\mathrm{w},\mathrm{f})$, the concentrations c_i $(i=\mathrm{l},\mathrm{m},\mathrm{w},\mathrm{f})$, and the volume fractions θ_u, θ_d, and θ_w. We then collect coefficients of ε^0 to obtain the leading-order system in each layer. Beginning in the lumen $(0<y<1)$ and omitting the subscript 0 from the

leading-order variables, the O(1) equations are

$$\frac{\partial u_\mathrm{l}}{\partial x}+\frac{\partial v_\mathrm{l}}{\partial y}=0, \qquad \frac{\partial^2 u_\mathrm{l}}{\partial y^2}=\frac{\partial p_\mathrm{l}}{\partial x}, \qquad \frac{\partial p_\mathrm{l}}{\partial y}=0, \qquad \frac{\partial^2 c_\mathrm{l}}{\partial y^2}=0, \tag{4.18}$$

and in the porous membrane ($1<y<1+h_2$)

$$u_\mathrm{m}\equiv 0, \qquad v_\mathrm{m}=-\kappa_\mathrm{m}\frac{\partial p_\mathrm{m}}{\partial y}, \qquad \frac{\partial^2 p_\mathrm{m}}{\partial y^2}=0, \qquad \frac{\partial^2 c_\mathrm{m}}{\partial y^2}=0. \tag{4.19}$$

In the cell layer ($1+h_2<y<H-h_4$) the no voids condition is

$$\theta_\mathrm{u}+\theta_\mathrm{d}+\theta_\mathrm{w}+\theta_\mathrm{s}=1, \tag{4.20}$$

the cell phase equations are

$$\frac{\partial \theta_i}{\partial t}+\frac{\partial}{\partial x}\left(\theta_i u_i\right)+\frac{\partial}{\partial y}\left(\theta_i v_i\right)=J_i \quad (i=\mathrm{u},\mathrm{d}), \tag{4.21}$$

$$-\theta_i\frac{\partial p_\mathrm{w}}{\partial x}-\frac{\partial}{\partial x}\left(\theta_i\Pi_i\right)+\psi_\mathrm{ns}\theta_\mathrm{s}\frac{\partial \theta_i}{\partial x}-\zeta_\mathrm{ns}\theta_i\theta_\mathrm{s}u_i+\frac{\partial}{\partial y}\left(\theta_i\frac{\partial u_i}{\partial y}\right)=0 \quad (i=\mathrm{u},\mathrm{d}), \tag{4.22}$$

$$-\theta_i\frac{\partial p_\mathrm{w}}{\partial y}-\frac{\partial}{\partial y}\left(\theta_i\Pi_i\right)+\psi_\mathrm{ns}\theta_\mathrm{s}\frac{\partial \theta_i}{\partial y}=0 \quad (i=\mathrm{u},\mathrm{d}), \tag{4.23}$$

the water phase equations are

$$\frac{\partial \theta_\mathrm{w}}{\partial t}+\frac{\partial}{\partial x}\left(\theta_\mathrm{w}u_\mathrm{w}\right)+\frac{\partial}{\partial y}\left(\theta_\mathrm{w}v_\mathrm{w}\right)=J_\mathrm{w}=-J_\mathrm{u}-J_\mathrm{d}, \tag{4.24}$$

$$-\theta_\mathrm{w}\frac{\partial p_\mathrm{w}}{\partial x}-\zeta_\mathrm{ws}\theta_\mathrm{w}\theta_\mathrm{s}u_\mathrm{w}=0, \qquad -\theta_\mathrm{w}\frac{\partial p_\mathrm{w}}{\partial y}=0, \tag{4.25a,b}$$

and the solute equation is

$$\frac{\partial}{\partial y}\left(\theta_\mathrm{w}\frac{\partial c_\mathrm{w}}{\partial y}\right)=0. \tag{4.26}$$

Finally, the leading-order equations in the upper fluid layer ($H-h_4<y<H$) are

$$\frac{\partial u_\mathrm{f}}{\partial x}+\frac{\partial v_\mathrm{f}}{\partial y}=0, \qquad \frac{\partial^2 u_\mathrm{f}}{\partial y^2}=\frac{\partial p_\mathrm{f}}{\partial x}, \qquad \frac{\partial p_\mathrm{f}}{\partial y}=0, \qquad \frac{\partial^2 c_\mathrm{f}}{\partial y^2}=0. \tag{4.27}$$

The leading-order boundary conditions on the lumen centreline are

$$\frac{\partial u_\mathrm{l}}{\partial y}=0, \qquad v_\mathrm{l}=0, \qquad \frac{\partial c_\mathrm{l}}{\partial y}=0 \qquad \text{on} \quad y=0, \tag{4.28}$$

on the lumen/porous membrane interface

$$u_\mathrm{l}=v_\mathrm{l}=0, \qquad p_\mathrm{l}=p_\mathrm{m}, \qquad c_\mathrm{l}=c_\mathrm{m}, \qquad \frac{\partial c_\mathrm{l}}{\partial y}=\phi_\mathrm{m}\frac{\partial c_\mathrm{m}}{\partial y} \qquad \text{on} \quad y=1, \tag{4.29}$$

on the porous membrane/cell layer interface

$$u_i = v_i = 0 \quad (i = \mathrm{u}, \mathrm{d}), \qquad v_\mathrm{w} = -\frac{\kappa_\mathrm{m}\phi_\mathrm{m}}{\theta_\mathrm{w}}\frac{\partial p_\mathrm{m}}{\partial y}, \qquad p_\mathrm{m} = p_\mathrm{w},$$
$$c_\mathrm{m} = c_\mathrm{w}, \qquad \phi_\mathrm{m}\frac{\partial c_\mathrm{m}}{\partial y} = \theta_\mathrm{w}\frac{\partial c_\mathrm{w}}{\partial y} \qquad \text{on} \quad y = 1 + h_2, \tag{4.30a-f}$$

on the cell layer/upper fluid layer interface

$$\frac{\partial u_i}{\partial y} = 0, \qquad v_i = 0 \quad (i = \mathrm{u}, \mathrm{d}), \qquad u_\mathrm{f} = v_\mathrm{f} = 0, \qquad p_\mathrm{w} = p_\mathrm{f},$$
$$c_\mathrm{w} = c_\mathrm{f}, \qquad \theta_\mathrm{w}\frac{\partial c_\mathrm{w}}{\partial y} = \frac{\partial c_\mathrm{f}}{\partial y} \qquad \text{on} \quad y = H - h_4, \tag{4.31a-g}$$

and on the bioreactor top

$$u_\mathrm{f} = v_\mathrm{f} = 0, \qquad \frac{\partial c_\mathrm{f}}{\partial y} = 0 \qquad \text{on} \quad y = H. \tag{4.32}$$

We also now introduce the up- and downstream boundary conditions on the fluid velocities and pressures in the lumen and upper fluid layer, as they are identical to those in Chapter 3 and so that they can be used in the model reduction below. We therefore prescribe the inlet fluid fluxes and outlet pressures in both the lumen and upper fluid layer, setting

$$Q_\mathrm{l,in} = \int_0^1 u_\mathrm{l}\,\mathrm{d}y, \qquad Q_\mathrm{f,in} = \int_{H-h_4}^{H} u_\mathrm{f}\,\mathrm{d}y \qquad \text{at} \quad x = 0, \tag{4.33}$$
$$p_\mathrm{l} = P_\mathrm{dwn}, \qquad p_\mathrm{f} = 0 \qquad \text{at} \quad x = 1. \tag{4.34}$$

For the leading-order system to reduce in a similar manner to Chapter 3, we must show that the cell volume fractions θ_u and θ_d are independent of y. Given that $\partial p_\mathrm{w}/\partial y = 0$ from (4.25b), the leading-order cell phase y-momentum equations (4.23) can be put into the following matrix form:

$$\begin{pmatrix} -\Pi_\mathrm{u} - \theta_\mathrm{u}\frac{\partial \Pi_\mathrm{u}}{\partial \theta_\mathrm{u}} + \psi_\mathrm{ns}\theta_\mathrm{s} & -\theta_\mathrm{u}\frac{\partial \Pi_\mathrm{u}}{\partial \theta_\mathrm{d}} \\ -\theta_\mathrm{d}\frac{\partial \Pi_\mathrm{d}}{\partial \theta_\mathrm{u}} & -\Pi_\mathrm{d} - \theta_\mathrm{d}\frac{\partial \Pi_\mathrm{d}}{\partial \theta_\mathrm{d}} + \psi_\mathrm{ns}\theta_\mathrm{s} \end{pmatrix} \begin{pmatrix} \frac{\partial \theta_\mathrm{u}}{\partial y} \\ \frac{\partial \theta_\mathrm{d}}{\partial y} \end{pmatrix} = \mathbf{0}. \tag{4.35}$$

In general, the determinant of the matrix in (4.35) will be non-zero, *i.e.*

$$\left(-\Pi_\mathrm{u} - \theta_\mathrm{u}\frac{\partial \Pi_\mathrm{u}}{\partial \theta_\mathrm{u}} + \psi_\mathrm{ns}\theta_\mathrm{s}\right)\left(-\Pi_\mathrm{d} - \theta_\mathrm{d}\frac{\partial \Pi_\mathrm{d}}{\partial \theta_\mathrm{d}} + \psi_\mathrm{ns}\theta_\mathrm{s}\right) - \theta_\mathrm{u}\theta_\mathrm{d}\frac{\partial \Pi_\mathrm{u}}{\partial \theta_\mathrm{d}}\frac{\partial \Pi_\mathrm{d}}{\partial \theta_\mathrm{u}} \neq 0, \tag{4.36}$$

from which we can conclude that we must have $\partial\theta_\mathrm{u}/\partial y = \partial\theta_\mathrm{d}/\partial y = 0$. Hence, similarly to the single cell population models, we have $\theta_i = \theta_i(x,t)$ $(i = \mathrm{u}, \mathrm{d})$. We also find that the solute equations and boundary conditions again yield

$$c_i := c(x,t) \quad (i = \mathrm{l}, \mathrm{m}, \mathrm{w}, \mathrm{f}), \tag{4.37}$$

for some $c(x,t)$ to be determined.

The remaining leading-order variables can be found in a similar manner to before, in terms of the cell volume fractions $\theta_{\rm u}$ and $\theta_{\rm d}$, and the solute concentration c. In the lumen we have

$$p_{\rm l} = 3Q_{\rm l,in}(1-x) + P_{\rm dwn}, \qquad u_{\rm l} = \frac{3}{2}Q_{\rm l,in}(1-y^2), \qquad v_{\rm l} \equiv 0, \tag{4.38}$$

and in the membrane

$$\begin{gathered} p_{\rm m} = \frac{1}{h_2}\left[\left(\frac{12Q_{\rm f,in}}{h_4^3} - 3Q_{\rm l,in}\right)(1-x) - P_{\rm dwn}\right](y-1) + 3Q_{\rm l,in}(1-x) + P_{\rm dwn}, \\ u_{\rm m} \equiv 0, \qquad v_{\rm m} = -\frac{\kappa_{\rm m}}{h_2}\left[\left(\frac{12Q_{\rm f,in}}{h_4^3} - 3Q_{\rm l,in}\right)(1-x) - P_{\rm dwn}\right]. \end{gathered} \tag{4.39}$$

In the cell layer, we consider the leading-order x-momentum equations for each cell phase,

$$-\theta_i\frac{\partial p_{\rm w}}{\partial x} - \frac{\partial}{\partial x}(\theta_i\Pi_i) + \theta_i\frac{\partial^2 u_i}{\partial y^2} + \psi_{\rm ns}\theta_{\rm s}\frac{\partial\theta_i}{\partial x} - \zeta_{\rm ns}\theta_i\theta_{\rm s}u_i = 0 \quad (i = {\rm u},{\rm d}). \tag{4.40}$$

These can be solved, along with (4.30a) and (4.31a), to find

$$u_i = \frac{\widetilde{M}_i(x,t)}{\zeta_{\rm ns}\theta_{\rm s}}\left\{\frac{\cosh\left[\sqrt{\zeta_{\rm ns}\theta_{\rm s}}\,(H-h_4-y)\right]}{\cosh\left(\sqrt{\zeta_{\rm ns}\theta_{\rm s}}h_3\right)} - 1\right\} \quad (i = {\rm u},{\rm d}), \tag{4.41}$$

where

$$\begin{gathered} \widetilde{M}_i := \frac{\partial p_{\rm w}}{\partial x} + \frac{1}{\theta_i}\tilde{\Phi}_i(\theta_{\rm u},\theta_{\rm d})\frac{\partial\theta_i}{\partial x} + \frac{\partial\Pi_i}{\partial\theta_j}\frac{\partial\theta_j}{\partial x}, \\ \tilde{\Phi}_i := \Pi_i + \theta_i\frac{\partial\Pi_i}{\partial\theta_i} - \psi_{\rm ns}\theta_{\rm s} \quad (i,j = {\rm u},{\rm d},\ i\neq j). \end{gathered} \tag{4.42}$$

The remaining cell layer variables are

$$p_{\rm w} = \frac{12Q_{\rm f,in}}{h_4^3}(1-x), \qquad u_{\rm w} = \frac{12Q_{\rm f,in}}{h_4^3\theta_{\rm s}\zeta_{\rm ws}}, \tag{4.43a,b}$$

with $v_{\rm u}$ and $v_{\rm d}$ given implicitly by their respective mass equations in (4.21), and $v_{\rm w}$ by (4.24). Finally, in the upper fluid layer we find

$$p_{\rm f} = \frac{12Q_{\rm f,in}}{h_4^3}(1-x), \qquad u_{\rm f} = -\frac{6Q_{\rm f,in}}{h_4^3}\left[y^2 + (h_4-2H)(y-H) - H^2\right], \qquad v_{\rm f} \equiv 0. \tag{4.44}$$

Given the increased size of $\varepsilon^2{\rm Pe}$ here compared to Chapters 2 and 3, we must consider the solute system of equations at $\mathrm{O}(\varepsilon)$ to determine an equation for the leading-order concentration c. At this order we have (briefly returning to subscript $0,1$ notation for clarity)

$$\varepsilon{\rm Pe}u_{\rm l_0}\frac{\partial c}{\partial x} = \frac{\partial^2 c_{\rm l_1}}{\partial y^2}, \qquad \frac{\partial^2 c_{\rm m_1}}{\partial y^2} = 0, \qquad \theta_{\rm w_0}\frac{\partial^2 c_{\rm w_1}}{\partial y^2} = -\mathcal{R}, \qquad \varepsilon{\rm Pe}u_{\rm f_0}\frac{\partial c}{\partial x} = \frac{\partial^2 c_{\rm f_1}}{\partial y^2}, \tag{4.45}$$

together with the corresponding continuity of solute and of solute flux conditions on the interfaces between layers, and no flux of solute conditions on the lumen centreline and bioreactor top. Integrating the equations in (4.45) across their respective layers (appropriately weighted in the membrane and cell layer) and adding together the resulting equations yields the following equation for c:

$$\varepsilon \mathrm{Pe}(Q_{\mathrm{l,in}} + Q_{\mathrm{f,in}}) \frac{\partial c}{\partial x} = h_3 \mathcal{R}\left(\theta_{\mathrm{u}}, \theta_{\mathrm{d}}\right). \tag{4.46}$$

This couples to the equations for the remaining unknowns θ_{u} and θ_{d}, obtained by integrating the mass equations in (4.21) across the cell layer:

$$\frac{\partial \theta_i}{\partial t} + \frac{\partial Q_i}{\partial x} = J_i(\theta_{\mathrm{u}}, \theta_{\mathrm{d}}, c) \quad (i = \mathrm{u}, \mathrm{d}), \tag{4.47}$$

where

$$Q_i = \frac{\widetilde{M}_i(x,t)}{\zeta_{\mathrm{ns}}\theta_{\mathrm{s}}} \left(\frac{\tanh(\alpha)}{\alpha} - 1 \right) \theta_i \quad (i = \mathrm{u}, \mathrm{d}), \qquad \alpha := \sqrt{\zeta_{\mathrm{ns}}\theta_{\mathrm{s}}} h_3, \tag{4.48}$$

and $\widetilde{M}_i$ $(i = \mathrm{u}, \mathrm{d})$ are defined in (4.42).

We must finally prescribe the remaining up- and downstream conditions which are needed in order to close the system. These are very similar to those in the single cell population model in Chapter 3, except that only one boundary condition is needed on c as equation (4.46) is only first-order in c. Thus we choose the condition most directly relevant to an experimental setup, a prescribed inlet concentration. We also impose no flux of cells out of the cell layer, and therefore have

$$Q_i = 0 \quad (i = \mathrm{u}, \mathrm{d}) \qquad \text{at} \quad x = 0, 1, \tag{4.49}$$

$$c = c_{\mathrm{in}} \qquad \text{at} \quad x = 0. \tag{4.50}$$

4.3.4 Summary of the reduced model

In summary, we have reduced the 4-layer, two cell population model to a coupled system of three PDEs to solve for the leading-order cell volume fractions θ_{u} and θ_{d} and solute concentration c. Thus we have

$$\begin{aligned} &\frac{\partial \theta_i}{\partial t} + \frac{\partial Q_i}{\partial x} = J_i(\theta_{\mathrm{u}}, \theta_{\mathrm{d}}, c) \quad (i = \mathrm{u}, \mathrm{d}), \\ &\varepsilon \mathrm{Pe}(Q_{\mathrm{l,in}} + Q_{\mathrm{f,in}}) \frac{\partial c}{\partial x} = h_3 \mathcal{R}\left(\theta_{\mathrm{u}}, \theta_{\mathrm{d}}\right), \end{aligned} \tag{4.51a,b}$$

subject to

$$Q_i = 0 \quad (i = \mathrm{u}, \mathrm{d}) \qquad \text{at} \quad x = 0, 1, \tag{4.52}$$

$$c = c_{\mathrm{in}} \qquad \text{at} \quad x = 0, \tag{4.53}$$

and where Q_i $(i = \mathrm{u}, \mathrm{d})$ are given in (4.48).

4.3.5 Reduced 3-layer model

If only three layers are considered (so that the whole of the ECS is filled with cells), we must solve for p_{w} as well as θ_{u}, θ_{d}, and c, as in the single cell population model in Chapter 2. The analysis follows through in a similar manner (but, as in §4.3.3, going to $\mathrm{O}(\varepsilon)$ instead of $\mathrm{O}(\varepsilon^2)$ to determine the solute equation), and the resulting coupled system of equations to solve is

$$\begin{gathered} \frac{\partial \theta_i}{\partial t} + \frac{\partial Q_i}{\partial x} = J_i \quad (i = \mathrm{u}, \mathrm{d}), \qquad \varepsilon \mathrm{Pe} Q_{\mathrm{l,in}} \frac{\partial c}{\partial x} = h_3 \mathcal{R}, \\ \frac{\partial}{\partial x}\left(Q_{\mathrm{u}} + Q_{\mathrm{d}} + Q_{\mathrm{w}}\right) = -\frac{\kappa_{\mathrm{m}} \phi_{\mathrm{m}}}{h_2 h_3}\left[p_{\mathrm{w}} - 3Q_{\mathrm{l,in}}(1 - x) - P_{\mathrm{dwn}}\right], \end{gathered} \tag{4.54a-c}$$

where

$$Q_i = \frac{\widetilde{M}_i(x,t)\theta_i}{\zeta_{\mathrm{ns}}\theta_{\mathrm{s}}\alpha \sinh(\alpha)}\left[2\cosh(\alpha) - \alpha \sinh(\alpha) - 2\right] \quad (i = \mathrm{u}, \mathrm{d}),$$

$$\alpha := \sqrt{\zeta_{\mathrm{ns}}\theta_{\mathrm{s}}}\, h_3, \tag{4.55}$$

$$Q_{\mathrm{w}} = -\frac{\theta_{\mathrm{w}}}{\zeta_{\mathrm{ws}}\theta_{\mathrm{s}}} \frac{\partial p_{\mathrm{w}}}{\partial x}, \tag{4.56}$$

subject to the boundary conditions

$$Q_i = 0 \quad (i = \mathrm{u}, \mathrm{d}) \qquad \text{at} \quad x = 0, 1, \tag{4.57}$$

$$Q_{\mathrm{w}} = \frac{Q_{\mathrm{e,in}}}{h_3}, \qquad c = c_{\mathrm{in}} \qquad \text{at} \quad x = 0, \tag{4.58}$$

$$p_{\mathrm{w}} = 0 \qquad \text{at} \quad x = 1, \tag{4.59}$$

where $\widetilde{M}_i$ $(i = \mathrm{u}, \mathrm{d})$ is defined in (4.42).

4.4 Numerical results

Numerical results were once again obtained using the method of lines described in §2.6.1. Details of the convergence tests performed are given in Appendix A.2. However, as equations (4.51*b*) and (4.54*b*) now only involve an advection term for the solute concentration,

a regularising diffusion term was included for the purposes of numerical solution. The coefficient of this term was taken to be $\mathrm{O}(10^{-4})$ for all results presented here, and it was verified that reduction of this coefficient to $\mathrm{O}(10^{-5})$ had no significant impact upon results (maximum absolute difference between solutions of $\mathrm{O}(10^{-7})$, less than the $\mathrm{O}(\varepsilon^2)$ accuracy of the scheme; details not shown). Due to a lack of experimental data for initial cell volume fractions, all results were obtained with the initial conditions $\theta_{\mathrm{u}} = 0.3$ and $\theta_{\mathrm{d}} = 0$, and we note that the value of θ_{u} would need to be verified in order to obtain quantitative predictions.

In the following sections we present results from two different case studies, each relating to a specific constitutive choice for J_{u} and J_{d}, motivated by experimental observations of cell differentiation stimuli. In both cases we will assume that the cells take up the growth factor, and that both populations do so at the same rate, so that the constitutive form for $\mathcal{R}$ is given by

$$\mathcal{R} = -\Gamma_{\mathrm{R1}} c \theta_{\mathrm{w}} \theta_{\mathrm{u}} - \Gamma_{\mathrm{R1}} c \theta_{\mathrm{w}} \theta_{\mathrm{d}} = -\Gamma_{\mathrm{R1}} c \theta_{\mathrm{w}} \left(\theta_{\mathrm{u}} + \theta_{\mathrm{d}}\right), \tag{4.60}$$

similar to that used for solute uptake in the chemoattractant case studies in Chapter 2.

Experimentally, minimising the necessary quantity of growth factor is of particular importance due to the high cost of these proteins, for example, just 100 μg of BMP-2 currently costs £1562 [68]. Mathematical modelling could therefore be of use, for instance, in determining the minimum growth factor concentration needed to obtain a particular percentage/yield of differentiated cells after a certain time, or optimum operating conditions which ensure that a given percentage/yield of differentiated cells can be obtained given a fixed amount of available growth factor. As an example to illustrate how our model may be used in this way, for each case study we discuss experimental operating conditions (inlet fluid fluxes, inlet concentration, and experiment end time $\tilde{t}$) which result in a minimum percentage (98%, following our discussion in §4.3.1) of differentiated cells being reached, whilst also taking into account the yield of differentiated cells and amount of growth factor used. Once validated, similar analysis of our model could be used to make more quantitative predictions and inform experimental protocol.

We denote the percentage of cells which are of the differentiated phenotype at time t by $\pi_{\mathrm{d}}(t)$, and the yield of differentiated cells by $\mu_{\mathrm{d}}(t)$. These are defined, respectively, by

$$\pi_{\mathrm{d}}(t) := \frac{100\mu_{\mathrm{d}}(t)}{\mu_{\mathrm{u}}(t) + \mu_{\mathrm{d}}(t)}, \tag{4.61}$$

and

$$\mu_i(t) := \int_0^1 \theta_i(x,t)\,\mathrm{d}x \quad (i = \mathrm{u}, \mathrm{d}). \tag{4.62}$$

We also estimate the quantity of growth factor q_{in} supplied to the system by the leading-order flux of solute that has entered the system at time t. In the 3-layer model this is

$$q_{\mathrm{in}}(t) := \varepsilon \mathrm{Pe} \int_0^t \int_0^1 c(x,t') u_{\mathrm{l}}(y,t')\big|_{x=0}\,\mathrm{d}y\,\mathrm{d}t' = \varepsilon \mathrm{Pe} Q_{\mathrm{l,in}} t c_{\mathrm{in}}, \tag{4.63}$$

and in the 4-layer model

$$\begin{aligned} q_{\mathrm{in}}(t) &:= \varepsilon \mathrm{Pe} \int_0^t \left(\int_0^1 c(x,t') u_{\mathrm{l}}(y,t')\big|_{x=0}\,\mathrm{d}y + \int_{H-h_4}^H c(x,t') u_{\mathrm{f}}(y,t')\big|_{x=0}\,\mathrm{d}y \right) \mathrm{d}t' \\ &= \varepsilon \mathrm{Pe}(Q_{\mathrm{l,in}} + Q_{\mathrm{f,in}}) t c_{\mathrm{in}}. \end{aligned} \tag{4.64}$$

Finally, we calculate the amount of growth factor taken up by the cells at leading order by time t, q_{up}. For both the 3- and 4-layer models this is given by

$$q_{\mathrm{up}}(t) := -h_3 \int_0^t \int_0^1 \mathcal{R}(x,t')\,\mathrm{d}x\,\mathrm{d}t', \tag{4.65}$$

where we note that the minus sign results in a positive value for q_{up}. The quantities $q_{\mathrm{in}}(t)$ and $q_{\mathrm{up}}(t)$ give estimates for the total amount of growth factor supplied during the experiment up to time t (assuming the culture medium is not recycled during the experiment, which could be the case) and the amount of growth factor 'lost' during the experiment up to time t, respectively. This provides a measure of how expensive each set of operating conditions are likely to be based on the amount of growth factor required, assuming that any not taken up by the cells can be retained and used later. Practically, however, only around 95% of any unused growth factor can be recovered [1] and so q_{up} should be interpreted as an underestimate. We estimate the integrals in (4.61)-(4.65) from our numerical solutions using the MATLAB function `trapz`.

4.4.1 Growth factor-dependent differentiation

In the first case study, we consider cell differentiation which is dependent solely on growth factor concentration. Several examples of this type of relationship can be found in the experimental literature, in particular relating to osteogenesis [106, 110] and endothelial differentiation [18, 106, 132]. We take the following forms for the mass transfer functions:

$$J_{\mathrm{u}} = \Gamma_{\mathrm{nw}} \theta_{\mathrm{u}} \theta_{\mathrm{w}} - \Gamma_{\mathrm{ud}} \theta_{\mathrm{u}} \theta_{\mathrm{w}} \frac{c}{K+c} - \Gamma_{\mathrm{wn}} \theta_{\mathrm{u}}, \tag{4.66}$$

$$J_{\mathrm{d}} = \Gamma_{\mathrm{nw}} \theta_{\mathrm{d}} \theta_{\mathrm{w}} + \Gamma_{\mathrm{ud}} \theta_{\mathrm{u}} \theta_{\mathrm{w}} \frac{c}{K+c} - \Gamma_{\mathrm{wn}} \theta_{\mathrm{d}}. \tag{4.67}$$

In the above, the first and last terms in each of J_{u} and J_{d} are the same as the cell proliferation and death terms in Chapter 2 in which nutrient is assumed to be in abundance. As mentioned in §4.3.1, we have assumed for simplicity that each cell population proliferates and dies at the same rate. The middle terms in each constitutive law represent the differentiation of the θ_{u} cell population to the θ_{d} cell population, with a constant differentiation rate coefficient Γ_{ud}. The differentiation rate is assumed proportional to the volume fraction of undifferentiated cells so that, in particular, no differentiation occurs in the absence of undifferentiated cells. Finally, the dependence of cell differentiation rate on the growth factor concentration is included via a Michaelis-Menten type term.

Results for this case study, in which the inlet concentration c_{in} is varied, can be seen in Figure 4.2. Only results from the 3-layer model are plotted, as in this case the 4-layer model results are very similar (not shown). This suggests that, for this case study, solving the less computationally intensive (three instead of four coupled PDEs) 4-layer model is sufficient to determine the behaviour of either system in response to variations in c_{in}. Figure 4.2(a) shows that the differentiated cell percentage π_{d} increases over time for all c_{in} values, with a more rapid initial increase and greater final value for higher values of the inlet concentration c_{in}. This is to be expected given the dependence of cell differentiation on c in (4.66) and (4.67). Furthermore, the decreasing difference between subsequent π_{d} plots as c_{in} increases shows that, at higher inlet concentrations, the differentiation term is approaching its saturating value $\Gamma_{\mathrm{ud}}\theta_{\mathrm{u}}\theta_{\mathrm{w}}$.

However, for all c_{in} values, the differentiated cell yield μ_{d} reaches a peak before decreasing towards the end of the experiment due to cell death (see Figure 4.2(b), where we note that this behaviour for $c_{\mathrm{in}} = 0.1$ is out of the range of t considered). The peak value is greater, and achieved at earlier times, as c_{in} increases, behaviours which can be attributed to two factors. Firstly, for higher c_{in} values the rate of differentiation will be greater, and so μ_{d} will increase more quickly and to a higher value. Secondly, a higher differentiated cell yield also results in a higher cell death rate (see equation (4.67)), and so its effect in decreasing μ_{d} becomes apparent at earlier times. Figure 4.2(c) shows a plot of π_{d} versus μ_{d} which clearly shows the trends discussed above: as π_{d} increases over time, at a particular point the maximum yield is reached and thereafter μ_{d} decreases.

From Figure 4.2 we can see that the required value of $\pi_{\mathrm{d}} = 98$ is only reached by the end of the simulation time (which we recall corresponds to a typical maximum experimental

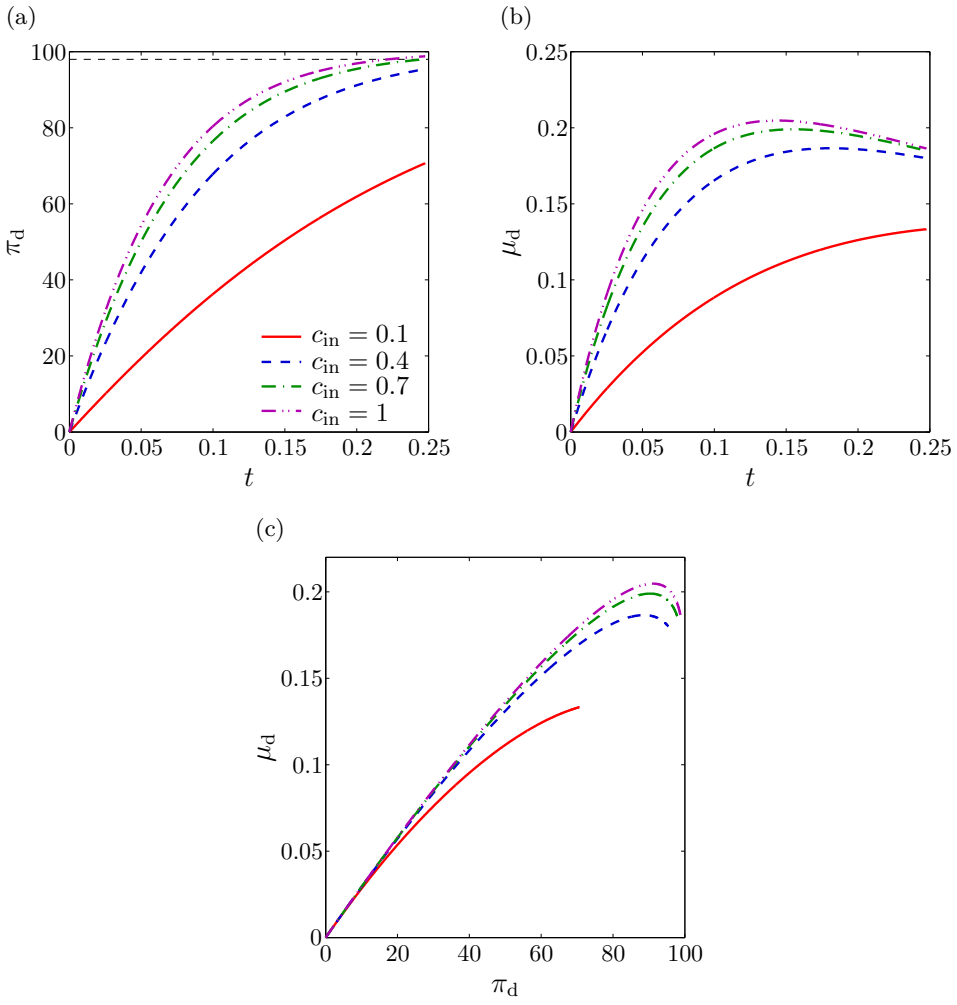

Figure 4.2: Results for the growth factor-dependent differentiation case study. (a) Percentage of differentiated cells π_d versus t, with the horizontal dashed black line denoting $\pi_d = 98$; (b) differentiated cell yield μ_d versus t; and (c) a direct comparison π_d versus μ_d, for the 3-layer model and varying inlet concentration values c_{in}. The legend in (a) applies to all subfigures. The lumen inlet flux was fixed at $Q_{l,in} = 1$ and all other parameter values take their fixed values from Table 4.2.

end time of 4 weeks) for $c_{in} = 0.7$ and 1, with corresponding values of $\mu_d = 0.185$ and 0.193, and at times $\tilde{t} = 0.247$ and 0.222, respectively. The resulting quantities of growth factor supplied and used are $q_{in}(\tilde{t}) = 0.885$ and 1.138, and $q_{up}(\tilde{t}) = 0.043$ and 0.056, respectively. Thus, although setting $c_{in} = 1$ reaches the required value of π_d earlier than if $c_{in} = 0.7$, and with a higher yield of cells, a larger quantity of growth factor is needed and more is also used overall (in fact 30% more). In this case, therefore, a compromise must be made between the quantity of growth factor and yield of cells.

We note that in this case study, changing the inlet fluid flux values will affect the distribution of growth factor and therefore also π_{d} and μ_{d}. However, trends were shown to be qualitatively similar to those obtained in the next case study, and we therefore postpone discussion of varying fluid fluxes until §4.4.2.

4.4.2 Growth factor- and shear stress-dependent differentiation

Next we consider the case where cell differentiation is dependent both on growth factor concentration and fluid shear stress, as observed by Wu *et al.* [181] for endothelial cell differentiation. We take the same approximation for the fluid shear stress S as in §3.4, that is,

$$S = \frac{\left|\frac{\partial p_{\mathrm{w}}}{\partial x}\right|}{\theta_{\mathrm{w}}}. \tag{4.68}$$

In calculating S for the 3-layer setup in which we do not have an explicit expression for p_{w}, we estimate the pressure gradient $\partial p_{\mathrm{w}}/\partial x$ from the numerical solution to p_{w} using central differences. The constitutive forms for J_{u} and J_{d} in this case are

$$J_{\mathrm{u}} = \Gamma_{\mathrm{nw}}\theta_{\mathrm{u}}\theta_{\mathrm{w}} - \Gamma_{\mathrm{ud}}\theta_{\mathrm{u}}F(S)\theta_{\mathrm{w}}\frac{c}{K+c} - \Gamma_{\mathrm{wn}}\theta_{\mathrm{u}}, \tag{4.69}$$

$$J_{\mathrm{d}} = \Gamma_{\mathrm{nw}}\theta_{\mathrm{d}}\theta_{\mathrm{w}} + \Gamma_{\mathrm{ud}}\theta_{\mathrm{u}}F(S)\theta_{\mathrm{w}}\frac{c}{K+c} - \Gamma_{\mathrm{wn}}\theta_{\mathrm{d}}, \tag{4.70}$$

where the cell proliferation and death terms are unchanged from §4.4.1, and $F(S)$ has been added to the cell differentiation term to represent the functional dependence of the cell differentiation on the shear stress. Given that shear stress has been observed to increase cell differentiation only once a certain physiological threshold of shear stress is reached [181], the form we choose for $F(S)$ is similar to that used in Chapter 3:

$$F(S) = 0.3 + 0.5\tanh(2S-2) - 0.8\tanh(2S-15). \tag{4.71}$$

The coefficients in (4.71) have again been chosen to capture the possible behaviours of the cell population within the range of computed shear stresses in our model, and we assume that if high enough levels of shear stress are exceeded then differentiation is no longer promoted. A plot of $F(S)$ can be seen in Figure 4.3.

In this case study we consider the effect of varying both the inlet growth factor concentration and inlet fluid fluxes on differentiated cell percentage, with results shown in Figures 4.4-4.6. Firstly, in Figure 4.4 the inlet concentration c_{in} is varied for two different values of $Q_{\mathrm{l,in}}$ and results are plotted for both the 3- and 4-layer models, showing qualitatively

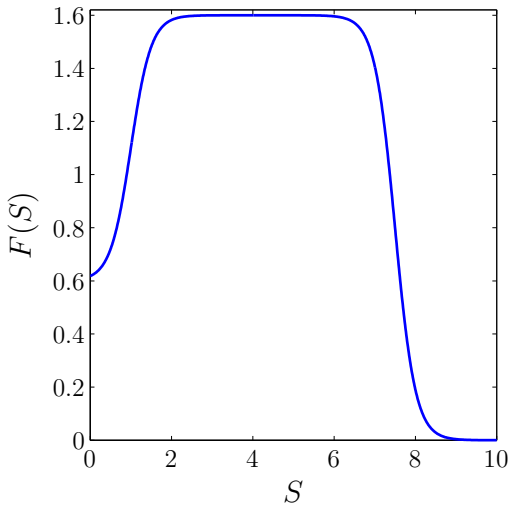

Figure 4.3: Plot of $F(S)$ versus the shear stress S, within the range of values achieved by our model.

similar trends to results from §4.4.1. Figures 4.4(a) and (b) show that for the lower value of $Q_{\mathrm{l,in}} = 0.05$, π_{d} and μ_{d} are always lower in the 3-layer model than in the 4-layer model, whereas the opposite is true for the higher lumen flux of $Q_{\mathrm{l,in}} = 1$ (see Figures 4.4(c) and (d)). This is due to the dependence of the shear stress on the lumen inlet fluid flux in the 3-layer model: for $Q_{\mathrm{l,in}} = 0.05$, $F(S)$ in the 3-layer model is on average lower than that in the 4-layer model, so that differentiation is promoted more in the latter, and vice versa at the higher fluid flux value (results not shown). These plots demonstrate that, with the additional shear stress dependence, there is a greater difference between the 3- and 4-layer model results compared to §4.4.1.

The dependence on the lumen inlet fluid flux is shown in Figure 4.5. Changing $Q_{\mathrm{l,in}}$ has very little effect on π_{d} or μ_{d} for the 4-layer model, as θ_{u}, θ_{d}, and c do not vary much with variations in $Q_{\mathrm{l,in}}$, and the reduced water pressure $\partial p_{\mathrm{w}}/\partial x$ (which contributes to S) is independent of the lumen inlet fluid flux (see equation (4.43a)). Plots of π_{d} and μ_{d} are therefore only given for $Q_{\mathrm{l,in}} = 1$ but can be taken to be representative of all lumen inlet flux values. For the 3-layer model, π_{d} increases more quickly and reaches a higher final value as $Q_{\mathrm{l,in}}$ increases, until $Q_{\mathrm{l,in}} = 2$. For large enough times t, this trend is then reversed as $Q_{\mathrm{l,in}}$ is increased above 2. This non-monotonic behaviour is also found in μ_{d}, as well as the peaked trends in time seen in §4.4.1, with $Q_{\mathrm{l,in}} = 2$ achieving the maximum yield over the range of time considered. This non-monotonicity is partly due to the effect of shear stress. As $Q_{\mathrm{l,in}}$ increases from 2 to 5, the value of S near $x = 1$ for the time range considered increases from

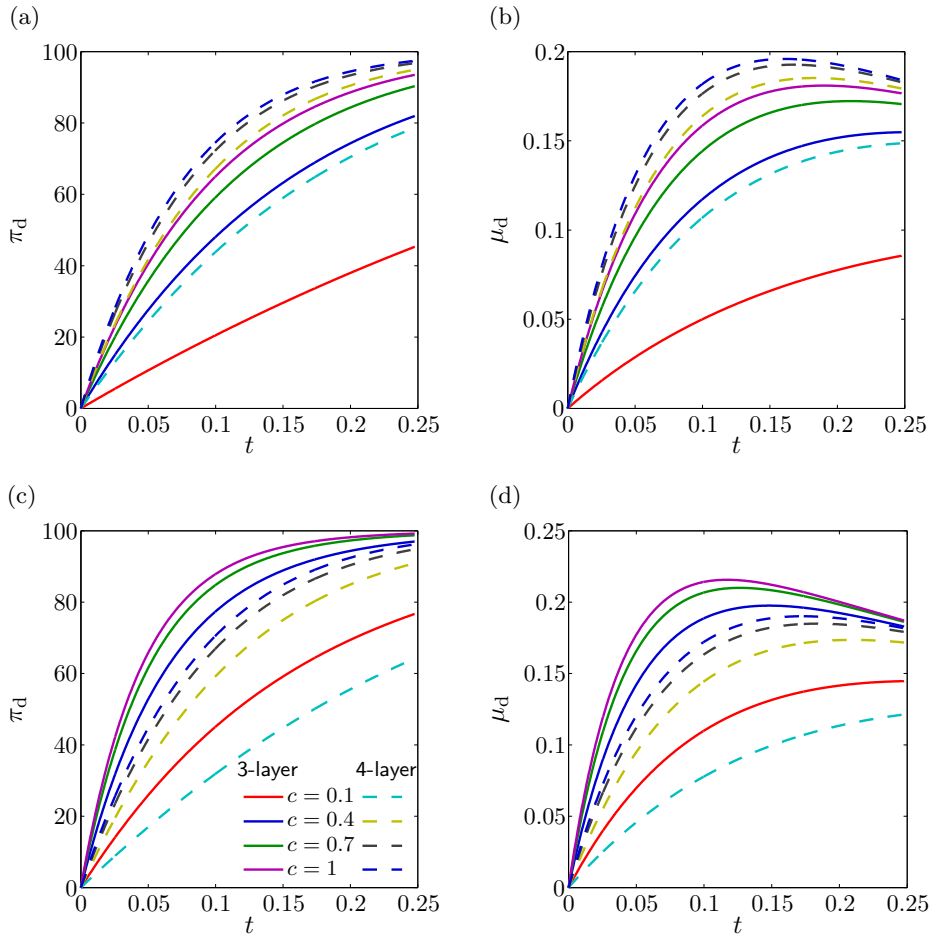

Figure 4.4: Plots of π_d and μ_d versus t for varying values of the inlet growth factor concentration c_{in} in the combined growth factor- and shear stress-dependent differentiation case study, for the 3- and 4-layer models. In (a), (b) $Q_{l,in} = 0.05$, and in (c), (d) $Q_{l,in} = 1$. The legend in (c) applies to all subfigures. The upper fluid layer inlet flux and cell layer height (for the 4-layer model) were fixed at $Q_{f,in} = 0.1$ and $h_3 = 1$ respectively. All other parameter values take their fixed values from Table 4.2.

around 3 to more than 10 (results not shown), and so $F(S)$ goes from the region in which differentiation is enhanced, into that at which the shear stress is too high and differentiation is no longer stimulated. However, similar non-monotonic behaviour is observed in π_d and μ_d if $Q_{l,in}$ is varied in the case study from §4.4.1 in which the effects of shear stress on cell differentiation are not accounted for (results not shown), and so the effect cannot be due to shear stress alone. This second contribution is less straightforward to see as it arises from the nonlinearities in the model. For large enough values of $Q_{l,in}$, advection becomes strong enough to 'sweep' more cells downstream, and this results in local variations in the values

of θ_u and θ_d. These differences feed into the cell proliferation, differentiation, and death rates (in a nonlinear way for the first two), and it is this complex combination which also contributes to the non-monotonic trends in π_d and μ_d discussed above. This hypothesis is supported by repeating the same simulations with either an increased cell-scaffold drag ζ_{ns} or cell-scaffold traction parameter η. In both cases we would expect advection to have a lesser effect on cell distribution (due to cells being 'swept' downstream less readily), and we find that the non-monotonic behaviour does not arise between $Q_{l,in} = 2$ and 2.5, but only for higher values of $Q_{l,in}$ (results not shown).

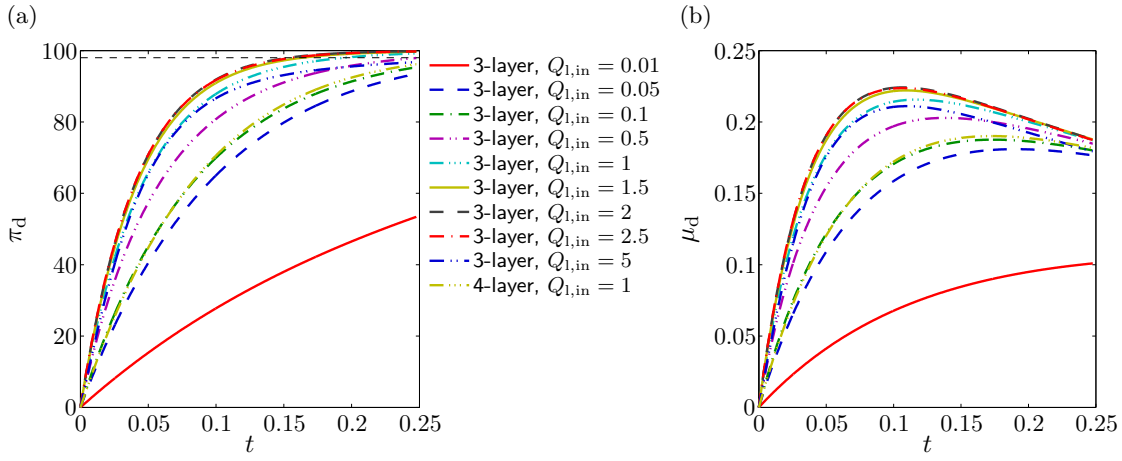

Figure 4.5: Plots of (a) π_d, and (b) μ_d, versus t for varying values of the lumen inlet flux $Q_{l,in}$, for both the 3- and 4-layer models in the combined growth factor- and shear stress-dependent differentiation case study. The horizontal dashed black line in (a) denotes $\pi_d = 98$. The legend in (a) applies to both subfigures. The inlet concentration was fixed at $c_{in} = 1$, and (for the 4-layer model) the upper fluid layer inlet flux $Q_{f,in} = 0.1$ and cell layer height $h_3 = 1$. All other parameter values take their fixed values from Table 4.2.

As can be seen in Figure 4.5, π_d reaches 98% for $Q_{l,in} = 1, 1.5, 2$, and 2.5. The times $\tilde{t}$ at which this value is achieved, along with the corresponding values of μ_d, q_{in}, and q_{up} can be found in Table 4.3, and show that q_{in} increases with $Q_{l,in}$, whilst $\tilde{t}$, μ_d, and q_{up} follow the non-monotonic dependence of π_d, with their trends reversing between $Q_{l,in} = 2$ and $Q_{l,in} = 2.5$. Hence in this case, setting $Q_{l,in}$ to 2 results in both the highest cell yield and the lowest growth factor consumption. However, if growth factor was not easily recoverable in a particular experiment, it may be worth setting the lumen inlet fluid flux to a lower value to reduce the amount q_{in} supplied to the system, with a slight compromise on cell yield.

Table 4.3: Values of the time $\tilde{t}$, differentiated cell yield μ_{d}, supplied growth factor q_{in}, and used growth factor q_{up} corresponding to the point at which the percentage of differentiated cells π_{d} reaches 98 for the combined case study, for the 3-layer ($Q_{\mathrm{l,in}}$ varying) and 4-layer ($Q_{\mathrm{f,in}}$ varying) models.

Model	Inlet fluid flux and value	$\tilde{t}$	$\mu_{\mathrm{d}}(\tilde{t})$	$q_{\mathrm{in}}(\tilde{t})$	$q_{\mathrm{up}}(\tilde{t})$
3-layer	$Q_{\mathrm{l,in}} = 1$	0.1944	0.2017	0.9958	0.049
3-layer	$Q_{\mathrm{l,in}} = 1.5$	0.1635	0.2126	1.2563	0.0419
3-layer	$Q_{\mathrm{l,in}} = 2$	0.1533	0.2163	1.5706	0.0395
3-layer	$Q_{\mathrm{l,in}} = 2.5$	0.1565	0.2149	2.0042	0.0403
4-layer	$Q_{\mathrm{f,in}} = 0.5$	0.1273	0.2268	0.974	0.0217
4-layer	$Q_{\mathrm{f,in}} = 1$	0.1372	0.2219	1.3997	0.0289

Finally, in Figure 4.6 the dependence of π_{d} and μ_{d} on $Q_{\mathrm{f,in}}$ can be seen for the 4-layer model. Here we also see the effect of the non-monotonic form for $F(S)$, as π_{d} increases more quickly and to a greater final value as $Q_{\mathrm{f,in}}$ increases up to 0.5, but then the opposite trend is seen for higher fluid flux values. The differentiated cell yield follows a similar trend, with the greatest final value of μ_{d} also achieved when $Q_{\mathrm{f,in}} = 0.5$. In addition, for $Q_{\mathrm{f,in}} < 2$, μ_{d} reaches a peak value before the maximum end time $T = 0.2477$, as seen in previous graphs. The shape of π_{d} over time changes once $Q_{\mathrm{f,in}}$ reaches 2, increasing more slowly at first and then more sharply at later times; this is the opposite to the trend for lower fluid flux values. As $Q_{\mathrm{f,in}}$ increases above 2, π_{d} increases approximately linearly with time but takes much lower values. From these results, it can be seen that π_{d} only reaches a value of 98 for $Q_{\mathrm{f,in}} = 0.5$ and 1, and hence it is not beneficial in this case to increase the upper fluid layer flux further. Corresponding values of $\tilde{t}$, μ_{d}, q_{in}, and q_{up} can be found in Table 4.3 and show that here the best choice of operating condition is clear, as setting $Q_{\mathrm{f,in}} = 0.5$ results in not only a higher final yield and percentage than if $Q_{\mathrm{l,in}} = 1$, but also consumes less growth factor, independent of whether it is recoverable or not.

4.5 Conclusions

We have solved a multiphase model for fluid flow, solute concentration, and the evolution of two cell populations, one undifferentiated and one differentiated, in a simplified HFMB setup. We have considered case studies in which cell differentiation is dependent either on the concentration of a growth factor, or on both growth factor concentration and fluid shear stress. Within these case studies, we varied the fluid fluxes into the lumen and upper fluid

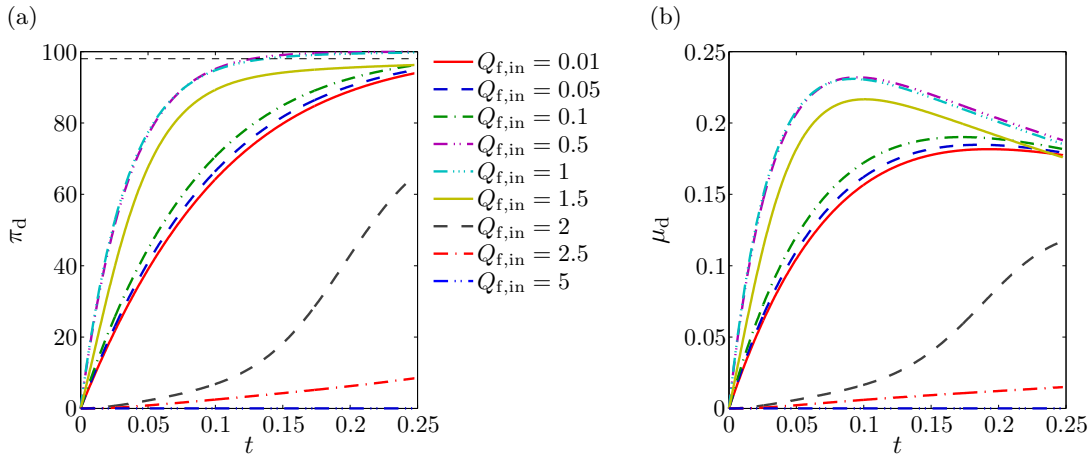

Figure 4.6: Plots of (a) π_d, and (b) μ_d, versus t for varying values of the upper fluid layer inlet flux $Q_{f,in}$, in the combined growth factor- and shear stress-dependent differentiation case study and for the 4-layer model. The horizontal dashed black line in (a) denotes $\pi_d = 98$. The legend in (a) applies to both subfigures. The inlet concentration was fixed at $c_{in} = 1$, the lumen inlet flux $Q_{l,in} = 1$, and the cell layer height $h_3 = 1$. All other parameter values take their fixed values from Table 4.2.

layer, as well as the inlet growth factor concentration in order to determine their effect on the percentage and yield of differentiated cells within an experimental time frame. Furthermore, for a candidate required percentage of differentiated cells, we compared the corresponding differentiated cell yield, experiment end time, and quantity of growth factor used/required for different operating conditions, to illustrate their relative merits and how our model could be used to inform experimental procedure once validated. In each case, the results have identified ranges of the experimentally controllable parameter values within which the required percentage of differentiated cells was achieved. These could be used as starting points for a more thorough parameter analysis to determine ideal operating conditions.

We have simplified the setup somewhat by assuming that parameters appearing in the cell drag and pressure terms, namely ψ_{ns}, ν, δ_a, and γ_{ns}, are the same for each cell population. We note that it would be straightforward to repeat the analysis of this chapter with parameters which differ between cell populations.

Results presented here are qualitative in nature, but the model derivation is general and could easily be applied to a specific experimental setup given appropriate parameter values. For a target differentiated cell percentage, this model could be used to optimise operating conditions (specifically, end time, inlet fluid fluxes, and inlet growth factor concentration) to achieve the required quantity of differentiated cells in an efficient manner, *e.g.* by minimising

the amount of growth factor needed to reduce costs.

Chapter 5

Rigid porous cell layer model

5.1 Introduction

In this chapter, we again consider the alternative experimental setup introduced in Chapter 3 in which the up- and downstream ECS ports are open and the cell-scaffold construct only fills part of the ECS, so that there is an additional exterior layer of free-flowing fluid between the construct and bioreactor edge.

In Chapters 2-4, the timescale of interest was that of fluid flow through the porous membrane/ECS/cell layer, and these flow rates were sufficiently slow that it was appropriate to include cell proliferation, motility, and death in the mathematical model. Here we consider higher flow rates, such that the timescale of interest (that of fluid transport in the lumen) is on the order of minutes and therefore much shorter than those of cell kinetics (which are typically days). It is therefore appropriate to neglect cell kinetics on this timescale, as well as the effects of the fluid shear stress on the cells which we would expect to become apparent over a longer timescale (for instance through a change in proliferation or differentiation rate). Thus, we assume that the cell-scaffold construct can be modelled as a rigid, porous medium similarly to the fibre membrane. The only role of the cells in this scenario is to contribute to the solid fraction of the porous medium, and to take up a solute (such as oxygen) which is supplied to the system at the upstream ends of the lumen and exterior fluid layer. This allows us to focus on the solute distribution throughout the system in a setup which is more analytically tractable than the multiphase models of previous chapters. Models in the literature which have taken this approach include work by Shipley and co-authors [153,155]. This simplification also allows detailed analysis of the up- and downstream regions of the bioreactor containing the ECS ports which have been neglected thus far.

In addition, the higher flow rates considered in this chapter lead to the reduced Péclet number being comparable in size to the small lumen aspect ratio. We note that, although this ratio of advective to diffusive effects in the lumen is the same asymptotic size as the reduced Péclet number used in Chapter 4, the transport regimes are not the same. As well as looking on a different timescale of interest, in Chapter 4 both the diffusion coefficient for the solute in water, D, and the porous membrane velocity scale, U^*, were lower than we consider in this chapter.

The simpler setup and different transport regime considered here permit a more thorough analysis of the solute concentration. In fact, it will be shown that the dispersion of solute is enhanced by the increased flow in a manner analogous to classical Taylor dispersion [11, 162, 163]. This adds to the findings of Griffiths *et al.* [62], who determined a generalised dispersion coefficient for flow in a long, thin porous-walled tube. We note that other models have also considered the effect on Taylor dispersion of porous media, or porous boundaries (see, for example, [87, 126, 171]), and solute absorption [108, 113, 169], but are rarely motivated by questions relevant to tissue engineering scenarios. In the following section we give a brief overview of the Taylor dispersion literature most pertinent to the work of this chapter.

5.1.1 Taylor dispersion

In his work of 1953 [162], Taylor described the dispersion of a solute in a fluid flowing slowly through a cylindrical tube. He showed that the molecular diffusion of the solute and the (non-zero) transverse velocity gradient of the fluid combine to enhance the longitudinal diffusion of the solute, and found an effective diffusion coefficient which describes this spread. His theoretical work was validated by experiments involving flow of potassium permanganate solution through a horizontal glass tube. This phenomenon subsequently became known as 'Taylor dispersion' and the original work has since been extended by many authors. We present here a brief review of the area, with a focus on porous media and permeable or absorbing boundaries as these are the applications with most relevance to our work.

Taylor's initial paper was generalised by Aris [11] to a pipe of arbitrary cross section. A new method using the moments of the solute distribution was also introduced, which removed certain parameter restrictions necessary in [162]. This method has been widely used since (see, for example, [108, 112, 113, 170, 171]). A detailed comparison of this and other common techniques used to determine the dispersion tensor for flow through porous

media, such as multiple scale analysis and random walks, can be found in [147]. When deriving the equations for classical Taylor dispersion from our system in Appendix D we use the multiple scale approach discussed by Salles *et al.* [147], which involves splitting the fluid velocities and solute concentrations into mean and fluctuating parts before considering an asymptotic expansion.

A number of different geometries have been explored, often motivated by specific applications. The cylindrical pipe setup first considered by Taylor was extended to consider dispersion in a core with porous surrounding walls in [62, 171]. In [171], Vikhansky and Wang considered the flow of a non-Newtonian fluid in the core, neglecting flow in the surrounding porous medium, and applied this to a capillary surrounded by tissue. Griffiths *et al.* [62] considered flow of a Newtonian fluid both in the pipe and the surrounding porous membrane (where Darcy's law was employed), and showed that this mimics flow in a HFMB. In an application to chromatography, Aris [12] considered a pipe containing gas and liquid flowing in two coaxial cylinders, with a specified rate of solute transfer across the interface. Mondal and Mazumder considered the dispersion of a solute in an annulus with an absorbing outer boundary in two different flow configurations: steady laminar flow [113], and pulsatile flow [108]. Both setups were applied to the problem of dispersion in a catheterised artery, and the dependence of the results on the annulus aspect ratio and reaction rate was analysed.

Taylor dispersion in a two-dimensional channel has also been considered, and the relative simplicity of this setup allows both more complicated boundary conditions to be employed and the determination of solutions that are more analytically transparent. Van den Broeck and Dekempeneer [169] determined the effective diffusion coefficient when either one or both of the channel boundaries were absorbing. They also considered the effect of sedimentation of the solute, and the case where the channel was filled with a 'network' in which solute particles could become trapped, with applications to chromatography. In a different study, Pal *et al.* [126] considered a two-dimensional channel with porous boundaries, analogous to capillary blood vessels in the lung. Flow in the porous media was assumed to be governed by Darcy's law. The dispersion coefficient arising from a Beavers-Joseph slip condition [16] on the walls was compared with that using a no slip boundary condition, and slip was found to be significant if the walls were permeable to the solvent only and not the tracer particles, but insignificant if they were permeable to both. Kumar and co-workers [87]

investigated the effect of dispersion in a channel consisting of two regions, each filled with a fluid of different viscosity, density, and velocity. In addition, one region was porous, and the Brinkman equation was used to describe the fluid flow in this area. Finally, in [170], flow through shallow micro-channels was modelled. Parabolic, elliptical, and triangular cross sections were considered, and numerical results for the solute dispersion in each setup were compared.

The literature discussed so far has been primarily concerned with unidirectional flow, one exception being [108] which instead considered oscillatory flow. This also features in [112], where a periodic pressure gradient resulted in a pulsatile flow through a two-dimensional channel with absorbing walls. Solute dispersion in the cases where the flow has a zero and non-zero mean value were compared to unidirectional flow. Two further studies [121, 174] investigated the effect of solute dispersion when flow was driven by oscillating walls, motivated by the motion of a heart beating. In [174] a two-dimensional pulsating channel with solute uptake at the walls was modelled. Results were applied to perfusion of oxygenated blood in channels surgically drilled in a patient's heart in order to treat severe coronary artery disease. Diffusion in coronary artery flow also motivated the work of O'Dea and Waters [121], where an axisymmetric tube was surrounded by a homogeneous medium which consumes solute. Flow was induced by oscillations in the length and radius of the tube, and also by a twisting motion of the tube walls. Finally we note that turbulent flow has also been considered, initially by Taylor [164] and Aris [11], but also by Fredberg [51], motivated by diffusion in the central airways of the lung.

5.1.2 Chapter outline

We begin in §5.2 by describing the model setup in a two-dimensional, 4-layer geometry. The governing equations and boundary conditions are presented in each layer, and those for the cell layer are derived from the generalised multiphase model introduced in §1.4. In §5.3 we consider a simplified geometry in order to make analytical progress, which allows the dynamics of the bulk of the bioreactor region to be studied through the solution of an 'outer' problem similar to those of previous chapters. We discuss relevant parameter values in §5.3.3, which motivate our choice of non-dimensionalisation in §5.3.4. In §5.3.5 and §5.3.6 we solve for the flow velocities and solute concentrations in each layer at leading and first order in the lumen aspect ratio. This includes specifying the axial boundary conditions which must be applied in order to match with the inner problems in the regions

near the bioreactor inlets and outlets, details of which are given in Appendix B. This allows us to investigate the y-variation in the solute concentration which enters at $\mathrm{O}(\varepsilon)$, and also picks up the axial diffusion term which comes into the Taylor dispersion analysis later. In §5.3.7, in the special case of constant inlet concentration, we are able to determine explicit expressions for the solute concentration at leading and first order. In §5.3.8 we sum the depth-averaged version of the leading- and first-order equations governing the solute concentration to obtain a single reaction-advection-diffusion equation for the (depth-averaged) mean solute concentration, suitable for efficient numerical simulations. This combined-order equation also allows us to put our matched asymptotic analysis in the context of Taylor dispersion, in a system consisting of four layers, the inner two being of differing porosities (and one with solute uptake), and the outer two having differing free fluid flow. To the best of our knowledge, this is a new result not present in the literature. Furthermore, in the limit of an impermeable membrane and cell layer the classical Taylor dispersion equations for flow in a two-dimensional pipe can be recovered in both the lumen and upper fluid layer. Results for the constant inlet concentration system are presented in §5.4.1, investigating the dependence of the first-order concentration in each layer on key dimensionless parameters that are controllable experimentally. In §5.4.2, we investigate the dependence of the effective diffusion coefficient on these key parameters, and consider the effect that they have on the mean solute uptake and solute exposure time throughout the bioreactor. In §5.5 we briefly discuss an extension to the model, which considers a non-constant cell layer porosity. Finally we conclude our findings in §5.6.

5.2 Model description

We again consider a two-dimensional simplified HFMB shown schematically in Figure 5.1, in which (x, y) are Cartesian coordinates and we have included two up- and two downstream ECS ports to mimic the connectivity of the three-dimensional setup. However, it is worth noting that, given that this model is greatly simplified compared to those of previous chapters as a result of neglecting cell kinetics, the work presented here readily carries over to the three-dimensional case, provided an axisymmetric geometry is assumed in the central 'outer' region. Although the analysis would in itself be straightforward, we have chosen not to pursue this here as it would yield highly complicated algebra even in an axisymmetric geometry, inhibiting clear exposition of the underlying asymptotics. Instead our choice of

a two-dimensional Cartesian domain permits a clearer presentation of results, whilst still demonstrating typical behaviours of the system.

As in previous chapters, the layers Ω_i $(i = 1, 2, 3, 4)$ respectively denote the lumen, porous membrane, cell layer, and upper fluid layer, and $\partial\Omega_{ij}$ $(i, j = 1, 2, 3, 4,\ i \neq j)$ denote the (permeable) interfaces between layers. The remaining (impermeable) boundaries for each layer are denoted by $\partial\Omega_i$ $(i = 2, 3, 4)$. Finally $\mathcal{A}$, $\mathcal{B}$, $\mathcal{C}$, and $\mathcal{D}$ represent line segments across the inlet/outlet pipes a finite distance away from the lumen inlet, upstream ECS ports, lumen outlet, and downstream ECS ports respectively. In anticipation of the asymptotic analysis which is to follow, we have labelled the central 'outer' region in which we will solve for the outer solution. This will need to be matched with the inner solutions in the up- and downstream 'inner' regions which include the complicated geometry of the ECS ports. For the purposes of this analysis we take these inner regions to be of O(1) aspect ratio, with their width comparable to their height, both of which are much smaller than the bioreactor length.

5.2.1 Governing equations

We begin by presenting the governing equations in the lumen, porous membrane, and upper fluid layer, which are unchanged from Chapter 3. We still work with reduced pressures throughout as, even at these higher flow rates, gravity cannot be neglected in our asymptotic analysis. We then present a reduction of the generalised multiphase model which leads to the correct governing equations in the cell layer for flow through a porous medium. As in previous chapters, water variables in the lumen, membrane, cell layer, and upper fluid layer are denoted by subscripts l, m, w, and f respectively, with the velocities given by $\mathbf{u}_i = (u_i, v_i)$, the stress tensors by $\boldsymbol{\sigma}_i$, the (reduced) water pressures by p_i, and the solute concentrations per unit volume of water by c_i $(i = \mathrm{l}, \mathrm{m}, \mathrm{w}, \mathrm{f})$.

In the lumen and upper fluid layer (Ω_1 and Ω_4), the reduced Reynolds number is much smaller than the lumen aspect ratio (this is again confirmed *a posteriori*, see §5.3.3). For the work presented here, this means that inertial effects will only appear at higher orders than we consider (specifically, at second order in the lumen aspect ratio). We thus neglect these effects from the start for simplicity, so that the appropriate governing equations for the fluid flow in these layers are:

$$\nabla \cdot \mathbf{u}_i = 0, \qquad \nabla \cdot \boldsymbol{\sigma}_i = 0, \qquad \boldsymbol{\sigma}_i = -p_i \mathbf{I} + \mu_{\mathrm{w}} \left(\nabla \mathbf{u}_i + (\nabla \mathbf{u}_i)^{\mathrm{T}} \right) \quad (i = \mathrm{l}, \mathrm{f}). \tag{5.1}$$

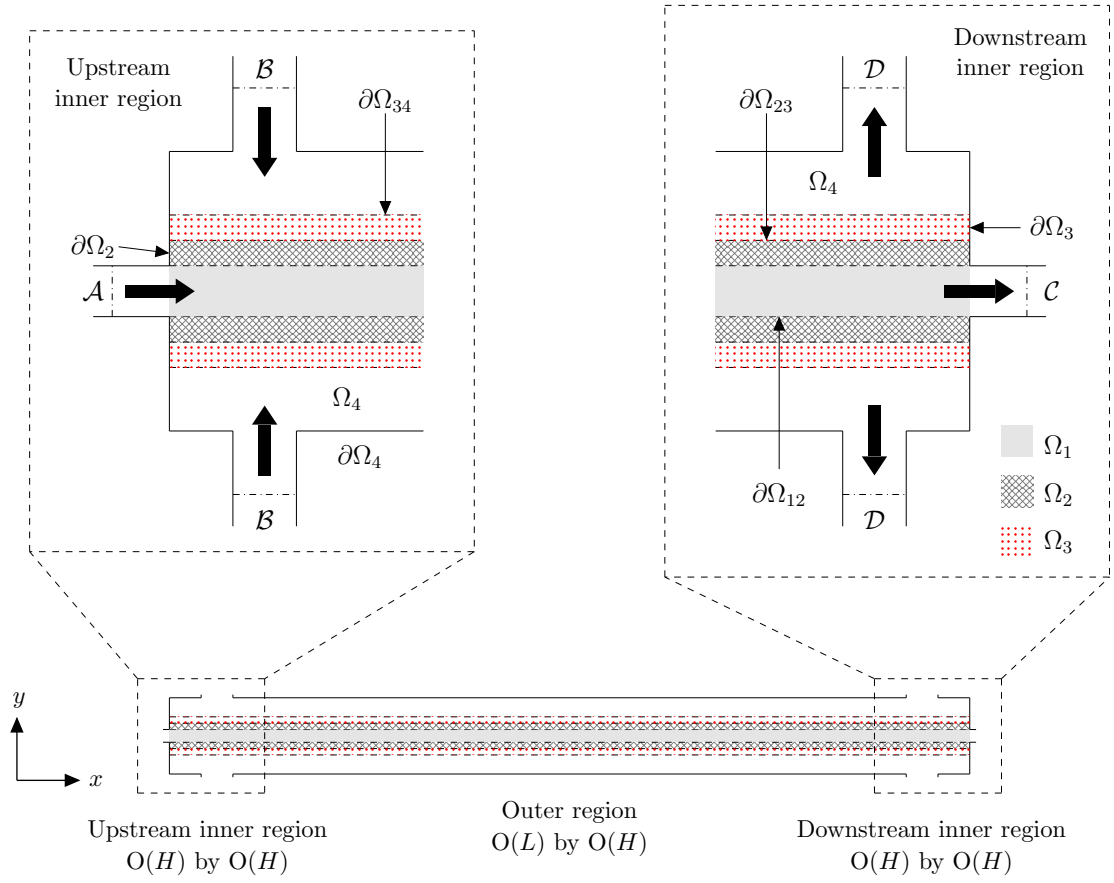

Figure 5.1: Full modelling domain in a two-dimensional Cartesian geometry, with the up- and downstream inner regions near the ECS ports enlarged (not to scale). For ease of comparison with previous chapters, the novel aspect of this model has been depicted in red: this is the cell layer, which is now regarded as a rigid porous medium as opposed to a multiphase layer. The solid black arrows denote the direction of fluid flow. The lumen, porous membrane, cell layer, and upper fluid layer respectively occupy Ω_i $(i = 1, 2, 3, 4)$. Dashed lines represent permeable boundaries $\partial\Omega_{ij}$ between layers Ω_i and Ω_j, and solid lines denote impermeable boundaries $\partial\Omega_i$ where applicable. The dash-dotted lines $\mathcal{A}$, $\mathcal{B}$, $\mathcal{C}$, and $\mathcal{D}$ respectively denote line segments across the width of the pipes a finite distance away from the lumen inlet, upstream ECS ports, lumen outlet, and downstream ECS ports respectively. As in previous chapters, H and L, $H \ll L$, are typical vertical and horizontal length scales respectively, and will be specified in §5.3.4.

The porous membrane (Ω_2) is assumed to have constant permeability k_m and porosity ϕ_m, and the governing equations are those for Darcy flow in a porous medium:

$$\nabla \cdot \mathbf{u}_\mathrm{m} = 0, \qquad \mathbf{u}_\mathrm{m} = -\frac{k_\mathrm{m}}{\mu_\mathrm{w}} \nabla p_\mathrm{m}. \tag{5.2}$$

Mass transport in the lumen, porous membrane, and upper fluid layer is again described by the relevant conservation of mass advection-diffusion equation. Thus we have

$$\begin{aligned} \frac{\partial c_\mathrm{i}}{\partial t} + \nabla \cdot (c_i \mathbf{u}_i) &= D \nabla^2 c_i \quad (i = \mathrm{l}, \mathrm{f}), \\ \frac{\partial c_\mathrm{m}}{\partial t} + \nabla \cdot (c_\mathrm{m} \mathbf{u}_\mathrm{m}) &= D \nabla^2 c_\mathrm{m}, \end{aligned} \tag{5.3}$$

where D is the (constant) diffusion coefficient of the solute in water.

It now remains to derive the governing equations for the fluid flow and mass transport in the cell layer (Ω_3), which we present below.

5.2.2 Reduction of the generalised multiphase model for a rigid, porous cell layer

We now recover the governing equations for the fluid flow and mass transport in the porous cell layer from the generalised multiphase system in §1.4 by taking a suitable parameter limit in which the cells are included as part of the solid porous scaffold.

We begin with the (dimensional) equation governing mass transport (1.12),

$$\frac{\partial}{\partial t}(\theta_\mathrm{w} c_\mathrm{w}) + \nabla \cdot (\theta_\mathrm{w} c_\mathrm{w} \mathbf{u}_\mathrm{w}) = D \nabla \cdot (\theta_\mathrm{w} \nabla c_\mathrm{w}) + \mathcal{R}. \tag{5.4}$$

If θ_w is assumed to be constant, (5.4) is already of the form required for mass transport with uptake in a porous medium of constant porosity θ_w. We will assume constant uptake per unit volume of mixture provided the solute concentration is non-zero, *i.e.* we set $\mathcal{R} = 0$ if $c_\mathrm{w} = 0$ and constant otherwise. We note that this constant uptake can be derived from the high concentration limit of Michaelis-Menten kinetics; although it is not clear if the concentration is always sufficiently high here, we retain this form for simplicity.

We now turn our attention to the (dimensional) conservation of mass and momentum equations for the cell and water phases, which are given by

$$\frac{\partial \theta_\mathrm{n}}{\partial t} + \frac{\partial}{\partial x}(\theta_\mathrm{n} u_\mathrm{n}) + \frac{\partial}{\partial y}(\theta_\mathrm{n} v_\mathrm{n}) = J_\mathrm{n}, \tag{5.5}$$

$$-\nabla \cdot (\theta_\mathrm{n} \boldsymbol{\sigma}_\mathrm{n}) + \psi_\mathrm{ns} \theta_\mathrm{s} \nabla \theta_\mathrm{n} - \gamma_\mathrm{ns} \theta_\mathrm{s} \theta_\mathrm{n} \mathbf{u}_\mathrm{n} + \gamma_\mathrm{wn} \theta_\mathrm{w} \theta_\mathrm{n} (\mathbf{u}_\mathrm{w} - \mathbf{u}_\mathrm{n}) = \mathbf{0}, \tag{5.6}$$

$$\frac{\partial \theta_\mathrm{w}}{\partial t} + \frac{\partial}{\partial x}(\theta_\mathrm{w} u_\mathrm{w}) + \frac{\partial}{\partial y}(\theta_\mathrm{w} v_\mathrm{w}) = -J_\mathrm{n}, \tag{5.7}$$

$$-\theta_\mathrm{w} \nabla p_\mathrm{w} - \gamma_\mathrm{ws} \theta_\mathrm{w} \theta_\mathrm{s} \mathbf{u}_\mathrm{w} + \gamma_\mathrm{wn} \theta_\mathrm{w} \theta_\mathrm{n} (\mathbf{u}_\mathrm{n} - \mathbf{u}_\mathrm{w}) = \mathbf{0}, \tag{5.8}$$

where we have retained the cell-water drag term involving γ_{wn} which was neglected in the multiphase reductions in Chapters 2-4. We now non-dimensionalise (5.5)-(5.8) according to

$$\begin{gathered} x = L\hat{x}, \qquad y = \varepsilon L\hat{y}, \qquad t = T^*\hat{t}, \qquad u_i = U^*\hat{u}_i, \qquad v_i = \varepsilon U^*\hat{v}_i \quad (i = \mathrm{m}, \mathrm{w}), \\ \boldsymbol{\sigma}_{\mathrm{n}} = \frac{\mu_{\mathrm{n}} U^*}{\varepsilon^2 L}\hat{\boldsymbol{\sigma}}_{\mathrm{n}}, \qquad p_{\mathrm{w}} = \frac{\mu_{\mathrm{n}} U^*}{\varepsilon^2 L}\hat{p}_{\mathrm{w}}, \qquad J_{\mathrm{n}} = J^*\hat{J}_{\mathrm{n}}, \end{gathered} \tag{5.9}$$

so that, as in the models of previous chapters, the scalings for x, y, $\mathbf{u}_{\mathrm{n}} = (u_{\mathrm{n}}, v_{\mathrm{n}})$, and $\mathbf{u}_{\mathrm{w}} = (u_{\mathrm{w}}, v_{\mathrm{w}})$ are motivated by the small aspect ratio of the bioreactor and the stress/pressure scaling is based on the cell viscosity μ_{n}. We have kept the time scale T^* and mass transfer scale J^* general. This yields (dropping hats on dimensionless variables, and splitting (5.6) and (5.8) into x- and y-components)

$$\frac{L}{U^*T^*}\frac{\partial \theta_{\mathrm{n}}}{\partial t} + \frac{\partial}{\partial x}\left(\theta_{\mathrm{n}} u_{\mathrm{n}}\right) + \frac{\partial}{\partial y}\left(\theta_{\mathrm{n}} v_{\mathrm{n}}\right) = \frac{LJ^*}{U^*} J_{\mathrm{n}}, \tag{5.10}$$

$$\frac{\partial \sigma_{\mathrm{n1,1}}}{\partial x} + \frac{\partial \sigma_{\mathrm{n2,1}}}{\partial y} + \psi_{\mathrm{ns}}\theta_{\mathrm{s}}\frac{\partial \theta_{\mathrm{n}}}{\partial x} - \zeta_{\mathrm{ns}}\theta_{\mathrm{s}}\theta_{\mathrm{n}}u_{\mathrm{n}} + \zeta_{\mathrm{wn}}\theta_{\mathrm{w}}\theta_{\mathrm{n}}(u_{\mathrm{w}} - u_{\mathrm{n}}) = 0, \tag{5.11}$$

$$\frac{\partial \sigma_{\mathrm{n2,1}}}{\partial x} + \frac{\partial \sigma_{\mathrm{n2,2}}}{\partial y} + \psi_{\mathrm{ns}}\theta_{\mathrm{s}}\frac{\partial \theta_{\mathrm{n}}}{\partial y} - \varepsilon^2\zeta_{\mathrm{ns}}\theta_{\mathrm{s}}\theta_{\mathrm{n}}v_{\mathrm{n}} + \varepsilon^2\zeta_{\mathrm{wn}}\theta_{\mathrm{w}}\theta_{\mathrm{n}}(v_{\mathrm{w}} - v_{\mathrm{n}}) = 0, \tag{5.12}$$

$$\frac{L}{U^*T^*}\frac{\partial \theta_{\mathrm{w}}}{\partial t} + \frac{\partial}{\partial x}\left(\theta_{\mathrm{w}} u_{\mathrm{w}}\right) + \frac{\partial}{\partial y}\left(\theta_{\mathrm{w}} v_{\mathrm{w}}\right) = -\frac{LJ^*}{U^*} J_{\mathrm{n}}, \tag{5.13}$$

$$-\theta_{\mathrm{w}}\frac{\partial p_{\mathrm{w}}}{\partial x} - \zeta_{\mathrm{ws}}\theta_{\mathrm{w}}\theta_{\mathrm{s}}u_{\mathrm{w}} + \zeta_{\mathrm{wn}}\theta_{\mathrm{w}}\theta_{\mathrm{n}}(u_{\mathrm{n}} - u_{\mathrm{w}}) = 0, \tag{5.14}$$

$$-\theta_{\mathrm{w}}\frac{\partial p_{\mathrm{w}}}{\partial y} - \varepsilon^2\zeta_{\mathrm{ws}}\theta_{\mathrm{w}}\theta_{\mathrm{s}}v_{\mathrm{w}} + \varepsilon^2\zeta_{\mathrm{wn}}\theta_{\mathrm{w}}\theta_{\mathrm{n}}(v_{\mathrm{n}} - v_{\mathrm{w}}) = 0, \tag{5.15}$$

where $\zeta_{ij} = \varepsilon^2 L^2\gamma_{ij}/\mu_{\mathrm{n}}$ $(i, j = \mathrm{n}, \mathrm{w}, \mathrm{s},\ i \neq j)$ are the dimensionless drag coefficients, $\varepsilon = h_1/L$ is the lumen aspect ratio, and we have denoted the (i, j)th entry of $\boldsymbol{\sigma}_{\mathrm{n}}$ using subscript i, j.

Large drag limit

We now consider the limit in which the cell-scaffold drag is very large, *i.e.* $\zeta_{\mathrm{ns}} \to \infty$. To retain a balance between the dominant terms in (5.11) and (5.12) it is consistent to also take

$$u_{\mathrm{n}},\ v_{\mathrm{n}} = \mathrm{O}\left(\zeta_{\mathrm{ns}}^{-1}\right), \tag{5.16}$$

so that the cell velocity tends to zero in the limit considered, but $\zeta_{\mathrm{ns}}\mathbf{u}_{\mathrm{n}}$ is held constant. Given the form of $\boldsymbol{\sigma}_{\mathrm{n}}$ in (1.6), we find that each term of the deviatoric stress tensor also scales with ζ_{ns}^{-1} as $\zeta_{\mathrm{ns}} \to \infty$. We also assume that the remaining parameters and dependent variables, namely ε, ζ_{wn}, ζ_{ws}, ψ_{ns}, $\mathbf{u}_{\mathrm{w}}$, p_{w}, and J_{n}, are fixed as $\zeta_{\mathrm{ns}} \to \infty$. From this, we can readily determine the dominant terms in the dimensionless system (5.10)-(5.15) and

therefore the corresponding relevant limit of the dimensional equations (5.5)-(5.8). We begin by returning to (5.10), which in the limit $\zeta_{\rm ns} \to \infty$ reduces to

$$\frac{1}{T^*}\frac{\partial \theta_{\rm n}}{\partial t} = J^* J_{\rm n}. \tag{5.17}$$

If we additionally neglect mass transfer by setting $J_{\rm n} = 0$, then we find that $\theta_{\rm n}$, and hence $\theta_{\rm w}$, are independent of t. We then find that equation (5.13) becomes

$$\frac{\partial}{\partial x}\left(\theta_{\rm w} u_{\rm w}\right) + \frac{\partial}{\partial y}\left(\theta_{\rm w} v_{\rm w}\right) = 0, \tag{5.18}$$

which, if $\theta_{\rm n}$, and therefore $\theta_{\rm w}$, are further assumed to be constant, is just the continuity equation

$$\frac{\partial u_{\rm w}}{\partial x} + \frac{\partial v_{\rm w}}{\partial y} = 0. \tag{5.19}$$

We also have from equations (5.14) and (5.15) respectively, the relationships

$$u_{\rm w} = -\frac{1}{\zeta_{\rm ws}\theta_{\rm s} + \zeta_{\rm wn}\theta_{\rm n}}\frac{\partial p_{\rm w}}{\partial x}, \qquad v_{\rm w} = -\frac{1}{\varepsilon^2\left(\zeta_{\rm ws}\theta_{\rm s} + \zeta_{\rm wn}\theta_{\rm n}\right)}\frac{\partial p_{\rm w}}{\partial y}. \tag{5.20}$$

Finally, (5.11) and (5.12) yield

$$\zeta_{\rm ns}\theta_{\rm s}\theta_{\rm n} u_{\rm n} = \zeta_{\rm wn}\theta_{\rm w}\theta_{\rm n} u_{\rm w} + \psi_{\rm ns}\theta_{\rm s}\frac{\partial \theta_{\rm n}}{\partial x}, \tag{5.21}$$

$$\varepsilon^2\zeta_{\rm ns}\theta_{\rm s}\theta_{\rm n} v_{\rm n} = \varepsilon^2\zeta_{\rm wn}\theta_{\rm w}\theta_{\rm n} v_{\rm w} + \psi_{\rm ns}\theta_{\rm s}\frac{\partial \theta_{\rm n}}{\partial y}, \tag{5.22}$$

which, for constant $\theta_{\rm n}$, reduce to

$$\zeta_{\rm ns}\theta_{\rm s}\theta_{\rm n} u_{\rm n} = \zeta_{\rm wn}\theta_{\rm w}\theta_{\rm n} u_{\rm w}, \qquad \varepsilon^2\zeta_{\rm ns}\theta_{\rm s}\theta_{\rm n} v_{\rm n} = \varepsilon^2\zeta_{\rm wn}\theta_{\rm w}\theta_{\rm n} v_{\rm w}. \tag{5.23}$$

If we now re-dimensionalise equations (5.19), (5.20), and (5.23), we find that (5.19) is unchanged, *viz.*

$$\frac{\partial u_{\rm w}}{\partial x} + \frac{\partial v_{\rm w}}{\partial y} = 0, \tag{5.24}$$

and (combining x- and y-components) the remaining equations yield

$$\mathbf{u}_{\rm w} = -\frac{1}{\gamma_{\rm ws}\theta_{\rm s} + \gamma_{\rm wn}\theta_{\rm n}}\nabla p_{\rm w}, \tag{5.25}$$

and

$$\mathbf{u}_{\rm n} = \frac{\gamma_{\rm wn}\theta_{\rm w}}{\gamma_{\rm ns}\theta_{\rm s}}\mathbf{u}_{\rm w}. \tag{5.26}$$

In (5.25) we can recognise Darcy's law for the cell layer if we define the permeability $k_{\rm w}$ by

$$k_{\rm w} := \frac{\mu_{\rm w}}{\gamma_{\rm ws}\theta_{\rm s} + \gamma_{\rm wn}\theta_{\rm n}}. \tag{5.27}$$

Furthermore, (5.26) yields an expression for the cell velocity in terms of the water and scaffold volume fractions, water velocity, and cell-scaffold and cell-water drag coefficients. Hence, although decoupled from equations (5.24) and (5.25) for the water phase, the cell velocity can still be found once $\mathbf{u}_\mathrm{w}$ is known. We note that this also enables the cell stress $\boldsymbol{\sigma}_\mathrm{n}$ to be determined via equation (1.6).

In summary, in (5.24) and (5.25) we have recovered the governing equations for a rigid porous cell layer with (constant) porosity θ_w and permeability k_w. From now on we will denote the porosity of the cell layer by the constant ϕ_w for consistency with the notation used in the porous membrane.

5.2.3 Boundary conditions

We now impose boundary conditions to couple the layers and close the problem. On each of the interfaces between the layers, we impose continuity of fluid flux, of normal stress, of solute concentration, and of solute flux. In addition, the lumen/membrane and cell/upper fluid layer interfaces are at the boundary between free fluid flow and flow through porous media and hence need an extra condition; in both cases this is given by no slip of fluid in the free-flowing layer.

In the following, $\mathbf{t}_{ij}$ is the unit tangent to $\partial\Omega_{ij}$, $\mathbf{n}_i$ is the outward unit normal to $\partial\Omega_i$, and $\mathbf{n}_{ij}$ is the unit normal to $\partial\Omega_{ij}$ pointing into Ω_j. We begin with the lumen/membrane interface $\partial\Omega_{12}$, where we impose no slip of fluid, continuity of fluid flux and of normal stress, and continuity of concentration and of solute flux:

$$\begin{gathered}\mathbf{u}_\mathrm{l}\cdot\mathbf{t}_{12}=0, \qquad \mathbf{u}_\mathrm{l}\cdot\mathbf{n}_{12}=\phi_\mathrm{m}\mathbf{u}_\mathrm{m}\cdot\mathbf{n}_{12}, \qquad \mathbf{n}_{12}\cdot\boldsymbol{\sigma}_\mathrm{l}\cdot\mathbf{n}_{12}=\mathbf{n}_{12}\cdot\boldsymbol{\sigma}_\mathrm{m}\cdot\mathbf{n}_{12},\\ c_\mathrm{l}=c_\mathrm{m}, \qquad \nabla c_\mathrm{l}\cdot\mathbf{n}_{12}=\phi_\mathrm{m}\nabla c_\mathrm{m}\cdot\mathbf{n}_{12} \qquad \text{on} \quad \partial\Omega_{12},\end{gathered} \tag{5.28}$$

where $\boldsymbol{\sigma}_\mathrm{m}=-p_\mathrm{m}\mathbf{I}$ and we have again assumed that all the stress is taken up by the water in the membrane. The no slip condition is motivated by the results from [156] as discussed in §2.3.4. On the membrane/cell layer and cell/upper fluid layer interfaces $\partial\Omega_{23}$, $\partial\Omega_{34}$, we impose continuity of fluid flux, of normal stress, of concentration, and of solute flux:

$$\begin{gathered}\phi_\mathrm{m}\mathbf{u}_\mathrm{m}\cdot\mathbf{n}_{23}=\phi_\mathrm{w}\mathbf{u}_\mathrm{w}\cdot\mathbf{n}_{23}, \qquad \mathbf{n}_{23}\cdot\boldsymbol{\sigma}_\mathrm{m}\cdot\mathbf{n}_{23}=\mathbf{n}_{23}\cdot\boldsymbol{\sigma}_\mathrm{w}\cdot\mathbf{n}_{23},\\ c_\mathrm{m}=c_\mathrm{w}, \qquad \phi_\mathrm{m}\nabla c_\mathrm{m}\cdot\mathbf{n}_{23}=\phi_\mathrm{w}\nabla c_\mathrm{w}\cdot\mathbf{n}_{23} \qquad \text{on} \quad \partial\Omega_{23},\end{gathered} \tag{5.29}$$

and

$$\begin{gathered}\phi_\mathrm{w}\mathbf{u}_\mathrm{w}\cdot\mathbf{n}_{34}=\mathbf{u}_\mathrm{f}\cdot\mathbf{n}_{34}, \qquad \mathbf{n}_{34}\cdot\boldsymbol{\sigma}_\mathrm{w}\cdot\mathbf{n}_{34}=\mathbf{n}_{34}\cdot\boldsymbol{\sigma}_\mathrm{f}\cdot\mathbf{n}_{34},\\ c_\mathrm{w}=c_\mathrm{f}, \qquad \phi_\mathrm{w}\nabla c_\mathrm{w}\cdot\mathbf{n}_{34}=\nabla c_\mathrm{f}\cdot\mathbf{n}_{34} \qquad \text{on} \quad \partial\Omega_{34},\end{gathered} \tag{5.30}$$

where $\boldsymbol{\sigma}_\mathrm{w} = -p_\mathrm{w}\mathbf{I}$, and again we have assumed that the water takes up all the stress. In addition, we also prescribe no slip of fluid on the cell/upper fluid layer interface (as discussed in §3.2):

$$\mathbf{u}_\mathrm{f} \cdot \mathbf{t}_{34} = 0 \qquad \text{on} \quad \partial\Omega_{34}. \tag{5.31}$$

On the edges of the bioreactor $\partial\Omega_i$ $(i = 2, 3, 4)$ we impose no flux of fluid and, on $\partial\Omega_4$, no slip of fluid and no flux of solute:

$$\mathbf{u}_\mathrm{m} \cdot \mathbf{n}_2 = 0, \qquad \nabla c_\mathrm{m} \cdot \mathbf{n}_2 = 0 \qquad \text{on} \quad \partial\Omega_2, \tag{5.32}$$

$$\mathbf{u}_\mathrm{w} \cdot \mathbf{n}_3 = 0, \qquad \nabla c_\mathrm{w} \cdot \mathbf{n}_3 = 0 \qquad \text{on} \quad \partial\Omega_3, \tag{5.33}$$

$$\mathbf{u}_\mathrm{f} = 0, \qquad \nabla c_\mathrm{f} \cdot \mathbf{n}_4 = 0 \qquad \text{on} \quad \partial\Omega_4. \tag{5.34}$$

It now remains to prescribe boundary conditions at the lumen inlet and outlet, and the ECS ports. These are identical to those in Chapter 3. In the pipes entering the lumen inlet and upstream ECS ports, we assume that the flow is of Poiseuille form with prescribed volume fluxes in per unit length in the z-direction $Q_\mathrm{l,in}$ and $Q_\mathrm{f,in}$, respectively. We also prescribe the solute concentration at these inlets, so that

$$c_\mathrm{l} = c_\mathrm{l,in}(t) \qquad \text{at} \quad \mathcal{A}, \tag{5.35}$$

$$c_\mathrm{f} = c_\mathrm{f,in}(t) \qquad \text{at} \quad \mathcal{B}, \tag{5.36}$$

for some $c_\mathrm{l,in}$ and $c_\mathrm{f,in}$ which (for now) are assumed to be functions of time. Experimentally, the lumen outlet pressure is controlled by a clamp, and the pipe connected to the downstream ECS port is left open to the atmosphere as discussed previously. We prescribe continuity of normal stress and no transverse flow at these positions, and thus the appropriate conditions are

$$\mathbf{n}_\mathcal{C} \cdot \boldsymbol{\sigma}_\mathrm{l} \cdot \mathbf{n}_\mathcal{C} = P_\mathrm{dwn}, \qquad \mathbf{u}_\mathrm{l} \cdot \mathbf{t}_\mathcal{C} = 0 \qquad \text{at} \quad \mathcal{C}, \tag{5.37}$$

$$\mathbf{n}_\mathcal{D} \cdot \boldsymbol{\sigma}_\mathrm{f} \cdot \mathbf{n}_\mathcal{D} = p_\mathrm{atm}, \qquad \mathbf{u}_\mathrm{f} \cdot \mathbf{t}_\mathcal{D} = 0 \qquad \text{at} \quad \mathcal{D}, \tag{5.38}$$

where P_dwn is a given constant (reduced) downstream pressure, p_atm is (reduced) atmospheric pressure, $\mathbf{n}_\mathcal{C}$ $(\mathbf{t}_\mathcal{C})$ and $\mathbf{n}_\mathcal{D}$ $(\mathbf{t}_\mathcal{D})$ are the outward pointing normals (tangents) at $\mathcal{C}$ and $\mathcal{D}$ respectively, and $\boldsymbol{\sigma}_i$ $(i = \mathrm{l}, \mathrm{f})$ respectively are the viscous fluid stress tensors in the lumen and upper fluid layer. Finally, we must impose a condition on the solute concentration on the line segments $\mathcal{C}$ and $\mathcal{D}$. As discussed in previous chapters, there is no experimental

constraint here and so we prescribe no diffusive flux of solute. This condition is considered more carefully in our subsequent boundary layer analysis in Appendix C. Hence we have

$$\nabla c_{\mathrm{l}} \cdot \mathbf{n}_{\mathcal{C}} = 0 \qquad \text{at} \quad \mathcal{C}, \tag{5.39}$$

$$\nabla c_{\mathrm{f}} \cdot \mathbf{n}_{\mathcal{D}} = 0 \qquad \text{at} \quad \mathcal{D}. \tag{5.40}$$

5.3 Outer solution

The geometry of the modelling domain as illustrated in Figure 5.1 is complicated by the up- and downstream ECS ports. As discussed in previous chapters, numerical approaches would be needed to make any progress in solving this system, and this would be computationally expensive. As mentioned in §5.2, we instead concentrate on determining the solution in the central outer region, excluding the ECS ports, as it greatly simplifies the geometry yet still incorporates the majority of the bioreactor. This will be sufficient to obtain a general understanding of the fluid flow and solute distribution in this system, and their dependence on certain key experimental parameters. However, the simpler setup of this model compared to the multiphase models of Chapters 2-4 permits a more in-depth analysis of the up- and downstream regions. Here, the up- and downstream boundary conditions for the outer problem are determined by matching with the solutions in the up- and downstream inner regions, details of which are given in Appendix B. It is worth noting that the analysis used to determine the leading-order up- and downstream boundary conditions in Appendix B follows through in a similar manner in the multiphase systems of Chapters 2-4.

5.3.1 Geometry for the outer solution

The modelling domain for the outer solution is depicted in Figure 5.2. As in previous chapters, we consider the upper half of the bioreactor only, given the symmetry of the two-dimensional system depicted in Figure 5.1. The coordinate system is fixed from the full setup in Figure 5.1: the origin $(x, y) = (0, 0)$ is taken to be at the far left of the full domain, on the lumen centreline. Thus (in the limit $\varepsilon \to 0$, where ε is the small lumen aspect ratio) the bottom left-hand corner of the outer region corresponds to $(x, y) = (0^+, 0)$, with the axial dimension of the outer bioreactor region defined by $0^+ < x < L^-$. For the remainder of this chapter we will remove the $+$ and $-$ superscripts for presentational purposes, but they should be implicitly understood. They are reintroduced in Appendices B and C for clarity. The lumen then occupies $0 < y < h_1$ in the transverse direction and the membrane

$h_1 < y < h_1 + h_2$. We take the cell layer to be of comparable thickness to the membrane, defined by $h_1 + h_2 < y < h_1 + h_2 + h_3 =: H - h_4$, and the upper fluid layer to occupy the remaining $H - h_4 < y < H$.

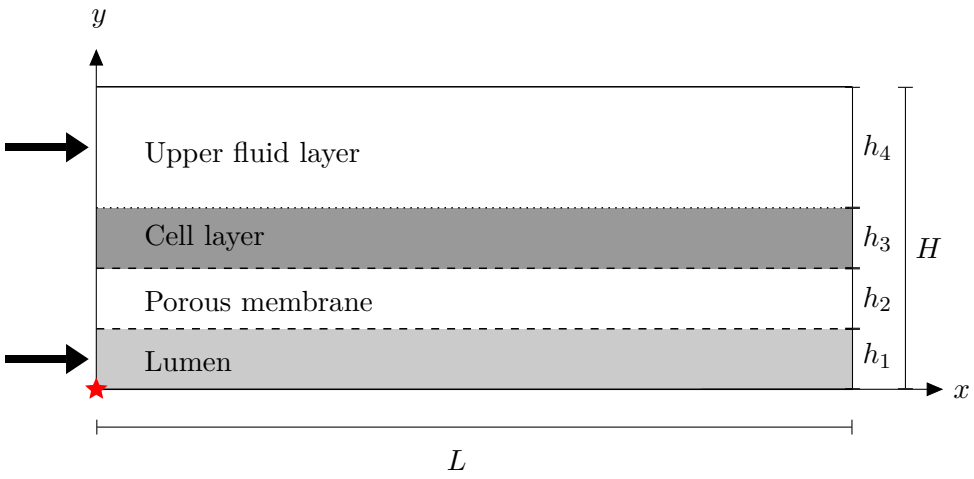

Figure 5.2: Upper-central bioreactor region representing the modelling domain for the outer problem in a two-dimensional Cartesian geometry (not to scale). The red star denotes the point $(x, y) = (0, 0)$ and solid black arrows denote the direction and location of the fluid flow into this outer region.

5.3.2 Governing equations and boundary conditions for the outer solution

The governing equations in each layer are unchanged from §5.2.1, as are the boundary conditions on the interfaces between the layers and on the outer bioreactor boundary $\partial\Omega_4$. Only the boundary conditions at the up- and downstream ends of this central outer region are altered. These can be determined from matching with the corresponding inner solutions at each end (see Appendix B for details) and are introduced as required in §5.3.5 and §5.3.6. In addition, as we now consider the upper half of the outer region only, we require the following symmetry conditions on the lumen centreline:

$$\frac{\partial u_\mathrm{l}}{\partial y} = 0, \qquad v_\mathrm{l} = 0, \qquad \frac{\partial c_\mathrm{l}}{\partial y} = 0 \qquad \text{on} \quad y = 0. \tag{5.41}$$

5.3.3 Parameter values

Dimensional parameters which are new to this chapter are given in Table 5.1 (for others see Table 2.1), and all dimensionless parameter values required for this model can be found in Table 5.2. Where possible, values have been taken from the literature, or estimated based on

Table 5.1: Dimensional parameters new to this chapter.

Parameter	Dimensional value and units	Ref.
$h_3 + h_4$	600 μm	[156]
$Q_{\mathrm{l,in}}$, $Q_{\mathrm{f,in}}$	1.33×10^{-9} - 1.33×10^{-6} m^2 s^{-1}	†
$\mathcal{R}$	4.8×10^{-5} mol m^{-3} s^{-1}	[155]
U^*	1.33×10^{-6} m s^{-1}	†

†Values based on estimations by our experimental collaborators.

discussions with experimentalists. The lumen aspect ratio is given by $\varepsilon = h_1/L \ll 1$. The imposed fluid fluxes into the bioreactor can vary greatly experimentally and, as mentioned in Chapter 1, optimal operating regimes for HFMBs are not currently known [1]. In this chapter we have chosen to investigate a different flow regime which could be implemented experimentally, in which the range of three-dimensional fluid fluxes considered is higher than that of Chapters 2-4 (specifically, 5×10^{-5} - 0.05 ml min^{-1}). Fluxes within this range have also been used in perfusion bioreactor culture [36, 167] and these choices result in different asymptotic bounds on both the reduced Reynolds number $\varepsilon^2\mathrm{Re} = \varepsilon\rho_{\mathrm{w}}LU^*/\mu_{\mathrm{w}}$ and reduced Péclet number $\varepsilon^2\mathrm{Pe} = \varepsilon LU^*/D$ (see Table 5.2). The horizontal lumen/upper fluid layer velocity scaling U^*/ε was calculated from the mid-range three-dimensional flux value 5×10^{-3} ml min^{-1}. It was then assumed, as before, that the horizontal fluid flow in the porous layers was an order of ε smaller, so that the corresponding velocity scale in the porous membrane/cell layer is U^*. As in previous chapters, the two-dimensional fluid fluxes into the lumen and upper fluid layer were determined from the corresponding three-dimensional values by first calculating the corresponding velocity and then multiplying by the length scale in the y-direction, εL. The concentration scaling C^* is taken to be a typical inlet concentration for oxygen used in culturing a variety of cell types [155]. The dimensionless inlet concentrations $c_{\mathrm{l,in}}$ and $c_{\mathrm{f,in}}$ are thus assumed to be of O(1). Finally, the reaction term $\mathcal{R}$ can also vary in size significantly; here a representative value is taken which corresponds to the rate of oxygen uptake in bovine chondrocytes [155].

In some cases either we have not been able to obtain experimental values, or a wide range of possible values exists. In such situations we make choices which retain the greatest number of features at leading order in our model. Specifically, the values of the cell layer permeability k_{w} and porosity ϕ_{w} will vary greatly depending on the type of scaffold and cells used, and the seeding regime employed. We have therefore taken k_{w} such that its

Table 5.2: Dimensionless parameters used in this chapter, along with any bounds imposed either physically or by the asymptotic analysis.

Parameter	Definition	Value	Restriction	Ref.
$\hat{h}_2$	$h_2/(\varepsilon L)$	1	$\hat{h}_2 > 0$	-
$\hat{h}_3 + \hat{h}_4$	$(h_3 + h_4)/(\varepsilon L)$	3	$\hat{h}_3$, $\hat{h}_4 > 0$	-
ε	h_1/L	2×10^{-3}	$0 < \varepsilon \ll 1$	-
$\varepsilon^2\mathrm{Pe}$	$\varepsilon L U^*/D$	0.0884	$\varepsilon^2 \ll \varepsilon^2\mathrm{Pe} \ll 1$	-
$\varepsilon^2\mathrm{Re}$	$\varepsilon \rho_\mathrm{w} L U^*/\mu_\mathrm{w}$	2.66×10^{-4}	$\varepsilon^2\mathrm{Re} \ll \varepsilon$	-
ϕ_m	-	0.77	$0 < \phi_\mathrm{m} < 1$	[109]
ϕ_w	-	0.54	$0 < \phi_\mathrm{w} < 1$	[155]
κ_m	$k_\mathrm{m}/(\varepsilon^5 L^2)$	2.1	$\varepsilon \ll \kappa_\mathrm{m} \ll 1/\varepsilon$	-
κ_w	$k_\mathrm{w}/(\varepsilon^5 L^2)$	1	$\varepsilon \ll \kappa_\mathrm{w} \ll 1/\varepsilon$	-
$\hat{Q}_{i,\mathrm{in}}$ $(i = \mathrm{l}, \mathrm{f})$	$Q_{i,\mathrm{in}}/(LU^*)$	0.01 - 10	$\varepsilon \ll \hat{Q}_{i,\mathrm{in}} \ll 1/\varepsilon$	-
$\hat{\mathcal{R}}$	$\varepsilon L^2 \mathcal{R}/(DC^*)$	1.454	$\varepsilon \ll \hat{\mathcal{R}} \ll 1/\varepsilon$	-
$\hat{c}_{\mathrm{l,in}}$	$c_{\mathrm{l,in}}/C^*$	1	$\varepsilon \ll \hat{c}_{\mathrm{l,in}} \ll 1/\varepsilon$	-
$\hat{c}_{\mathrm{f,in}}$	$c_{\mathrm{f,in}}/C^*$	1	$\varepsilon \ll \hat{c}_{\mathrm{f,in}} \ll 1/\varepsilon$	-

dimensionless equivalent κ_w is of O(1) to keep the model as general as possible. The porosity ϕ_w must take values between 0 and 1, and in what follows we will examine its influence on the results of the model. When its value must be fixed, we take $\phi_\mathrm{w} = 0.54$ based on calculations by Shipley and Waters in [155].

5.3.4 Non-dimensionalisation

We use the same scalings in the upper fluid layer as in the lumen, since both have a small aspect ratio and are supplied with prescribed fluid fluxes of the same order of magnitude at the upstream end. As in previous chapters, we employ a viscous pressure scaling throughout. We set the timescale of interest to be that for advection in the lumen (≈ 2.5 mins given the choice of velocity scale in Table 5.1). Hence the relevant non-dimensionalisation is as follows:

$$\begin{gathered} x = L\hat{x}, \qquad y = \varepsilon L\hat{y}, \qquad h_i = \varepsilon L\hat{h}_i \quad (i = 2,3,4), \qquad H = \varepsilon L\hat{H}, \qquad t = \frac{\varepsilon L}{U^*}\hat{t}, \\ u_i = \frac{U^*}{\varepsilon}\hat{u}_i, \qquad v_i = U^*\hat{v}_i \quad (i = \mathrm{l}, \mathrm{f}), \qquad u_i = U^*\hat{u}_i, \qquad v_i = \varepsilon U^*\hat{v}_i \quad (i = \mathrm{m}, \mathrm{w}), \\ p_i = p_\mathrm{atm} + \frac{\mu_\mathrm{w} U^*}{\varepsilon^3 L}\hat{p}_i, \qquad c_i = C^*\hat{c}_i \quad (i = \mathrm{l}, \mathrm{m}, \mathrm{w}, \mathrm{f}), \qquad \mathcal{R} = \frac{DC^*}{\varepsilon L^2}\hat{\mathcal{R}}. \end{gathered} \tag{5.42}$$

Dropping hats on dimensionless variables and substituting in for p_m and p_w in place of u_m, v_m, u_w, and v_w where relevant, the governing equations are, in the lumen $(0 < y < 1)$

$$\begin{gathered}\frac{\partial u_\mathrm{l}}{\partial x} + \frac{\partial v_\mathrm{l}}{\partial y} = 0, \qquad -\frac{\partial p_\mathrm{l}}{\partial x} + \varepsilon^2\frac{\partial^2 u_\mathrm{l}}{\partial x^2} + \frac{\partial^2 u_\mathrm{l}}{\partial y^2} = 0, \qquad -\frac{\partial p_\mathrm{l}}{\partial y} + \varepsilon^4\frac{\partial^2 v_\mathrm{l}}{\partial x^2} + \varepsilon^2\frac{\partial^2 v_\mathrm{l}}{\partial y^2} = 0, \\ \varepsilon^2\mathrm{Pe}\left(\frac{\partial c_\mathrm{l}}{\partial t} + \nabla\cdot(c_\mathrm{l}\mathbf{u}_\mathrm{l})\right) = \varepsilon^2\frac{\partial^2 c_\mathrm{l}}{\partial x^2} + \frac{\partial^2 c_\mathrm{l}}{\partial y^2},\end{gathered} \tag{5.43}$$

in the porous membrane $(1 < y < 1 + h_2)$

$$\begin{gathered}u_\mathrm{m} = -\varepsilon^2\kappa_\mathrm{m}\frac{\partial p_\mathrm{m}}{\partial x}, \qquad v_\mathrm{m} = -\kappa_\mathrm{m}\frac{\partial p_\mathrm{m}}{\partial y}, \qquad \varepsilon^2\frac{\partial^2 p_\mathrm{m}}{\partial x^2} + \frac{\partial^2 p_\mathrm{m}}{\partial y^2} = 0, \\ \varepsilon^2\mathrm{Pe}\left(\frac{\partial c_\mathrm{m}}{\partial t} + \varepsilon\nabla\cdot(c_\mathrm{m}\mathbf{u}_\mathrm{m})\right) = \varepsilon^2\frac{\partial^2 c_\mathrm{m}}{\partial x^2} + \frac{\partial^2 c_\mathrm{m}}{\partial y^2},\end{gathered} \tag{5.44}$$

in the cell layer $(1 + h_2 < y < H - h_4)$

$$\begin{gathered}u_\mathrm{w} = -\varepsilon^2\kappa_\mathrm{w}\frac{\partial p_\mathrm{w}}{\partial x}, \qquad v_\mathrm{w} = -\kappa_\mathrm{w}\frac{\partial p_\mathrm{w}}{\partial y}, \qquad \varepsilon^2\frac{\partial^2 p_\mathrm{w}}{\partial x^2} + \frac{\partial^2 p_\mathrm{w}}{\partial y^2} = 0, \\ \varepsilon^2\mathrm{Pe}\left(\frac{\partial c_\mathrm{w}}{\partial t} + \varepsilon\nabla\cdot(c_\mathrm{w}\mathbf{u}_\mathrm{w})\right) = \varepsilon^2\frac{\partial^2 c_\mathrm{w}}{\partial x^2} + \frac{\partial^2 c_\mathrm{w}}{\partial y^2} - \frac{\varepsilon\mathcal{R}}{\phi_\mathrm{w}},\end{gathered} \tag{5.45}$$

and in the upper fluid layer $(H - h_4 < y < H)$

$$\begin{gathered}\frac{\partial u_\mathrm{f}}{\partial x} + \frac{\partial v_\mathrm{f}}{\partial y} = 0, \qquad -\frac{\partial p_\mathrm{f}}{\partial x} + \varepsilon^2\frac{\partial^2 u_\mathrm{f}}{\partial x^2} + \frac{\partial^2 u_\mathrm{f}}{\partial y^2} = 0, \qquad -\frac{\partial p_\mathrm{f}}{\partial y} + \varepsilon^4\frac{\partial^2 v_\mathrm{f}}{\partial x^2} + \varepsilon^2\frac{\partial^2 v_\mathrm{f}}{\partial y^2} = 0, \\ \varepsilon^2\mathrm{Pe}\left(\frac{\partial c_\mathrm{f}}{\partial t} + \nabla\cdot(c_\mathrm{f}\mathbf{u}_\mathrm{f})\right) = \varepsilon^2\frac{\partial^2 c_\mathrm{f}}{\partial x^2} + \frac{\partial^2 c_\mathrm{f}}{\partial y^2}.\end{gathered} \tag{5.46}$$

Here $\kappa_\mathrm{m} = k_\mathrm{m}/(\varepsilon^5 L^2)$ and $\kappa_\mathrm{w} = k_\mathrm{w}/(\varepsilon^5 L^2)$ are the dimensionless permeabilities of the membrane and cell layer respectively. As well as κ_m, we also take κ_w to be of O(1) as stated in §5.3.3 and so the leading-order flow in both porous layers is in the transverse direction. The Péclet number for axial flow in the lumen and upper fluid layer, $\mathrm{Pe} = LU^*/(\varepsilon D)$, is of $\mathrm{O}(1/\varepsilon)$ (see Table 5.2) and so advection dominates axial diffusion in these layers.

The dimensionless boundary conditions are as follows (again substituting in for p_m and p_w where applicable):

$$\frac{\partial u_\mathrm{l}}{\partial y} = 0, \qquad v_\mathrm{l} = 0, \qquad \frac{\partial c_\mathrm{l}}{\partial y} = 0 \qquad \text{on} \quad y = 0, \tag{5.47}$$

$$\begin{gathered}u_\mathrm{l} = 0, \qquad v_\mathrm{l} = -\varepsilon\kappa_\mathrm{m}\phi_\mathrm{m}\frac{\partial p_\mathrm{m}}{\partial y}, \qquad p_\mathrm{l} + \frac{2\varepsilon^2}{3}\left(\frac{\partial u_\mathrm{l}}{\partial x} - 2\frac{\partial v_\mathrm{l}}{\partial y}\right) = p_\mathrm{m}, \\ c_\mathrm{l} = c_\mathrm{m}, \qquad \frac{\partial c_\mathrm{l}}{\partial y} = \phi_\mathrm{m}\frac{\partial c_\mathrm{m}}{\partial y} \qquad \text{on} \quad y = 1,\end{gathered} \tag{5.48}$$

$$\begin{aligned} \phi_{\mathrm{m}}\kappa_{\mathrm{m}}\frac{\partial p_{\mathrm{m}}}{\partial y} = \phi_{\mathrm{w}}\kappa_{\mathrm{w}}\frac{\partial p_{\mathrm{w}}}{\partial y}, \qquad p_{\mathrm{m}} = p_{\mathrm{w}}, \\ c_{\mathrm{m}} = c_{\mathrm{w}}, \qquad \phi_{\mathrm{m}}\frac{\partial c_{\mathrm{m}}}{\partial y} = \phi_{\mathrm{w}}\frac{\partial c_{\mathrm{w}}}{\partial y} \qquad \text{on} \quad y = 1 + h_2, \end{aligned} \tag{5.49}$$

$$\begin{aligned} u_{\mathrm{f}} = 0, \qquad -\varepsilon\phi_{\mathrm{w}}\kappa_{\mathrm{w}}\frac{\partial p_{\mathrm{w}}}{\partial y} = v_{\mathrm{f}}, \qquad p_{\mathrm{w}} = p_{\mathrm{f}} + \frac{2\varepsilon^2}{3}\left(\frac{\partial u_{\mathrm{f}}}{\partial x} - 2\frac{\partial v_{\mathrm{f}}}{\partial y}\right), \\ c_{\mathrm{w}} = c_{\mathrm{f}}, \qquad \phi_{\mathrm{w}}\frac{\partial c_{\mathrm{w}}}{\partial y} = \frac{\partial c_{\mathrm{f}}}{\partial y} \qquad \text{on} \quad y = H - h_4, \end{aligned} \tag{5.50}$$

$$u_{\mathrm{f}} = v_{\mathrm{f}} = 0, \qquad \frac{\partial c_{\mathrm{f}}}{\partial y} = 0 \qquad \text{on} \quad y = H. \tag{5.51}$$

Next we analytically solve for the fluid velocities and reduced pressures at O(1) and O(ε), before using these expressions to derive equations for the solute concentrations at equivalent orders.

5.3.5 Flow solution

To find the leading- and first-order fluid velocities and reduced pressures, we expand all variables in powers of ε, for instance setting $u_{\mathrm{l}} \sim u_{\mathrm{l}_0} + \varepsilon u_{\mathrm{l}_1} + \varepsilon^2 u_{\mathrm{l}_2} + \ldots$, and similarly for the remaining velocities and reduced pressures. At leading order (dropping the subscript 0), this yields the following governing equations in the lumen

$$\frac{\partial u_{\mathrm{l}}}{\partial x} + \frac{\partial v_{\mathrm{l}}}{\partial y} = 0, \qquad \frac{\partial^2 u_{\mathrm{l}}}{\partial y^2} = \frac{\partial p_{\mathrm{l}}}{\partial x}, \qquad \frac{\partial p_{\mathrm{l}}}{\partial y} = 0, \tag{5.52}$$

in the porous membrane

$$u_{\mathrm{m}} \equiv 0, \qquad v_{\mathrm{m}} = -\kappa_{\mathrm{m}}\frac{\partial p_{\mathrm{m}}}{\partial y}, \qquad \frac{\partial^2 p_{\mathrm{m}}}{\partial y^2} = 0, \tag{5.53}$$

in the cell layer

$$u_{\mathrm{w}} \equiv 0, \qquad v_{\mathrm{w}} = -\kappa_{\mathrm{w}}\frac{\partial p_{\mathrm{w}}}{\partial y}, \qquad \frac{\partial^2 p_{\mathrm{w}}}{\partial y^2} = 0, \tag{5.54}$$

and in the upper fluid layer

$$\frac{\partial u_{\mathrm{f}}}{\partial x} + \frac{\partial v_{\mathrm{f}}}{\partial y} = 0, \qquad \frac{\partial^2 u_{\mathrm{f}}}{\partial y^2} = \frac{\partial p_{\mathrm{f}}}{\partial x}, \qquad \frac{\partial p_{\mathrm{f}}}{\partial y} = 0. \tag{5.55}$$

The leading-order boundary conditions are given by

$$\frac{\partial u_{\mathrm{l}}}{\partial y} = 0, \qquad v_{\mathrm{l}} = 0 \qquad \text{on} \quad y = 0, \tag{5.56}$$

$$u_{\mathrm{l}} = v_{\mathrm{l}} = 0, \qquad p_{\mathrm{l}} = p_{\mathrm{m}} \qquad \text{on} \quad y = 1, \tag{5.57}$$

$$\phi_{\mathrm{m}}\kappa_{\mathrm{m}}\frac{\partial p_{\mathrm{m}}}{\partial y} = \phi_{\mathrm{w}}\kappa_{\mathrm{w}}\frac{\partial p_{\mathrm{w}}}{\partial y}, \qquad p_{\mathrm{m}} = p_{\mathrm{w}} \qquad \text{on} \quad y = 1 + h_2, \tag{5.58}$$

$$u_{\mathrm{f}} = v_{\mathrm{f}} = 0, \qquad p_{\mathrm{w}} = p_{\mathrm{f}} \qquad \text{on} \quad y = H - h_4, \tag{5.59}$$

$$u_{\mathrm{f}} = v_{\mathrm{f}} = 0 \qquad \text{on} \quad y = H. \tag{5.60}$$

Finally, we impose the up- and downstream boundary conditions found from matching with the inner solutions in Appendix B. Analysis of the fluid equations in the upstream inner region shows that fluid flux is conserved in both the lumen and upper fluid layer at O(1), and so the inlet fluid flux conditions are (having non-dimensionalised appropriately):

$$Q_{\mathrm{l,in}} = \int_0^1 u_{\mathrm{l}}\,\mathrm{d}y, \qquad Q_{\mathrm{f,in}} = \int_{H-h_4}^{H} u_{\mathrm{f}}\,\mathrm{d}y \qquad \text{at} \quad x = 0. \tag{5.61}$$

Similarly, analysis of the fluid equations in the downstream inner region shows that the reduced pressure in the lumen and upper fluid layer is constant at O(1), and so the outlet pressure conditions on the outer solution at leading order are:

$$p_{\mathrm{l}} = P_{\mathrm{dwn}}, \qquad p_{\mathrm{f}} = 0 \qquad \text{at} \quad x = 1. \tag{5.62}$$

We are thus able to solve for the leading-order velocities and reduced pressures analytically, to find in the lumen

$$u_{\mathrm{l}} = -\frac{3}{2}Q_{\mathrm{l,in}}(y^2 - 1), \qquad v_{\mathrm{l}} \equiv 0, \qquad p_{\mathrm{l}} = 3Q_{\mathrm{l,in}}(1-x) + P_{\mathrm{dwn}}, \tag{5.63}$$

in the porous membrane

$$u_{\mathrm{m}} \equiv 0, \qquad v_{\mathrm{m}} = -\kappa_{\mathrm{m}}F_{\mathrm{m}}(x), \qquad p_{\mathrm{m}} = F_{\mathrm{m}}(x)(y-1) + 3Q_{\mathrm{l,in}}(1-x) + P_{\mathrm{dwn}}, \tag{5.64}$$

in the cell layer

$$\begin{gathered} u_{\mathrm{w}} \equiv 0, \qquad v_{\mathrm{w}} = -\frac{\phi_{\mathrm{m}}\kappa_{\mathrm{m}}}{\phi_{\mathrm{w}}}F_{\mathrm{m}}(x), \\ p_{\mathrm{w}} = \frac{\phi_{\mathrm{m}}\kappa_{\mathrm{m}}}{\phi_{\mathrm{w}}\kappa_{\mathrm{w}}}\left[y - (1+h_2)\right]F_{\mathrm{m}}(x) + h_2F_{\mathrm{m}}(x) + 3Q_{\mathrm{l,in}}(1-x) + P_{\mathrm{dwn}}, \end{gathered} \tag{5.65}$$

and in the upper fluid layer

$$u_{\mathrm{f}} = -\frac{6Q_{\mathrm{f,in}}}{h_4^3}(y-H)\left[y-(H-h_4)\right], \qquad v_{\mathrm{f}} \equiv 0, \qquad p_{\mathrm{f}} = \frac{12Q_{\mathrm{f,in}}}{h_4^3}(1-x), \tag{5.66}$$

where for algebraic convenience we have set

$$\begin{gathered} F_{\mathrm{m}}(x) := A_{\mathrm{m}}x + B_{\mathrm{m}}, \qquad A_{\mathrm{m}} := -\frac{\phi_{\mathrm{w}}\kappa_{\mathrm{w}}}{\phi_{\mathrm{m}}\kappa_{\mathrm{m}}h_3 + \phi_{\mathrm{w}}\kappa_{\mathrm{w}}h_2}\left(\frac{12Q_{\mathrm{f,in}}}{h_4^3} - 3Q_{\mathrm{l,in}}\right), \\ B_{\mathrm{m}} := -A_{\mathrm{m}} - \frac{\phi_{\mathrm{w}}\kappa_{\mathrm{w}}P_{\mathrm{dwn}}}{\phi_{\mathrm{m}}\kappa_{\mathrm{m}}h_3 + \phi_{\mathrm{w}}\kappa_{\mathrm{w}}h_2}. \end{gathered} \tag{5.67}$$

To determine equations for the solute concentrations up to O(ε) in §5.3.6, we also require the O(ε) velocities in the lumen and upper fluid layer. In the lumen, the governing equations at this order are (temporarily returning to subscript 0, 1 notation for clarity)

$$\frac{\partial u_{\mathrm{l}_1}}{\partial x} + \frac{\partial v_{\mathrm{l}_1}}{\partial y} = 0, \qquad \frac{\partial p_{\mathrm{l}_1}}{\partial y} = 0, \qquad \frac{\partial^2 u_{\mathrm{l}_1}}{\partial y^2} = \frac{\partial p_{\mathrm{l}_1}}{\partial x}, \tag{5.68}$$

subject to

$$\begin{gathered}\frac{\partial u_{\mathrm{l}_1}}{\partial y}=0, \qquad v_{\mathrm{l}_1}=0 \qquad \text{on} \quad y=0, \\ u_{\mathrm{l}_1}=0, \qquad v_{\mathrm{l}_1}=-\kappa_{\mathrm{m}}\phi_{\mathrm{m}}\frac{\partial p_{\mathrm{m}_0}}{\partial y}, \qquad p_{\mathrm{l}_1}=p_{\mathrm{m}_1} \qquad \text{on} \quad y=1,\end{gathered} \tag{5.69}$$

and

$$\int_0^1 u_{\mathrm{l}_1}\,\mathrm{d}y=0 \qquad \text{on} \quad x=0, \tag{5.70}$$

where the zero flux condition again follows from the inner region analysis in Appendix B, which shows that fluid flux in the lumen is also conserved at $\mathrm{O}(\varepsilon)$. This $\mathrm{O}(\varepsilon)$ system can be solved to find

$$u_{\mathrm{l}_1}=-\frac{3\kappa_{\mathrm{m}}\phi_{\mathrm{m}}}{2}\left(\frac{A_{\mathrm{m}}}{2}x^2+B_{\mathrm{m}}x\right)(y^2-1), \qquad v_{\mathrm{l}_1}=\frac{3\kappa_{\mathrm{m}}\phi_{\mathrm{m}}}{2}(A_{\mathrm{m}}x+B_{\mathrm{m}})\left(\frac{y^3}{3}-y\right). \tag{5.71}$$

Similarly in the upper fluid layer, the $\mathrm{O}(\varepsilon)$ governing equations are

$$\frac{\partial u_{\mathrm{f}_1}}{\partial x}+\frac{\partial v_{\mathrm{f}_1}}{\partial y}=0, \qquad \frac{\partial p_{\mathrm{f}_1}}{\partial y}=0, \qquad \frac{\partial^2 u_{\mathrm{f}_1}}{\partial y^2}=\frac{\partial p_{\mathrm{f}_1}}{\partial x}, \tag{5.72}$$

with

$$\begin{gathered}u_{\mathrm{f}_1}=0, \qquad v_{\mathrm{f}_1}=-\kappa_{\mathrm{w}}\phi_{\mathrm{w}}\frac{\partial p_{\mathrm{w}_0}}{\partial y}, \qquad p_{\mathrm{w}_1}=p_{\mathrm{f}_1} \qquad \text{on} \quad y=H-h_4, \\ u_{\mathrm{f}_1}=0, \qquad v_{\mathrm{f}_1}=0 \qquad \text{on} \quad y=H,\end{gathered} \tag{5.73}$$

and, as above,

$$\int_{H-h_4}^{H} u_{\mathrm{f}_1}\,\mathrm{d}y=0 \qquad \text{on} \quad x=0. \tag{5.74}$$

Solving these yields

$$\begin{gathered}u_{\mathrm{f}_1}=\frac{6\phi_{\mathrm{m}}\kappa_{\mathrm{m}}}{h_4^3}\left(\frac{A_{\mathrm{m}}}{2}x^2+B_{\mathrm{m}}x\right)(y-H)\left[y-(H-h_4)\right], \\ v_{\mathrm{f}_1}=-\frac{6\phi_{\mathrm{m}}\kappa_{\mathrm{m}}}{h_4^3}(A_{\mathrm{m}}x+B_{\mathrm{m}})\left[\frac{y^3}{3}-\frac{1}{2}(2H-h_4)y^2+H(H-h_4)y-H^2\left(\frac{H}{3}-\frac{h_4}{2}\right)\right].\end{gathered} \tag{5.75}$$

5.3.6 Mass transport

Now we return to the governing equations for the solute in (5.43)-(5.46), expanding the concentration in each layer in powers of ε as in §5.3.5. At leading order (dropping the subscript 0), we find that diffusion in the y-direction dominates throughout, so that

$$\frac{\partial^2 c_i}{\partial y^2}=0 \quad (i=\mathrm{l},\mathrm{m},\mathrm{w},\mathrm{f}), \tag{5.76}$$

with the corresponding boundary conditions

$$\frac{\partial c_\mathrm{l}}{\partial y} = 0 \qquad \text{on} \quad y = 0, \tag{5.77}$$

$$c_\mathrm{l} = c_\mathrm{m}, \qquad \frac{\partial c_\mathrm{l}}{\partial y} = \phi_\mathrm{m}\frac{\partial c_\mathrm{m}}{\partial y} \qquad \text{on} \quad y = 1, \tag{5.78}$$

$$c_\mathrm{m} = c_\mathrm{w}, \qquad \phi_\mathrm{m}\frac{\partial c_\mathrm{m}}{\partial y} = \phi_\mathrm{w}\frac{\partial c_\mathrm{w}}{\partial y} \qquad \text{on} \quad y = 1 + h_2, \tag{5.79}$$

$$c_\mathrm{w} = c_\mathrm{f}, \qquad \phi_\mathrm{w}\frac{\partial c_\mathrm{w}}{\partial y} = \frac{\partial c_\mathrm{f}}{\partial y} \qquad \text{on} \quad y = H - h_4, \tag{5.80}$$

$$\frac{\partial c_\mathrm{f}}{\partial y} = 0 \qquad \text{on} \quad y = H. \tag{5.81}$$

Solving this system implies that (as in Chapter 4 and the lower Pe regimes of Chapters 2 and 3) the leading-order concentration is independent of y and hence common to all layers, that is, $c_i := c_0(x,t)$ $(i = \mathrm{l}, \mathrm{m}, \mathrm{w}, \mathrm{f})$. Hence the solute concentration must be independent of y at leading order as it leaves the upstream inner region in order to match with this outer solution. We denote this limit of the inner concentration by $c_\mathrm{in}(t)$ and, given the conservation of fluid flux across this inner region, we have (see Appendix B for details)

$$c_0(0,t) := c_\mathrm{in}(t) = \frac{Q_\mathrm{l,in}c_\mathrm{l,in}(t) + Q_\mathrm{f,in}c_\mathrm{f,in}(t)}{Q_\mathrm{l,in} + Q_\mathrm{f,in}} \qquad \text{at} \quad x = 0. \tag{5.82}$$

No condition is required downstream, and we note that the concentration in the inner region will be determined by the value of c_0 as $x \to 1$.

To determine the leading-order concentration c_0 we must consider the $\mathrm{O}(\varepsilon)$ solute system. In doing so we will also be able to find the next-order correction to the solute concentration in each layer up to an unknown function of x and t, which can be determined by considering the $\mathrm{O}(\varepsilon^2)$ set of equations. In the following, we again return to subscript 0, 1 notation for clarity.

Equating coefficients of ε in each layer, with $\varepsilon\mathrm{Pe} = \mathrm{O}(1)$ as $\varepsilon \to 0$, yields

$$\begin{gathered}
\varepsilon\mathrm{Pe}\left(\frac{\partial c_0}{\partial t} + \frac{3}{2}Q_\mathrm{l,in}(1-y^2)\frac{\partial c_0}{\partial x}\right) = \frac{\partial^2 c_{\mathrm{l}_1}}{\partial y^2}, \qquad \varepsilon\mathrm{Pe}\frac{\partial c_0}{\partial t} = \frac{\partial^2 c_{\mathrm{m}_1}}{\partial y^2}, \\
\varepsilon\mathrm{Pe}\frac{\partial c_0}{\partial t} = \frac{\partial^2 c_{\mathrm{w}_1}}{\partial y^2} - \frac{\mathcal{R}}{\phi_\mathrm{w}}, \qquad \varepsilon\mathrm{Pe}\left(\frac{\partial c_0}{\partial t} + \frac{6}{h_4^3}Q_\mathrm{f,in}(y-H)(H-h_4-y)\frac{\partial c_0}{\partial x}\right) = \frac{\partial^2 c_{\mathrm{f}_1}}{\partial y^2},
\end{gathered} \tag{5.83}$$

where we have also substituted in the known forms for $\mathbf{u}_{\mathrm{l}_0}$ and $\mathbf{u}_{\mathrm{f}_0}$ from (5.63) and (5.66),

respectively. The boundary conditions at this order are

$$\frac{\partial c_{\mathrm{l}_1}}{\partial y} = 0 \qquad \text{on} \quad y = 0, \tag{5.84}$$

$$c_{\mathrm{l}_1} = c_{\mathrm{m}_1}, \qquad \frac{\partial c_{\mathrm{l}_1}}{\partial y} = \phi_{\mathrm{m}} \frac{\partial c_{\mathrm{m}_1}}{\partial y} \qquad \text{on} \quad y = 1, \tag{5.85}$$

$$c_{\mathrm{m}_1} = c_{\mathrm{w}_1}, \qquad \phi_{\mathrm{m}} \frac{\partial c_{\mathrm{m}_1}}{\partial y} = \phi_{\mathrm{w}} \frac{\partial c_{\mathrm{w}_1}}{\partial y} \qquad \text{on} \quad y = 1 + h_2, \tag{5.86}$$

$$c_{\mathrm{w}_1} = c_{\mathrm{f}_1}, \qquad \phi_{\mathrm{w}} \frac{\partial c_{\mathrm{w}_1}}{\partial y} = \frac{\partial c_{\mathrm{f}_1}}{\partial y} \qquad \text{on} \quad y = H - h_4, \tag{5.87}$$

$$\frac{\partial c_{\mathrm{f}_1}}{\partial y} = 0 \qquad \text{on} \quad y = H. \tag{5.88}$$

Beginning in the lumen, the system (5.83)-(5.88) can be solved to find

$$c_{\mathrm{l}_1} = \varepsilon \mathrm{Pe} \left[\frac{y^2}{2} \frac{\partial c_0}{\partial t} + \frac{Q_{\mathrm{l,in}}}{8} \left(6y^2 - y^4 \right) \frac{\partial c_0}{\partial x} + g(x,t) \right], \tag{5.89}$$

along with

$$c_{\mathrm{m}_1} = \varepsilon \mathrm{Pe} \left\{ \left[\frac{y^2}{2} + \left(\frac{1}{\phi_{\mathrm{m}}} - 1 \right) (y-1) \right] \frac{\partial c_0}{\partial t} + Q_{\mathrm{l,in}} \left(\frac{y-1}{\phi_{\mathrm{m}}} + \frac{5}{8} \right) \frac{\partial c_0}{\partial x} + g(x,t) \right\}, \tag{5.90}$$

$$c_{\mathrm{w}_1} = \varepsilon \mathrm{Pe} \left[A_{\mathrm{w}}(y) \frac{\partial c_0}{\partial t} + Q_{\mathrm{l,in}} \left(\frac{y - (1+h_2)}{\phi_{\mathrm{w}}} + \frac{h_2}{\phi_{\mathrm{m}}} + \frac{5}{8} \right) \frac{\partial c_0}{\partial x} + \frac{\mathcal{R}}{2\varepsilon \mathrm{Pe} \phi_{\mathrm{w}}} (1 + h_2 - y)^2 + g(x,t) \right], \tag{5.91}$$

$$c_{\mathrm{f}_1} = \varepsilon \mathrm{Pe} \left[A_{\mathrm{f}}(y) \frac{\partial c_0}{\partial t} + \frac{Q_{\mathrm{f,in}}}{h_4^3} B_{\mathrm{f}}(y) \frac{\partial c_0}{\partial x} + Q_{\mathrm{l,in}} \left(\frac{h_2}{\phi_{\mathrm{m}}} + \frac{h_3}{\phi_{\mathrm{w}}} + \frac{5}{8} \right) \frac{\partial c_0}{\partial x} + \frac{h_3^2 \mathcal{R}}{2\varepsilon \mathrm{Pe} \phi_{\mathrm{w}}} + g(x,t) \right], \tag{5.92}$$

for some unknown function $g(x,t)$ to be determined from the $\mathrm{O}(\varepsilon^2)$ solvability condition, where

$$A_{\mathrm{w}}(y) := \frac{y^2}{2} - (1+h_2)y + (1+h_2)^2 + \frac{1 + h_2 \phi_{\mathrm{m}}}{\phi_{\mathrm{w}}} \left[y - (1+h_2) \right] + h_2 \left(\frac{1}{\phi_{\mathrm{m}}} - 1 \right), \tag{5.93}$$

$$A_{\mathrm{f}}(y) := \frac{y^2}{2} - Hy + \frac{1}{2} \left[H^2 - h_4^2 + h_3^2 + (1+h_2)^2 \right] + \frac{h_3 \left(1 + h_2 \phi_{\mathrm{m}} \right)}{\phi_{\mathrm{w}}} + h_2 \left(\frac{1}{\phi_{\mathrm{m}}} - 1 \right), \tag{5.94}$$

$$B_{\mathrm{f}}(y) := -\frac{y^4}{2} + (2H - h_4) y^3 - 3H(H - h_4) y^2 - H^2 (3h_4 - 2H) y - \frac{H^4}{2} + h_4 H^3 - \frac{h_4^4}{2}. \tag{5.95}$$

Furthermore, in applying the continuity of solute flux condition from (5.87) on $y = H - h_4$, we also obtain the following solvability condition for c_0:

$$\bar{h}\frac{\partial c_0}{\partial t} + (Q_{\mathrm{l,in}} + Q_{\mathrm{f,in}})\frac{\partial c_0}{\partial x} = -\frac{h_3\mathcal{R}}{\varepsilon \mathrm{Pe}}, \tag{5.96}$$

subject to

$$c_0 = c_{\mathrm{in}}(t) \qquad \text{at} \quad x = 0, \tag{5.97}$$

and where

$$\bar{h} := 1 + h_2\phi_{\mathrm{m}} + h_3\phi_{\mathrm{w}} + h_4. \tag{5.98}$$

To find $g(x,t)$, we consider the solute equations from (5.43)-(5.46) at $\mathrm{O}(\varepsilon^2)$ in each layer, which are

$$\varepsilon\mathrm{Pe}\left(\frac{\partial c_{\mathrm{l}_1}}{\partial t} + \frac{\partial}{\partial x}(c_0 u_{\mathrm{l}_1} + c_{\mathrm{l}_1} u_{\mathrm{l}_0}) + \frac{\partial}{\partial y}(c_0 v_{\mathrm{l}_1})\right) = \frac{\partial^2 c_0}{\partial x^2} + \frac{\partial^2 c_{\mathrm{l}_2}}{\partial y^2}, \tag{5.99}$$

$$\varepsilon\mathrm{Pe}\frac{\partial c_{\mathrm{m}_1}}{\partial t} = \frac{\partial^2 c_0}{\partial x^2} + \frac{\partial^2 c_{\mathrm{m}_2}}{\partial y^2}, \tag{5.100}$$

$$\varepsilon\mathrm{Pe}\frac{\partial c_{\mathrm{w}_1}}{\partial t} = \frac{\partial^2 c_0}{\partial x^2} + \frac{\partial^2 c_{\mathrm{w}_2}}{\partial y^2}, \tag{5.101}$$

$$\varepsilon\mathrm{Pe}\left(\frac{\partial c_{\mathrm{f}_1}}{\partial t} + \frac{\partial}{\partial x}(c_0 u_{\mathrm{f}_1} + c_{\mathrm{f}_1} u_{\mathrm{f}_0}) + \frac{\partial}{\partial y}(c_0 v_{\mathrm{f}_1})\right) = \frac{\partial^2 c_0}{\partial x^2} + \frac{\partial^2 c_{\mathrm{f}_2}}{\partial y^2}. \tag{5.102}$$

Integrating equations (5.99) and (5.102) with respect to y across the lumen and upper fluid layer respectively, and substituting in the known forms for the leading- and first-order variables from (5.63), (5.66), (5.71), (5.75), and (5.89)-(5.92), yields

$$(\varepsilon\mathrm{Pe})^2\left(\frac{\alpha_1}{\varepsilon\mathrm{Pe}}\frac{\partial c_0}{\partial x} + \alpha_2\frac{\partial^2 c_0}{\partial x\partial t} + \alpha_3\frac{\partial^2 c_0}{\partial t^2} + \alpha_4\frac{\partial^2 c_0}{\partial x^2} + \frac{\partial g}{\partial t} + Q_{\mathrm{l,in}}\frac{\partial g}{\partial x}\right) = \frac{\partial^2 c_0}{\partial x^2} + \left.\frac{\partial c_{\mathrm{l}_2}}{\partial y}\right|_{y=1}, \tag{5.103}$$

and

$$(\varepsilon\mathrm{Pe})^2\left(\frac{\beta_1}{\varepsilon\mathrm{Pe}}\frac{\partial c_0}{\partial x} + \beta_2\frac{\partial^2 c_0}{\partial x\partial t} + \beta_3\frac{\partial^2 c_0}{\partial t^2} + \beta_4\frac{\partial^2 c_0}{\partial x^2} + h_4\frac{\partial g}{\partial t} + Q_{\mathrm{f,in}}\frac{\partial g}{\partial x}\right) = h_4\frac{\partial^2 c_0}{\partial x^2} - \left.\frac{\partial c_{\mathrm{f}_2}}{\partial y}\right|_{y=H-h_4}, \tag{5.104}$$

where

$$\alpha_1 := \kappa_{\mathrm{m}}\phi_{\mathrm{m}}\left(\frac{A_{\mathrm{m}}}{2}x^2 + B_{\mathrm{m}}x\right), \qquad \alpha_2 := \frac{13}{40}Q_{\mathrm{l,in}}, \qquad \alpha_3 := \frac{1}{6}, \qquad \alpha_4 := \frac{39}{280}Q_{\mathrm{l,in}}^2, \tag{5.105}$$

and

$$\begin{aligned}
\beta_1 &:= -\alpha_1, \\
\beta_2 &:= Q_{\mathrm{f,in}}\left(\frac{1+h_2^2+h_3^2}{2}+\frac{h_2}{\phi_{\mathrm{m}}}+\frac{h_3}{\phi_{\mathrm{w}}}+\frac{h_2h_3\phi_{\mathrm{m}}}{\phi_{\mathrm{w}}}-\frac{7h_4^2}{10}\right)+Q_{\mathrm{l,in}}h_4\left(\frac{h_2}{\phi_{\mathrm{m}}}+\frac{h_3}{\phi_{\mathrm{w}}}+\frac{5}{8}\right), \\
\beta_3 &:= h_4\left(\frac{1+h_2^2+h_3^2}{2}+\frac{h_2}{\phi_{\mathrm{m}}}+\frac{h_3}{\phi_{\mathrm{w}}}-\frac{h_4^2}{3}+\frac{h_2h_3\phi_{\mathrm{m}}}{\phi_{\mathrm{w}}}\right), \\
\beta_4 &:= Q_{\mathrm{f,in}}\left[Q_{\mathrm{l,in}}\left(\frac{h_2}{\phi_{\mathrm{m}}}+\frac{h_3}{\phi_{\mathrm{w}}}+\frac{5}{8}\right)-\frac{13h_4Q_{\mathrm{f,in}}}{35}\right].
\end{aligned} \tag{5.106}$$

To eliminate $\partial c_{\mathrm{l}_2}/\partial y|_{y=1}$ and $\partial c_{\mathrm{f}_2}/\partial y|_{y=H-h_4}$, we can integrate equations (5.100) and (5.101) for the evolution of c_{m_2} and c_{w_2} across the porous membrane and cell layer, respectively, and use the following $\mathrm{O}(\varepsilon^2)$ boundary conditions

$$\frac{\partial c_{\mathrm{l}_2}}{\partial y} = \phi_{\mathrm{m}}\frac{\partial c_{\mathrm{m}_2}}{\partial y} \qquad \text{on} \quad y=1, \tag{5.107}$$

$$\phi_{\mathrm{m}}\frac{\partial c_{\mathrm{m}_2}}{\partial y} = \phi_{\mathrm{w}}\frac{\partial c_{\mathrm{w}_2}}{\partial y} \qquad \text{on} \quad y=1+h_2, \tag{5.108}$$

$$\phi_{\mathrm{w}}\frac{\partial c_{\mathrm{w}_2}}{\partial y} = \frac{\partial c_{\mathrm{f}_2}}{\partial y} \qquad \text{on} \quad y=H-h_4, \tag{5.109}$$

to find that

$$\begin{aligned}
\left.\frac{\partial c_{\mathrm{l}_2}}{\partial y}\right|_{y=1} = (\varepsilon\mathrm{Pe})^2\left(\gamma_2\frac{\partial^2 c_0}{\partial x\partial t}+\gamma_3\frac{\partial^2 c_0}{\partial t^2}-(h_2\phi_{\mathrm{m}}+h_3\phi_{\mathrm{w}})\frac{\partial g}{\partial t}\right) \\
+(h_2\phi_{\mathrm{m}}+h_3\phi_{\mathrm{w}})\frac{\partial^2 c_0}{\partial x^2}+\left.\frac{\partial c_{\mathrm{f}_2}}{\partial y}\right|_{y=H-h_4},
\end{aligned} \tag{5.110}$$

where

$$\begin{aligned}
\gamma_2 &:= -Q_{\mathrm{l,in}}\left(\frac{15}{24}(h_2\phi_{\mathrm{m}}+h_3\phi_{\mathrm{w}})+\frac{h_2^2+h_3^2}{2}+\frac{h_2h_3\phi_{\mathrm{w}}}{\phi_{\mathrm{m}}}\right), \\
\gamma_3 &:= -\left(\frac{(1+h_2^2+h_3^2)(1+h_2\phi_{\mathrm{m}}+h_3\phi_{\mathrm{w}})}{2}-\frac{1}{2}-\frac{h_2^3\phi_{\mathrm{m}}+h_3^3\phi_{\mathrm{w}}}{3}+\frac{h_2h_3\phi_{\mathrm{w}}}{\phi_{\mathrm{m}}}\right).
\end{aligned} \tag{5.111}$$

Hence, by adding together (5.103) and (5.104) we can obtain the following solvability condition for $g(x,t)$:

$$\begin{aligned}
&\bar{h}\frac{\partial g}{\partial t}+(Q_{\mathrm{l,in}}+Q_{\mathrm{f,in}})\frac{\partial g}{\partial x} = \\
&\quad(\gamma_2-\alpha_2-\beta_2)\frac{\partial^2 c_0}{\partial x\partial t}+(\gamma_3-\alpha_3-\beta_3)\frac{\partial^2 c_0}{\partial t^2}+\left(\frac{\bar{h}}{(\varepsilon\mathrm{Pe})^2}-\alpha_4-\beta_4\right)\frac{\partial^2 c_0}{\partial x^2}.
\end{aligned} \tag{5.112}$$

However, the physical interpretation of $g(x,t)$ is not immediately clear. To formulate this system in a more physically relevant way, we rewrite equation (5.112) in terms of the globally

averaged concentration at $\mathrm{O}(\varepsilon)$, which we denote by $\bar{c}_1$. To determine $\bar{c}_1$, we average the $\mathrm{O}(\varepsilon)$ concentrations in each layer in turn, and then add them together, with appropriate weighting by porosity in the membrane and cell layer:

$$\bar{c}_1 := \bar{c}_{\mathrm{l}_1} + h_2\phi_{\mathrm{m}}\bar{c}_{\mathrm{m}_1} + h_3\phi_{\mathrm{w}}\bar{c}_{\mathrm{w}_1} + h_4\bar{c}_{\mathrm{f}_1}, \tag{5.113}$$

where

$$\begin{aligned} \bar{c}_{\mathrm{l}_1} &= \int_0^1 c_{\mathrm{l}_1}\,\mathrm{d}y, \qquad \bar{c}_{\mathrm{m}_1} = \frac{1}{h_2}\int_1^{1+h_2} c_{\mathrm{m}_1}\,\mathrm{d}y, \\ \bar{c}_{\mathrm{w}_1} &= \frac{1}{h_3}\int_{1+h_2}^{1+h_2+h_3} c_{\mathrm{w}_1}\,\mathrm{d}y, \qquad \bar{c}_{\mathrm{f}_1} = \frac{1}{h_4}\int_{H-h_4}^{H} c_{\mathrm{f}_1}\,\mathrm{d}y. \end{aligned} \tag{5.114}$$

Using the expressions for the $\mathrm{O}(\varepsilon)$ concentrations from equations (5.89)-(5.92), we find

$$\bar{c}_1 = \varepsilon\mathrm{Pe}\left(\lambda_1\frac{\partial c_0}{\partial t} + \lambda_2\frac{\partial c_0}{\partial x} + \frac{h_3^2(h_3\phi_{\mathrm{w}} + 3h_4)\mathcal{R}}{6\varepsilon\mathrm{Pe}\phi_{\mathrm{w}}} + \bar{h}g(x,t)\right), \tag{5.115}$$

where

$$\begin{aligned} \lambda_1 := \frac{1}{2}\left(1 + h_2^2 + h_3^2\right)\bar{h} - \frac{1 + h_2^3\phi_{\mathrm{m}} + h_3^3\phi_{\mathrm{w}} + h_4^3}{3} \\ + h_4\left(\frac{h_2}{\phi_{\mathrm{m}}} + \frac{h_3}{\phi_{\mathrm{w}}}\right) + \frac{h_2h_3\phi_{\mathrm{w}}}{\phi_{\mathrm{m}}} + \frac{h_2h_3h_4\phi_{\mathrm{m}}}{\phi_{\mathrm{w}}}, \end{aligned} \tag{5.116}$$

$$\begin{aligned} \lambda_2 := Q_{\mathrm{l,in}}\left[\frac{1}{2}(h_2^2 + h_3^2) + \frac{5}{8}(h_2\phi_{\mathrm{m}} + h_3\phi_{\mathrm{w}} + h_4)\right. \\ \left. + \frac{h_2h_3\phi_{\mathrm{w}}}{\phi_{\mathrm{m}}} + h_4\left(\frac{h_2}{\phi_{\mathrm{m}}} + \frac{h_3}{\phi_{\mathrm{w}}}\right) + \frac{9}{40}\right] - \frac{7h_4^2Q_{\mathrm{f,in}}}{20}. \end{aligned} \tag{5.117}$$

We can therefore rewrite equation (5.112) for $g(x,t)$ in terms of $\bar{c}_1$, which yields

$$\varepsilon\mathrm{Pe}\left(\bar{h}\frac{\partial\bar{c}_1}{\partial t} + (Q_{\mathrm{l,in}} + Q_{\mathrm{f,in}})\frac{\partial\bar{c}_1}{\partial x}\right) = \bar{h}^2\left[1 + (\varepsilon\mathrm{Pe})^2\,\widetilde{K}\right]\frac{\partial^2 c_0}{\partial x^2}, \tag{5.118}$$

where we have used the fact that differentiating equation (5.96) with respect to x yields the relationship

$$\frac{\partial^2 c_0}{\partial x\partial t} = -\frac{(Q_{\mathrm{l,in}} + Q_{\mathrm{f,in}})}{\bar{h}}\frac{\partial^2 c_0}{\partial x^2}, \tag{5.119}$$

in order to eliminate $\partial^2 c_0/\partial x\partial t$. We also note that the coefficients of $\partial^2 c_0/\partial t^2$ cancel, so that this term does not appear in the final equation. The $\mathrm{O}(1)$ constant $\widetilde{K}$ is given in terms of previous constants by

$$\widetilde{K} := \frac{1}{\bar{h}^2}\left((Q_{\mathrm{l,in}} + Q_{\mathrm{f,in}})(\alpha_2 + \beta_2 - \gamma_2) - \frac{(Q_{\mathrm{l,in}} + Q_{\mathrm{f,in}})^2\,\lambda_1}{\bar{h}} - \bar{h}(\alpha_4 + \beta_4)\right). \tag{5.120}$$

We now again consider the upstream inner region, and through the analysis in Appendix B.1 find that there is an $\mathrm{O}(\varepsilon)$ contribution to the outer inlet concentration, due to uptake

of solute in the inner region at this order. This will affect the outer solution through the boundary condition on $\bar{c}_1$ at $x = 0$, and is an unknown function of t which would need to be determined by numerically solving the full inner problem (see Appendix B.1 for details). This would be extremely computationally expensive due to the complex geometry of the ECS ports and lies beyond the scope of this chapter. Instead, we denote this degree of freedom by $\bar{h}\bar{c}_{\mathrm{u}}(t)$ (we have introduced $\bar{h}$ for algebraic convenience later on), so that the appropriate upstream boundary condition to apply on $\bar{c}_1$ is

$$\bar{c}_1(0,t) = \bar{h}\bar{c}_{\mathrm{u}}(t). \tag{5.121}$$

Given $\bar{c}_{\mathrm{u}}$, this then fully determines the solute concentrations at this order and hence again no condition needs to be applied downstream, with the outer solution instead influencing the $\mathrm{O}(\varepsilon)$ downstream inner solution.

Through equations (5.96) and (5.118), and boundary conditions (5.97) and (5.121), we therefore have the following system to solve for c_0 and $\bar{c}_1$:

$$\begin{gathered}
\bar{h}\frac{\partial c_0}{\partial t} + (Q_{\mathrm{l,in}} + Q_{\mathrm{f,in}})\frac{\partial c_0}{\partial x} = -\frac{h_3\mathcal{R}}{\varepsilon\mathrm{Pe}}, \\
\varepsilon\mathrm{Pe}\left(\bar{h}\frac{\partial \bar{c}_1}{\partial t} + (Q_{\mathrm{l,in}} + Q_{\mathrm{f,in}})\frac{\partial \bar{c}_1}{\partial x}\right) = \bar{h}^2\left[1 + (\varepsilon\mathrm{Pe})^2\,\widetilde{K}\right]\frac{\partial^2 c_0}{\partial x^2}, \\
c_0 = c_{\mathrm{in}}(t), \qquad \bar{c}_1 = \bar{h}\bar{c}_{\mathrm{u}}(t) \qquad \text{at} \quad x = 0,
\end{gathered} \tag{5.122}$$

given appropriate forms for $c_{\mathrm{in}}(t)$ and $\bar{c}_{\mathrm{u}}(t)$, and initial conditions for c_0 and $\bar{c}_1$.

5.3.7 Constant inlet concentration

Firstly, we consider the simplest case in which c_{in} is constant in time, *i.e.* the lumen and upper fluid layer inlets are maintained at constant concentration. The corresponding time-dependent inlet concentration problem is considered in Appendices B and C. We use the method of characteristics to solve (5.122), subject to the initial conditions $c_0(x,0) = \bar{c}_1(x,0) = 0$. For simplicity, and given that we do not have a form for $\bar{c}_{\mathrm{u}}$, we also assume that $\bar{c}_{\mathrm{u}}$ (and so, in steady state, $\bar{c}_1$), is a constant. This yields

$$c_0 = \begin{cases} -\dfrac{h_3\mathcal{R}}{\varepsilon\mathrm{Pe}(Q_{\mathrm{l,in}} + Q_{\mathrm{f,in}})}x + c_{\mathrm{in}} & \text{for} \quad 0 \le x \le \xi, \\ 0 & \text{otherwise,} \end{cases} \tag{5.123}$$

$$\bar{c}_1 = \begin{cases} \bar{h}\bar{c}_{\mathrm{u}} & \text{for} \quad 0 \le x \le \xi, \\ 0 & \text{otherwise,} \end{cases} \tag{5.124}$$

where

$$\xi := \min\left[\frac{(Q_{\mathrm{l,in}}+Q_{\mathrm{f,in}})}{\bar{h}}t, \frac{\varepsilon \mathrm{Pe}(Q_{\mathrm{l,in}}+Q_{\mathrm{f,in}})c_{\mathrm{in}}}{h_3\mathcal{R}}, 1\right]. \tag{5.125}$$

The first term in the definition of ξ denotes the x coordinate that the wave of solute has reached by time t, whilst the second term represents the x value at which the concentration reaches zero due to uptake. Thus, as expected, constant uptake of solute in the cell layer results in a linear concentration profile at leading order.

5.3.8 Averaged formulation

To investigate numerically the unsteady results arising from situations in which c_{in} is not constant, and motivated by similar problems in the literature (as discussed in §5.1), we return to the system (5.122) along with initial conditions

$$c_0 = 0, \qquad \bar{c}_1 = 0 \qquad \text{at} \quad t = 0. \tag{5.126}$$

By setting

$$\bar{c}_0 := \bar{h}c_0, \tag{5.127}$$

we can combine equations (5.96) and (5.118) to yield

$$\frac{\partial \bar{c}}{\partial t} + \frac{(Q_{\mathrm{l,in}}+Q_{\mathrm{f,in}})}{\bar{h}}\frac{\partial \bar{c}}{\partial x} = D_{\mathrm{eff}}\frac{\partial^2 \bar{c}}{\partial x^2} - \frac{h_3\mathcal{R}}{\varepsilon \mathrm{Pe}}, \tag{5.128}$$

where

$$\bar{c} = \bar{c}_0 + \varepsilon \bar{c}_1 \tag{5.129}$$

and

$$D_{\mathrm{eff}} := \frac{1}{\mathrm{Pe}}\left[1 + (\varepsilon \mathrm{Pe})^2\,\widetilde{K}\right], \tag{5.130}$$

where $\widetilde{K}$ is defined in equation (5.120). Equation (5.128) describes the transport of the averaged, combined-order solute concentration $\bar{c}$ throughout the bioreactor, accurate up to and including terms of $\mathrm{O}(\varepsilon)$. If we consider the form of D_{eff} we recognise it as an effective diffusion coefficient (of $\mathrm{O}(1/\mathrm{Pe}) = \mathrm{O}(\varepsilon)$) of a similar form to that found in classical Taylor dispersion [11, 162, 163], illustrating the fact that the diffusion of the (averaged) solute throughout the bioreactor is enhanced by the flow field. In §5.4.2 we will investigate the dependence of this enhanced diffusion on relevant dimensionless parameters in our model.

We note that in combining the $\mathrm{O}(1)$ and $\mathrm{O}(\varepsilon)$ equations we have, through the addition of a diffusion term at leading order, moved from a coupled system of two hyperbolic PDEs

with the necessary two upstream boundary conditions to a single, parabolic PDE with a single boundary condition:

$$\bar{c} = \bar{h}[c_{\text{in}}(t) + \varepsilon \bar{c}_{\text{u}}(t)] \qquad \text{at} \quad x = 0. \tag{5.131}$$

The parabolic nature of the system will be advantageous for solving the problem numerically; however, to do so we require an additional boundary condition which we impose at $x = 1$. The exact choice is unimportant, as long as the selected boundary condition does not introduce significant errors. Any such error will become apparent in a boundary layer near $x = 1$ in which the diffusion term is no longer smaller than the remaining terms in equation (5.128) and instead there is a dominant balance between advection and diffusion. From analysis of this boundary layer (see Appendix C), we find that choosing the condition

$$\frac{\partial \bar{c}}{\partial x} = 0 \qquad \text{at} \quad x = 1 \tag{5.132}$$

results in an error of $\mathrm{O}(\varepsilon^2)$ away from this boundary layer, and of $\mathrm{O}(\varepsilon)$ within the boundary layer. Hence, except for in a region of width $\mathrm{O}(\varepsilon)$ near $x = 1$ the introduced errors only come in at orders greater than the accuracy of the system. This is therefore an appropriate choice for the second boundary condition to impose on (5.128).

In the limit of an impermeable membrane and cell layer ($\phi_{\text{m}},\ \phi_{\text{w}} \to 0$), we recover from our asymptotic analysis the equations of classical Taylor dispersion in a pipe. This is done by averaging the solute governing equations in the lumen and upper fluid layer at $\mathrm{O}(1)$ and $\mathrm{O}(\varepsilon)$, combining orders and re-dimensionalising (see Appendix D for details), which gives

$$\frac{\partial \bar{c}_{\text{l}}}{\partial t} + \bar{u}_{\text{l}} \frac{\partial \bar{c}_{\text{l}}}{\partial x} = D \left(1 + \frac{1}{210} \frac{(2h_1)^2 \bar{u}_{\text{l}}^2}{D^2} \right) \frac{\partial^2 \bar{c}_{\text{l}}}{\partial x^2}, \tag{5.133}$$

$$\frac{\partial \bar{c}_{\text{f}}}{\partial t} + \bar{u}_{\text{f}} \frac{\partial \bar{c}_{\text{f}}}{\partial x} = D \left(1 + \frac{1}{210} \frac{(h_4)^2 \bar{u}_{\text{f}}^2}{D^2} \right) \frac{\partial^2 \bar{c}_{\text{f}}}{\partial x^2}, \tag{5.134}$$

where the mean velocities $\bar{u}_{\text{l}}$ and $\bar{u}_{\text{f}}$ are respectively given by

$$\bar{u}_{\text{l}} = \frac{1}{h_1} \int_0^{h_1} u_{\text{l}} \, \mathrm{d}y, \qquad \bar{u}_{\text{f}} = \frac{1}{h_4} \int_{H-h_4}^{H} u_{\text{f}} \, \mathrm{d}y. \tag{5.135}$$

We note that the mean velocity in the lumen is the same whether we consider the half-lumen $0 < y < h_1$ or the full lumen $-h_1 < y < h_1$. Hence the result for the half-lumen problem considered here is equivalent to that for the full lumen, only valid for a different range of y values. The classical Taylor dispersion result corresponds to Poiseuille flow in a full channel of width $2h_1$, and hence here we must consider the full lumen for the purposes

of comparison. The classical Taylor dispersion result for flow in a two-dimensional channel of width d and mean velocity U is [12, 162]

$$\frac{\partial c}{\partial t} + U\frac{\partial c}{\partial x} = D\left(1 + \frac{U^2 d^2}{210 D^2}\right)\frac{\partial^2 c}{\partial x^2}, \tag{5.136}$$

and thus equation (5.133) agrees with the classical result for the (full) lumen (width $2h_1$, mean velocity $Q_{\mathrm{l,in}}/h_1$) and equation (5.134) with the classical result for the upper fluid layer (width h_4, mean velocity $Q_{\mathrm{f,in}}/h_4$).

5.4 Results

We now investigate the behaviour of the solutions obtained in §5.3.7 and §5.3.8, focussing on how variations in key parameter values affect the distribution and uptake of solute throughout the outer region.

5.4.1 Constant inlet concentration

We first consider the solutions to the outer problem derived in §5.3.6 at both $\mathrm{O}(1)$ and $\mathrm{O}(\varepsilon)$ and investigate the qualitative trends arising from varying certain key parameters. We focus on the steady-state solutions (*i.e.* once the initial wave of solute has passed through the bioreactor) and so from (5.123)-(5.125) we have

$$c_0 = \begin{cases} -\dfrac{h_3\mathcal{R}}{\varepsilon \mathrm{Pe}(Q_{\mathrm{l,in}} + Q_{\mathrm{f,in}})}x + c_{\mathrm{in}} & \text{for} \quad 0 \le x \le \min\left[\dfrac{\varepsilon \mathrm{Pe}(Q_{\mathrm{l,in}} + Q_{\mathrm{f,in}})c_{\mathrm{in}}}{h_3\mathcal{R}}, 1\right], \\ 0 & \text{otherwise.} \end{cases} \tag{5.137}$$

Thus at leading order the nutrient concentration decreases linearly in x, and provided

$$c_{\mathrm{in}} > \frac{h_3\mathcal{R}}{\varepsilon \mathrm{Pe}(Q_{\mathrm{l,in}} + Q_{\mathrm{f,in}})}, \tag{5.138}$$

we have a non-zero solute concentration throughout the bioreactor. In steady state at $\mathrm{O}(\varepsilon)$, (5.124) tells us that $\bar{c}_1$ is constant in space provided (5.138) holds (which we henceforth assume is the case). We therefore note from equation (5.115) that, given the solution for c_0, g is also a constant. Hence (from (5.89)-(5.92)) the first-order outer solute concentrations c_{i_1} ($i = \mathrm{l}, \mathrm{m}, \mathrm{w}, \mathrm{f}$) are independent of both x and t. Thus, we investigate how the y-dependence of these solutions varies for different values of the inlet fluxes $Q_{\mathrm{l,in}}$ and $Q_{\mathrm{f,in}}$, the cell-scaffold porosity ϕ_{w} and the cell layer height h_3.

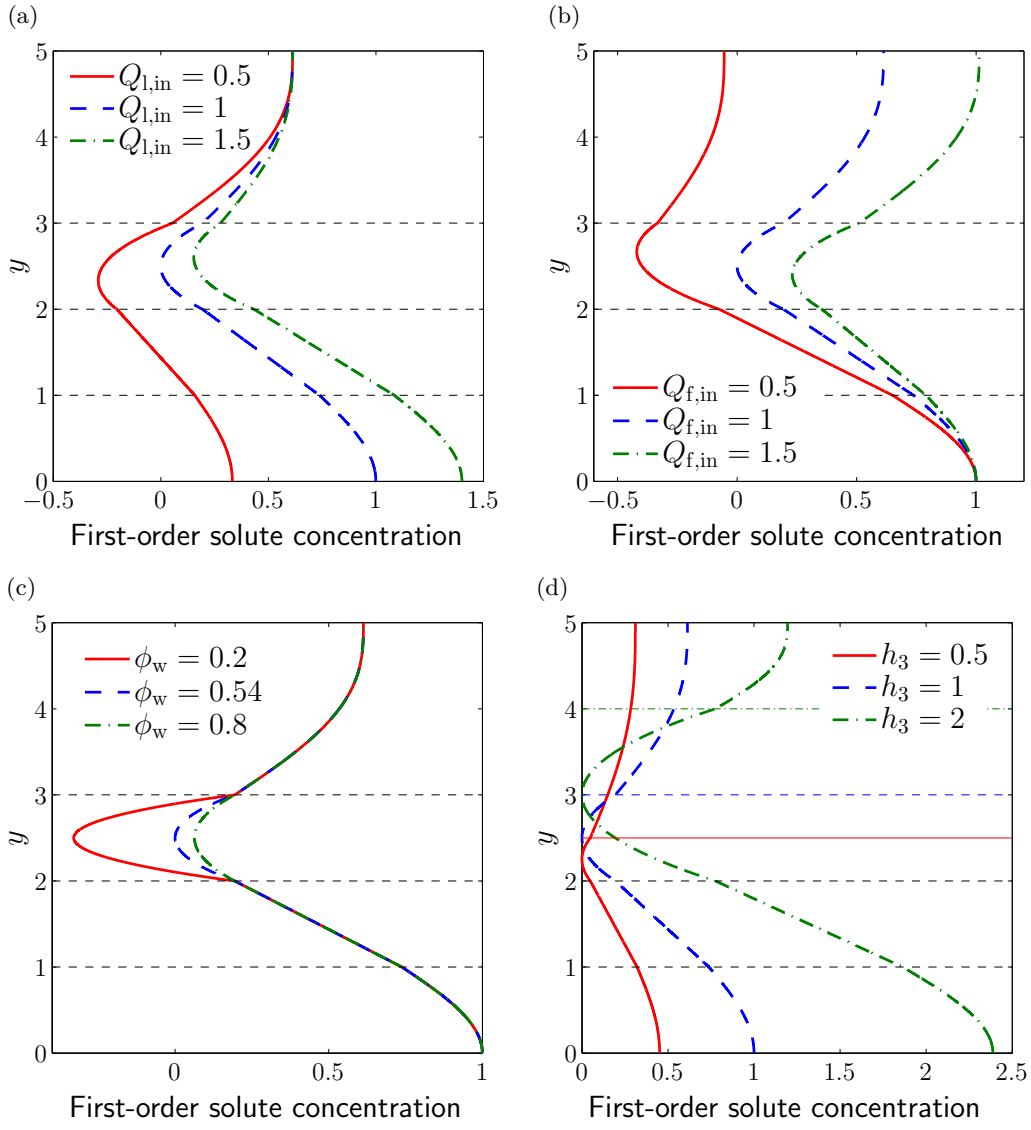

Figure 5.3: Plots of the first-order solute concentration in each layer for (a) varying lumen inlet flux $Q_{l,in}$, fixed point $y = 5$; (b) varying upper fluid layer inlet flux $Q_{f,in}$, fixed point $y = 0$; (c) varying cell layer porosity ϕ_w, fixed point $y = 0$; and (d) varying cell layer height h_3, fixed point minimum of the first-order solute concentration. In addition to translating to obtain a fixed point common to all 3 lines, plots have been normalised so that the dashed curved line representing results for the middle parameter value (which is the same for each plot) always lies between 0 and 1. Thin horizontal dashed lines denote the boundaries between the four layers; in (d) the cell layer/upper fluid layer interfaces are denoted using the same line style as the corresponding concentration. Fixed parameter values are as in Table 5.2, with $Q_{l,in} = Q_{f,in} = h_3 = 1$.

In Figure 5.3, we plot the first-order outer solute concentrations c_{i_1} $(i = \mathrm{l}, \mathrm{m}, \mathrm{w}, \mathrm{f})$ across the entire bioreactor height $0 < y < H$. The boundaries between each of the four layers are represented by horizontal lines. Given that the constant $\bar{c}_1$ (and so g, via (5.115)) could depend on any parameters (including those being varied), we focus on the qualitative differences which arise as a result of varying $Q_{\mathrm{l,in}}$, $Q_{\mathrm{f,in}}$, ϕ_{w}, and h_3, noting that the exact value of $\bar{c}_1$ (and so g) only affects the translation of each c_{i_1} curve in y-space, and not its shape. In order to compare the relative changes, firstly the whole plot is normalised so that the curve corresponding to the middle parameter value (the dashed blue line in each plot) lies between 0 and 1. This middle line uses the same parameter values for each of Figures 5.3(a)-(d), so that a direct comparison can be made between these plots. In addition, the other two curves are then translated so that all three curves take the same value at a particular fixed point. The choice of fixed point depends on the parameter being varied, and is chosen in order to make the differences between the relative shape of the curves as clear as possible.

In each of the plots in Figure 5.3 we observe that, as expected, the concentration is greatest in the lumen and upper fluid layer in each case, with a minimum in the cell layer. The point $y_{\mathrm{c,min}}$ at which this minimum occurs can be found by setting $\partial c_{\mathrm{w}_1}/\partial y = 0$ for c_0 given by equation (5.137), which yields

$$y_{\mathrm{c,min}} = 1 + h_2 + \frac{h_3 Q_{\mathrm{l,in}}}{Q_{\mathrm{l,in}} + Q_{\mathrm{f,in}}}. \tag{5.139}$$

Thus if $Q_{\mathrm{l,in}} = Q_{\mathrm{f,in}}$, the minimum occurs at $1 + h_2 + h_3/2$, *i.e.* in the middle of the cell layer. In the two limiting cases of no flow either in the lumen, $Q_{\mathrm{l,in}} = 0$, or in the upper fluid layer, $Q_{\mathrm{f,in}} = 0$, the minimum occurs on the membrane/cell layer interface and cell layer/upper fluid layer interface, respectively.

Figure 5.3(a) shows the trend resulting from varying $Q_{\mathrm{l,in}}$, where the fixed point is the concentration on the top of the bioreactor ($y = 5$). As $Q_{\mathrm{l,in}}$ increases, we see that the concentration in the lumen increases relative to that in the upper fluid layer as the solute is being advected more strongly in the lumen (and vice versa if $Q_{\mathrm{l,in}}$ is decreased). In both of the cases $Q_{\mathrm{l,in}} > Q_{\mathrm{f,in}}$ and $Q_{\mathrm{l,in}} < Q_{\mathrm{f,in}}$, the minimum concentration moves away from the centre of the cell layer, as expected from (5.139), towards the upper fluid layer and lumen, respectively. Figure 5.3(b) (where the fixed point is the concentration on the lumen centreline, $y = 0$) shows that corresponding trends are observed if $Q_{\mathrm{f,in}}$ is varied, with the upper fluid layer concentration either increasing or decreasing relative to that in the lumen.

We note that the concentration in the upper fluid layer is less than that in the lumen when the inlet fluxes are equal. Although, for $h_3 = 1$, the cell layer is in the 'middle' of our two-dimensional domain, this asymmetry is not unexpected since the remaining layers below are both porous and free-flowing, whilst above there is only free-flowing fluid. From (5.89) and (5.92) we can find the required inlet fluid flux ratio in order for the $\mathrm{O}(\varepsilon)$ concentrations on the lumen centreline and bioreactor top to be equal:

$$\frac{Q_{\mathrm{l,in}}}{Q_{\mathrm{f,in}}} = \frac{\frac{h_3}{\phi_{\mathrm{w}}} + h_4}{2\left(\frac{5}{8} + \frac{h_2}{\phi_{\mathrm{m}}} + \frac{h_3}{2\phi_{\mathrm{w}}}\right)}. \tag{5.140}$$

Figure 5.3(c) shows the trends arising from varying the cell layer porosity ϕ_{w}, again with fixed point the lumen centreline $y = 0$. To interpret these results, we recall that $\mathcal{R}$ is defined as the uptake per unit volume of mixture (see §1.4). Here, we find that the only qualitative change in concentration occurs in the cell layer, where the concentration decreases relative to elsewhere as ϕ_{w} decreases. This is due to the fact that decreasing ϕ_{w} is equivalent to increasing the uptake per unit volume of fluid ($\mathcal{R}/\phi_{\mathrm{w}}$). It could also be interpreted as an increase in cell population density, which would also result in more solute being taken up.

Finally, varying the height of the cell layer is investigated in Figure 5.3(d), where the fixed point is the minimum concentration value. For lower values of h_3 there is less overall variation in concentration throughout the bioreactor. This is due to the fact that a thinner cell layer implies less solute is being taken up by the cells, and is to be expected given that h_3 appears in the uptake term in (5.96). Additionally, and in agreement with our findings in equation (5.139), we observe that the minimum concentration is always in the middle of the cell layer.

5.4.2 Averaged formulation

We now consider features of the unsteady system derived in §5.3.8, beginning with the effective diffusion coefficient D_{eff} and its sensitivity to certain experimentally controlled parameters. We then solve the unsteady system in order to investigate variations in the mean solute uptake and solute exposure time.

Effective diffusion coefficient

The form of D_{eff} as given in (5.130) is algebraically complex and its dependence on the main varying parameters ϕ_{m}, ϕ_{w}, $Q_{\mathrm{l,in}}$, $Q_{\mathrm{f,in}}$, and h_3 is not transparent. In Figure 5.4, we have plotted the effective diffusion coefficient versus each of these parameters, taking into

account the range of validity and any physical constraints in each case. We also plot D_{eff} for a range of values of the Péclet number Pe to demonstrate the amount of variation obtained for $1 \ll \text{Pe} \ll \varepsilon^{-2}$. Figure 5.4(a) shows that D_{eff} monotonically decreases with increasing membrane porosity for $0 < \phi_{\text{m}} \leq 1$. When the cell layer porosity ϕ_{w} is increased, however, we see that after an initial decrease D_{eff} reaches a minimum and then increases again as ϕ_{w} approaches 1 (see Figure 5.4(b)). Figures 5.4(c) and (d) show the dependence of D_{eff} on the lumen and upper fluid layer inlet fluxes. For $Q_{\text{l,in}}$ or $Q_{\text{f,in}}$ sufficiently large ($\gtrsim 0.63, 1.23$ respectively for the parameter values used here), D_{eff} increases with increasing inlet fluid flux as would be expected from the classical Taylor result [12, 162]. However, below these minimum values, there is a slight increase in D_{eff} as the fluid flux decreases towards zero. We claim that this is due to the nonlinearity of D_{eff}, which has terms that depend on $Q_{\text{l,in}}Q_{\text{f,in}}$ as well as their respective squares. We note that if we set $Q_{\text{l,in}} = Q_{\text{f,in}}$ then D_{eff} increases monotonically with inlet fluid flux (results not shown). In Figure 5.4(e) we can see that there is a gradual decrease in D_{eff} as the cell layer height h_3 increases to around 1. For values greater than this, however, the effective diffusion coefficient increases more rapidly with h_3. This is an interesting observation, but it is not straightforward to determine from the form of D_{eff} given that increasing h_3 results in a corresponding decrease of the upper fluid layer h_4, both of which contribute to D_{eff}. Finally, Figure 5.4(f) shows the expected combination of linear and inverse dependence of D_{eff} on Pe. This is included for completeness and to show the magnitude of the variation in D_{eff} which can be obtained by varying Pe.

Pulse of solute

We move on to investigate the behaviour of the unsteady system (5.128) by considering what happens to a pulse of solute introduced upstream. To make analysis of the results more transparent, we simplify the boundary condition at $x = 0$ by taking $\bar{c}_{\text{u}}(t) \equiv 0$ and setting

$$\bar{c}(0,t) = \bar{h}c_{\text{in}}(t) = \frac{10}{\sqrt{\pi}}\text{e}^{-100t^2}, \tag{5.141}$$

where the form of $\bar{h}c_{\text{in}}(t)$ is motivated by a similar condition in [62]. At leading order, this could be interpreted physically as setting the concentration into the upstream ECS port to be zero, and sending a pulse of solute into the lumen inlet such that (see equation (5.82))

$$c_{\text{l,in}}(t) = \frac{(Q_{\text{l,in}} + Q_{\text{f,in}})}{\bar{h}Q_{\text{l,in}}}\frac{10}{\sqrt{\pi}}\text{e}^{-100t^2}. \tag{5.142}$$

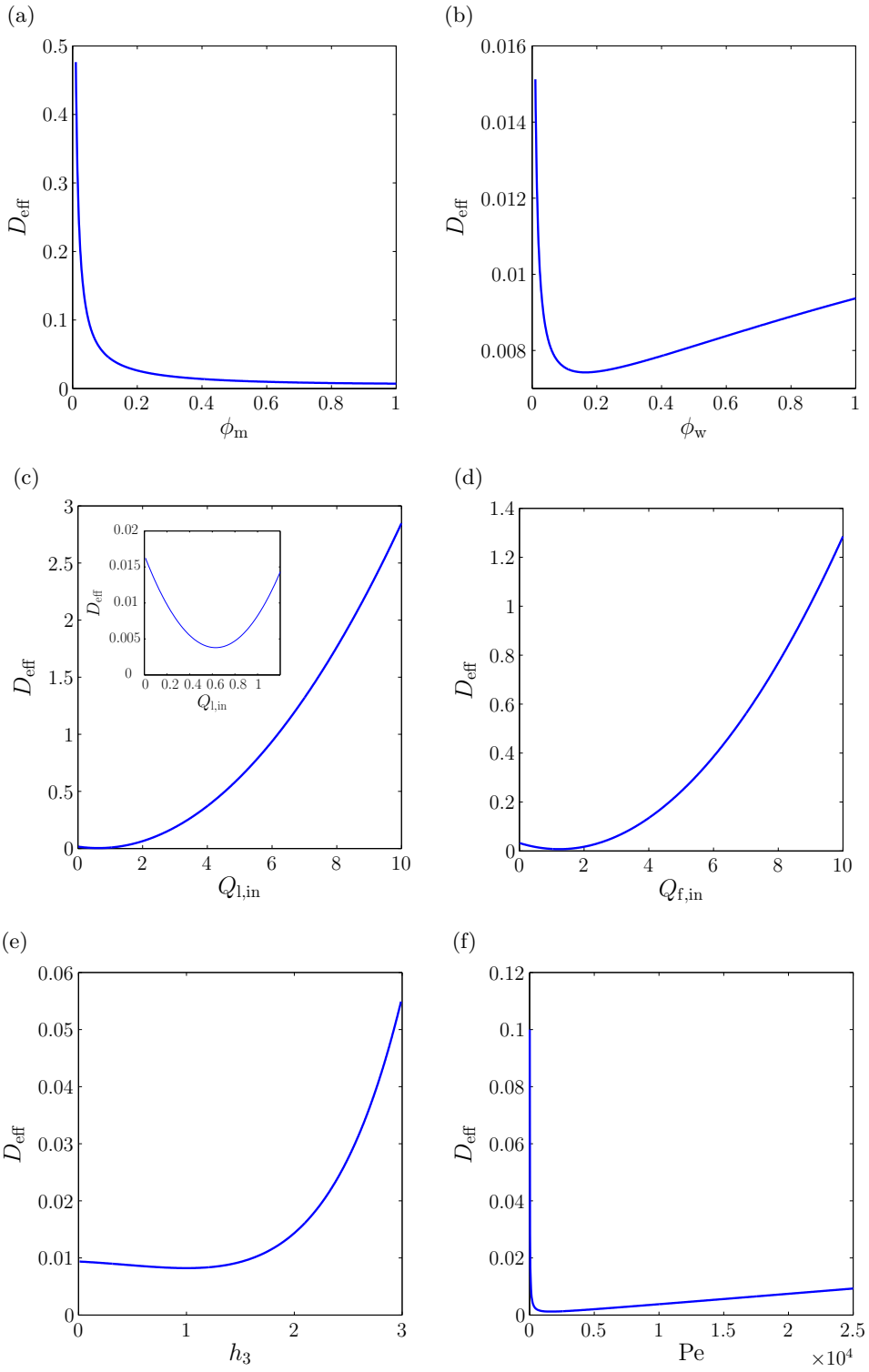

Figure 5.4: Plots of D_{eff} versus (a) the membrane porosity ϕ_{m}, (b) the cell layer porosity ϕ_{w}, (c) the lumen inlet flux $Q_{\text{l,in}}$ (inset showing detail at the minimum of D_{eff}), (d) the upper fluid layer inlet flux $Q_{\text{f,in}}$, (e) the cell layer height h_3, and (f) the Péclet number Pe. Fixed parameter values are as in Table 5.2, with $Q_{\text{l,in}} = Q_{\text{f,in}} = h_3 = 1$.

We close the system with the boundary condition (5.132) as discussed previously. The system (5.128), (5.132), and (5.141) was solved in MATLAB using the method of lines discussed in §2.6.1 and the inbuilt solver `ode15s`. Given that the order of accuracy of this system is $\mathrm{O}(\varepsilon^2)$, the reaction rate $\mathcal{R}$ was set to be zero for $\bar{c} < 10^{-6} = \mathrm{O}\left(\varepsilon^2\right)$ and equal to the constant value from Table 5.2 otherwise. Figure 5.5 shows a typical solution, demonstrating the evolution of the pulse of solute throughout the bioreactor. The effect of advection and diffusion on the solute concentration can clearly be seen, and we note that the uptake of solute can also be calculated (results not shown).

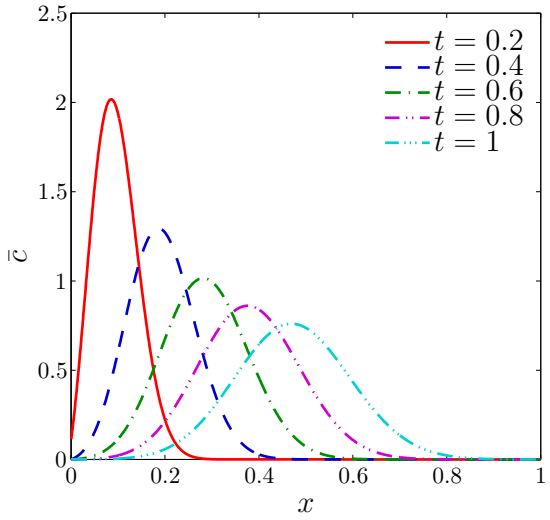

Figure 5.5: Plot of $\bar{c}$ versus x at fixed times between 0 and 1, with inlet condition given by equation (5.141). Fixed parameter values are as in Table 5.2, with $Q_{\mathrm{l,in}} = Q_{\mathrm{f,in}} = h_3 = 1$.

Next, we investigate how the solute exposure time and the (spatial and temporal) mean solute uptake varies with certain parameter values. To do this, we define the 'solute exposure time' T to be the time at which the concentration is less than 10^{-6} $(= \mathrm{O}\left(\varepsilon^2\right))$ throughout the bioreactor, *i.e.* the time it takes for the pulse of solute to leave the bioreactor, up to the order of accuracy of the system. We then compute the uptake $J(x,t)$ for $0 < x < 1$, $0 < t < T$ where

$$J(x,t) := \begin{cases} \dfrac{h_3 \mathcal{R}}{\varepsilon \mathrm{Pe}} & \text{if} \quad \bar{c} > 10^{-6}, \\ 0 & \text{otherwise.} \end{cases} \tag{5.143}$$

We define the mean uptake μ to be

$$\mu := \int_0^T \int_0^1 J(x,t)\, \mathrm{d}x\, \mathrm{d}t, \tag{5.144}$$

where we use the MATLAB function `trapz` to approximate the integrals using our numerical solution for $\bar{c}$. Figure 5.6 shows the dependence of μ and T on the parameter values ϕ_{m}, ϕ_{w}, $Q_{\mathrm{l,in}}$, $Q_{\mathrm{f,in}}$, h_3, and Pe. We note that the graphs of μ and T show identical trends for ϕ_{m}, ϕ_{w}, $Q_{\mathrm{l,in}}$, and $Q_{\mathrm{f,in}}$, indicating the fact that a longer solute exposure time correlates with a greater mean uptake as would be expected. The same is not true for the dependence of μ and T on h_3 and Pe, as these parameter values also affect the rate of solute uptake. However, Figures 5.6(e) and (f) do show that the maximum values of μ and T occur for the same values of h_3 and Pe, respectively. With the exception of the dependence of μ on h_3 and Pe, all graphs in Figures 5.6(a)-(f) demonstrate non-monotonic behaviour. This is likely to arise from the fact that the inlet fluid fluxes, porosities, and cell layer height all contribute (often nonlinearly) to both the advection speed $(Q_{\mathrm{l,in}} + Q_{\mathrm{f,in}})/\bar{h}$ and diffusion coefficient D_{eff}, which in turn have different effects on both μ and T. For instance, we would expect an increased advection speed to reduce the solute exposure time in the bioreactor T, and thereby also the mean uptake μ, as the cells have less time in which to take up nutrient. On the contrary, we would expect an increased diffusion coefficient to increase both μ and T, as it results in a more 'spread out' pulse of solute, and thus the cells are exposed to a significant concentration for longer.

5.5 Model extension

We recall our assumption in §5.2.2 of a constant cell layer porosity ϕ_{w}, but note that this is likely to not be the case. Therefore, we now briefly consider an extension to the model presented thus far, by deriving an expression for the leading-order steady-state concentration in the case where the cell layer porosity ϕ_{w} is not constant, but can vary in x and t.

5.5.1 Non-constant cell layer porosity

We revisit the analysis of §5.2 and §5.3 without the assumption that the cell volume fraction is constant, corresponding to a cell layer porosity ϕ_{w} $(= \theta_{\mathrm{w}})$ which can vary in x and t (but not y, motivated by the solutions to the multiphase systems). It therefore also follows that the cell volume fraction θ_{n} will vary in x and t, by virtue of the no voids condition $\theta_{\mathrm{n}} + \theta_{\mathrm{w}} + \theta_{\mathrm{s}} = 1$, and hence we need an additional equation compared to §5.2 and §5.3. Returning to the multiphase reduction presented in §5.2.2 but with θ_{n} and θ_{w} non-constant,

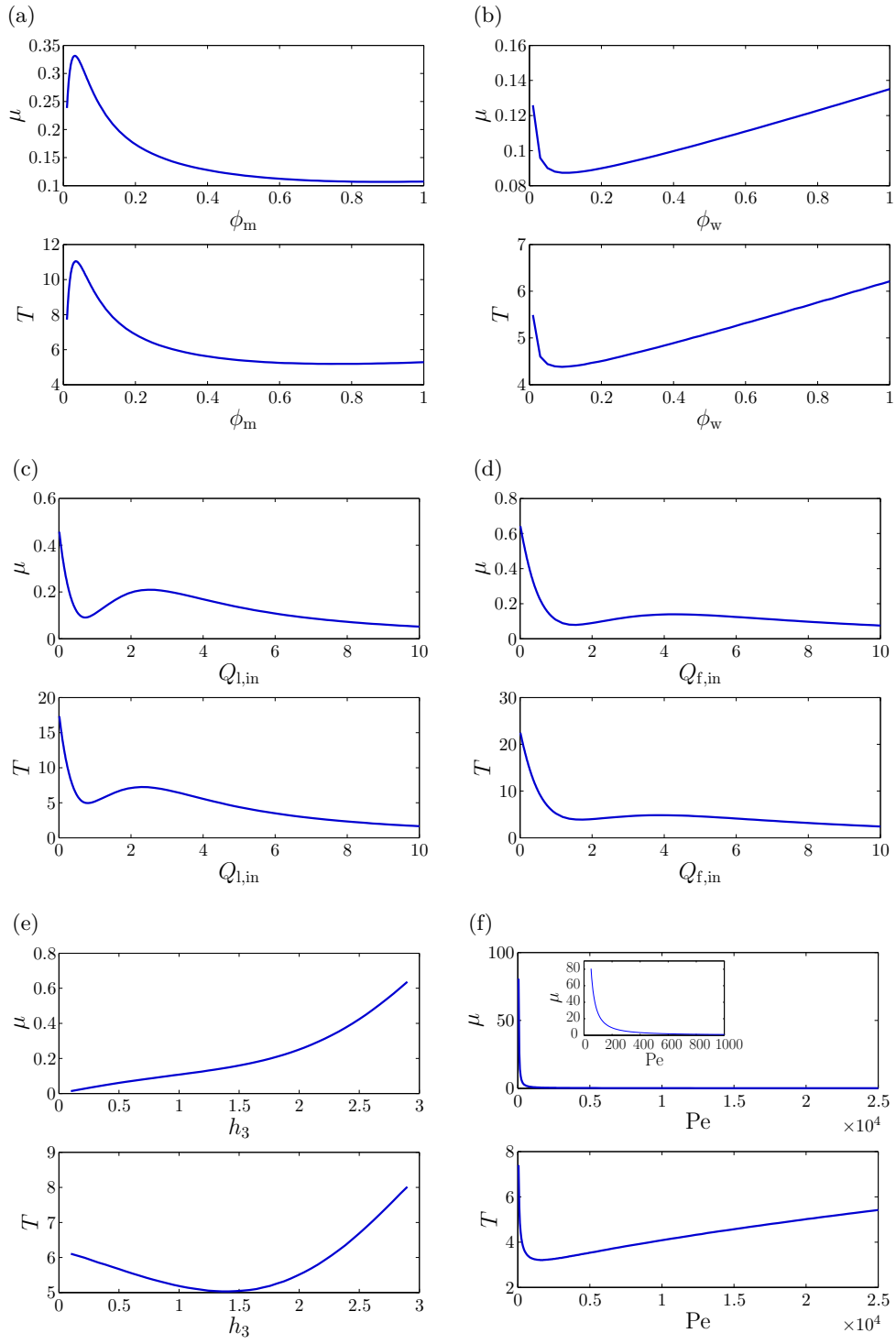

Figure 5.6: Plots of the mean solute uptake μ (top of each subfigure) and solute exposure time T (bottom) versus (a) the membrane porosity ϕ_{m}, (b) the cell layer porosity ϕ_{w}, (c) the lumen inlet flux $Q_{\mathrm{l,in}}$, (d) the upper fluid layer inlet flux $Q_{\mathrm{f,in}}$, (e) the cell layer height h_3, and (f) the Péclet number Pe (inset showing the detail for Pe < 1000). Fixed parameter values are as in Table 5.2, with $Q_{\mathrm{l,in}} = Q_{\mathrm{f,in}} = h_3 = 1$.

we find that the cell layer dynamics are governed via θ_n by equation (5.17)

$$\frac{\partial \theta_\mathrm{n}}{\partial t} = J_\mathrm{n}(\theta_\mathrm{n}, c), \tag{5.145}$$

and we also have the continuity equation in the cell layer, which takes the form (5.18)

$$\frac{\partial}{\partial x}\left(\phi_\mathrm{w} u_\mathrm{w}\right) + \frac{\partial}{\partial y}\left(\phi_\mathrm{w} v_\mathrm{w}\right) = 0. \tag{5.146}$$

We further assume that the solute reaction term $\mathcal{R}$ depends on x and t through ϕ_w. We non-dimensionalise with the same scalings as in §5.3.4 and, following the asymptotic analysis from §5.3.5 and §5.3.6, the leading-order system to solve for c is (dropping the subscript 0)

$$\bar{h}\frac{\partial c}{\partial t} + (Q_\mathrm{l,in} + Q_\mathrm{f,in})\frac{\partial c}{\partial x} + h_3 c\frac{\partial \phi_\mathrm{w}}{\partial t} = -\frac{h_3 \mathcal{R}(\phi_\mathrm{w})}{\varepsilon \mathrm{Pe}}. \tag{5.147}$$

We are interested in the steady state to which this system evolves on the long timescale. We would expect the solute concentration to settle down to a steady state on a relatively short timescale given the flow regime we consider, and then the cell layer porosity to reach steady state over a longer timescale (that of the previously neglected cell kinetics). These steady states, once reached, will be governed by the steady states of equations (5.145) and (5.147):

$$J_\mathrm{n}(\theta_\mathrm{n}, c) = 0, \qquad \frac{\partial c}{\partial x} = -\frac{h_3 \mathcal{R}(\phi_\mathrm{w})}{\varepsilon \mathrm{Pe}(Q_\mathrm{l,in} + Q_\mathrm{f,in})}. \tag{5.148a,b}$$

The solution for c and ϕ_w (via θ_n) then depends on the exact form of J_n and $\mathcal{R}$. Taking a typical form for J_n in the case of nutrient-dependent cell growth used in Chapters 2 and 3,

$$J_\mathrm{n} = \frac{\Gamma_\mathrm{nw}\theta_\mathrm{n}\theta_\mathrm{w} c}{K + c} - \Gamma_\mathrm{wn}\theta_\mathrm{n}, \tag{5.149}$$

and replacing θ_w by ϕ_w yields the following expression for ϕ_w in terms of c at steady state:

$$\phi_\mathrm{w} = \frac{\Gamma_\mathrm{wn}(K + c)}{\Gamma_\mathrm{nw} c}. \tag{5.150}$$

We note that, given this form for J_n, (5.150) does not guarantee that $\phi_\mathrm{w} < 1$ for all x, which would be a requirement for a more generally valid model. However, for the purposes of this brief analysis, the choice of parameter values in Figure 5.7 does ensure this condition is satisfied. If we now, for simplicity, set $\mathcal{R} = R\phi_\mathrm{w}$ for some constant R (which is then the rate of uptake per unit volume of fluid), then equation (5.150) for ϕ_w can be substituted into (5.148b) to give

$$\frac{\partial c}{\partial x} = -\frac{h_3 R \Gamma_\mathrm{wn}}{\varepsilon \mathrm{Pe}(Q_\mathrm{l,in} + Q_\mathrm{f,in})\Gamma_\mathrm{nw}}\left(1 + \frac{K}{c}\right). \tag{5.151}$$

We impose the steady-state constant inlet concentration condition

$$c = c_{\text{in}} \qquad \text{at} \quad x = 0, \tag{5.152}$$

which enables an implicit expression for c to be found:

$$c - K\ln(c+K) = -\frac{h_3 R\Gamma_{\text{wn}} x}{\varepsilon \text{Pe}(Q_{\text{l,in}} + Q_{\text{f,in}})\Gamma_{\text{nw}}} + c_{\text{in}} - K\ln(c_{\text{in}} + K). \tag{5.153}$$

Thus we have found an expression for the steady-state, leading-order solute concentration in a simple first case of non-constant $\mathcal{R}$ and ϕ_{w} which couples the fast-timescale fluid flow considered in this chapter with the slow-timescale cell kinetics neglected in the analysis thus far. Plots of c and ϕ_{w} at steady state can be seen in Figure 5.7 showing that, with this choice of J_{n} and $\mathcal{R}$ and representative parameter values, the steady-state cell layer porosity increases monotonically with x, *i.e.* the volume fraction of cells decreases along the length of the bioreactor. The nutrient concentration decreases from the inlet towards the downstream end of the bioreactor, as has been seen in the previous nutrient results of Chapter 2. This suggests that in this case the cells (slightly) preferentially grow upstream where there is more nutrient, but not at a sufficiently high density to deplete the nutrient in that region. With a higher uptake rate, however, this would not necessarily be the case. We also note that the corresponding first-order analysis is possible in this case, but becomes much more algebraically complex and so we do not pursue this here.

5.6 Conclusions

We have developed a two-dimensional model for a simplified HFMB in which the ECS consists of a rigid, porous cell layer below a free-flowing upper layer of fluid. Our aim was to determine the dependence of the solute concentration field on the underlying parameters of the system: the inlet fluid fluxes, membrane porosity, cell layer height and porosity (and hence, implicitly, solute uptake rate). By considering sufficiently high flow rates and focussing on a timescale characterised by advection in the lumen, cell motility, death, and proliferation, all of which occur on longer timescales, can be neglected and the cell layer assumed to have constant porosity and permeability. A solute, for instance a nutrient such as oxygen, is supplied at both the lumen and upper fluid layer inlets and is taken up by the cells at a constant rate per unit volume of mixture. The governing equations and boundary conditions have been non-dimensionalised, exploiting the small aspect ratio ε of the lumen.

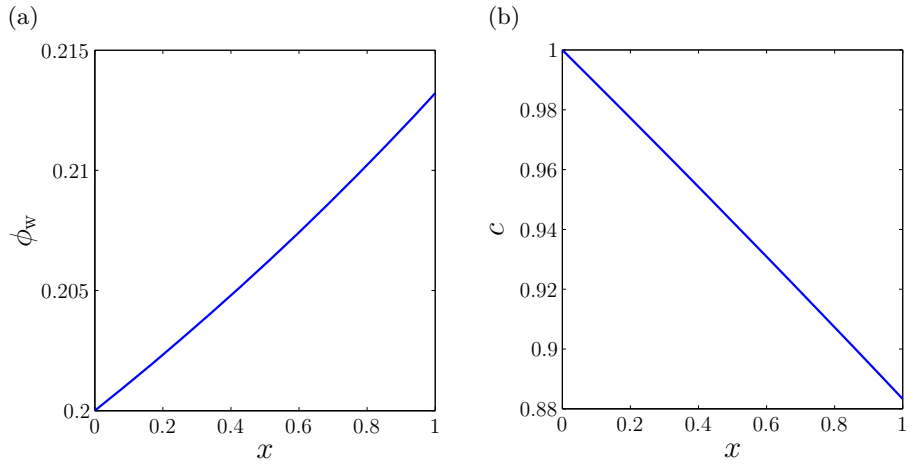

Figure 5.7: Steady-state plots of (a) the cell layer porosity ϕ_w, and (b) the leading-order solute concentration c, in the case where ϕ_w can vary in x. Representative parameter values were chosen as follows: $h_3 = 1$, $R = 50$, $\Gamma_{nw} = 10$, $\Gamma_{wn} = 1$, $K = 1$, $c_{in} = 1$, $Q_{l,in} = 1$, $Q_{f,in} = 1$, $\varepsilon \mathrm{Pe} = 44.2$.

The flow regime in which the Péclet number $\mathrm{Pe} = \mathrm{O}(1/\varepsilon)$ is considered, leading to advection dominating axial diffusion in the lumen and upper fluid layer. The system of equations for the fluid flow has been solved analytically at leading and first order in the small parameter ε, and these solutions have been used to obtain equations for the leading- and first-order solute concentration. We have identified the appropriate up- and downstream boundary conditions through analysis of the corresponding inner problems; these would need to be solved numerically in order to obtain the exact solution in the inner regions near the up- and downstream ECS ports. In addition, we have formulated our problem in the context of Taylor dispersion and derived the effective diffusion coefficient governing the dispersion of the averaged, combined-order solute concentration throughout the bioreactor. The resulting equations have also been shown to simplify to those of classical Taylor dispersion in a two-dimensional pipe in the case of an impermeable membrane and cell layer.

We considered the results of the outer asymptotics problem, where it is possible to solve analytically for the outer solute concentration at leading and first order in all four layers. From this we determined expressions for the lower bound on the (constant) inlet concentration c_{in} which ensures a non-zero concentration throughout the bioreactor; for the y value at which the minimum concentration is obtained in terms of the cell layer height and inlet fluid fluxes; and for the ratio required between the lumen and upper fluid layer inlet fluxes in order to obtain equal concentrations at the top and bottom of our

simplified bioreactor domain, all with an accuracy of O (ε^2). Furthermore, we investigated the qualitative trends which arise in the first-order solute concentrations when a number of key dimensionless parameters are varied. We note that to obtain more quantitative results it would be necessary to solve the full inner problem numerically at this order, something which we do not pursue here.

We also investigated the dependence of the effective diffusion coefficient D_{eff} on key dimensionless parameters. This revealed complex non-monotonic behaviours in all cases except the dependence on ϕ_{m}. These results are due to the interaction of the many different processes involved in the model, as D_{eff} contains effects from all four layers in the bioreactor. Finally, we solved the unsteady, combined-order equation in order to investigate the behaviour of a pulse of solute delivered into the system. Analysis of the dependence of the mean solute uptake and solute exposure time on key parameter values demonstrated how optimal operating parameters could be determined for a specific experimental setup which guaranteed sufficient nutrient delivery throughout the cell layer, ideal for generating a viable cell population. It should be noted that the results here are only qualitative in nature, and in order to predict the absolute variation in μ and T, values for the fixed parameters particular to an exact experimental setup would need to be used as inputs for the model, along with generalisation of the two-dimensional geometry presented here to a three-dimensional domain.

Finally, we have briefly shown that similar leading-order asymptotic analysis can be performed in the case where the cell layer porosity is non-constant, varying on a much slower timescale than that for fluid flow. We were able to determine an implicit analytical expression for the steady-state solute concentration, but note that a much more in-depth analysis would be needed to determine the time-dependent behaviour of this system.

Whether or not the cells receive sufficient nutrient in a particular setup remains an open question experimentally, and one which we have made some progress towards answering in this chapter. Equation (5.138) gives a minimum inlet concentration required in order to achieve a non-zero nutrient concentration throughout the bioreactor. If we take the nutrient to be oxygen (as in Chapter 2) and wish to check that the concentration is above the minimum required for cell viability (which is equivalent to a dimensionless value of 0.36, see Chapter 2 and [155] for relevant parameter values), we obtain a more restrictive constraint

on the inlet concentration:

$$c_{\text{in}} > \frac{h_3 \mathcal{R}}{\varepsilon \text{Pe}(Q_{\text{l,in}} + Q_{\text{f,in}})} + 0.36. \tag{5.154}$$

Both equations (5.138) and (5.154) are accurate up to leading order and depend on parameters which can be determined from the specific cell type and experimental conditions in a particular setup. To find more accurate constraints, it would be necessary to solve the upstream inner problem numerically to determine $\bar{c}_{\text{u}}$, as discussed previously. Although we do not undertake this numerical analysis here, we have found an equation for the y value at which the minimum concentration will be attained, again dependent on experimentally obtainable parameters (see (5.139)), and also qualitative trends to suggest how severe the depletion in the cell layer will be compared with the other layers (see Figure 5.3).

The system considered here is clearly simplified, but nonetheless enables a great deal of information to be obtained analytically regarding the fluid flow and solute concentration in a setup where the Péclet number is large (to be precise, of $\text{O}(1/\varepsilon)$). If we compare the nutrient concentration distributions obtained here to those for the nutrient-driven proliferation case study in §2.7.1, we see that in both cases we have a leading-order concentration which is independent of y. However, here we can find an analytical expression for this y-independent concentration, making the dependence on key parameters more transparent. The distribution obtained numerically in the multiphase system in §2.7.1 is approximately linear in x for fluid fluxes at the higher end of the range considered (which are closer to those used in this chapter; see, for instance, Figure 2.6(a)), and hence qualitatively matches the analytical linear distribution found here and given in equation (5.137). In addition, here we can obtain a great deal of information about the next-order correction to the solute distribution which was not possible in a multiphase context. As mentioned at the start of this chapter, this permits investigation of the y-variation in the solute concentration which comes in at $\text{O}(\varepsilon)$, as well as allowing analysis in the context of Taylor dispersion through the inclusion of the axial diffusion term. Finally, we reiterate our comment from §5.2 that the asymptotic analysis presented in this chapter is analogous to that needed for the three-dimensional case, provided an axisymmetric geometry is assumed in the outer region. It could be readily investigated, but the complexity of the resulting algebra would hinder a clear analytical interpretation of the results. We postpone further discussion of future work arising from this chapter until Chapter 6.

Chapter 6

Discussion

6.1 Summary of key results

In this thesis we have presented a number of models for fluid flow, mass transport, and cell dynamics in a HFMB, all based on porous flow mixture theory. Each model has been motivated by a different experimental scenario, and has been developed following discussions with our experimental collaborators in the Centre for Regenerative Medicine, University of Bath. Given the early stage of experiments in this field, there are currently no data available to validate our models. We have instead focussed on determining the possible range of qualitative behaviours demonstrated by each system, and have predicted the trends arising in response to variations in operating conditions. We have investigated the influence of key experimentally controllable parameters on the yield and distribution of the cell population(s), and on the solute concentration throughout the bioreactor domain. Our overall aim in deriving each successive modelling framework has not only been to demonstrate its potential through candidate experimental case studies, but also to present it in a general setting which is flexible and therefore, given appropriate data, could be readily applied to a specific physical setup. The hope is that this would enable the model to be validated and then used to inform future experimental work.

In §1.4 we presented a generalised multiphase model for k cell phases, one water phase, and one scaffold phase which provided the basis for the remaining work in this thesis. Each chapter thereafter considered a different reduction of this system, and used asymptotic analysis to obtain a simplified system which was solved numerically for key variables of interest. Table 6.1 summarises the main features of each model, which we also discuss below.

Table 6.1: Summary and comparison of thesis chapter content, where $\varepsilon \ll 1$ is the lumen aspect ratio.

	Chapter 2	Chapter 3	Chapter 4	Chapter 5
No. of layers	3	4	3/4	4
No. of cell types	1	1	2	1
Size of Péclet number	1	1	$1/\varepsilon$	$1/\varepsilon$
Multiphase model?	✓	✓	✓	×
Chemical sensitivity of cells?	✓	✓	✓	×
Proliferation	✓×	✓	×	×
Motility	✓×	×	×	×
Differentiation	×	×	✓	×
Mechanical sensitivity of cells?	×	✓	✓	×
Proliferation	×	✓	×	×
Differentiation	×	×	✓	×

In Chapter 2 we considered one cell population only, which was seeded in a scaffold throughout the ECS. A number of case studies were investigated, which considered the system dynamics in response to either nutrient-dependent proliferation, a delivered/produced chemoattractant, or a combination of the two. We also considered an alternative flow regime with backflow in the ECS. The results demonstrated how the interplay between advection and chemotaxis, or between opposing fluid flows, affected the cell yield and distribution as the inlet fluid fluxes were varied, and we were able to determine 'optimal' flow rates which led to a spatially uniform cell population. In those cases which tracked a nutrient, we were also able to verify whether or not the cells were exposed to sufficient concentrations to ensure viability under the given operating conditions.

In Chapter 3, the single cell population was seeded in a scaffold which only partially occupied the ECS, representing a possible alternative experimental setup. Here we chose to focus on mechanical, instead of chemical, effects on the cell dynamics, in particular the effect of fluid shear stress levels on cell proliferation. We demonstrated how the fluid shear stress can be beneficial in increasing the resulting uniformity of a cell population, both in cases where it enhances proliferation rate and where it limits cell growth. We also discovered that this seemingly more complicated setup (with four layers instead of three) results in a simpler numerical system to solve for the leading-order variables, with qualitatively similar results for corresponding case studies (not shown).

Chapter 4 looked at both the 3- and 4-layer setups of previous chapters, but was extended

to include two cell types. This system was analysed in the context of differentiated and undifferentiated cell populations, with differentiation either stimulated by growth factor concentration alone or by the combined effects of growth factor concentration and fluid shear stress. We presented results in the example case where a specific percentage of differentiated cells was required. Given this restriction, we demonstrated how our modelling could be used to find operating conditions which (as far as possible) satisfied the further requirements of a high yield of differentiated cells and the use of a minimal quantity of growth factor.

In the final model of Chapter 5, we considered a different reduction of the generalised multiphase model, looking on a longer timescale so that cell kinetics could be neglected. The subsequently simpler setup allowed us to focus on a more in-depth analysis of the fluid flow and solute concentration throughout the modelling domain. We found analytical expressions for the leading-order and first-order solute concentrations, and obtained an averaged, combined-order system which we showed exhibits behaviour analogous to Taylor dispersion. Through more careful consideration of the inner regions near the ECS ports, we were also able to determine the appropriate up- and downstream boundary conditions for the central outer region. This analysis showed that there is a single degree of freedom in the first-order outer problem and demonstrated how this remaining unknown parameter may be computed numerically to close the system. Performing the corresponding leading-order analysis in these regions in a multiphase setup yields the same up- and downstream boundary conditions for the central outer region. This justifies the choices of boundary conditions in the multiphase models of Chapters 2-4.

6.2 Further work

Throughout this thesis we have identified where necessary those assumptions (*e.g.* on parameter values, boundary conditions, and constitutive laws) which have been taken in the absence of relevant experimental data. In such cases we have tried to make choices which do not introduce further complexity into our models and which, where possible, are based on physical intuition. To potentially overcome these limitations, we now discuss a number of experiments which would provide data to greatly improve the parameterisation of our models and would be particularly useful as first steps towards our models being validated and used to quantitatively predict experimental outcomes.

Firstly, to gain insight into the fluid regime in the ECS, it would be useful to measure the flow rate in this region in the central part of the bioreactor (*i.e.* in our central modelling domain). This could be done through injection of fluid coloured with a soluble dye into the lumen inlet and subsequent tracking of its spread downstream, and would help determine the appropriate value for the lumen/ECS fluid flux ratio $Q_{\mathrm{l,in}}/Q_{\mathrm{e,in}}$ in Chapter 2. In addition, a similar method could be used to measure the flow rate through both the porous membrane and the cell-scaffold construct, to investigate the validity of our assumption on the velocity scales in these regions compared to the lumen/upper fluid layer. The permeability of the cell-scaffold construct at different stages of an experiment could be determined using the same method currently used to find the permeability of the fibre membrane, that is, imposing a fluid flow through the lumen inlet, weighing the retentate and permeate, and using the equations determined by Shipley *et al.* [156] which relate these quantities to one another. Finally, experiments to assess the response of different cell types to the mechanical and chemical stimuli considered in this thesis would also be of great use in validating our choices of constitutive laws for the mass transfer, reaction, and intra-/interphase force terms, but such experiments would be challenging to implement. Furthermore, not all the parameters in our models could be isolated and identified through experimental procedure; some must instead be determined by fitting the results of our models to relevant experimental data. The models could then be adjusted to reflect more accurately the outcomes of experiments, before performing further data fits and iterating this process until the models were validated to a desired degree of accuracy.

It would also be beneficial to relax certain simplifying assumptions to make the modelling more physically realistic. However, in these cases such a drastic analytical reduction of the governing equations may not be possible, and a numerical scheme may need to be implemented at an earlier stage. One such extension would be the incorporation of ECM deposition and degradation of the scaffold through a non-constant scaffold volume fraction θ_{s} and associated constitutive relationships. This would greatly increase the complexity of the multiphase modelling through the addition of an extra active phase, but is an important consideration if the relevant timescales (those of tissue growth [160]) are to be studied. In addition, we could include a more comprehensive description of mass transport by modelling the solute concentration within the cell phase, instead of just in the water phase. This would require prescription of constitutive laws for the transport of solute between the phases, as

well as the uptake within the cell phase.

The work in this thesis has been mainly analytical, as we have chosen to focus on explicitly reducing the governing equations to gain insight into the contribution of key parameters to the system dynamics. However, we greatly simplified the bioreactor geometry in order to obtain our two-dimensional rectangular modelling domain. Obtaining numerical results in the whole bioreactor region (including the ECS ports) in either two dimensions or the full three-dimensional geometry would give great insight into the validity of the model reduction presented here and allow a more detailed investigation of the problem. We have chosen not to pursue this here as any such methods would be extremely computationally expensive due to the complicated geometry and small aspect ratio of the HFMB, and this work is beyond the scope of this thesis.

There are a number of variations to our models which could easily be investigated, for instance if they were particularly relevant to an experimental setup or found to be more physically realistic than the choices taken in this thesis. Firstly, we have focussed on varying inlet fluid fluxes and solute concentrations, but we note that the outlet pressures can also be varied in an experiment. Our models could be used to investigate the influence of outlet pressures in their current form, and we note that such an investigation has also been carried out in the context of cell aggregate growth on the surface of hollow fibres in HFMBs [29]. Secondly, we have considered operating conditions (inlet fluid fluxes and solute concentrations) which are constant, with the exception of Chapter 5 where we allow the inlet concentration to be a prescribed function of time. It would be straightforward to include time variations in other parameters, for instance the inlet fluid fluxes, given candidate forms being investigated by experimentalists. Finally, we have focussed on achieving a uniform cell distribution in the majority of our case studies (required, for instance, for viable cartilage [98]), but note that we could readily investigate other desirable experimental outcomes, such as a non-uniform distribution of cells. This could be useful in modelling tissue engineering of liver, in an attempt to replicate the spatial variation in morphology and function (known as zonation) found along liver sinusoids [6].

It would also be interesting to use the results of our models to compare the environmental conditions (*e.g.* solute concentration and fluid shear stress distributions) in different bioreactors, for instance between HFMBs and perfusion bioreactors as considered in [120, 122, 123]. A direct comparison could only usefully be made between validated models, and if identical

constitutive laws were used, but could be instructive in determining preferential bioreactor systems for specific tissue types.

In conclusion, in this thesis we have developed and analysed a number of models for fluid flow, solute concentration, and cell population dynamics in a HFMB. The flexible modelling framework has allowed us to gain insight into the various qualitative behaviours which could be expected from each setup. Overall, each study has helped to improve our theoretical understanding of these systems and has the potential to be used to predict experimental outcomes for a range of protocols and operating conditions, and as a result to inform future research directions.

Appendix A

Verification of numerical schemes

In §A.1 we begin by detailing three different checks on the numerical scheme described in §2.6.1. We then present convergence graphs for the schemes from Chapters 3-5 in §A.2.

A.1 Verification of the numerical scheme for Chapter 2

This section focusses on the numerical scheme described in §2.6.1 which was used to obtain the numerical results for Chapter 2. We first carry out a convergence test in §A.1.1, before comparing numerical results for the growth rates and steady states to those obtained analytically for simplified systems in §A.1.2 and §A.1.3.

A.1.1 Convergence

The scheme described in §2.6.1 has an error of $\mathrm{O}\left((\Delta x)^2\right)$. In order to verify that this is the case for our solutions, we take the candidate forms for J_n and $\mathcal{R}$ in equation (2.98) and numerically solve the coupled system (2.82) subject to the stated boundary conditions (2.85) and (2.86) (with an imposed inlet concentration) and initial condition $\theta_\mathrm{n}(x,0) = 0.3$ for different step sizes Δx. The absolute and relative tolerances in the numerical solver `ode15s` were taken to be 10^{-9}, to ensure that the error in the time integration was $\mathrm{o}\left((\Delta x)^2\right)$ for all values of Δx considered, and the error we observe arises due to the spatial discretisation. For θ_n, c, and p_w the error is taken to be the maximum absolute difference between the numerical solutions obtained with step sizes Δx and $5\Delta x$, evaluated at $x = (1 - 5\Delta x)/2$, $t = 1.5$. The results can be seen in Figure A.1 and the log-log plots are approximately linear with gradient 2, confirming that the scheme is $\mathrm{O}\left((\Delta x)^2\right)$ accurate as expected.

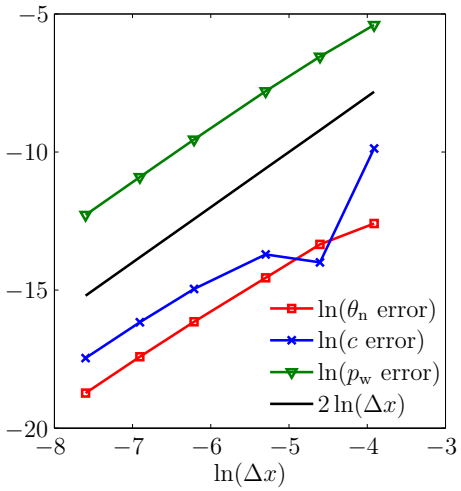

Figure A.1: Log-log plot of absolute error versus step size Δx for the numerical scheme from Chapter 2, showing an approximately linear relation with gradient 2 as expected for θ_n, c, and p_w. The error was taken to be the maximum absolute difference between numerical solutions obtained with step size Δx and $5\Delta x$, for $x = (1 - 5\Delta x)/2$, $t = 1.5$. Parameter values are as in Table 2.2 with $Q_\mathrm{l,in} = 1$.

A.1.2 Comparison to analytical growth rate

For a second verification of the numerical solution, we further simplify the system considered in §2.5.6 by neglecting solute concentration, so that the governing equations from (2.90) reduce to

$$\frac{\partial \theta_\mathrm{n}}{\partial t} + \frac{\partial Q_\mathrm{n}}{\partial x} = J_\mathrm{n}(\theta_\mathrm{n}), \tag{A.1}$$

where now

$$\begin{gathered} Q_\mathrm{n} = F\left(-\frac{\theta_\mathrm{s}\zeta_\mathrm{ws}Q_\mathrm{e,in}\theta_\mathrm{n}}{h_3\theta_\mathrm{w}} + \Phi(\theta_\mathrm{n})\frac{\partial \theta_\mathrm{n}}{\partial x}\right), \qquad F := \frac{2\cosh(\alpha) - \alpha\sinh(\alpha) - 2}{\theta_\mathrm{s}\zeta_\mathrm{ns}\alpha\sinh(\alpha)}, \\ \alpha := h_3\sqrt{\theta_\mathrm{s}\zeta_\mathrm{ns}}, \qquad \Phi(\theta_\mathrm{n}) := \Pi_\mathrm{n} + \theta_\mathrm{n}\Pi_\mathrm{n}' - \psi_\mathrm{ns}\theta_\mathrm{s}, \end{gathered} \tag{A.2}$$

and J_n is taken to have the form in equation (2.98). We carry out a linear stability analysis as described in §2.5.6, but this time on the bounded domain $0 < x < 1$. The zero cell flux condition cannot be satisfied up- and downstream at equilibrium however, and hence we impose the alternative boundary condition

$$Q_\mathrm{n} = Q_\mathrm{n,eq} = -\frac{F\theta_\mathrm{s}\zeta_\mathrm{ws}Q_\mathrm{e,in}\theta_\mathrm{n,eq}}{h_3(1 - \theta_\mathrm{s} - \theta_\mathrm{n,eq})} \qquad \text{at} \quad x = 0, 1, \tag{A.3}$$

where $\theta_\mathrm{n,eq}$ is the equilibrium solution from (2.99). Considering a general perturbation to this equilibrium solution of the form

$$\theta_\mathrm{n} = \theta_\mathrm{n,eq} + \delta\hat{\theta}_\mathrm{n}(x)e^{\sigma t}, \tag{A.4}$$

and substituting this into (A.1) yields at O(δ)

$$\hat{\theta}_{\mathrm{n}}(x) = Ae^{[G_1+G_2(\sigma)]x} + Be^{[G_1-G_2(\sigma)]x}, \tag{A.5}$$

for some constants of integration A and B, where

$$G_1 := \frac{\theta_{\mathrm{s}}\zeta_{\mathrm{ws}}Q_{\mathrm{e,in}}}{2h_3\Phi_{\mathrm{eq}}(1-\theta_{\mathrm{s}}-\theta_{\mathrm{n,eq}})}\left(1+\frac{\theta_{\mathrm{n,eq}}}{1-\theta_{\mathrm{s}}-\theta_{\mathrm{n,eq}}}\right), \tag{A.6}$$

$$G_2(\sigma) := \sqrt{G_1^2 - \frac{1}{F\Phi_{\mathrm{eq}}}[\sigma + (1-\theta_{\mathrm{s}})\Gamma_{\mathrm{nw}} - \Gamma_{\mathrm{wn}}]}. \tag{A.7}$$

The growth rate σ is determined by applying the equilibrium flux boundary conditions (A.3), which require for non-trivial solutions

$$G_2(\sigma) = k\pi i, \quad k \in \mathbb{Z}^+, \tag{A.8}$$

and hence

$$\sigma = F\Phi_{\mathrm{eq}}(G_1^2 + k^2\pi^2) + \Gamma_{\mathrm{wn}} - (1-\theta_{\mathrm{s}})\Gamma_{\mathrm{nw}}, \quad k \in \mathbb{Z}^+. \tag{A.9}$$

This analytical growth rate can now be compared to the growth rate of the numerical solution. We set the initial θ_{n} equal to

$$\theta_{\mathrm{n}}(x,0) = \theta_{\mathrm{n,eq}} + \delta\left[\left(1-\frac{G_1^2-k^2\pi^2}{G_1^2+k^2\pi^2}\right)\cos(k\pi x) + \frac{2k\pi G_1}{G_1^2+k^2\pi^2}\sin(k\pi x)\right]e^{G_1 x}, \quad k \in \mathbb{Z}^+, \tag{A.10}$$

where δ is small enough to ensure $\left|\delta\hat{\theta}_{\mathrm{n}}\right| \ll 1$ for all $x \in [0,1]$. The second term on the right-hand side of (A.10) (*i.e.* the chosen expression for $\hat{\theta}_{\mathrm{n}}$) corresponds to the real part of the mode from (A.5) in which $B = 1$ and (in order to satisfy (A.3))

$$A = -\frac{(G_1^2 - k^2\pi^2 + 2k\pi i)}{G_1^2 + k^2\pi^2}. \tag{A.11}$$

We numerically solve for θ_{n} in time, subject to (A.10) and the equilibrium flux boundary condition (A.3). The solution for θ_{n} should be (from the above analysis)

$$\theta_{\mathrm{n}}(x,t) = \theta_{\mathrm{n,eq}} + \delta\hat{\theta}_{\mathrm{n}}(x)e^{\sigma t}, \tag{A.12}$$

and hence if we plot

$$\log\left(\left|\frac{\theta_{\mathrm{n}}(x,t)|_{x=X} - \theta_{\mathrm{n,eq}}}{\delta\hat{\theta}_{\mathrm{n}}(x)\Big|_{x=X}}\right|\right) =: N(t) \tag{A.13}$$

versus time for some fixed $x = X$, we should (at least for small t) see a straight line with gradient σ. This gradient can be compared to the value of σ calculated using equation

Table A.1: Estimated values of σ obtained from numerical solutions ($0 < t < 10^{-4}$, averaged over $0 < x < 1$) compared to those from the linear stability analysis for different values of k. Initially θ_{n} was set to the form in equation (A.10), with $\delta = 10^{-8}$. Parameter values are as in Table 2.2 with $Q_{\mathrm{l,in}} = 1$ and the step size used was $\Delta x = 5 \times 10^{-4}$.

k	σ (numerical solution)	σ (linear stability analysis)	% error
1	−51.45	−51.48	0.0583
2	−114.4	−114.7	0.2616
3	−219.6	−219.9	0.1364
4	−366.4	−367.4	0.2722
5	−554.7	−556.9	0.395
6	−776.8	−788.5	1.484
7	−1042	−1062	1.883
8	−1344	−1378	2.467
9	−1683	−1736	3.053
10	−2088	−2136	2.247

(A.9). An example of such a plot is shown in Figure A.2, and values of σ from the linear stability analysis compared to the estimated values from the plots are given in Table A.1, showing good agreement between the two.

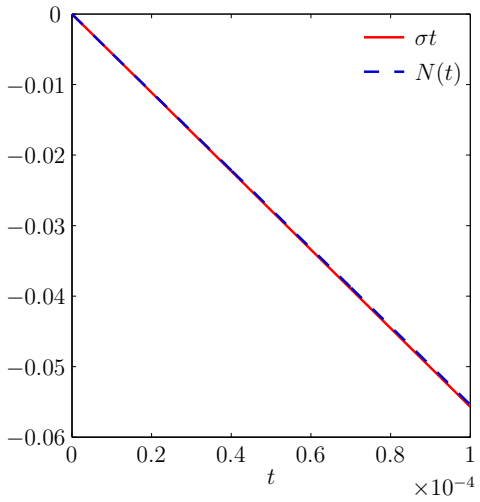

Figure A.2: Plot of $N(t)$ (dashed line) versus time at $x = 0.4998$, showing a linear relation as expected, with a gradient which matches well with the analytically obtained σ value (solid line, see Table A.1). Initially θ_{n} was set to the form in equation (A.10), with $\delta = 10^{-8}$ and $k = 5$. Parameter values are as in Table 2.2 with $Q_{\mathrm{l,in}} = 1$ and the step size used was $\Delta x = 5 \times 10^{-4}$.

A.1.3 Comparison to analytical steady state

A final check of the numerical scheme from Chapter 2 is performed by considering the simplified system from §2.5.6 once again:

$$\frac{\partial \theta_\mathrm{n}}{\partial t} + \frac{\partial Q_\mathrm{n}}{\partial x} = J_\mathrm{n}, \qquad \frac{\partial Q_\mathrm{c}}{\partial x} = -h_3 \mathcal{R}, \tag{A.14}$$

with the alternative boundary conditions

$$Q_\mathrm{n} = Q_{\mathrm{n,eq}} \qquad \text{at} \quad x = 0, 1, \tag{A.15}$$

$$c = c_\mathrm{eq} + \delta \tilde{c} \quad \text{at} \quad x = 0, \qquad \frac{\partial c}{\partial x} = 0 \quad \text{at} \quad x = 1, \tag{A.16}$$

where we have chosen to impose a lumen inlet concentration at $x = 0$, with $\delta \ll 1$ and $\tilde{c}$ some constant value. Choosing J_n and $\mathcal{R}$ to have the forms in equation (2.98), we note that $(\theta_{\mathrm{n,eq}}, c_\mathrm{eq})$ from equation (2.99) is an equilibrium solution to this system in the case where the inlet concentration is set equal to c_eq. By perturbing the inlet concentration above this value (*i.e.* setting $\delta > 0$), we can investigate alternative steady states of this system. We note that using this method, any new steady states will be near to the equilibrium state $(\theta_{\mathrm{n,eq}}, c_\mathrm{eq})$. As for the linear stability analysis, we perturb the leading-order solutions θ_n and c about the original steady state $(\theta_{\mathrm{n,eq}}, c_\mathrm{eq})$ but keep the forms of the perturbations general functions of x, and so seek solutions of the form

$$\theta_\mathrm{n} = \theta_{\mathrm{n,ss}}(x) = \theta_{\mathrm{n,eq}} + \delta \hat{\theta}_\mathrm{n}(x), \qquad c = c_\mathrm{ss}(x) = c_\mathrm{eq} + \delta \hat{c}(x). \tag{A.17}$$

We seek solutions for the functions $\hat{\theta}_\mathrm{n}(x)$ and $\hat{c}(x)$ by substituting these expansions into equations (A.14)-(A.16) and equating coefficients of δ^1. Upon eliminating $\hat{\theta}_\mathrm{n}$ we obtain a fourth-order ODE for $\hat{c}$:

$$\hat{c}^{(4)} + (A + \alpha)\hat{c}''' + (B + \beta + A\alpha - \xi G)\hat{c}'' + (A\beta + B\alpha)\hat{c}' + (B\beta - \gamma G)\hat{c} = 0, \tag{A.18}$$

where primes represent derivatives with respect to x,

$$\alpha := -\frac{\theta_\mathrm{s}\zeta_\mathrm{ws}Q_{\mathrm{e,in}}}{h_3\Phi_\mathrm{eq}(1-\theta_\mathrm{s}-\theta_{\mathrm{n,eq}})}\left(1 + \frac{\theta_{\mathrm{n,eq}}}{1-\theta_\mathrm{s}-\theta_{\mathrm{n,eq}}}\right), \qquad \beta := -\frac{\frac{\partial J_\mathrm{n}}{\partial \theta_\mathrm{n}}\Big|_\mathrm{eq}}{F\Phi_\mathrm{eq}}, \qquad \gamma := -\frac{\frac{\partial J_\mathrm{n}}{\partial c}\Big|_\mathrm{eq}}{F\Phi_\mathrm{eq}},$$

$$\xi := \frac{\theta_{\mathrm{n,eq}}\Pi'_{\mathrm{c,eq}}}{\Phi_\mathrm{eq}}, \qquad A := -\frac{\mathrm{Pe}Q_{\mathrm{l,in}}}{b_\mathrm{eq}}, \qquad B := \frac{h_3\,\frac{\partial \mathcal{R}}{\partial c}\Big|_\mathrm{eq}}{b_\mathrm{eq}}, \qquad G := \frac{h_3\,\frac{\partial \mathcal{R}}{\partial \theta_\mathrm{n}}\Big|_\mathrm{eq}}{b_\mathrm{eq}}, \tag{A.19}$$

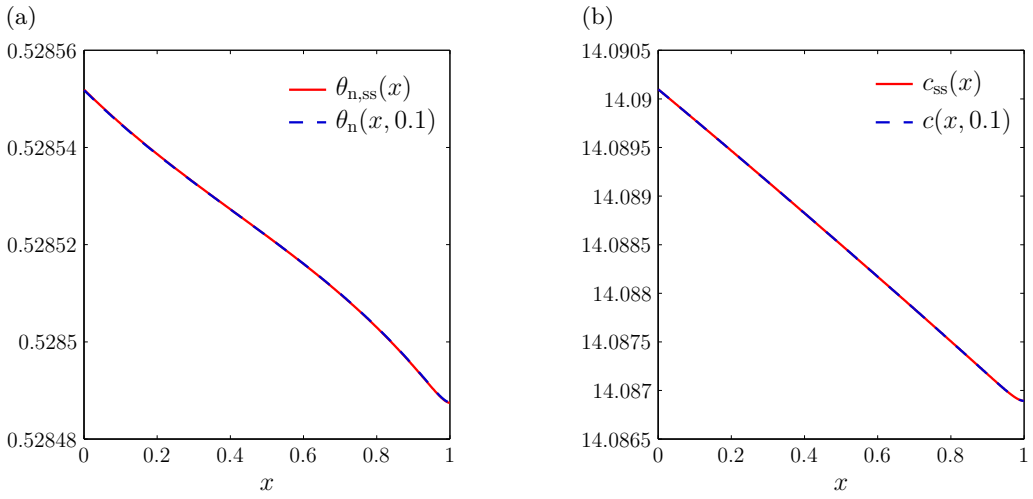

Figure A.3: Plots of analytical (subscript ss) and numerical (end time $t = 0.1$) steady-state solutions for (a) θ_{n}, and (b) c, for the simplified system (A.14) with equilibrium and perturbed boundary conditions. Maximum absolute errors between analytical and numerical θ_{n} and c solutions are 1.1247×10^{-7} and 1.1466×10^{-7} respectively. Parameter values are as in Table 2.2, with $Q_{\mathrm{l,in}} = 1$, $\delta = 0.1$, $\tilde{c} = 1$, $\bar{c} = c_{\mathrm{eq}}$, and step size $\Delta x = 10^{-3}$.

and $\hat{\theta}_{\mathrm{n}}$ is related to $\hat{c}$ via

$$\hat{\theta}_{\mathrm{n}} = -\frac{1}{G}\left(\hat{c}'' + A\hat{c}' + B\hat{c}\right). \tag{A.20}$$

The characteristic equation corresponding to (A.18) can be solved numerically to find the four solutions λ_1, λ_2, λ_3, and λ_4, so that (for real, distinct λ_i),

$$\hat{c}(x) = c_1 e^{\lambda_1 x} + c_2 e^{\lambda_2 x} + c_3 e^{\lambda_3 x} + c_4 e^{\lambda_4 x}, \tag{A.21}$$

for some constants c_1, c_2, c_3, and c_4. These can be determined using the boundary conditions

$$\hat{c} = \tilde{c} \quad \text{at} \quad x = 0, \qquad \hat{c}' = 0 \quad \text{at} \quad x = 1, \tag{A.22}$$

$$\hat{\theta}_{\mathrm{n}}' + \alpha\hat{\theta}_{\mathrm{n}} + \xi\hat{c}' = 0 \qquad \text{at} \quad x = 0, 1, \tag{A.23}$$

where condition (A.23) can be expressed in terms of $\hat{c}$ and its derivatives using equation (A.20), and $\hat{\theta}_{\mathrm{n}}$ then determined using equation (A.20). We used MATLAB to solve for λ_i ($i = 1, 2, 3, 4$) and thus find $\hat{c}$. We then once more used the method of lines to numerically solve the time-dependent system with the same boundary conditions, and with the initial conditions set to the original equilibrium state. Parameter values are as in Table 2.2 unless stated otherwise. Comparing the resulting analytical and long-time numerical solutions shows excellent agreement between the two for $\delta \lesssim 0.1$ (see Figure A.3).

A.2 Convergence graphs for Chapters 3-5

We carried out convergence tests on the numerical schemes used in Chapters 3-5 as described above in §A.1.1. All schemes had an estimated error of $\mathrm{O}\left((\Delta x)^2\right)$. In each case the relevant coupled system of PDEs was numerically solved for different step sizes Δx, and the absolute and relative tolerances in the numerical solver `ode15s` were taken to be 10^{-9}, to ensure that the error in the time integration was $\mathrm{o}\left((\Delta x)^2\right)$, and the error we observe arises due to the spatial discretisation. The error between solutions was taken to be the absolute difference between those obtained with step sizes Δx and $5\Delta x$, evaluated at $x = (1 - 5\Delta x)/2$ and a specified time t.

The results for Chapter 3 were obtained using the respective forms for $\mathcal{R}$ and J_{n} from (3.65) and (3.66) (with $F(S) \equiv 1$), and can be seen in Figure A.4. The results for Chapter 4 were obtained using the forms for $\mathcal{R}$, J_{u}, and J_{d} from (4.60), (4.66), and (4.67) respectively, and non-zero initial conditions ($\theta_{\mathrm{u}} = \theta_{\mathrm{d}} = 0.2$, $c = 1$, $p_{\mathrm{w}} = 1$) and can be seen in Figure A.5. The results for Chapter 5 were obtained by solving the unsteady combined-order system from §5.4.2 and can be seen in Figure A.6. All log-log plots are approximately linear with gradient 2 which confirms that the numerical schemes are converging as expected as Δx decreases.

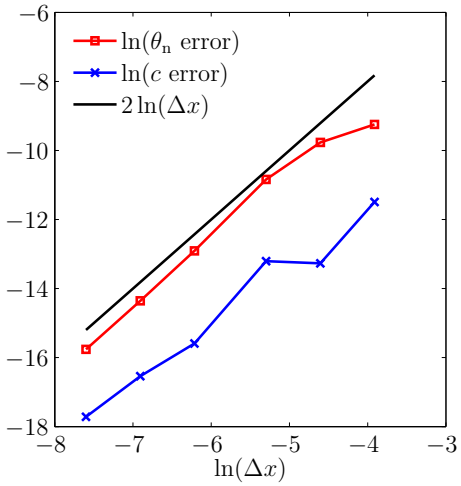

Figure A.4: Log-log plot of absolute error versus step size Δx for the numerical scheme from Chapter 3, showing an approximately linear relation with gradient 2 as expected for θ_{n} and c. The error was taken to be the absolute difference between numerical solutions obtained with step size Δx and $5\Delta x$, for $x = (1 - 5\Delta x)/2$, $t = 1.5$. Parameter values are as in Table 3.2 with $h_3 = 1$, $Q_{\mathrm{f,in}} = 1$, and $Q_{\mathrm{l,in}} = 1$.

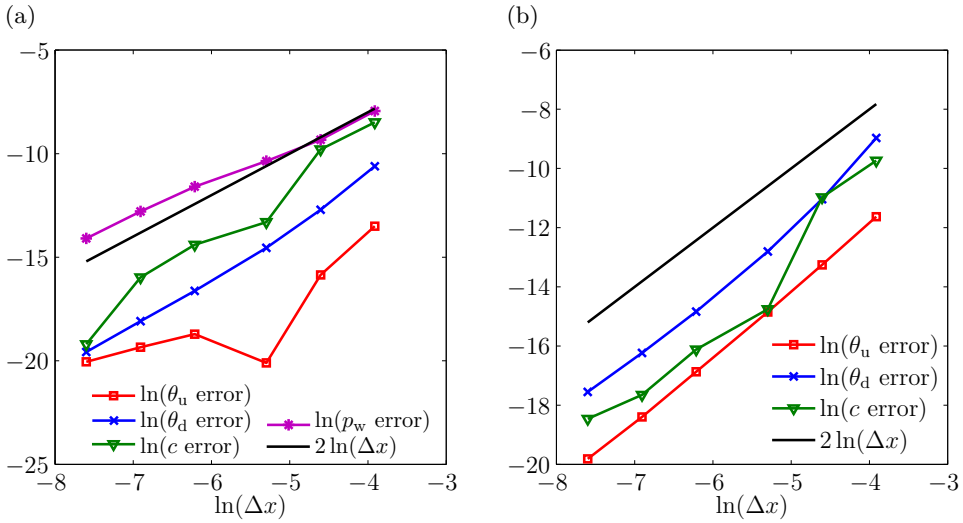

Figure A.5: Log-log plot of absolute error versus step size Δx for the numerical schemes from (a) the 3-layer model, and (b) the 4-layer model from Chapter 4 (end time $t = 0.25$), showing an approximately linear relation with gradient 2 as expected for θ_u, θ_d, c, and (in (a)) p_w. The error was taken to be the absolute difference between numerical solutions obtained with step size Δx and $5\Delta x$, for $x = (1-5\Delta x)/2$. Parameter values are as in Table 4.2 with $c_{in} = 1$, $Q_{f,in} = 0.1$, and $Q_{l,in} = 1$.

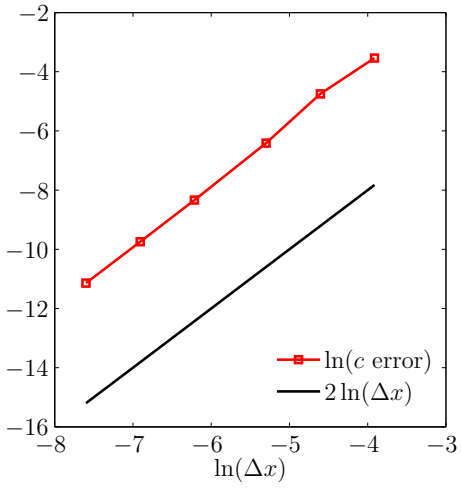

Figure A.6: Log-log plot of absolute error versus step size Δx for the numerical scheme from Chapter 5, showing an approximately linear relation with gradient 2 as expected for c. The error was taken to be the absolute difference between numerical solutions obtained with step size Δx and $5\Delta x$, for $x = (1 - 5\Delta x)/2$, $t = 2$. Parameter values are as in Table 5.2 with $h_3 = 1$, $Q_{f,in} = 1$, and $Q_{l,in} = 1$.

Appendix B

Inner region analysis

In §5.2 we introduced a two-dimensional model of a HFMB which included the regions near the up- and downstream ECS ports. We then excluded the inner regions near these ports in §5.3, and focussed on finding the solution valid in the central outer region. In this appendix, we analyse these previously neglected up- and downstream inner regions and determine the matching conditions needed to close the outer problem, which appear as up- and downstream conditions on our outer solutions in Chapter 5. We further note that the leading-order analysis presented in this appendix would also follow through in a multiphase setup (results not shown), and hence the corresponding up- and downstream boundary conditions applied in Chapters 2-4 were appropriate.

B.1 Upstream inner region

We begin with the upstream inner region, where we need to determine matching conditions for the inlet fluid fluxes and solute concentrations up to and including $\mathrm{O}(\varepsilon)$ in the outer region. We return to the dimensionless equations (5.43)-(5.46) and rescale to move into the upstream inner region depicted in Figure 5.1 in which $x = \mathrm{O}(\varepsilon)$. We set $x = \varepsilon X$ and $v_i = V_i/\varepsilon$ $(i = \mathrm{l}, \mathrm{m}, \mathrm{w}, \mathrm{f})$. For clarity we also set $p_i(x, y, t) = P_i(X, y, t)$, $c_i(x, y, t) = C_i(X, y, t)$, $u_i(x, y, t) = U_i(X, y, t)$ $(i = \mathrm{l}, \mathrm{m}, \mathrm{w}, \mathrm{f})$, and $\nabla_{\mathbf{X}} = \left(\frac{\partial}{\partial X}, \frac{\partial}{\partial y}\right)$, $\nabla^2_{\mathbf{X}} = \frac{\partial^2}{\partial X^2} + \frac{\partial^2}{\partial y^2}$. This promotes the x-derivatives that were neglected in the outer region due to the lubrication scaling, and thus results in both x- and y-derivatives contributing to the leading-order behaviour in

the inner region. The flow equations are now

$$\frac{\partial U_i}{\partial X}+\frac{\partial V_i}{\partial y}=0, \qquad -\frac{\partial P_i}{\partial X}+\varepsilon\nabla^2_{\mathbf{X}}U_i=0, \qquad -\frac{\partial P_i}{\partial y}+\varepsilon\nabla^2_{\mathbf{X}}V_i=0 \quad (i=\mathrm{l},\mathrm{f}), \tag{B.1}$$

$$U_\mathrm{m}=-\varepsilon\kappa_\mathrm{m}\frac{\partial P_\mathrm{m}}{\partial X}, \qquad V_\mathrm{m}=-\varepsilon\kappa_\mathrm{m}\frac{\partial P_\mathrm{m}}{\partial y}, \qquad \nabla^2_{\mathbf{X}}P_\mathrm{m}=0, \tag{B.2}$$

$$U_\mathrm{w}=-\varepsilon\kappa_\mathrm{w}\frac{\partial P_\mathrm{w}}{\partial X}, \qquad V_\mathrm{w}=-\varepsilon\kappa_\mathrm{w}\frac{\partial P_\mathrm{w}}{\partial y}, \qquad \nabla^2_{\mathbf{X}}P_\mathrm{w}=0, \tag{B.3}$$

while the transverse boundary conditions become

$$\frac{\partial U_\mathrm{l}}{\partial y}=0, \qquad V_\mathrm{l}=0 \qquad \text{on} \quad y=0, \tag{B.4}$$

$$\begin{gathered} U_\mathrm{l}=0, \qquad V_\mathrm{l}=-\varepsilon^2\kappa_\mathrm{m}\phi_\mathrm{m}\frac{\partial P_\mathrm{m}}{\partial y}, \\ P_\mathrm{l}+\frac{2\varepsilon}{3}\left(\frac{\partial U_\mathrm{l}}{\partial X}-2\frac{\partial V_\mathrm{l}}{\partial y}\right)=P_\mathrm{m} \qquad \text{on} \quad y=1, \end{gathered} \tag{B.5a-c}$$

$$\phi_\mathrm{m}\kappa_\mathrm{m}\frac{\partial P_\mathrm{m}}{\partial y}=\phi_\mathrm{w}\kappa_\mathrm{w}\frac{\partial P_\mathrm{w}}{\partial y}, \qquad P_\mathrm{m}=P_\mathrm{w} \qquad \text{on} \quad y=1+h_2, \tag{B.6}$$

$$\begin{gathered} U_\mathrm{f}=0, \qquad -\varepsilon^2\phi_\mathrm{w}\kappa_\mathrm{w}\frac{\partial P_\mathrm{w}}{\partial y}=V_\mathrm{f}, \\ P_\mathrm{w}=P_\mathrm{f}+\frac{2\varepsilon}{3}\left(\frac{\partial U_\mathrm{f}}{\partial X}-2\frac{\partial V_\mathrm{f}}{\partial y}\right) \qquad \text{on} \quad y=H-h_4, \end{gathered} \tag{B.7a-c}$$

$$U_\mathrm{f}=V_\mathrm{f}=0 \qquad \text{on} \quad y=H. \tag{B.8}$$

We also assume (as stated in §5.2.3) that there is a prescribed two-dimensional flux $Q_{\mathrm{l,in}}$ at the lumen inlet, and $Q_{\mathrm{f,in}}$ at each of the upstream ECS ports.

We note that the equations in (B.1) for the lumen and upper fluid layer are only valid at O(1) and O(ε) here, since the inertial terms would appear at O(ε^2) (see discussion in §5.2.1). However, this does not affect this analysis since only expressions for the leading-order inner velocities (which are found from the O(ε) system) are required, as will be seen below.

We first determine the fluid flux conditions to be imposed on the outer problem by considering how fluid transfers between layers. From inspection of boundary conditions (B.5b) and (B.7b), we can see that there is no flux of fluid across either the lumen/membrane or cell layer/upper fluid layer interfaces at O(1) or O(ε). Thus, at O(1) and O(ε), the flux into the inner region in the lumen and upper fluid layer must equal the flux out of the inner region in these layers, which in turn must equal the flux into the outer region in both layers.

Hence the correct inlet conditions to impose on the outer flow solution at leading and first order in §5.3.5 are given by (5.61), (5.70), and (5.74).

We now determine the correct upstream inlet conditions to apply on the solute concentration at O(1) and O(ε). The inner problem for the solute concentration in each layer is given by

$$\varepsilon \mathrm{Pe}\left(\varepsilon \frac{\partial C_\mathrm{l}}{\partial t} + \nabla_{\mathbf{X}} \cdot (C_\mathrm{l}\mathbf{U}_\mathrm{l})\right) = \nabla^2_{\mathbf{X}} C_\mathrm{l}, \tag{B.9}$$

$$\varepsilon^2 \mathrm{Pe}\left(\frac{\partial C_\mathrm{m}}{\partial t} + \nabla_{\mathbf{X}} \cdot (C_\mathrm{m}\mathbf{U}_\mathrm{m})\right) = \nabla^2_{\mathbf{X}} C_\mathrm{m}, \tag{B.10}$$

$$\varepsilon^2 \mathrm{Pe}\left(\frac{\partial C_\mathrm{w}}{\partial t} + \nabla_{\mathbf{X}} \cdot (C_\mathrm{w}\mathbf{U}_\mathrm{w})\right) = \nabla^2_{\mathbf{X}} C_\mathrm{w} - \frac{\varepsilon \mathcal{R}}{\phi_\mathrm{w}}, \tag{B.11}$$

$$\varepsilon \mathrm{Pe}\left(\varepsilon \frac{\partial C_\mathrm{f}}{\partial t} + \nabla_{\mathbf{X}} \cdot (C_\mathrm{f}\mathbf{U}_\mathrm{f})\right) = \nabla^2_{\mathbf{X}} C_\mathrm{f}, \tag{B.12}$$

for which the boundary conditions are

$$\frac{\partial C_\mathrm{l}}{\partial y} = 0 \qquad \text{on} \quad y = 0, \tag{B.13}$$

$$C_\mathrm{l} = C_\mathrm{m}, \qquad \frac{\partial C_\mathrm{l}}{\partial y} = \phi_\mathrm{m} \frac{\partial C_\mathrm{m}}{\partial y} \qquad \text{on} \quad y = 1, \tag{B.14}$$

$$C_\mathrm{m} = C_\mathrm{w}, \qquad \phi_\mathrm{m} \frac{\partial C_\mathrm{m}}{\partial y} = \phi_\mathrm{w} \frac{\partial C_\mathrm{w}}{\partial y} \qquad \text{on} \quad y = 1 + h_2, \tag{B.15}$$

$$C_\mathrm{w} = C_\mathrm{f}, \qquad \phi_\mathrm{w} \frac{\partial C_\mathrm{w}}{\partial y} = \frac{\partial C_\mathrm{f}}{\partial y} \qquad \text{on} \quad y = 1 + h_2 + h_3, \tag{B.16}$$

$$\frac{\partial C_\mathrm{f}}{\partial y} = 0 \qquad \text{on} \quad y = H, \tag{B.17}$$

together with the inlet conditions

$$C_\mathrm{l} = c_{\mathrm{l,in}}(t) \quad \text{at} \quad \mathcal{A}, \qquad C_\mathrm{f} = c_{\mathrm{f,in}}(t) \quad \text{at} \quad \mathcal{B}, \tag{B.18}$$

where we have assumed that the solute concentration is spatially uniform in the inlet pipes (to be expected experimentally if it comes from a well-mixed reservoir).

We begin with the leading-order problem. As in the outer region, we expand all variables in powers of ε, so that at O(1) we obtain (dropping the subscript 0)

$$\begin{aligned} &\varepsilon \mathrm{Pe} \nabla_{\mathbf{X}} \cdot (C_\mathrm{l}\mathbf{U}_\mathrm{l}) = \nabla^2_{\mathbf{X}} C_\mathrm{l}, \qquad \nabla^2_{\mathbf{X}} C_\mathrm{m} = 0, \\ &\nabla^2_{\mathbf{X}} C_\mathrm{w} = 0, \qquad \varepsilon \mathrm{Pe} \nabla_{\mathbf{X}} \cdot (C_\mathrm{f}\mathbf{U}_\mathrm{f}) = \nabla^2_{\mathbf{X}} C_\mathrm{f}. \end{aligned} \tag{B.19}$$

If $c_{\mathrm{l,in}} = c_{\mathrm{f,in}} = c_\mathrm{in}$, say, then we can see that $C_i \equiv c_\mathrm{in}$ ($i = \mathrm{l}, \mathrm{m}, \mathrm{w}, \mathrm{f}$) satisfies these leading order equations and the relevant boundary conditions, and hence is the (unique) leading-order solution. On the other hand, in the more general case where $c_{\mathrm{l,in}} \neq c_{\mathrm{f,in}}$, we note that

this full inner problem must be solved in order to determine C_i $(i = \mathrm{l}, \mathrm{m}, \mathrm{w}, \mathrm{f})$. However, as seen in §5.3.6, since the leading-order outer concentration is independent of y, the leading-order inner concentration must be independent of y as we leave the inner region. It can therefore be determined by appealing to global conservation of mass without knowing the solution of the O(1) inner problem. Hence we can equate the total flux of solute into the inner region and the total flux of solute out of the inner region at this order, which yields

$$c_{\mathrm{l,in}}(t)Q_{\mathrm{l,in}} + c_{\mathrm{f,in}}(t)Q_{\mathrm{f,in}} = c_{\mathrm{in}}(t)\left(Q_{\mathrm{l,in}} + Q_{\mathrm{f,in}}\right), \tag{B.20}$$

where $c_{\mathrm{in}}(t)$ is the (as yet unknown) inlet concentration for the outer solution, recalling $c_0(0^+, t) := c_{\mathrm{in}}(t)$. To obtain the expression (B.20), we have used the fact (from (B.18)) that there is only advective (and no diffusive) flux of the solute into the lumen and upper fluid layer, and that fluid flux in these layers is conserved at O(1) from above. Therefore the correct inlet condition for the O(1) solute in the outer region is (5.82),

$$c_0(0^+, t) = c_{\mathrm{in}}(t) = \frac{Q_{\mathrm{l,in}}c_{\mathrm{l,in}}(t) + Q_{\mathrm{f,in}}c_{\mathrm{f,in}}(t)}{Q_{\mathrm{l,in}} + Q_{\mathrm{f,in}}}. \tag{B.21}$$

The final upstream condition required is for the $\mathrm{O}(\varepsilon)$ inlet concentration. We therefore move on to the $\mathrm{O}(\varepsilon)$ problem for the concentration, and note that we do not state the momentum equations for the fluid velocities at this order as we only require the incompressibility condition on $\mathbf{U}_{\mathrm{l}_1}$ and $\mathbf{U}_{\mathrm{f}_1}$ in the following analysis. The $\mathrm{O}(\varepsilon)$ governing equations for the solute concentration are (reintroducing the subscripts 0, 1 for clarity)

$$\begin{gathered}\varepsilon\mathrm{Pe}\left(\frac{\partial C_{\mathrm{l}_0}}{\partial t} + \nabla_{\mathbf{X}}\cdot\left(C_{\mathrm{l}_0}\mathbf{U}_{\mathrm{l}_1} + C_{\mathrm{l}_1}\mathbf{U}_{\mathrm{l}_0}\right)\right) = \nabla^2_{\mathbf{X}}C_{\mathrm{l}_1}, \qquad \nabla^2_{\mathbf{X}}C_{\mathrm{m}_1} = \varepsilon\mathrm{Pe}\frac{\partial C_{\mathrm{m}_0}}{\partial t}, \\ \nabla^2_{\mathbf{X}}C_{\mathrm{w}_1} = \varepsilon\mathrm{Pe}\frac{\partial C_{\mathrm{w}_0}}{\partial t} + \frac{\mathcal{R}}{\phi_{\mathrm{w}}}, \qquad \varepsilon\mathrm{Pe}\left(\frac{\partial C_{\mathrm{f}_0}}{\partial t} + \nabla_{\mathbf{X}}\cdot\left(C_{\mathrm{f}_0}\mathbf{U}_{\mathrm{f}_1} + C_{\mathrm{f}_1}\mathbf{U}_{\mathrm{f}_0}\right)\right) = \nabla^2_{\mathbf{X}}C_{\mathrm{f}_1}.\end{gathered} \tag{B.22}$$

In general, solution of this system would be complicated by the appearance of $\mathbf{U}_{\mathrm{l}_1}$ and $\mathbf{U}_{\mathrm{f}_1}$, since inertia is not negligible at $\mathrm{O}(\varepsilon^2)$ in (B.1). However, progress can be made by considering the far-field expansion of the inner solutions as $X \to \infty$.

We begin by making the assumption that the leading-order fluid flow in both the lumen and upper fluid layer is Poiseuille as it leaves the inner region. That is, as $X \to \infty$,

$$\mathbf{U}_{\mathrm{l}_0} \sim \left(\frac{3}{2}Q_{\mathrm{l,in}}(1-y^2), 0\right), \qquad \mathbf{U}_{\mathrm{f}_0} \sim \left(\frac{6}{h_4^3}Q_{\mathrm{f,in}}(y-H)(H-h_4-y), 0\right). \tag{B.23}$$

Substituting these expressions into the far-field limits as $X \to \infty$ of the O(1) lumen and upper fluid layer equations for the solute concentration in (B.19), we find that

$$\frac{\partial^2 C_{i_0}}{\partial y^2} \sim 0 \quad (i = \mathrm{l}, \mathrm{m}, \mathrm{w}, \mathrm{f}) \quad \text{as} \quad X \to \infty, \tag{B.24}$$

and so, along with application of the leading-order transverse boundary conditions from (B.13)-(B.17), we find that the far-field O(1) concentration is constant in space in all four layers, and therefore equal across all layers; we set $C_{i_0} \sim C_0(t)$ $(i = \mathrm{l}, \mathrm{m}, \mathrm{w}, \mathrm{f})$ as $X \to \infty$ for some C_0. Hence, by the continuity equation, the terms involving $\mathbf{U}_{\mathrm{l}_1}$ and $\mathbf{U}_{\mathrm{f}_1}$ in (B.22) disappear in the far field.

As we have shown at leading order that C_0 is spatially constant in the far field, we could naïvely make the same choice at O(ε) for C_1. If we then consider $X \to \infty$ in (B.22) and substitute in for the leading-order far-field velocities from (B.23), we lose the advection terms in the lumen and upper fluid layer, and also the $\partial^2/\partial X^2$ terms in each layer. Following this through to solve for the O(ε) solute concentrations, we find that we can only match with the outer solution at O(1) if $c_{\mathrm{in}}(t)$ takes a specific form, namely $c_{\mathrm{in}}(t) = -h_3\mathcal{R}t/(\varepsilon\mathrm{Pe}\bar{h}) + \text{const.}$. Therefore to find a consistent match without such a restriction on $c_{\mathrm{in}}(t)$ we must consider an alternative dominant balance of the O(ε) equations. To retain the advection terms in the lumen and upper fluid layer as $X \to \infty$, and motivated by the fact that the leading-order outer solution c_0 is linear in x (see (5.123)), we pose the expansions

$$C_{i_1} \sim -\varphi(t)X + f_i(y,t) \quad (i = \mathrm{l}, \mathrm{m}, \mathrm{w}, \mathrm{f}) \quad \text{as} \quad X \to \infty, \tag{B.25}$$

for some $\varphi(t)$ and $f_i(y,t)$ $(i = \mathrm{l}, \mathrm{m}, \mathrm{w}, \mathrm{f})$ to be determined. It is straightforward to see that the coefficient $\varphi(t)$ of these linear terms must be the same in each layer, due to the continuity of concentration boundary conditions on the interfaces between layers.

Substituting these forms (and those for the leading-order far-field velocities) into the O(ε) governing equations in (B.22) and considering the resulting dominant balance as $X \to \infty$, we find

$$\begin{gathered}
\frac{\partial^2 f_{\mathrm{l}}}{\partial y^2} = \varepsilon\mathrm{Pe}\left(-\frac{3}{2}Q_{\mathrm{l,in}}\varphi(1-y^2) + C_0'(t)\right), \qquad \frac{\partial^2 f_{\mathrm{m}}}{\partial y^2} = \varepsilon\mathrm{Pe}C_0'(t), \\
\frac{\partial^2 f_{\mathrm{w}}}{\partial y^2} = \frac{\mathcal{R}}{\phi_{\mathrm{w}}} + \varepsilon\mathrm{Pe}C_0'(t), \qquad \frac{\partial^2 f_{\mathrm{f}}}{\partial y^2} = \varepsilon\mathrm{Pe}\left(-\frac{6}{h_4^3}Q_{\mathrm{f,in}}\varphi(y-H)(H-h_4-y) + C_0'(t)\right),
\end{gathered} \tag{B.26}$$

along with boundary conditions

$$\frac{\partial f_\mathrm{l}}{\partial y} = 0 \qquad \text{on} \quad y = 0, \tag{B.27}$$

$$f_\mathrm{l} = f_\mathrm{m}, \qquad \frac{\partial f_\mathrm{l}}{\partial y} = \phi_\mathrm{m}\frac{\partial f_\mathrm{m}}{\partial y} \qquad \text{on} \quad y = 1, \tag{B.28}$$

$$f_\mathrm{m} = f_\mathrm{w}, \qquad \phi\frac{\partial f_\mathrm{m}}{\partial y} = \phi_\mathrm{w}\frac{\partial f_\mathrm{w}}{\partial y} \qquad \text{on} \quad y = 1 + h_2, \tag{B.29}$$

$$f_\mathrm{w} = f_\mathrm{f}, \qquad \phi_\mathrm{w}\frac{\partial f_\mathrm{w}}{\partial y} = \frac{\partial f_\mathrm{f}}{\partial y} \qquad \text{on} \quad y = 1 + h_2 + h_3, \tag{B.30}$$

$$\frac{\partial f_\mathrm{f}}{\partial y} = 0 \qquad \text{on} \quad y = H. \tag{B.31}$$

These can be solved to find

$$f_\mathrm{l} = -\frac{\varepsilon\mathrm{Pe}Q_\mathrm{l,in}\varphi}{8}(6y^2 - y^4) + \frac{\varepsilon\mathrm{Pe}}{2}C_0'(t)y^2 + c_\infty(t), \tag{B.32}$$

$$f_\mathrm{m} = -\varepsilon\mathrm{Pe}Q_\mathrm{l,in}\varphi\left(\frac{y-1}{\phi_\mathrm{m}} + \frac{5}{8}\right) + \varepsilon\mathrm{Pe}C_0'(t)\left[\frac{y^2}{2} - \left(1 - \frac{1}{\phi_\mathrm{m}}\right)(y-1)\right] + c_\infty(t), \tag{B.33}$$

$$\begin{aligned} f_\mathrm{w} = {} & -\varepsilon\mathrm{Pe}Q_\mathrm{l,in}\varphi\left(\frac{y-(1+h_2)}{\phi_\mathrm{w}} + \frac{h_2}{\phi_\mathrm{m}} + \frac{5}{8}\right) + \frac{\mathcal{R}}{2\phi_\mathrm{w}}(1+h_2-y)^2 \\ & + \varepsilon\mathrm{Pe}C_0'(t)\left\{\frac{y^2}{2} - (1+h_2)y + (1+h_2)^2 + \frac{\phi_\mathrm{m}}{\phi_\mathrm{w}}\left(h_2 + \frac{1}{\phi_\mathrm{m}}\right)[y-(1+h_2)]\right. \\ & \left. -h_2\left(1 - \frac{1}{\phi_\mathrm{m}}\right)\right\} + c_\infty(t), \end{aligned} \tag{B.34}$$

$$\begin{aligned} f_\mathrm{f} = {} & -\frac{\varepsilon\mathrm{Pe}Q_\mathrm{f,in}\varphi}{h_4^3}B_\mathrm{f}(y) - \varepsilon\mathrm{Pe}Q_\mathrm{l,in}\varphi\left(\frac{h_2}{\phi_\mathrm{m}} + \frac{h_3}{\phi_\mathrm{w}} + \frac{5}{8}\right) \\ & + \varepsilon\mathrm{Pe}C_0'(t)\left[\frac{y^2}{2} - Hy + (1+h_2)^2 + (H-h_4)(h_3+h_4)\right. \\ & \left. + \frac{h_3\phi_\mathrm{m}}{\phi_\mathrm{w}}\left(h_2 + \frac{1}{\phi_\mathrm{m}}\right) - h_2\left(1 - \frac{1}{\phi_\mathrm{m}}\right)\right] + \frac{h_3^2\mathcal{R}}{2\phi_\mathrm{w}} + c_\infty(t), \end{aligned} \tag{B.35}$$

$$\begin{aligned} B_\mathrm{f}(y) := {} & -\frac{y^4}{2} + (2H - h_4)y^3 - 3H(H-h_4)y^2 - H^2(3h_4 - 2H)y \\ & - \frac{H^4}{2} + h_4H^3 - \frac{h_4^4}{2}, \end{aligned} \tag{B.36}$$

where

$$\varphi(t) = \frac{h_3\mathcal{R} + \varepsilon\mathrm{Pe}\bar{h}C_0'(t)}{\varepsilon\mathrm{Pe}(Q_\mathrm{l,in} + Q_\mathrm{f,in})}, \tag{B.37}$$

and $c_\infty(t)$ (appearing in the expressions for f_i) is a degree of freedom which, once known, and through matching with the outer solution, will determine the correct form for $\bar{h}\bar{c}_\mathrm{u}(t)$, the inlet condition for $\bar{c}_1$ from (5.121).

We now match the far-field inner solution with the outer solution obtained in §5.3.6 up to and including $\mathrm{O}(\varepsilon)$ using Van Dyke's rule "(n t. o.)(m t. i.) = (m t. i.)(n t. o.)" [67]. In

the outer region we have, from §5.3.6,

$$c_i = c_0(x,t) + \varepsilon c_{i_1}(x,y,t) \quad (i = \mathrm{l},\mathrm{m},\mathrm{w},\mathrm{f}), \tag{B.38}$$

where c_0 satisfies (5.96) and c_{i_1} $(i = \mathrm{l},\mathrm{m},\mathrm{w},\mathrm{f})$ are given in equations (5.89)-(5.92). We note that we can solve (5.96) for c_0 subject to the inlet condition (5.97) using the method of characteristics, which yields

$$c_0 = -\frac{h_3\mathcal{R}}{\varepsilon \mathrm{Pe}(Q_{\mathrm{l,in}} + Q_{\mathrm{f,in}})}x + c_{\mathrm{in}}\left(t - \frac{\bar{h}}{Q_{\mathrm{l,in}} + Q_{\mathrm{f,in}}}x\right), \tag{B.39}$$

where we do not need to worry about the range of x for which this solution is valid (*i.e.* non-negative) since we are only concerned with the limit as $x \to 0^+$, at which point c_0 will always be greater than or equal to zero (and zero if and only if c_{in} is zero).

In the far field of the inner region, from the above analysis we have

$$C_i \sim C_0(t) + \varepsilon\left[-\varphi(t)X + f_i(y,t)\right] \quad (i = \mathrm{l},\mathrm{m},\mathrm{w},\mathrm{f}), \tag{B.40}$$

where f_i $(i = \mathrm{l},\mathrm{m},\mathrm{w},\mathrm{f})$ are given in equations (B.32)-(B.35). Matching with $m = n = 1$ then yields

$$C_0(t) = c_0(0^+,t) = c_{\mathrm{in}}(t). \tag{B.41}$$

Matching with $m = 2$, $n = 1$ and $m = 1$, $n = 2$ is automatically satisfied in all layers and so we omit the details. Moving on to $m = n = 2$, in the lumen we have

$$(2\text{ t. i.}) = c_{\mathrm{in}}(t) - \varepsilon\varphi(t)X + \varepsilon f_{\mathrm{l}}(y,t) \tag{B.42}$$

$$= c_{\mathrm{in}}(t) - \varphi(t)\varepsilon X - \frac{\varepsilon^2 \mathrm{Pe} Q_{\mathrm{l,in}}\varphi(t)}{8}(6y^2 - y^4) + \frac{\varepsilon^2\mathrm{Pe}}{2}c'_{\mathrm{in}}(t)y^2 + \varepsilon c_\infty(t), \tag{B.43}$$

and so

$$(2\text{ t. o.})(2\text{ t. i.}) = c_{\mathrm{in}}(t) - \varphi(t)x - \frac{\varepsilon^2 \mathrm{Pe} Q_{\mathrm{l,in}}\varphi(t)}{8}(6y^2 - y^4) + \frac{\varepsilon^2\mathrm{Pe}}{2}c'_{\mathrm{in}}(t)y^2 + \varepsilon c_\infty(t). \tag{B.44}$$

We also have

$$(2\text{ t. o.}) = -\frac{h_3\mathcal{R}}{\varepsilon\mathrm{Pe}(Q_{\mathrm{l,in}}+Q_{\mathrm{f,in}})}x + c_{\mathrm{in}}\left(t - \frac{\bar{h}}{Q_{\mathrm{l,in}}+Q_{\mathrm{f,in}}}x\right) + \varepsilon^2\mathrm{Pe}\left[\frac{y^2}{2}\frac{\partial c_0}{\partial t} + \frac{Q_{\mathrm{l,in}}}{8}\left(6y^2-y^4\right)\frac{\partial c_0}{\partial x} + g(x,t)\right] \tag{B.45}$$

$$= -\frac{h_3\mathcal{R}}{\varepsilon\mathrm{Pe}(Q_{\mathrm{l,in}}+Q_{\mathrm{f,in}})}x + c_{\mathrm{in}}\left(t - \frac{\bar{h}}{Q_{\mathrm{l,in}}+Q_{\mathrm{f,in}}}x\right) + \frac{\varepsilon^2\mathrm{Pe}y^2}{2}c'_{\mathrm{in}}\left(t - \frac{\bar{h}}{Q_{\mathrm{l,in}}+Q_{\mathrm{f,in}}}x\right) + \frac{\varepsilon^2\mathrm{Pe}Q_{\mathrm{l,in}}}{8}\left(6y^2-y^4\right)\left[-\frac{h_3\mathcal{R}}{\varepsilon\mathrm{Pe}(Q_{\mathrm{l,in}}+Q_{\mathrm{f,in}})} - \frac{\bar{h}}{Q_{\mathrm{l,in}}+Q_{\mathrm{f,in}}}c'_{\mathrm{in}}\left(t - \frac{\bar{h}}{Q_{\mathrm{l,in}}+Q_{\mathrm{f,in}}}x\right)\right] + \varepsilon^2\mathrm{Pe}g(x,t), \tag{B.46}$$

and so

$$(2\text{ t. i.})(2\text{ t. o.}) = c_{\mathrm{in}}(t) - \frac{\bar{h}\varepsilon X}{Q_{\mathrm{l,in}}+Q_{\mathrm{f,in}}}c'_{\mathrm{in}}(t) - \frac{h_3\mathcal{R}}{\varepsilon\mathrm{Pe}(Q_{\mathrm{l,in}}+Q_{\mathrm{f,in}})}\varepsilon X + \varepsilon^2\mathrm{Pe}\frac{y^2}{2}c'_{\mathrm{in}}(t) + \frac{\varepsilon^2\mathrm{Pe}Q_{\mathrm{l,in}}}{8}\left(6y^2-y^4\right)\left(-\frac{h_3\mathcal{R}}{\varepsilon\mathrm{Pe}(Q_{\mathrm{l,in}}+Q_{\mathrm{f,in}})} - \frac{\bar{h}}{Q_{\mathrm{l,in}}+Q_{\mathrm{f,in}}}c'_{\mathrm{in}}(t)\right) + \varepsilon^2\mathrm{Pe}g(0^+,t). \tag{B.47}$$

Setting (2 t. o.)(2 t. i.) = (2 t. i.)(2 t. o.) and recalling the form for $\varphi(t)$ from (B.37) then yields

$$c_\infty(t) = \varepsilon^2\mathrm{Pe}g(0^+,t), \tag{B.48}$$

and so we have an expression for $g(0^+,t)$ (and hence $\bar{c}_{\mathrm{u}}(t)$ using (5.115) and (5.121)) in terms of $c_\infty(t)$. The matching with $m=n=2$ in the remaining 3 layers follows through in a similar manner and, given (B.48), is automatically satisfied so we omit the details.

In order to determine $c_\infty(t)$ (and hence $\bar{c}_{\mathrm{u}}(t)$ via $g(0^+,t)$) it would be necessary to solve the full inner problem numerically at O(1) and O(ε), which we do not pursue here. However, as discussed in §5.4.1, the exact form of $\bar{c}_{\mathrm{u}}$ will determine the magnitude of the first-order solute concentrations in the outer region, but will not affect their shape, and thus a qualitative analysis can still be performed without knowledge of $c_\infty(t)$.

From this analysis, we can see that the outer solution up to and including O(ε) is unaffected by the exact geometry of the inner region except through the unknown degree of freedom $c_\infty(t)$. Hence the exact position of the ECS ports in this region does not affect the

solute concentration in the outer region at leading order, and only comes into the solution for the $\mathrm{O}(\varepsilon)$ concentration through the time-varying (but spatially independent) $c_\infty(t)$.

B.2 Downstream inner region

We now move to the downstream inner region near $x = 1$, where we set $x = 1 - \varepsilon X$ and apply the same transverse velocity scaling $v_i = V_i/\varepsilon$ $(i = \mathrm{l}, \mathrm{m}, \mathrm{w}, \mathrm{f})$. This gives the same system to solve as the upstream inner region, except for sign changes in front of single X-derivatives, and with the downstream boundary conditions

$$P_\mathrm{l} = P_\mathrm{dwn} \quad \text{at} \quad \mathcal{C}, \qquad P_\mathrm{f} = 0 \quad \text{at} \quad \mathcal{D}. \tag{B.49}$$

We therefore find that the leading-order pressure in the downstream inner region of the lumen and upper fluid layer is a function of time only, and by the above boundary conditions we can deduce that, at leading order, $P_\mathrm{l} \equiv P_\mathrm{dwn}$ and $P_\mathrm{f} \equiv 0$. By matching with the outer solution as $X \to \infty$, this gives the correct downstream boundary conditions to apply on the leading-order outer system in §5.3.5 as

$$p_\mathrm{l} = P_\mathrm{dwn}, \qquad p_\mathrm{f} = 0 \qquad \text{at} \quad x = 1^-. \tag{B.50}$$

This analysis is sufficient for our purposes, however we note that this downstream inner problem would also need to be solved numerically if the full solution was required; for instance if it was necessary to know the fluid flux and solute concentration leaving the lumen outlet and downstream ECS ports in order to compare with experimental measurements.

Appendix C

Boundary layer analysis of the combined-order equation

In this appendix we revisit the combined-order solute concentration equation from §5.3.8. We analyse more closely our choice for the additional boundary condition (5.132),

$$\frac{\partial \bar{c}}{\partial x} = 0 \qquad \text{at} \quad x = 1^{-}, \tag{C.1}$$

which is required to close the averaged system (5.128) and (5.131):

$$\begin{gathered} \frac{\partial \bar{c}}{\partial t} + \frac{(Q_{\mathrm{l,in}} + Q_{\mathrm{f,in}})}{\bar{h}} \frac{\partial \bar{c}}{\partial x} = D_{\mathrm{eff}} \frac{\partial^2 \bar{c}}{\partial x^2} - \frac{h_3 \mathcal{R}}{\varepsilon \mathrm{Pe}}, \\ \bar{c} = \bar{h}(c_{\mathrm{in}} + \varepsilon \bar{c}_{\mathrm{u}}) \qquad \text{at} \quad x = 0^{+}. \end{gathered} \tag{C.2a,b}$$

As discussed in previous chapters, there is no constraint on the downstream solute concentration in an experiment. We are therefore free to choose a boundary condition and, as discussed in §5.3.8, although the exact choice is unimportant we aim to minimise the error between the combined-order solution and the asymptotic solutions up to the order considered (*i.e.* up to and including $\mathrm{O}(\varepsilon)$). Any error between these two solutions as a result of taking the averaged formulation will arise in a boundary layer near $x = 1$ in which the diffusion term in (C.2a) is no longer small compared to the remaining terms. To investigate the error that arises from our choice (C.1), here we solve the combined-order equation in both the outer region and the boundary layer near $x = 1$ up to and including $\mathrm{O}(\varepsilon)$ and compare the resulting composite solution with the globally averaged asymptotic solutions at $\mathrm{O}(1)$ and $\mathrm{O}(\varepsilon)$, namely $\bar{c}_0$ and $\bar{c}_1$. We assume throughout our analysis that, at the orders considered, the concentration is non-zero throughout the domain (*i.e.* large enough t and appropriate operating conditions). Otherwise, if the concentration is zero for some x, it is zero for all values downstream of that point, and hence boundary condition (C.1) is trivially satisfied.

We first solve the asymptotic equations and boundary conditions at O(1) and O(ε) from (5.122) and write in terms of averaged concentrations. This yields

$$\bar{c}_0 = -\frac{\bar{h}h_3\mathcal{R}}{\varepsilon \mathrm{Pe}(Q_{\mathrm{l,in}}+Q_{\mathrm{f,in}})}x + \bar{h}c_{\mathrm{in}}\left(t - \frac{\bar{h}}{Q_{\mathrm{l,in}}+Q_{\mathrm{f,in}}}x\right), \tag{C.3}$$

$$\bar{c}_1 = \frac{\bar{h}D_{\mathrm{eff}}}{\varepsilon}\left(\frac{\bar{h}}{Q_{\mathrm{l,in}}+Q_{\mathrm{f,in}}}\right)^3 x c_{\mathrm{in}}''\left(t - \frac{\bar{h}}{Q_{\mathrm{l,in}}+Q_{\mathrm{f,in}}}x\right) + \bar{h}\bar{c}_{\mathrm{u}}\left(t - \frac{\bar{h}}{Q_{\mathrm{l,in}}+Q_{\mathrm{f,in}}}x\right), \tag{C.4}$$

where $\bar{c}_0 = \bar{h}c_0$ and primes denote differentiation with respect to the argument of a function. We define the combined, averaged asymptotic solution up to and including O(ε) by $\bar{c}_{\mathrm{as}} := \bar{c}_0 + \varepsilon\bar{c}_1$, which will be compared to the composite solution to the combined-order equation later.

We now consider the combined-order concentration equation (C.2a), subject to the corresponding boundary conditions (C.1) and (C.2b). Firstly, we note that if we expand the combined-order concentration $\bar{c}$ in powers of ε and solve (C.2a) at O(1) and O(ε) subject to the inlet boundary condition at $x = 0^+$ only, this yields 'outer' solutions which are identical to $\bar{c}_0$ and $\bar{c}_1$ in (C.3) and (C.4). For clarity of notation when we form the composite solution later, we will denote this combined-order outer solution by $\bar{c}_{\mathrm{out}}$.

We now wish to find the inner solution in the boundary layer near $x = 1$ at O(1) and O(ε). To do so, we rescale

$$x = 1 - \varepsilon X \quad (X > 0), \qquad \bar{c}(x,t) = \bar{C}(X,t), \tag{C.5}$$

and (C.2a) then becomes

$$\varepsilon\frac{\partial \bar{C}}{\partial t} - \frac{(Q_{\mathrm{l,in}}+Q_{\mathrm{f,in}})}{\bar{h}}\frac{\partial \bar{C}}{\partial X} = \frac{D_{\mathrm{eff}}}{\varepsilon}\frac{\partial^2 \bar{C}}{\partial X^2} - \frac{h_3\mathcal{R}}{\mathrm{Pe}}, \tag{C.6}$$

subject to

$$\frac{\partial \bar{C}}{\partial X} = 0 \qquad \text{at} \quad X = 0, \tag{C.7}$$

and matching with $\bar{c}$ as $X \to \infty$. Recalling that $D_{\mathrm{eff}} = \mathrm{O}(\varepsilon)$ and $\mathrm{Pe} = \mathrm{O}(1/\varepsilon)$, and expanding $\bar{C}$ in powers of ε with the usual subscript notation, we find at O(1)

$$\begin{gathered} -\frac{(Q_{\mathrm{l,in}}+Q_{\mathrm{f,in}})}{\bar{h}}\frac{\partial \bar{C}_0}{\partial X} = \frac{D_{\mathrm{eff}}}{\varepsilon}\frac{\partial^2 \bar{C}_0}{\partial X^2}, \\ \frac{\partial \bar{C}_0}{\partial X} = 0 \qquad \text{at} \quad X = 0. \end{gathered} \tag{C.8}$$

Solving (C.8) implies that

$$\bar{C}_0 = \alpha(t), \tag{C.9}$$

for some function $\alpha(t)$, which can be determined through matching with $\bar{c}_0$ as $x \to 1$ and $X \to \infty$. Using Van Dyke's rule (n t. o.)(m t. i.) = (m t. i.)(n t. o.) [67] and setting $m = n = 1$ gives

$$\bar{C}_0 = \alpha(t) = -\frac{\bar{h}h_3\mathcal{R}}{\varepsilon \mathrm{Pe}(Q_{\mathrm{l,in}} + Q_{\mathrm{f,in}})} + \bar{h}c_{\mathrm{in}}\left(t - \frac{\bar{h}}{Q_{\mathrm{l,in}} + Q_{\mathrm{f,in}}}\right). \tag{C.10}$$

At $\mathrm{O}(\varepsilon)$ the system to solve is

$$\begin{gathered}\frac{\partial \bar{C}_0}{\partial t} - \frac{(Q_{\mathrm{l,in}} + Q_{\mathrm{f,in}})}{\bar{h}}\frac{\partial \bar{C}_1}{\partial X} = \frac{D_{\mathrm{eff}}}{\varepsilon}\frac{\partial^2 \bar{C}_1}{\partial X^2} - \frac{h_3\mathcal{R}}{\varepsilon \mathrm{Pe}}, \\ \frac{\partial \bar{C}_1}{\partial X} = 0 \qquad \text{at} \quad X = 0,\end{gathered} \tag{C.11}$$

which has solution

$$\begin{aligned}\bar{C}_1 = \frac{\bar{h}}{Q_{\mathrm{l,in}} + Q_{\mathrm{f,in}}}\Bigg[\frac{D_{\mathrm{eff}}\bar{h}}{\varepsilon(Q_{\mathrm{l,in}} + Q_{\mathrm{f,in}})}\exp\left(-\frac{\varepsilon(Q_{\mathrm{l,in}} + Q_{\mathrm{f,in}})}{\bar{h}D_{\mathrm{eff}}}X\right) \\ + X - \frac{D_{\mathrm{eff}}\bar{h}}{\varepsilon(Q_{\mathrm{l,in}} + Q_{\mathrm{f,in}})}\Bigg]\left[\bar{h}c'_{\mathrm{in}}\left(t - \frac{\bar{h}}{Q_{\mathrm{l,in}} + Q_{\mathrm{f,in}}}\right) + \frac{h_3\mathcal{R}}{\varepsilon \mathrm{Pe}}\right] + \beta(t),\end{aligned} \tag{C.12}$$

for some function $\beta(t)$. Matching is automatically satisfied for $m = 2$, $n = 1$ and $m = 1$, $n = 2$, and for $m = n = 2$ we find

$$\begin{aligned}\beta(t) = \frac{D_{\mathrm{eff}}}{\varepsilon}\left(\frac{\bar{h}}{Q_{\mathrm{l,in}} + Q_{\mathrm{f,in}}}\right)^2\Bigg[\bar{h}c'_{\mathrm{in}}\left(t - \frac{\bar{h}}{Q_{\mathrm{l,in}} + Q_{\mathrm{f,in}}}\right) + \frac{h_3\mathcal{R}}{\varepsilon \mathrm{Pe}} \\ + \frac{\bar{h}^2}{Q_{\mathrm{l,in}} + Q_{\mathrm{f,in}}}c''_{\mathrm{in}}\left(t - \frac{\bar{h}}{Q_{\mathrm{l,in}} + Q_{\mathrm{f,in}}}\right)\Bigg] + \bar{h}\bar{c}_{\mathrm{u}}\left(t - \frac{\bar{h}}{Q_{\mathrm{l,in}} + Q_{\mathrm{f,in}}}\right).\end{aligned} \tag{C.13}$$

From (C.10) and (C.12) we can thus obtain the combined-order inner solution, defined as $\bar{C}_{\mathrm{in}} := \bar{C}_0 + \varepsilon\bar{C}_1$, and then also construct an additive composite solution to the combined-order equation,

$$\bar{c}_{\mathrm{comp}} := \bar{c}_{\mathrm{out}} + \bar{C}_{\mathrm{in}} - \bar{c}_{\mathrm{over}}, \tag{C.14}$$

where $\bar{c}_{\mathrm{over}}$ is the 'overlap' between the outer and inner solutions which is given by the (2 t. i.)(2 t. o.) terms. We can now compare the composite solution $\bar{c}_{\mathrm{comp}}$ to the combined-order equation (C.2a) to the combined, averaged asymptotic solution, $\bar{c}_{\mathrm{as}}$. Given the analysis presented here, we expect the two solutions to match up to $\mathrm{O}(\varepsilon^2)$, except in the boundary layer of width $\mathrm{O}(\varepsilon)$ near $x = 1$ within which we expect an error of $\mathrm{O}(\varepsilon)$ as the additional diffusion term in (C.2a) becomes significant. The plots in Figure C.1 confirm that this is the case, and hence (C.1) is an appropriate choice of boundary condition for the combined-order system in §5.3.8.

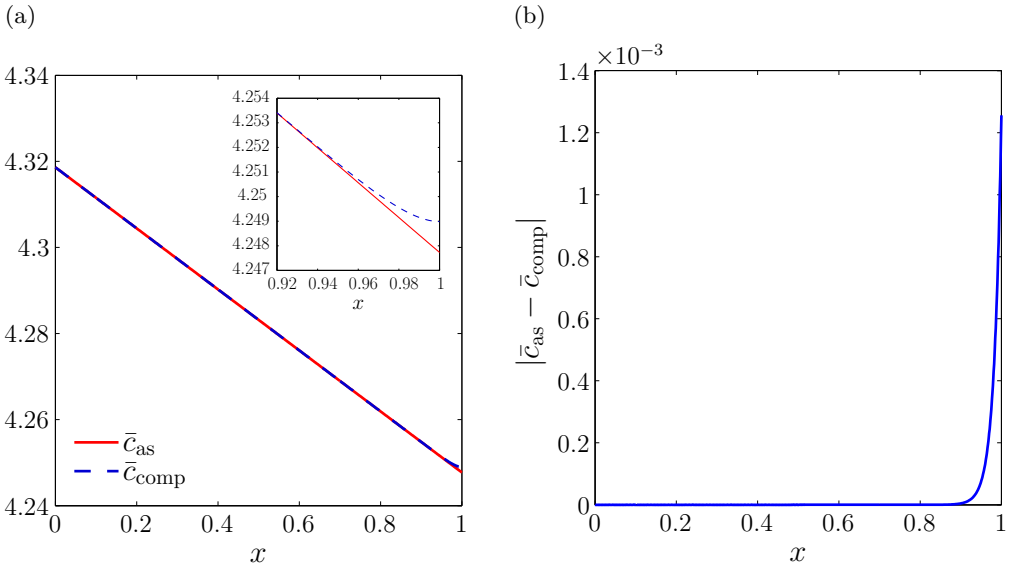

Figure C.1: Plots of (a) the combined-order asymptotic solution $\bar{c}_{\mathrm{as}}$ and the composite averaged solution $\bar{c}_{\mathrm{comp}}$ (inset showing detail of the boundary layer region near $x = 1$), and (b) the absolute error $|\bar{c}_{\mathrm{as}} - \bar{c}_{\mathrm{comp}}|$. Inlet conditions were set to be constant, with $c_{\mathrm{in}} = \bar{c}_{\mathrm{u}} = 1$. Fixed parameter values are as in Table 5.2, with $Q_{\mathrm{l,in}} = Q_{\mathrm{f,in}} = h_3 = 1$.

Appendix D

Reduction to classical Taylor dispersion

In this appendix, we revisit the combined-order analysis of §5.3.8 and show that the equations for classical Taylor dispersion in the lumen and upper fluid layer can be recovered from our 4-layer system in the limit of an impermeable membrane and cell layer. This corresponds to taking the limit ϕ_{m}, $\phi_{\mathrm{w}} \to 0$, and these parameters come into (5.128) via $\bar{h}$ (specifically, $1/\bar{h}$) and the effective dispersion coefficient D_{eff}. However, both $1/\bar{h}$ and D_{eff} tend to infinity as the porosities tend to zero (the latter of which is confirmed in Figures 5.4(a) and (b)) and so we cannot take the limit of (5.128) as ϕ_{m}, $\phi_{\mathrm{w}} \to 0$ as it stands. We instead return to the dimensionless solute governing equations in the lumen and upper fluid layer (first presented in §5.3.4) and re-derive the combined-order, averaged equations by decomposing the solute concentrations in these layers into average and fluctuating parts, before taking the impermeable limit.

D.1 Lumen

Beginning in the lumen, we return to the dimensionless solute governing equation from (5.43),

$$\varepsilon^2 \mathrm{Pe}\left(\frac{\partial c_{\mathrm{l}}}{\partial t} + \frac{\partial}{\partial x}(c_{\mathrm{l}} u_{\mathrm{l}}) + \frac{\partial}{\partial y}(c_{\mathrm{l}} v_{\mathrm{l}})\right) = \varepsilon^2 \frac{\partial^2 c_{\mathrm{l}}}{\partial x^2} + \frac{\partial^2 c_{\mathrm{l}}}{\partial y^2}, \tag{D.1}$$

together with the boundary conditions

$$\frac{\partial c_{\mathrm{l}}}{\partial y} = 0 \qquad \text{on} \quad y = 0, \tag{D.2}$$

$$c_{\mathrm{l}} = c_{\mathrm{m}}, \qquad \frac{\partial c_{\mathrm{l}}}{\partial y} = \phi_{\mathrm{m}} \frac{\partial c_{\mathrm{m}}}{\partial y} \qquad \text{on} \quad y = 1, \tag{D.3}$$

$$c_{\mathrm{l}} = c_{\mathrm{l,in}} \qquad \text{on} \quad x = 0. \tag{D.4}$$

We define the dimensionless average in the lumen by

$$\langle \cdot \rangle_{\mathrm{l}} := \int_0^1 \cdot \, \mathrm{d}y, \tag{D.5}$$

and decompose the solute concentration and water velocity into y-independent (denoted by a bar) and fluctuating (denoted by a prime) components as follows:

$$c_{\mathrm{l}}(x,y,t) = \bar{c}_{\mathrm{l}}(x,t) + c'_{\mathrm{l}}(x,y,t), \qquad \mathbf{u}_{\mathrm{l}}(x,y,t) = \bar{\mathbf{u}}_{\mathrm{l}}(x,t) + \mathbf{u}'_{\mathrm{l}}(x,y,t), \tag{D.6}$$

so that $\langle c'_{\mathrm{l}} \rangle_{\mathrm{l}} = \langle u'_{\mathrm{l}} \rangle_{\mathrm{l}} = \langle v'_{\mathrm{l}} \rangle_{\mathrm{l}} = 0$ by definition. Substituting the ansätze in (D.6) into (D.1) yields

$$\varepsilon^2 \mathrm{Pe} \left\{ \left(\frac{\partial \bar{c}_{\mathrm{l}}}{\partial t} + \frac{\partial c'_{\mathrm{l}}}{\partial t} \right) + \frac{\partial}{\partial x} \left[(\bar{u}_{\mathrm{l}} + u'_{\mathrm{l}})(\bar{c}_{\mathrm{l}} + c'_{\mathrm{l}}) \right] + \frac{\partial}{\partial y} \left[(\bar{v}_{\mathrm{l}} + v'_{\mathrm{l}})(\bar{c}_{\mathrm{l}} + c'_{\mathrm{l}}) \right] \right\} = \varepsilon^2 \left(\frac{\partial^2 \bar{c}_{\mathrm{l}}}{\partial x^2} + \frac{\partial^2 c'_{\mathrm{l}}}{\partial x^2} \right) + \frac{\partial^2 c'_{\mathrm{l}}}{\partial y^2}, \tag{D.7}$$

whilst averaging equation (D.1) across the layer $0 < y < 1$ leads to

$$\varepsilon^2 \mathrm{Pe} \left(\frac{\partial}{\partial t} \langle c_{\mathrm{l}} \rangle_{\mathrm{l}} + \frac{\partial}{\partial x} \langle c_{\mathrm{l}} u_{\mathrm{l}} \rangle_{\mathrm{l}} + c_{\mathrm{l}} v_{\mathrm{l}} \big|_{y=1} \right) = \varepsilon^2 \frac{\partial^2}{\partial x^2} \langle c_{\mathrm{l}} \rangle_{\mathrm{l}} + \left. \frac{\partial c'_{\mathrm{l}}}{\partial y} \right|_{y=1}. \tag{D.8}$$

Substituting the decomposition (D.6) into this averaged equation (D.8) and using the fact that the average of the fluctuations is zero gives

$$\varepsilon^2 \mathrm{Pe} \left(\frac{\partial \bar{c}_{\mathrm{l}}}{\partial t} + \frac{\partial}{\partial x} (\bar{c}_{\mathrm{l}} \bar{u}_{\mathrm{l}}) + \frac{\partial}{\partial x} \langle c'_{\mathrm{l}} u'_{\mathrm{l}} \rangle_{\mathrm{l}} + c_{\mathrm{l}} v_{\mathrm{l}} \big|_{y=1} \right) = \varepsilon^2 \frac{\partial^2 \bar{c}_{\mathrm{l}}}{\partial x^2} + \left. \frac{\partial c'_{\mathrm{l}}}{\partial y} \right|_{y=1}. \tag{D.9}$$

Finally, subtracting equation (D.9) from (D.7) yields

$$\varepsilon^2 \mathrm{Pe} \left(\frac{\partial c'_{\mathrm{l}}}{\partial t} + \frac{\partial}{\partial x} (c'_{\mathrm{l}} \bar{u}_{\mathrm{l}} + \bar{c}_{\mathrm{l}} u'_{\mathrm{l}} + c'_{\mathrm{l}} u'_{\mathrm{l}}) - \frac{\partial}{\partial x} \langle c'_{\mathrm{l}} u'_{\mathrm{l}} \rangle_{\mathrm{l}} + \frac{\partial}{\partial y} (c'_{\mathrm{l}} \bar{v}_{\mathrm{l}} + \bar{c}_{\mathrm{l}} v'_{\mathrm{l}} + c'_{\mathrm{l}} v'_{\mathrm{l}}) - c_{\mathrm{l}} v_{\mathrm{l}} \big|_{y=1} \right) = \varepsilon^2 \frac{\partial^2 c'_{\mathrm{l}}}{\partial x^2} + \frac{\partial^2 c'_{\mathrm{l}}}{\partial y^2} - \left. \frac{\partial c'_{\mathrm{l}}}{\partial y} \right|_{y=1}. \tag{D.10}$$

The corresponding boundary conditions are given by

$$\frac{\partial c'_{\mathrm{l}}}{\partial y} = 0 \qquad \text{on} \quad y = 0, \tag{D.11}$$

$$\bar{c}_{\mathrm{l}} + c'_{\mathrm{l}} = c_{\mathrm{m}}, \qquad \frac{\partial c'_{\mathrm{l}}}{\partial y} = \phi_{\mathrm{m}} \frac{\partial c_{\mathrm{m}}}{\partial y} \qquad \text{on} \quad y = 1. \tag{D.12}$$

We now expand $\bar{c}_{\mathrm{l}}$, c'_{l}, $\bar{\mathbf{u}}_{\mathrm{l}}$ and $\mathbf{u}'_{\mathrm{l}}$ in powers of ε as before, aiming to find an expression for c'_{l} from (D.10) which can be substituted into (D.9) and thereby obtain an equation for $\bar{c}_{\mathrm{l}}$ accurate up to and including $\mathrm{O}(\varepsilon)$. This analysis will make use of the leading-order velocities, and so we introduce the flow solution from §5.3.5,

$$u_{\mathrm{l}_0} = -\frac{3}{2} Q_{\mathrm{l,in}} (y^2 - 1), \qquad v_{\mathrm{l}_0} \equiv 0, \tag{D.13}$$

noting that this gives

$$\bar{u}_{\mathrm{l}_0} = Q_{\mathrm{l,in}}, \qquad u'_{\mathrm{l}_0} = \frac{Q_{\mathrm{l,in}}}{2}(1-3y^2). \tag{D.14a,b}$$

The analysis of §5.3.6 indicates that the leading-order concentration is independent of y and hence common to all layers. We therefore expect $c'_{\mathrm{l}_0} \equiv 0$, and note that this satisfies equation (D.10) at leading order and the corresponding boundary conditions

$$\frac{\partial c'_{\mathrm{l}_0}}{\partial y} = 0 \qquad \text{on} \quad y = 0, 1, \tag{D.15}$$

$$\bar{c}_{\mathrm{l}_0} + c'_{\mathrm{l}_0} = c_{\mathrm{m}_0} \qquad \text{on} \quad y = 1, \tag{D.16}$$

together with the requirement $\langle c'_{\mathrm{l}_0}\rangle_{\mathrm{l}} = 0$. At $\mathrm{O}(\varepsilon)$, equation (D.10) becomes

$$\varepsilon \mathrm{Pe} u'_{\mathrm{l}_0} \frac{\partial \bar{c}_{\mathrm{l}_0}}{\partial x} = \frac{\partial^2 c'_{\mathrm{l}_1}}{\partial y^2} - \left.\frac{\partial c'_{\mathrm{l}_1}}{\partial y}\right|_{y=1}, \tag{D.17}$$

while the relevant boundary conditions for c'_{l_1} are

$$\frac{\partial c'_{\mathrm{l}_1}}{\partial y} = 0 \qquad \text{on} \quad y = 0, \tag{D.18}$$

$$\bar{c}_{\mathrm{l}_1} + c'_{\mathrm{l}_1} = c_{\mathrm{m}_1}, \qquad \frac{\partial c'_{\mathrm{l}_1}}{\partial y} = \phi_{\mathrm{m}} \frac{\partial c_{\mathrm{m}_1}}{\partial y} \qquad \text{on} \quad y = 1. \tag{D.19}$$

Substituting into (D.17) the known form (D.14b) for u'_{l_0}, integrating with respect to y, and applying boundary condition (D.18) yields

$$\frac{\partial c'_{\mathrm{l}_1}}{\partial y} = \frac{\varepsilon \mathrm{Pe} Q_{\mathrm{l,in}}}{2}(y - y^3)\frac{\partial \bar{c}_{\mathrm{l}_0}}{\partial x} + \left.\frac{\partial c'_{\mathrm{l}_1}}{\partial y}\right|_{y=1} y. \tag{D.20}$$

Integrating (D.20) with respect to y and using the fact that we require $\langle c'_{\mathrm{l}_1}\rangle_{\mathrm{l}} = 0$, we find

$$c'_{\mathrm{l}_1} = \frac{\varepsilon \mathrm{Pe} Q_{\mathrm{l,in}}}{8}\left(2y^2 - y^4 - \frac{7}{15}\right)\frac{\partial \bar{c}_{\mathrm{l}_0}}{\partial x} + \frac{1}{6}(3y^2-1)\left.\frac{\partial c'_{\mathrm{l}_1}}{\partial y}\right|_{y=1}. \tag{D.21}$$

Furthermore, we can now compute

$$\frac{\partial}{\partial x}\langle c'_{\mathrm{l}_1} u'_{\mathrm{l}_0}\rangle_{\mathrm{l}} = -\frac{2\varepsilon \mathrm{Pe} Q_{\mathrm{l,in}}^2}{105}\frac{\partial^2 \bar{c}_{\mathrm{l}_0}}{\partial x^2} - \frac{Q_{\mathrm{l,in}}}{15}\frac{\partial}{\partial x}\left.\frac{\partial c'_{\mathrm{l}_1}}{\partial y}\right|_{y=1}. \tag{D.22}$$

We return to equation (D.9), noting that all terms at leading order are now zero. Upon dividing through by ε (recalling that $\mathrm{Pe} = \mathrm{O}(1/\varepsilon)$), we consider the resulting $\mathrm{O}(1)$ and $\mathrm{O}(\varepsilon)$ equations which are, respectively,

$$\varepsilon \mathrm{Pe}\left(\frac{\partial \bar{c}_{\mathrm{l}_0}}{\partial t} + \frac{\partial}{\partial x}\left(\bar{c}_{\mathrm{l}_0}\bar{u}_{\mathrm{l}_0}\right)\right) = \left.\frac{\partial c'_{\mathrm{l}_1}}{\partial y}\right|_{y=1}, \tag{D.23}$$

$$\varepsilon \mathrm{Pe}\left(\frac{\partial \bar{c}_{\mathrm{l}_1}}{\partial t} + \frac{\partial}{\partial x}\left(\bar{c}_{\mathrm{l}_1}\bar{u}_{\mathrm{l}_0} + \bar{c}_{\mathrm{l}_0}\bar{u}_{\mathrm{l}_1}\right) + \frac{\partial}{\partial x}\langle c'_{\mathrm{l}_1} u'_{\mathrm{l}_0}\rangle_{\mathrm{l}} + \bar{c}_{\mathrm{l}_0} v_{\mathrm{l}_1}|_{y=1}\right) = \frac{\partial^2 \bar{c}_{\mathrm{l}_0}}{\partial x^2} + \left.\frac{\partial c'_{\mathrm{l}_2}}{\partial y}\right|_{y=1}. \tag{D.24}$$

If we now set $\bar{c}_\mathrm{l} = \bar{c}_{\mathrm{l}_0} + \varepsilon \bar{c}_{\mathrm{l}_1}$ and substitute (D.21) and (D.22) into (D.23) and (D.24), respectively, we can combine the equations (weighting (D.24) by ε) to find

$$\frac{\partial \bar{c}_\mathrm{l}}{\partial t} + \frac{\partial}{\partial x}\left(\bar{c}_\mathrm{l}\bar{u}_{\mathrm{l}_0}\right) + \varepsilon \frac{\partial}{\partial x}\left(\bar{c}_\mathrm{l}\bar{u}_{\mathrm{l}_1}\right) = \frac{1}{\mathrm{Pe}}\left(1 + \frac{2\varepsilon^2 \mathrm{Pe}^2 Q_{\mathrm{l,in}}^2}{105}\right)\frac{\partial^2 \bar{c}_\mathrm{l}}{\partial x^2} + \frac{\varepsilon Q_{\mathrm{l,in}}}{15}\frac{\partial}{\partial x}\left.\frac{\partial c'_{\mathrm{l}_1}}{\partial y}\right|_{y=1} - \varepsilon \bar{c}_\mathrm{l} v_{\mathrm{l}_1}\big|_{y=1} + \frac{1}{\varepsilon \mathrm{Pe}}\left.\frac{\partial c'_{\mathrm{l}_1}}{\partial y}\right|_{y=1} + \frac{1}{\mathrm{Pe}}\left.\frac{\partial c'_{\mathrm{l}_2}}{\partial y}\right|_{y=1}, \tag{D.25}$$

which is accurate up to and including $\mathrm{O}(\varepsilon)$. In the following section, we present the corresponding analysis for the upper fluid layer, before taking the impermeable limit $\phi_\mathrm{m},\ \phi_\mathrm{w} \to 0$.

D.2 Upper fluid layer

Next we carry out a similar procedure in the upper fluid layer, where the dimensionless mass transport equation from (5.46) is

$$\varepsilon^2 \mathrm{Pe}\left(\frac{\partial c_\mathrm{f}}{\partial t} + \frac{\partial}{\partial x}(c_\mathrm{f} u_\mathrm{f}) + \frac{\partial}{\partial y}(c_\mathrm{f} v_\mathrm{f})\right) = \varepsilon^2 \frac{\partial^2 c_\mathrm{f}}{\partial x^2} + \frac{\partial^2 c_\mathrm{f}}{\partial y^2}, \tag{D.26}$$

along with boundary conditions

$$\frac{\partial c_\mathrm{f}}{\partial y} = 0 \qquad \text{on} \quad y = H, \tag{D.27}$$

$$c_\mathrm{f} = c_\mathrm{w}, \qquad \frac{\partial c_\mathrm{f}}{\partial y} = \phi_\mathrm{w}\frac{\partial c_\mathrm{w}}{\partial y} \qquad \text{on} \quad y = H - h_4. \tag{D.28}$$

We define the (dimensionless) average in the upper fluid layer by

$$\langle\,\cdot\,\rangle_\mathrm{f} := \frac{1}{h_4}\int_{H-h_4}^{H} \cdot\, \mathrm{d}y, \tag{D.29}$$

and once again decompose the solute concentration and water velocity into mean and fluctuating components:

$$c_\mathrm{f}(x,y,t) = \bar{c}_\mathrm{f}(x,t) + c'_\mathrm{f}(x,y,t), \qquad \mathbf{u}_\mathrm{f}(x,y,t) = \bar{\mathbf{u}}_\mathrm{f}(x,t) + \mathbf{u}'_\mathrm{f}(x,y,t). \tag{D.30}$$

Performing the same averaging and decomposition analysis on equation (D.26) as in the lumen yields two equations, the first corresponding to (D.9),

$$\varepsilon^2 \mathrm{Pe}\left(\frac{\partial \bar{c}_\mathrm{f}}{\partial t} + \frac{\partial}{\partial x}(\bar{c}_\mathrm{f}\bar{u}_\mathrm{f}) + \frac{\partial}{\partial x}\langle c'_\mathrm{f} u'_\mathrm{f}\rangle_\mathrm{f} - \frac{1}{h_4}\,c_\mathrm{f} v_\mathrm{f}\big|_{y=H-h_4}\right) = \varepsilon^2 \frac{\partial^2 \bar{c}_\mathrm{f}}{\partial x^2} - \frac{1}{h_4}\left.\frac{\partial c'_\mathrm{f}}{\partial y}\right|_{y=H-h_4}, \tag{D.31}$$

and the second to (D.10),

$$\varepsilon^2\mathrm{Pe}\left(\frac{\partial c_\mathrm{f}'}{\partial t}+\frac{\partial}{\partial x}\left(c_\mathrm{f}'\bar{u}_\mathrm{f}+\bar{c}_\mathrm{f}u_\mathrm{f}'+c_\mathrm{f}'u_\mathrm{f}'\right)-\frac{\partial}{\partial x}\langle c_\mathrm{f}'u_\mathrm{f}'\rangle_\mathrm{f}\right.$$
$$\left.+\frac{\partial}{\partial y}\left(c_\mathrm{f}'\bar{v}_\mathrm{f}+\bar{c}_\mathrm{f}v_\mathrm{f}'+c_\mathrm{f}'v_\mathrm{f}'\right)+\frac{1}{h_4}\,c_\mathrm{f}v_\mathrm{f}|_{y=H-h_4}\right)=\varepsilon^2\frac{\partial^2 c_\mathrm{f}'}{\partial x^2}+\frac{\partial^2 c_\mathrm{f}'}{\partial y^2}+\frac{1}{h_4}\,\frac{\partial c_\mathrm{f}'}{\partial y}\bigg|_{y=H-h_4}. \tag{D.32}$$

The corresponding boundary conditions are

$$\frac{\partial c_\mathrm{f}'}{\partial y}=0 \qquad \text{on} \quad y=H, \tag{D.33}$$

$$\bar{c}_\mathrm{f}+c_\mathrm{f}'=c_\mathrm{w}, \qquad \frac{\partial c_\mathrm{f}'}{\partial y}=\phi_\mathrm{w}\frac{\partial c_\mathrm{w}}{\partial y} \qquad \text{on} \quad y=H-h_4. \tag{D.34}$$

Next we expand $\bar{c}_\mathrm{f}$, c_f', $\bar{\mathbf{u}}_\mathrm{f}$ and $\mathbf{u}_\mathrm{f}'$ in powers of ε as in the lumen, with the aim of finding an expression for c_{f_1}'. We will again need to use the leading-order flow solution in the upper fluid layer,

$$u_{\mathrm{f}_0}=\frac{6Q_{\mathrm{f,in}}}{h_4^3}(y-H)(H-h_4-y), \qquad v_{\mathrm{f}_0}\equiv 0, \tag{D.35}$$

which gives

$$\bar{u}_{\mathrm{f}_0}=\frac{Q_{\mathrm{f,in}}}{h_4}, \qquad u_{\mathrm{f}_0}'=-\frac{Q_{\mathrm{f,in}}}{h_4}\left\{\frac{6}{h_4^2}(y-H)\left[y-(H-h_4)\right]+1\right\}. \tag{D.36a,b}$$

As in the lumen, at O(1) we expect that $c_{\mathrm{f}_0}'\equiv 0$. We note that this satisfies equation (D.32) at leading order, the corresponding boundary conditions

$$\frac{\partial c_{\mathrm{f}_0}'}{\partial y}=0 \qquad \text{on} \quad y=H-h_4, H, \tag{D.37}$$

$$\bar{c}_{\mathrm{f}_0}+c_{\mathrm{f}_0}'=c_{\mathrm{w}0} \qquad \text{on} \quad y=H-h_4, \tag{D.38}$$

and also the requirement $\langle c_{\mathrm{f}_0}'\rangle_\mathrm{f}=0$.

We move on to O(ε), where equation (D.32) yields

$$\varepsilon\mathrm{Pe}u_{\mathrm{f}_0}'\frac{\partial\bar{c}_{\mathrm{f}_0}}{\partial x}=\frac{\partial^2 c_{\mathrm{f}_1}'}{\partial y^2}+\frac{1}{h_4}\,\frac{\partial c_{\mathrm{f}_1}'}{\partial y}\bigg|_{y=H-h_4}, \tag{D.39}$$

with corresponding boundary conditions for c_{f_1}'

$$\frac{\partial c_{\mathrm{f}_1}'}{\partial y}=0 \qquad \text{on} \quad y=H, \tag{D.40}$$

$$\frac{\partial c_{\mathrm{f}_1}'}{\partial y}=\phi_\mathrm{w}\frac{\partial c_{\mathrm{w}_1}}{\partial y} \qquad \text{on} \quad y=H-h_4, \tag{D.41}$$

$$\bar{c}_{\mathrm{f}_1}+c_{\mathrm{f}_1}'=c_{\mathrm{w}_1} \qquad \text{on} \quad y=H-h_4. \tag{D.42}$$

Integrating twice and applying boundary conditions (D.40) and (D.41), along with $\langle c'_{\mathrm{f}_1}\rangle_{\mathrm{f}} = 0$, yields

$$c'_{\mathrm{f}_1} = \frac{\varepsilon \mathrm{Pe} Q_{\mathrm{f,in}}}{h_4^3}\left[-\frac{y^4}{2} + (2H-h_4)y^3 + \left(-3H^2 + 3Hh_4 - \frac{h_4^2}{2}\right)y^2 \right. \\ \left. + (2H^3 - 3H^2h_4 + Hh_4^2)y + H^3h_4 + \frac{h_4^4}{60} - \frac{H^2h_4^2}{2} - \frac{H^4}{2}\right]\frac{\partial \bar{c}_{\mathrm{f}_0}}{\partial x} \\ + \frac{1}{2h_4}\left(y(2H-y) + \frac{h_4^2}{3} - H^2\right)\left.\frac{\partial c'_{\mathrm{f}_1}}{\partial y}\right|_{y=H-h_4}, \tag{D.43}$$

which enables us to find

$$\langle u'_{\mathrm{f}_0}\frac{\partial c'_{\mathrm{f}_1}}{\partial x}\rangle_{\mathrm{f}} = -\frac{Q_{\mathrm{f,in}}}{420}\left(2\varepsilon \mathrm{Pe} Q_{\mathrm{f,in}}\frac{\partial^2 \bar{c}_{\mathrm{f}_0}}{\partial x^2} - 7\frac{\partial}{\partial x}\left.\frac{\partial c'_{\mathrm{f}_1}}{\partial y}\right|_{y=H-h_4}\right). \tag{D.44}$$

We now return to (D.31), and divide through by ε as it is again zero at leading order. Equating coefficients of ε^0 and ε^1 then yields, respectively,

$$\varepsilon \mathrm{Pe}\left(\frac{\partial \bar{c}_{\mathrm{f}_0}}{\partial t} + \frac{\partial}{\partial x}\left(\bar{c}_{\mathrm{f}_0}\bar{u}_{\mathrm{f}_0}\right)\right) = -\frac{1}{h_4}\left.\frac{\partial c'_{\mathrm{f}_1}}{\partial y}\right|_{y=H-h_4}, \tag{D.45}$$

and

$$\varepsilon \mathrm{Pe}\left(\frac{\partial \bar{c}_{\mathrm{f}_1}}{\partial t} + \frac{\partial}{\partial x}\left(\bar{c}_{\mathrm{f}_1}\bar{u}_{\mathrm{f}_0} + \bar{c}_{\mathrm{f}_0}\bar{u}_{\mathrm{f}_1}\right) + \frac{\partial}{\partial x}\langle c'_{\mathrm{f}_1}u'_{\mathrm{f}_0}\rangle_{\mathrm{f}} - \frac{1}{h_4}\bar{c}_{\mathrm{f}_0}v_{\mathrm{f}_1}|_{y=H-h_4}\right) = \frac{\partial^2 \bar{c}_{\mathrm{f}_0}}{\partial x^2} - \frac{1}{h_4}\frac{\partial c'_{\mathrm{f}_2}}{\partial y}. \tag{D.46}$$

We now set $\bar{c}_{\mathrm{f}} = \bar{c}_{\mathrm{f}_0} + \varepsilon \bar{c}_{\mathrm{f}_1}$, substitute in (D.43) and (D.44), and combine (D.45) and (D.46) (multiplying the latter by ε) to find

$$\frac{\partial \bar{c}_{\mathrm{f}}}{\partial t} + \frac{\partial}{\partial x}(\bar{c}_{\mathrm{f}}\bar{u}_{\mathrm{f}_0}) + \varepsilon\frac{\partial}{\partial x}\left(\bar{c}_{\mathrm{f}}\bar{u}_{\mathrm{f}_1}\right) = \frac{1}{\mathrm{Pe}}\left(1 + \frac{\varepsilon^2\mathrm{Pe}^2Q_{\mathrm{f,in}}^2}{210}\right)\frac{\partial^2 \bar{c}_{\mathrm{f}}}{\partial x^2} - \frac{\varepsilon Q_{\mathrm{f,in}}}{60}\frac{\partial}{\partial x}\left.\frac{\partial c'_{\mathrm{f}_1}}{\partial y}\right|_{y=H-h_4} \\ + \varepsilon\bar{c}_{\mathrm{f}}v_{\mathrm{f}_1}|_{y=H-h_4} - \frac{1}{\varepsilon \mathrm{Pe} h_4}\left.\frac{\partial c'_{\mathrm{f}_1}}{\partial y}\right|_{y=H-h_4} \\ - \frac{1}{\mathrm{Pe}h_4}\left.\frac{\partial c'_{\mathrm{f}_2}}{\partial y}\right|_{y=H-h_4}. \tag{D.47}$$

This is again accurate up to and including $\mathrm{O}(\varepsilon)$ and corresponds to (D.25).

D.3 Impermeable limit

We are now in a position to consider the limit in which $\phi_{\mathrm{m}},\ \phi_{\mathrm{w}} \to 0$ in equations (D.25) and (D.47), *i.e.* the limit in which the membrane and cell layer are both impermeable. We note

that in this case, as taking $\phi_\mathrm{m},\ \phi_\mathrm{w} \to 0$ changes the physical problem, there are changes to the flux boundary conditions affecting the lumen and upper fluid layer solutions, namely

$$v_\mathrm{l} = 0, \qquad \frac{\partial c_\mathrm{l}}{\partial y} = 0 \qquad \text{on} \quad y = 1, \tag{D.48}$$

$$v_\mathrm{f} = 0, \qquad \frac{\partial c_\mathrm{f}}{\partial y} = 0 \qquad \text{on} \quad y = H - h_4. \tag{D.49}$$

This results in the $\mathrm{O}(\varepsilon)$ (and indeed higher-order) velocities in the lumen and upper fluid layer being identically zero (*i.e.* $\mathbf{u}_{\mathrm{l}_1} \equiv \mathbf{u}_{\mathrm{f}_1} \equiv \mathbf{0}$), and also the y-derivatives of c_l and c_f being zero at all orders on the lumen/membrane and cell layer/upper fluid layer interfaces respectively.

Hence in this limit, and given the forms of $\bar{u}_{\mathrm{l}_0}$ and $\bar{u}_{\mathrm{f}_0}$ from (D.14*a*) and (D.36*a*), respectively, equations (D.25) and (D.47) become

$$\frac{\partial \bar{c}_\mathrm{l}}{\partial t} + Q_{\mathrm{l,in}} \frac{\partial \bar{c}_\mathrm{l}}{\partial x} = \frac{1}{\mathrm{Pe}} \left(1 + \frac{2\varepsilon^2 \mathrm{Pe}^2 Q_{\mathrm{l,in}}^2}{105} \right) \frac{\partial^2 \bar{c}_\mathrm{l}}{\partial x^2}, \tag{D.50}$$

$$\frac{\partial \bar{c}_\mathrm{f}}{\partial t} + \frac{Q_{\mathrm{f,in}}}{h_4} \frac{\partial \bar{c}_\mathrm{f}}{\partial x} = \frac{1}{\mathrm{Pe}} \left(1 + \frac{\varepsilon^2 \mathrm{Pe}^2 Q_{\mathrm{f,in}}^2}{210} \right) \frac{\partial^2 \bar{c}_\mathrm{f}}{\partial x^2}. \tag{D.51}$$

Upon re-dimensionalising both equations (noting that the appropriate scaling for $Q_{\mathrm{l,in}}$ and $Q_{\mathrm{f,in}}$ is LU^*), we arrive at

$$\frac{\partial \bar{c}_\mathrm{l}}{\partial t} + \frac{Q_{\mathrm{l,in}}}{h_1} \frac{\partial \bar{c}_\mathrm{l}}{\partial x} = D \left[1 + \frac{1}{210} \frac{(2h_1)^2}{D^2} \left(\frac{Q_{\mathrm{l,in}}}{h_1} \right)^2 \right] \frac{\partial^2 \bar{c}_\mathrm{l}}{\partial x^2}, \tag{D.52}$$

$$\frac{\partial \bar{c}_\mathrm{f}}{\partial t} + \frac{Q_{\mathrm{f,in}}}{h_4} \frac{\partial \bar{c}_\mathrm{f}}{\partial x} = D \left[1 + \frac{1}{210} \frac{(h_4)^2}{D^2} \left(\frac{Q_{\mathrm{f,in}}}{h_4} \right)^2 \right] \frac{\partial^2 \bar{c}_\mathrm{f}}{\partial x^2}. \tag{D.53}$$

We can also find the dimensional axial velocities in the lumen and upper layer which are, respectively,

$$u_\mathrm{l} = \frac{3Q_{\mathrm{l,in}}}{2h_1} \left(1 - \frac{y^2}{h_1^2} \right), \qquad u_\mathrm{f} = -\frac{6Q_{\mathrm{f,in}}}{h_4^3} \left[y^2 - (2H - h_4)y + H(H - h_4) \right], \tag{D.54}$$

and hence the dimensional mean velocities are

$$\bar{u}_\mathrm{l} = \frac{1}{h_1} \int_0^{h_1} u_\mathrm{l} \, \mathrm{d}y = \frac{Q_{\mathrm{l,in}}}{h_1}, \qquad \bar{u}_\mathrm{f} = \frac{1}{h_4} \int_{H-h_4}^{H} u_\mathrm{f} \, \mathrm{d}y = \frac{Q_{\mathrm{l,in}}}{h_4}. \tag{D.55}$$

Equations (D.52) and (D.53) can now be compared to the classical result for Taylor dispersion in a two-dimensional channel, with average velocities given in (D.55); details of this comparison are presented in §5.3.8.

Bibliography

[1] Personal communication with Dr Marianne Ellis, Centre for Regenerative Medicine, University of Bath.

[2] N. S. Abdullah and D. B. Das. Modelling nutrient transport in hollow fibre membrane bioreactor for growing bone tissue with consideration of multi-component interactions. *Chem. Eng. Sci.*, **62**(21):5821–5839, 2007.

[3] N. S. Abdullah, D. R. Jones, and D. B. Das. Nutrient transport in bioreactors for bone tissue growth: Why do hollow fibre membrane bioreactors work? *Chem. Eng. Sci.*, **64**(1):109–125, 2009.

[4] S. Akimoto, M. Mitsumata, T. Sasaguri, and Y. Yoshida. Laminar shear stress inhibits vascular endothelial cell proliferation by inducing cyclin-dependent kinase inhibitor $p21^{Sdi1/Cip1/Waf1}$. *Circ. Res.*, **86**(2):185–190, 2000.

[5] J. W. Allen, T. Hassanein, and S. N. Bhatia. Advances in bioartificial liver devices. *Hepatology*, **34**(3):447–455, 2001.

[6] J. W. Allen, S. R. Khetani, and S. N. Bhatia. In vitro zonation and toxicity in a hepatocyte bioreactor. *Toxicol. Sci.*, **84**(1):110–119, 2005.

[7] W. Alt. Biased random walk models for chemotaxis and related diffusion approximations. *J. Math. Biol.*, **9**(2):147–177, 1980.

[8] W. Alt and M. Dembo. Cytoplasm dynamics and cell motion: Two-phase flow models. *Math. Biosci.*, **156**(1-2):207–228, 1999.

[9] A. R. A. Anderson and M. A. J. Chaplain. Continuous and discrete mathematical models of tumor-induced angiogenesis. *Bull. Math. Biol.*, **60**(5):857–899, 1998.

[10] A. G. Ardakani, U. Cheema, R. A. Brown, and R. J. Shipley. Quantifying the correlation between spatially defined oxygen gradients and cell fate in an engineered three-dimensional culture model. *J. R. Soc. Interface*, **11**(98), 2014.

[11] R. Aris. On the dispersion of a solute in a fluid flowing through a tube. *Proc. R. Soc. A*, **235**(1200):67–77, 1956.

[12] R. Aris. On the dispersion of a solute by diffusion, convection and exchange between phases. *Proc. R. Soc. A*, **252**(1271):538–550, 1959.

[13] E. J. Arnsdorf, P. Tummala, R. Y. Kwon, and C. R. Jacobs. Mechanically induced osteogenic differentiation – the role of RhoA, ROCKII and cytoskeletal dynamics. *J. Cell Sci.*, **122**(4):546–553, 2009.

[14] R. E. Baker, C. A. Yates, and R. Erban. From microscopic to macroscopic descriptions of cell migration on growing domains. *Bull. Math. Biol.*, **72**(3):719–762, 2010.

[15] G. N. Bancroft, V. I. Sikavitsas, J. van den Dolder, T. L. Sheffield, C. G. Ambrose, J. A. Jansen, and A. G. Mikos. Fluid flow increases mineralized matrix deposition in 3D perfusion culture of marrow stromal osteoblasts in a dose-dependent manner. *Proc. Natl. Acad. Sci. USA*, **99**(20):12600–12605, 2002.

[16] G. S. Beavers and D. D. Joseph. Boundary conditions at a naturally permeable wall. *J. Fluid Mech.*, **30**(1):197–207, 1967.

[17] M. J. Berridge. Cell Signalling Biology. http://www.biochemj.org/csb/.

[18] G. Breier, U. Albrecht, S. Sterrer, and W. Risau. Expression of vascular endothelial growth factor during embryonic angiogenesis and endothelial cell differentiation. *Development*, **114**(2):521–532, 1992.

[19] M. Brittberg, T. Tallheden, E. Sjögren-Jansson, A. Lindahl, and L. Peterson. Autologous chondrocytes used for articular cartilage repair. *Clin. Orthop. Relat. Res.*, **391S**:S337–S348, 2001.

[20] J. D. Brotherton and P. C. Chau. Modeling of axial-flow hollow fiber cell culture bioreactors. *Biotechnol. Prog.*, **12**(5):575–590, 1996.

[21] J. E. M. Brouwers, C. C. van Donkelaar, B. G. Sengers, and R. Huiskes. Can the growth factors PTHrP, Ihh and VEGF, together regulate the development of a long bone? *J. Biomech.*, **39**(15):2774–2782, 2006.

[22] J. A. Burdick and G. Vunjak-Novakovic. Engineered microenvironments for controlled stem cell differentiation. *Tissue Eng. Part A*, **15**(2):205–219, February 2009.

[23] D. P. Byrne, D. Lacroix, J. A. Planell, D. J. Kelly, and P. J. Prendergast. Simulation of tissue differentiation in a scaffold as a function of porosity, Young's modulus and dissolution rate: Application of mechanobiological models in tissue engineering. *Biomaterials*, **28**(36):5544–5554, 2007.

[24] H. M. Byrne, J. R. King, D. L. S. McElwain, and L. Preziosi. A two-phase model of solid tumour growth. *Appl. Math. Lett.*, **16**(4):567–573, 2003.

[25] H. M. Byrne and M. R. Owen. A new interpretation of the Keller-Segel model based on multiphase modelling. *J. Math. Biol.*, **49**:604–626, 2004.

[26] H. M. Byrne, M. R. Owen, T. Alarcon, J. Murphy, and P. K. Maini. Modelling the response of vascular tumours to chemotherapy: A multiscale approach. *Math. Models Methods Appl. Sci.*, **16**(7S):1219–1241, 2006.

[27] R. Cancedda, B. Dozin, P. Giannoni, and R. Quarto. Tissue engineering and cell therapy of cartilage and bone. *Matrix Biol.*, **22**(1):81–91, 2003.

[28] M. A. J. Chaplain and A. M. Stuart. A model mechanism for the chemotactic response of endothelial cells to tumour angiogenesis factor. *Math. Med. Biol.*, **10**(3):149–168, 1993.

[29] L. A. C. Chapman, R. J. Shipley, J. P. Whiteley, M. J. Ellis, H. M. Byrne, and S. L. Waters. Optimising cell aggregate expansion in a perfused hollow fibre bioreactor via mathematical modelling. *PLOS ONE*, 2014. doi:10.1371/journal.pone.0105813.

[30] R. R. Chen and D. J. Mooney. Polymeric growth factor delivery strategies for tissue engineering. *Pharm. Res.*, **20**:1103–1112, 2003.

[31] I. E. Chesnick, F. A. Avallone, R. D. Leapman, W. J. Landis, N. Eidelman, and K. Potter. Evaluation of bioreactor-cultivated bone by magnetic resonance microscopy and FTIR microspectroscopy. *Bone*, **40**(4):904–912, 2007.

[32] N. G. Cogan and R. D. Guy. Multiphase flow models of biogels from crawling cells to bacterial biofilms. *HFSP J.*, **4**(1):11–25, 2010.

[33] N. G. Cogan and J. P. Keener. The role of the biofilm matrix in structural development. *Math. Med. Biol.*, **21**(2):147–166, 2004.

[34] R. Cortesini. Stem cells, tissue engineering and organogenesis in transplantation. *Transpl. Immunol.*, **15**(2):81–89, 2005.

[35] V. Cristini, X. Li, J. S. Lowengrub, and S. M. Wise. Nonlinear simulations of solid tumor growth using a mixture model: Invasion and branching. *J. Math. Biol.*, **58**(4-5):723–763, 2009.

[36] Z. F. Cui, X. Xu, N. Trainor, J. T. Triffitt, J. P. G. Urban, and U. K. Tirlapur. Application of multiple parallel perfused microbioreactors and three-dimensional stem cell culture for toxicity testing. *Toxicol. in Vitro*, **21**(7):1318–1324, 2007. Fourteenth International Workshop on In Vitro Toxicology.

[37] L. J. Cummings and S. L. Waters. Tissue growth in a rotating bioreactor. Part II: Fluid flow and nutrient transport problems. *Math. Med. Biol.*, **24**(2):169–208, 2007.

[38] A. Curtis and M. Riehle. Tissue engineering: The biophysical background. *Phys. Med. Biol.*, **46**(4):R47–R65, 2001.

[39] J. C. Dallon and H. G. Othmer. A discrete cell model with adaptive signalling for aggregation of dictyostelium discoideum. *Phil. Trans. R. Soc. B*, **352**(1351):391–417, 1997.

[40] D. B. Das. Multiscale simulation of nutrient transport in hollow fibre membrane bioreactor for growing bone tissue: Sub-cellular scale and beyond. *Chem. Eng. Sci.*, **62**(13):3627–3639, 2007.

[41] A. J. Davidson, M. J. Ellis, and J. B. Chaudhuri. A theoretical method to improve and optimize the design of bioartificial livers. *Biotechnol. Bioeng.*, **106**(6):980–988, 2010.

[42] Y. Davit, C. G. Bell, H. M. Byrne, L. A. C. Chapman, L. S. Kimpton, G. E. Lang, K. H. L. Leonard, J. M. Oliver, N. C. Pearson, R. J. Shipley, S. L. Waters, J. P. Whiteley, B. D. Wood, and M. Quintard. Homogenization via formal multiscale asymptotics and volume averaging: How do the two techniques compare? *Adv. Water Resour.*, **62, Part B**:178–206, 2013. A tribute to Stephen Whitaker.

[43] J. I. Dawson and R. O. C. Oreffo. Bridging the regeneration gap: Stem cells, biomaterials and clinical translation in bone tissue engineering. *Arch. Biochem. Biophys.*, **473**(2):124–131, 2008.

[44] D. A. Drew. Mathematical modeling of two-phase flow. *Annu. Rev. Fluid Mech.*, **15**(1):261–291, 1983.

[45] N. J. B. Driessen, R. A. Boerboom, J. M. Huyghe, C. V. C. Bouten, and F. P. T. Baaijens. Computational analyses of mechanically induced collagen fiber remodeling in the aortic heart valve. *J. Biomech. Eng.*, **125**:549–557, 2003.

[46] A. J. El Haj and S. H. Cartmell. Bioreactors for bone tissue engineering. *Proc. Inst. Mech. Eng. H J. Eng. Med.*, **224**(12):1523–1532, 2010.

[47] A. J. El Haj, S. L. Minter, S. C. F. Rawlinson, R. Suswillo, and L. E. Lanyon. Cellular responses to mechanical loading in vitro. *J. Bone Miner. Res.*, **5**(9):923–932, 1990.

[48] M. J. Ellis and J. B. Chaudhuri. Poly(lactic-co-glycolic acid) hollow fibre membranes for use as a tissue engineering scaffold. *Biotechnol. Bioeng.*, **96**(1):177–187, 2007.

[49] B. Fornberg. Calculation of weights in finite difference formulas. *SIAM Rev.*, **40**(3):685–691, 1998.

[50] S. J. Franks and J. R. King. Interactions between a uniformly proliferating tumour and its surroundings: Uniform material properties. *Math. Med. Biol.*, **20**(1):47–89, 2003.

[51] J. J. Fredberg. Augmented diffusion in the airways can support pulmonary gas exchange. *J. Appl. Physiol.*, **49**(2):232–238, 1980.

[52] Y. Fukuchi, H. Nakajima, D. Sugiyama, I. Hirose, T. Kitamura, and K. Tsuji. Human placenta-derived cells have mesenchymal stem/progenitor cell potential. *Stem Cells*, **22**(5):649–658, 2004.

[53] K. Fukumitsu, H. Yagi, and A. Soto-Gutierrez. Bioengineering in organ transplantation: Targeting the liver. *Transplant. Proc.*, **43**(6):2137–2138, 2011.

[54] C. V. Gemmiti and R. E. Guldberg. Fluid flow increases type II collagen deposition and tensile mechanical properties in bioreactor-grown tissue-engineered cartilage. *Tissue Eng.*, **12**(3):469–479, March 2006.

[55] L. Geris, A. Gerisch, and R. Schugart. Mathematical modeling in wound healing, bone regeneration and tissue engineering. *Acta Biotheor.*, **58**:355–367, 2010.

[56] W. V. Giannobile. Periodontal tissue engineering by growth factors. *Bone*, **19**(1, Supplement 1):S23–S37, 1996.

[57] M. J. Gramer and D. M. Poeschl. Comparison of cell growth in T-flasks, in micro hollow fiber bioreactors, and in an industrial scale hollow fiber bioreactor system. *Cytotechnology*, **34**(1-2):111–119, 2000.

[58] W. G. Gray. A derivation of the equations for multi-phase transport. *Chem. Eng. Sci.*, **30**(2):229–233, 1975.

[59] J. E. F. Green, S. L. Waters, K. M. Shakesheff, and H. M. Byrne. A mathematical model of liver cell aggregation *in vitro*. *Bull. Math. Biol.*, **71**:906–930, 2009.

[60] L. G. Griffith and G. Naughton. Tissue engineering – current challenges and expanding opportunities. *Science*, **295**(5557):1009–1014, 2002.

[61] L. G. Griffith and M. A. Swartz. Capturing complex 3D tissue physiology in vitro. *Nat. Rev. Mol. Cell Biol.*, **7**(3):211–224, Mar. 2006.

[62] I. M. Griffiths, P. D. Howell, and R. J. Shipley. Control and optimization of solute transport in a thin porous tube. *Phys. Fluids (1994-present)*, **25**(3):033101–1–18, 2013.

[63] S. Gronthos, J. Brahim, W. Li, L. W. Fisher, N. Cherman, A. Boyde, P. DenBesten, P. G. Robey, and S. Shi. Stem cell properties of human dental pulp stem cells. *J. Dent. Res.*, **81**(8):531–535, 2002.

[64] P. D. Hay, A. R. Veitch, and J. D. S. Gaylor. Oxygen transfer in a convection-enhanced hollow fiber bioartificial liver. *Artif. Organs*, **25**(2):119–130, 2001.

[65] A. L. Hazel and T. J. Pedley. Vascular endothelial cells minimize the total force on their nuclei. *Biophys. J.*, **78**(1):47–54, 2000.

[66] T. Hillen and K. J. Painter. A user's guide to PDE models for chemotaxis. *J. Math. Biol.*, **58**(1-2):183–217, 2009.

[67] E. J. Hinch. *Perturbation Methods*. Cambridge University Press, 1995.

[68] http://www.lifetechnologies.com/order/catalog/product/PHC7141?ICID=search product.

[69] H. Huang, R. D. Kamm, and R. T. Lee. Cell mechanics and mechanotransduction: Pathways, probes, and physiology. *Am. J. Physiol. Cell Physiol.*, **287**(1):C1–11, July 2004.

[70] B. Imberti, D. Seliktar, R. M. Nerem, and A. Remuzzi. The response of endothelial cells to fluid shear stress using a co-culture model of the arterial wall. *Endothelium J. Endoth.*, **9**(1):11–23, 2002.

[71] N. L. Jeon, H. Baskaran, S. K. W. Dertinger, G. M. Whitesides, L. Van De Water, and M. Tomer. Neutrophil chemotaxis in linear and complex gradients of interleukin-8 formed in a microfabricated device. *Nat. Biotechnol.*, **20**:826–830, 2002.

[72] D. D. Joseph and L. N. Tao. The effect of permeability on the slow motion of a porous sphere in a viscous liquid. *Z. Angew. Math. Mech.*, **44**(8-9):361–364, 1964.

[73] P. Jungebluth, E. Alici, S. Baiguera, *et al.* Tracheobronchial transplantation with a stem-cell-seeded bioartificial nanocomposite: A proof-of-concept study. *Lancet*, **378**(9808):1997–2004, 2011.

[74] S. Kapur, D. J. Baylink, and K.-H. W. Lau. Fluid flow shear stress stimulates human osteoblast proliferation and differentiation through multiple interacting and competing signal transduction pathways. *Bone*, **32**(3):241–251, 2003.

[75] H. Kawakita, K. Sugita, K. Saito, M. Tamada, T. Sugo, and H. Kawamoto. Production of cycloisomaltooligosaccharides from dextran using enzyme immobilized in multilayers onto porous membranes. *Biotechnol. Prog.*, **18**(3):465–469, 2002.

[76] E. F. Keller and L. A. Segel. Model for chemotaxis. *J. Theor. Biol.*, **30**(2):225–234, 1971.

[77] E. F. Keller and L. A. Segel. Traveling bands of chemotactic bacteria: A theoretical analysis. *J. Theor. Biol.*, **30**(2):235–248, 1971.

[78] I. Kerkis, A. Kerkis, D. Dozortsev, G. C. Stukart-Parsons, S. M. G. Massironi, L. V. Pereira, A. I. Caplan, and H. F. Cerruti. Isolation and characterization of a population of immature dental pulp stem cells expressing OCT-4 and other embryonic stem cell markers. *Cells Tissues Organs*, **184**:105–116, 2006.

[79] A. Khademhosseini, R. Langer, J. Borenstein, and J. P. Vacanti. Microscale technologies for tissue engineering and biology. *Proc. Natl. Acad. Sci. USA*, **103**(8):2480–2487, 2006.

[80] L. S. Kimpton, J. P. Whiteley, S. L. Waters, J. R. King, and J. M. Oliver. Multiple travelling-wave solutions in a minimal model for cell motility. *Math. Med. Biol.*, **30**(3):241–272, 2012.

[81] L. S. Kimpton, J. P. Whiteley, S. L. Waters, and J. M. Oliver. The effect of membrane-regulated actin polymerization on a two-phase flow model for cell motility. *IMA J. Appl. Math.*, **79**(4):603–635, 2014.

[82] L. S. Kimpton, J. P. Whiteley, S. L. Waters, and J. M. Oliver. On a poroviscoelastic model for cell crawling. *J. Math. Biol.*, pages 1–39, 2014.

[83] J. A. King and W. M. Miller. Bioreactor development for stem cell expansion and controlled differentiation. *Curr. Opin. Chem. Biol.*, **11**(4):394–398, 2007.

[84] J. R. King and J. M. Oliver. Thin-film modelling of poroviscous free surface flows. *Eur. J. Appl. Math.*, **16**(4):519–553, 2005.

[85] R. A. Knazek, P. M. Gullino, P. O. Kohler, and R. L. Dedrick. Cell culture on artificial capillaries: An approach to tissue growth in vitro. *Science*, **178**(4056):65–67, 1972.

[86] R. A. Knazek, P. O. Kohler, and P. M. Gullino. Hormone production by cells grown in vitro on artificial capillaries. *Exp. Cell Res.*, **84**(1-2):251–254, 1974.

[87] J. P. Kumar, J. C. Umavathi, A. J. Chamkha, and A. Basawaraj. Solute dispersion between two parallel plates containing porous and fluid layers. *J. Porous Media*, **15**(11):1031–1047, 2012.

[88] D. Lacroix and P. J. Prendergast. Three-dimensional simulation of fracture repair in the human tibia. *Comput. Methods Biomech. Biomed. Engin.*, **5**(5):369–376, 2002.

[89] D. C. Latimer, B. J. Roth, and K. K. Parker. Analytical model for predicting mechanotransduction effects in engineered cardiac tissue. *Tissue Eng.*, **9**:283–289, 2003.

[90] O. K. Lee, T. K. Kuo, W.-M. Chen, K.-D. Lee, S.-L. Hsieh, and T.-H. Chen. Isolation of multipotent mesenchymal stem cells from umbilical cord blood. *Blood*, **103**(5):1669–1675, 2003.

[91] G. Lemon and J. R. King. Multiphase modelling of cell behaviour on artificial scaffolds: Effects of nutrient depletion and spatially nonuniform porosity. *Math. Med. Biol.*, **24**(1):57–83, 2007.

[92] G. Lemon, J. R. King, H. M. Byrne, O. E. Jensen, and K. M. Shakesheff. Mathematical modelling of engineered tissue growth using a multiphase porous flow mixture theory. *J. Math. Biol.*, **52**:571–594, 2006.

[93] W.-J. Li, R. Tuli, C. Okafor, A. Derfoul, K. G. Danielson, D. J. Hall, and R. S. Tuan. A three-dimensional nanofibrous scaffold for cartilage tissue engineering using human mesenchymal stem cells. *Biomaterials*, **26**(6):599–609, 2005.

[94] C.-M. Lin, T. X. Jiang, R. E. Baker, P. K. Maini, R. B. Widelitz, and C.-M. Chuong. Spots and stripes: Pleomorphic patterning of stem cells via p-ERK-dependent cell chemotaxis shown by feather morphogenesis and mathematical simulation. *Dev. Biol.*, **334**(2):369–382, 2009.

[95] Y. Liu, T. Liu, X. Fan, X. Ma, and Z. Cui. Ex vivo expansion of hematopoietic stem cells derived from umbilical cord blood in rotating wall vessel. *J. Biotechnol.*, **124**(3):592–601, 2006.

[96] L. L. Lu, Y. J. Liu, S. G. Yang, Q. J. Zhao, X. Wang, W. Gong, Z. B. Han, Z. S. Xu, Y. X. Lu, D. Liu, Z. Z. Chen, and Z. C. Han. Isolation and characterization of human umbilical cord mesenchymal stem cells with hematopoiesis-supportive function and other potentials. *Haematologica*, **91**(8):1017–1026, 2006.

[97] M. J. Lysaght and J. Reyes. The growth of tissue engineering. *Tissue Eng.*, **7**(5):485–493, 2001.

[98] Z. Ma, C. Gao, Y. Gong, and J. Shen. Cartilage tissue engineering PLLA scaffold with surface immobilized collagen and basic fibroblast growth factor. *Biomaterials*, **26**(11):1253–1259, 2005.

[99] F. Mac Gabhann, M. T. Yang, and A. S. Popel. Monte Carlo simulations of VEGF binding to cell surface receptors in vitro. *Biochim. Biophys. Acta Mol. Cell Res.*, **1746**(2):95–107, 2005.

[100] B. D. MacArthur, C. P. Please, M. Taylor, and R. O. C. Oreffo. Mathematical modelling of skeletal repair. *Biochem. Biophys. Res. Commun.*, **313**(4):825–833, 2004.

[101] P. Malaviya and R. M. Nerem. Fluid-induced shear stress stimulates chondrocyte proliferation partially mediated via TGF-β1. *Tissue Eng.*, **8**(4):581–590, 2002.

[102] C. F. Mandenius, T. B. Andersson, P. M. Alves, *et al.* Toward preclinical predictive drug testing for metabolism and hepatotoxicity by using in vitro models derived from human embryonic stem cells and human cell lines – a report on the Vitrocellomics EU-project. *Altern. Lab. Anim.*, **39**(2):147–171, May 2011.

[103] J. J. Marler, J. Upton, R. Langer, and J. P. Vacanti. Transplantation of cells in matrices for tissue regeneration. *Adv. Drug Deliv. Rev.*, **33**(1-2):165–182, 1998.

[104] I. Martin, D. Wendt, and M. Heberer. The role of bioreactors in tissue engineering. *Trends Biotechnol.*, **22**(2):80–86, 2004.

[105] Y. Martin and P. Vermette. Bioreactors for tissue mass culture: Design, characterization, and recent advances. *Biomaterials*, **26**(35):7481–7503, 2005.

[106] H. Mayer, H. Bertram, W. Lindenmaier, T. Korff, H. Weber, and H. Weich. Vascular endothelial growth factor (VEGF-A) expression in human mesenchymal stem cells: Autocrine and paracrine role on osteoblastic and endothelial differentiation. *J. Cell. Biochem.*, **95**(4):827–839, 2005.

[107] U. Mayr-Wohlfart, J. Waltenberger, H. Hausser, S. Kessler, K.-P. Günther, C. Dehio, W. Puhl, and R. E. Brenner. Vascular endothelial growth factor stimulates chemotactic migration of primary human osteoblasts. *Bone*, **30**(3):472–477, 2002.

[108] B. S. Mazumder and K. K. Mondal. On solute transport in oscillatory flow through an annular pipe with a reactive wall and its application to a catheterized artery. *Q. J. Mech. Appl. Math.*, **58**(3):349–365, 2005.

[109] G. Meneghello, D. J. Parker, B. J. Ainsworth, S. P. Perera, J. B. Chaudhuri, M. J. Ellis, and P. A. De Bank. Fabrication and characterization of poly(lactic-co-glycolic acid)/polyvinyl alcohol blended hollow fibre membranes for tissue engineering applications. *J. Membr. Sci.*, **344**(1-2):55–61, 2009.

[110] V. Midy and J. Plouet. Vasculotropin/vascular endothelial growth factor induces differentiation in cultured osteoblasts. *Biochem. Biophys. Res. Commun.*, **199**(1):380–386, 1994.

[111] D. Mohebbi-Kalhori, A. Behzadmehr, C. J. Doillon, and A. Hadjizadeh. Computational modeling of adherent cell growth in a hollow-fiber membrane bioreactor for large-scale 3-D bone tissue engineering. *J. Artif. Organs*, **15**:250–265, 2012.

[112] K. K. Mondal and B. S. Mazumder. On solute dispersion in pulsatile flow through a channel with absorbing walls. *Int. J. Nonlinear Mech.*, **40**(1):69–81, 2005.

[113] K. K. Mondal and B. S. Mazumder. On the solute dispersion in a pipe of annular cross-section with absorption boundary. *Z. Angew. Math. Mech.*, **85**(6):422–430, 2005.

[114] K. W. Morton and D. F. Mayers. *Numerical Solutions of Partial Differential Equations*. Cambridge University Press, 2003.

[115] W. L. Murphy, M. C. Peters, D. H. Kohn, and D. J. Mooney. Sustained release of vascular endothelial growth factor from mineralized poly(lactide-co-glycolide) scaffolds for tissue engineering. *Biomaterials*, **21**(24):2521–2527, 2000.

[116] G. A. Murrell, M. J. Francis, and L. Bromley. Modulation of fibroblast proliferation by oxygen free radicals. *Biochem. J.*, **265**(3):659–665, 1990.

[117] S. Naka, K. Takeshita, T. Yamamoto, T. Tani, and M. Kodama. Bioartificial liver support system using porcine hepatocytes entrapped in a three-dimensional hollow fiber module with collagen gel: An evaluation in the swine acute liver failure model. *Artif. Organs*, **23**(9):822–828, 1999.

[118] S. Obi, K. Yamamoto, N. Shimizu, S. Kumagaya, T. Masumura, T. Sokabe, T. Asahara, and J. Ando. Fluid shear stress induces arterial differentiation of endothelial progenitor cells. *J. Appl. Physiol.*, **106**(1):203–211, 2009.

[119] R. D. O'Dea, H. M. Byrne, and S. L. Waters. *Continuum Modelling of In Vitro Tissue Engineering: A Review*. Springer, 2013.

[120] R. D. O'Dea, J. M. Osborne, A. J. El Haj, H. M. Byrne, and S. L. Waters. The interplay between tissue growth and scaffold degradation in engineered tissue constructs. *J. Math. Biol.*, **67**:1199–1225, 2013.

[121] R. D. O'Dea and S. L. Waters. Flow and solute uptake in a twisting tube. *J. Fluid Mech.*, **562**:173–182, 2006.

[122] R. D. O'Dea, S. L. Waters, and H. M. Byrne. A two-fluid model for tissue growth within a dynamic flow environment. *Eur. J. Appl. Math.*, **19**(6):607–634, 2008.

[123] R. D. O'Dea, S. L. Waters, and H. M. Byrne. A multiphase model for tissue construct growth in a perfusion bioreactor. *Math. Med. Biol.*, **27**(2):95–127, 2010.

[124] J. M. Oliver, J. R. King, K. J. McKinlay, P. D. Brown, D. M. Grant, C. A. Scotchford, and J. V. Wood. Thin-film theories for two-phase reactive flow models of active cell motion. *Math. Med. Biol.*, **22**(1):53–98, 2005.

[125] J. M. Osborne, R. D. O'Dea, J. P. Whiteley, H. M. Byrne, and S. L. Waters. The influence of bioreactor geometry and the mechanical environment on engineered tissues. *J. Biomech. Eng.*, **132**(5):051006–1–12, May 2010.

[126] D. Pal, R. Veerabhadraiah, P. N. Shivakumar, and N. Rudraiah. Longitudinal dispersion of tracer particles in a channel bounded by porous media using slip condition. *Int. J. Math. Math. Sci.*, **7**(4):755–764, 1984.

[127] M. Papadaki, L. V. McIntire, and S. G. Eskin. Effects of shear stress on the growth kinetics of human aortic smooth muscle cells in vitro. *Biotechnol. Bioeng.*, **50**(5):555–561, 1996.

[128] J. F. Patzer. Oxygen consumption in a hollow fiber bioartificial liver – revisited. *Artif. Organs*, **28**(1):83–98, 2004.

[129] N. C. Pearson, R. J. Shipley, S. L. Waters, and J. M. Oliver. Multiphase modelling of the influence of fluid flow and chemical concentration on tissue growth in a hollow fibre membrane bioreactor. *Math. Med. Biol.*, 2013. doi:10.1093/imammb/dqt015.

[130] N. C. Pearson, R. J. Shipley, S. L. Waters, and J. M. Oliver. Dispersion-enhanced solute transport in a cell-seeded hollow fibre membrane bioreactor. *Submitted to J. Eng. Math.*, 2014.

[131] N. C. Pearson, S. L. Waters, J. M. Oliver, and R. J. Shipley. Multiphase modelling of the effect of fluid shear stress on cell yield and distribution in a hollow fibre membrane bioreactor. *Biomech. Model. Mechan.*, pages 1–16, 2014. doi:10.1007/s10237-014-0611-7.

[132] K. G. Peters, C. De Vries, and L. T. Williams. Vascular endothelial growth factor receptor expression during embryogenesis and tissue repair suggests a role in endothelial differentiation and blood vessel growth. *Proc. Natl. Acad. Sci. USA*, **90**(19):8915–8919, 1993.

[133] G. J. Pettet, H. M. Byrne, D. L. S. McElwain, and J. Norbury. A model of wound-healing angiogenesis in soft tissue. *Math. Biosci.*, **136**(1):35–63, 1996.

[134] J. M. Piret and C. L. Cooney. Mammalian cell and protein distributions in ultrafiltration hollow fiber bioreactors. *Biotechnol. Bioeng.*, **36**(9):902–910, 1990.

[135] C. Planchamp, T. L. Vu, J. M. Mayer, M. Reist, and B. Testa. Hepatocyte hollow-fibre bioreactors: Design, set-up, validation and applications. *J. Pharm. Pharmacol.*, **55**(9):1181–1198, 2003.

[136] M. J. Plank, B. D. Sleeman, and P. F. Jones. A mathematical model of tumour angiogenesis, regulated by vascular endothelial growth factor and the angiopoietins. *J. Theor. Biol.*, **229**(4):435–454, 2004.

[137] R. Pörtner, S. Nagel-Heyer, C. Goepfert, P. Adamietz, and N. M. Meenen. Bioreactor design for tissue engineering. *J. Biosci. Bioeng.*, **100**(3):235–245, 2005.

[138] A. E. Postlethwaite, J. Keski-Oja, H. L. Moses, and A. H. Kang. Stimulation of the chemotactic migration of human fibroblasts by transforming growth factor β. *J. Exp. Med.*, **165**(1):251–256, 1987.

[139] I. Pountos, D. Corscadden, P. Emery, and P. V. Giannoudis. Mesenchymal stem cell tissue engineering: Techniques for isolation, expansion and application. *Injury*, **38S4**:S23–S33, 2007.

[140] M. P. Prabhakaran, J. R. Venugopal, and S. Ramakrishna. Mesenchymal stem cell differentiation to neuronal cells on electrospun nanofibrous substrates for nerve tissue engineering. *Biomaterials*, **30**(28):4996–5003, 2009.

[141] P. J. Prendergast, R. Huiskes, and K. Søballe. Biophysical stimuli on cells during tissue differentiation at implant interfaces. *J. Biomech.*, **30**(6):539–548, 1997.

[142] M. Quintard and S. Whitaker. Transport in ordered and disordered porous media II: Generalized volume averaging. *Transp. Porous Media*, **14**:179–206, 1994.

[143] S. Riordan and R. Williams. Bioartificial liver support: Developments in hepatocyte culture and bioreactor design. *Brit. Med. Bull.*, **53**(4):730–744, 1997.

[144] M. V. Risbud and M. Sittinger. Tissue engineering: Advances in *in vitro* cartilage generation. *Trends Biotechnol.*, **20**(8):351–356, 2002.

[145] P. R. Rony. Hollow fiber enzyme reactors. *J. Am. Chem. Soc.*, **94**(23):8247–8248, 1972.

[146] A. J. Salgado, O. P. Coutinho, and R. L. Reis. Bone tissue engineering: State of the art and future trends. *Macromol. Biosci.*, **4**(8):743–765, 2004.

[147] J. Salles, J.-F. Thovert, R. Delannay, L. Prevors, J.-L. Auriault, and P. M. Adler. Taylor dispersion in porous media. Determination of the dispersion tensor. *Phys. Fluids A*, **5**(10):2348–2376, 1993.

[148] J. A. Sanz-Herrera, J. M. García-Aznar, and M. Doblaré. A mathematical approach to bone tissue engineering. *Phil. Trans. R. Soc. A*, **367**(1895):2055–2078, 2009.

[149] J. A. Sanz-Herrera, J. M. García-Aznar, and M. Doblaré. On scaffold designing for bone regeneration: A computational multiscale approach. *Acta Biomater.*, **5**(1):219–229, 2009.

[150] B. G. Sengers, M. Taylor, C. P. Please, and R. O. C. Oreffo. Computational modelling of cell spreading and tissue regeneration in porous scaffolds. *Biomaterials*, **28**(10):1926–1940, 2007.

[151] L. Shampine and M. Reichelt. The MATLAB ODE suite. *SIAM J. Sci. Comput.*, **18**(1):1–22, 1997.

[152] L. Shampine, M. Reichelt, and J. Kierzenka. Solving index-1 DAEs in MATLAB and Simulink. *SIAM Rev.*, **41**(3):538–552, 1999.

[153] R. J. Shipley, A. J. Davidson, K. Chan, J. B. Chaudhuri, S. L. Waters, and M. J. Ellis. A strategy to determine operating parameters in tissue engineering hollow fiber bioreactors. *Biotechnol. Bioeng.*, **108**(6):1450–1461, 2011.

[154] R. J. Shipley, G. W. Jones, R. J. Dyson, B. G. Sengers, C. L. Bailey, C. J. Catt, C. P. Please, and J. Malda. Design criteria for a printed tissue engineering construct: A mathematical homogenization approach. *J. Theor. Biol.*, **259**(3):489–502, 2009.

[155] R. J. Shipley and S. L. Waters. Fluid and mass transport modelling to drive the design of cell-packed hollow fibre bioreactors for tissue engineering applications. *Math. Med. Biol.*, **29**:329–359, 2012.

[156] R. J. Shipley, S. L. Waters, and M. J. Ellis. Definition and validation of operating equations for poly(vinyl alcohol)-poly(lactide-co-glycolide) microfiltration membrane-scaffold bioreactors. *Biotechnol. Bioeng.*, **107**(2):382–392, 2010.

[157] M. M. Stevens. Biomaterials for bone tissue engineering. *Mater. Today*, **11**(5):18–25, 2008.

[158] U. A. Stock and J. P. Vacanti. Tissue engineering: Current state and prospects. *Annu. Rev. Med.*, **52**(1):443–451, 2001.

[159] C. L. Stokes and D. A. Lauffenburger. Analysis of the roles of microvessel endothelial cell random motility and chemotaxis in angiogenesis. *J. Theor. Biol.*, **152**(3):377–403, 1991.

[160] H.-J. Sung, C. Meredith, C. Johnson, and Z. S. Galis. The effect of scaffold degradation rate on three-dimensional cell growth and angiogenesis. *Biomaterials*, **25**(26):5735–5742, 2004.

[161] Y. Tabata. The importance of drug delivery systems in tissue engineering. *Pharm. Sci. Technol. Today*, **3**(3):80–89, 2000.

[162] G. Taylor. Dispersion of soluble matter in solvent flowing slowly through a tube. *Proc. R. Soc. A*, **219**(1137):186–203, 1953.

[163] G. Taylor. Conditions under which dispersion of a solute in a stream of solvent can be used to measure molecular diffusion. *Proc. R. Soc. A*, **225**(1163):473–477, 1954.

[164] G. Taylor. The dispersion of matter in turbulent flow through a pipe. *Proc. R. Soc. A*, **223**(1155):446–468, 1954.

[165] J. P. Tharakan and P. C. Chau. A radial flow hollow fiber bioreactor for the large-scale culture of mammalian cells. *Biotechnol. Bioeng.*, **28**(3):329–342, 1986.

[166] D. D. Theodorakopoulos. Dynamic pressures on a pair of rigid walls retaining poroelastic soil. *Soil Dyn. Earthq. Eng.*, **23**(1):41–51, 2003.

[167] R. M. Tostões, S. B. Leite, M. Serra, J. Jensen, P. Björquist, M. J. T. Carrondo, C. Brito, and P. M. Alves. Human liver cell spheroids in extended perfusion bioreactor culture for repeated-dose drug testing. *Hepatology*, **55**(4):1227–1236, 2012.

[168] R. S. Tuan, G. Boland, and R. Tuli. Adult mesenchymal stem cells and cell-based tissue engineering. *Arthritis Res. Ther.*, **5**(1):1–14, 2002.

[169] C. Van den Broeck and E. Dekempeneer. The effect of boundary absorption on longitudinal dispersion in steady laminar flows. *Z. Angew. Math. Phys.*, **34**(4):489–501, 1983.

[170] A. Vikhansky. Taylor dispersion in shallow micro-channels: Aspect ratio effect. *Microfluid. Nanofluidics*, **7**(1):91–95, 2009.

[171] A. Vikhansky and W. Wang. Taylor dispersion in finite-length capillaries. *Chem. Eng. Sci.*, **66**(4):642–649, 2011.

[172] X.-M. Wang and T. D. Waite. Gel layer formation and hollow fiber membrane filterability of polysaccharide dispersions. *J. Membr. Sci.*, **322**(1):204–213, 2008.

[173] J. N. Warnock and M. Al-Rubeai. Bioreactor systems for the production of biopharmaceuticals from animal cells. *Biotechnol. Appl. Biochem.*, **45**(1):1–12, 2006.

[174] S. L. Waters. Solute uptake through the walls of a pulsating channel. *J. Fluid Mech.*, **433**:193–208, 2001.

[175] S. D. Webb, M. R. Owen, H. M. Byrne, C. Murdoch, and C. E. Lewis. Macrophage-based anti-cancer therapy: Modelling different modes of tumour targeting. *Bull. Math. Biol.*, **69**(5):1747–1776, 2007.

[176] S. Whitaker. Diffusion and dispersion in porous media. *AIChE J.*, **13**(3):420–427, 1967.

[177] S. Whitaker. The transport equations for multi-phase systems. *Chem. Eng. Sci.*, **28**(1):139–147, 1973.

[178] R. J. Whittaker, R. Booth, R. Dyson, *et al.* Mathematical modelling of fibre-enhanced perfusion inside a tissue-engineering bioreactor. *J. Theor. Biol.*, **256**(4):533–546, 2009.

[179] D. P. Williams, R. Shipley, M. J. Ellis, S. Webb, J. Ward, I. Gardner, and S. Creton. Novel *in vitro* and mathematical models for the prediction of chemical toxicity. *Toxicol. Res.*, **2**:40–59, 2013.

[180] T. Wintgens, J. Rosen, T. Melin, C. Brepols, K. Drensla, and N. Engelhardt. Modelling of a membrane bioreactor system for municipal wastewater treatment. *J. Membr. Sci.*, **216**(1-2):55–65, 2003.

[181] C.-C. Wu, Y.-C. Chao, C.-N. Chen, S. Chien, Y.-C. Chen, C.-C. Chien, J.-J. Chiu, and B. L. Yen. Synergism of biochemical and mechanical stimuli in the differentiation of human placenta-derived multipotent cells into endothelial cells. *J. Biomech.*, **41**(4):813–821, 2008.

[182] F. J. Wu, M. V. Peshwa, F. B. Cerra, and W. Hu. Entrapment of hepatocyte spheroids in a hollow fiber bioreactor as a potential bioartificial liver. *Tissue Eng.*, **1**(1):29–40, 1995.

[183] L. Xia, S. Ng, R. Han, X. Tuo, G. Xiao, H. L. Leo, T. Cheng, and H. Yu. Laminar-flow immediate-overlay hepatocyte sandwich perfusion system for drug hepatotoxicity testing. *Biomaterials*, **30**(30):5927–5936, 2009.

[184] K. Yamamoto, T. Sokabe, T. Watabe, K. Miyazono, J. K. Yamashita, S. Obi, N. Ohura, A. Matsushita, A. Kamiya, and J. Ando. Fluid shear stress induces differentiation of Flk-1-positive embryonic stem cells into vascular endothelial cells in vitro. *Am. J. Physiol. Heart Circ. Physiol.*, **288**(4):H1915–H1924, 2005.

[185] K. Yamamoto, T. Takahashi, T. Asahara, N. Ohura, T. Sokabe, A. Kamiya, and J. Ando. Proliferation, differentiation, and tube formation by endothelial progenitor cells in response to shear stress. *J. Appl. Physiol.*, **95**(5):2081–2088, 2003.

[186] H. Ye, D. B. Das, J. T. Triffitt, and Z. Cui. Modelling nutrient transport in hollow fibre membrane bioreactors for growing three-dimensional bone tissue. *J. Membr. Sci.*, **272**(1-2):169–178, 2006.

[187] H. Ye, Z. Xia, D. J. P. Ferguson, J. T. Triffitt, and Z. Cui. Studies on the use of hollow fibre membrane bioreactors for tissue generation by using rat bone marrow fibroblastic cells and a composite scaffold. *J. Mater. Sci. Mater. Med.*, **18**(4):641–648, 2007.